UNIVERSITY OF CAPE TOWN

FACULTY OF ENGINEERING AND THE BUILT ENVIRONMENT

Department of Civil Engineering

Investigating the Dynamic Soil Behaviour of Cape Flat Sands Under Earthquake Cyclic Loading

Author: Otim Gerald Innocent
Main Supervisor: Prof. Denis Kalumba
Co-Supervisor: Prof. Jie Han

A thesis submitted in partial fulfilment of the requirement for award of the degree of Master of Science in Civil Engineering Specializing in Geotechnical Engineering at the University of Cape Town

[June, 2023]

Plagiarism declaration

I know the meaning of plagiarism and declare that all the work in the document, save for that which is properly acknowledged, is my own. This thesis/dissertation has been submitted to the Turnitin module (or equivalent similarity and originality checking software) and I confirm that my supervisor has seen my report and any concerns revealed by such have been resolved with my supervisor.

Signed by candidate

Signature: _____ **Date:** 30th June, 2023

Student Name: Otim Gerald Innocent

Dedication

This research project is dedicated to the future of geotechnical earthquake engineering in Southern Africa and the continent at large.

Acknowledgements

I wish to acknowledge certain institutions and individuals for their contributions towards completing this research study report.

I want to thank my course mates and friends for their unconditional support in enabling me to complete this research study.

Special thanks go to the geotechnical research group for providing a fully equipped geotechnical laboratory, well-qualified laboratory technicians and laboratory manager. At all times, laboratory consumables were well stocked, and customized requests for consumables were fulfilled within the shortest time possible. The research group also coordinated interactive webinars, workshops and scientific research writing seminars that boosted my knowledge base in this research field. I also thank the civil engineering department for having a well-structured organizational system that allowed me to seek administrational assistance. I also thank the UCT library for having an up-to-date database from which I could get the most recent research journals and articles that provided a foundation for his research.

I want to thank EduPro Civil Systems, Inc for upgrading my version of EduShake software (version 2.0, an open-source software available on the website) with limited ground responses analyses to a professional version of ProShake (2.0.1.14) for up to six months, which enabled me to utilize customized ".AT2" files from Pacific Earthquake Engineering Research (PEER) website and present the output within this study.

Lastly, I humbly acknowledge with sincere gratitude my main supervisor, Prof. Denis Kalumba and co-supervisor, Prof. Jie Han, for their advice, inspiration, and guidance during the research activities, which made the research activities enhancing and a developmental experience. It is their persistent criticism that has brought hope and confidence during the execution of this research. Their input was constructive when writing and compiling this report and is worth noting. Although the contents expressed in this report remain my own, the ability to engage in debates and discussions remains the responsibility of my research supervisors.

For all the great assistance, may the almighty God bless the works of their hands.

Abstract

Most geotechnical structures are surrounded by partially or unsaturated soils, which can greatly affect their dynamic properties, such as shear modulus and damping ratio. Therefore, this necessitates an inclusive methodology to consider and incorporate the degree of saturation in seismic analyses to ensure that seismic designs are not overly conservative based on local soil conditions. In Cape Town, South Africa, limited soil characterization on cyclic testing has been executed on Cape Flat Sands, although the area is in a sensitive seismic region of magnitude M_L 6.1 - 7.5. As a result, geotechnical engineers may be using dynamic correlations that are too conservative due to limited assumptions about soil type, earthquake response, relative density, plasticity, confining pressure, and saturation level.

The cyclic properties of the Cape Flat Sands were evaluated at ten different cyclic axial strains (0.005%, 0.01%, 0.02%, 0.05%, 0.1%, 0.2%, 0.4%, 0.6%, 0.8% and 1.0%), three relative densities (loose dense, medium dense, and dense), and five saturation levels (0%, 25%, 50%, 75% and 100%). The tests were conducted using cyclic triaxial equipment, and soil classification tests were performed according to the latest standards of the American Society for Testing Materials (ASTM).

The Unified Soil Classification System classified the Cape Flat Sands as poorly graded sand. The results of the undrained cyclic triaxial tests, which measured shear modulus, damping ratio, and excess pore pressure ratio, are also included. Based on the results, correlations were developed to determine the relationship between the damping ratio and normalized shear modulus. Additionally, the applicability of existing dynamic models was evaluated by superimposing them on the test data for shear modulus, damping ratio, and excess pore pressure ratio. To identify the factors and their interactions that affected the values of the shear modulus, damping ratio, and excess pore pressure ratio, MANOVA was conducted. Repeatability and quality control of results was carried out to ensure that the results were precise and reproducible using the same test standard and operator. A ground response and free vibration analysis of a five-storied building were executed using ProShake software and Plaxis 2D software. This was achieved using the normalized shear modulus and damping ratio with shear strain curves against a soil profile obtained along the R300 road within the Cape Flats region. A water table underlay this soil profile at 2.45m depth, enabling varying saturation states to be adopted. The Nahanni (1985)-RSN497 ground motion from the PEER NGA ground database was adapted for dynamic analysis. The results of the ground response analysis, free vibration and earthquake analysis showed that the different saturation states, relative density, and equivalent dynamic properties influenced the behavior of the ground motion parameters for each respective sandy layer. This study has provided invaluable insights into the dynamic properties of Cape Flat Sands under earthquake cyclic loading and it has also highlighted specific areas that require further research to enhance its understanding.

Table Of Contents

List of Figures

List of Tables

Notations and Abbreviations

ACU	Anisotropically Consolidated Undrained
ASTM	American Society for Testing and Materials
AT2	File extension for Auto Template file
atm	atmosphere
B	Skempton's B value
BH	Bore Hole
CBR	California Bearing Ratio
C_c	coefficient of curvature
CHT	Cross-Hole Test
CO_2	Carbon dioxide
CPT	Cone Penetration Test
CPTu	Piezocone Test
CPU	Central Processing Unit
CRR	Cyclic Resistance Ratio
CSR	Cyclic Shear Stress Ratio
C_u	coefficient of uniformity
DHT	Down-Hole Test
DMT	Dilatometer Test
D_R, D_r	Relative density
e	void ratio
EMS	European Macroseismic Scale
EP	External Pressure
EPRI	Electric Power Research Institute
EQL	Equivalent Linear
EPWP	Excess Pore Water Pressure
F(e)	function of void ratio e,
G	shear modulus
G_{max}	Maximum shear modulus
GMPEs	Ground Motion Prediction Equations
G_{sec}	secant shear modulus
G_{tan}	tangent shear modulus
Hz	Hertz
IAEA	International Atomic Energy Agency
I_p, PI	Plasticity Index
JMA	Japanese Meteorological Agency
k	Over-consolidation ratio exponent
k_c	consolidation ratios
LCD	Liquid Crystal Display
LDT	Local Displacement Transducer
LEMA	Linear Electro-Mechanical Actuator
M	Earthquake moment magnitude
MANOVA	Multivariate analysis of variance
M_b	Body wave magnitude
MCS	Mercalli-Cancani-Seiberg
M_L	Local (Richter) magnitude
MM	Modified Mercalli
mm	millimeter
M_s	Surface wave magnitude
MSF	Magnitude Scaling Factor
MSK	Medvedev-Sponheuer-Karnik

M_w	Moment magnitude
N	number of loading cycles
n.a	Not applicable
NC	Normally Consolidated
NGA	Next Generation Attenuation Relationships
NP	Non-plastic
OCR	Over consolidation Ratio
PEER	Pacific Earthquake Engineering Research
PGA	Peak Ground Acceleration
PGD	peak ground displacement
PGV	peak ground velocity
PL	Plastic Limit
PMT	Pressuremeter Test
PPV	Peak Particle Velocity
PSHA	Probabilistic Seismic Hazard Assessment
PWPR	Pore Water Pressure Ratio
RSN	Record Serial Number
r_u	Excess Pore Water Pressure Ratio
SANS	South African National Standard
SANSN	South African National Seismograph Network
SASW	Spectral Analysis of Surface Waves
SCPT	Seismic Cone Penetrometer Test
SCR	Stable Continental Region
sec./s	seconds
smc	File extension for strong motion CD-ROM file
SP	Poorly graded sands
SPSS	Statistical Package for the Social Sciences
SPT	Standard Penetration Test
S_r, SAT	degree of saturation
SSI	Soil Structure Interactions
STR	Cyclic axial strain
T	fundamental period of vibration
URM	unreinforced masonry
USA	United States of America
V_p	P-wave velocity
V_R	Rayleigh wave velocity
V_s	S-wave velocity
γ_{1v}	Volumetric cyclic threshold shear strain
γ_{c1}	very small strain elastic regime
γ_{td}	large strain threshold
γ_{tv}	volumetric cyclic threshold shear strain
Δu	excess pore water pressure
ε_a	Cyclic Axial Strain Cycles
λ	Damping ratio
λ_{max}	Maximum damping ratio
σ'_{3c}	minor effective consolidation stress
σ'_{3c}	minor effective consolidation stress
γ	Shear strain
γ_r	reference strain
ρ	Bulk density

1 Introduction

1.1 Background

Civil engineering infrastructure are designed to withstand numerous environmental load intensities like earthquakes, winds, ocean waves, explosions, machinery vibrations, cyclic transient loading, and related dynamic loads (Jia, 2018; Seymour, 2018; Mawer et al., 2017; Kiptoo et al., 2017). These load intensities induce dynamic loadings that are transferred to the soils and/or foundations, which when well-accounted for during the design phase, can lead to sound integrity, operational functionality and structural integrity of any infrastructure (Chowdhury, Ghosh, & Dasgupta, 2016). Under these loading intensities, the soil response entirely depends on both the imposed nature of the dynamic loads and mechanical soil properties (Jia, 2018). These dynamic properties that are used to characterize dynamic properties include shear modulus, degradation indices, damping, Poisson's ratio, and density (Yang, Luo, Chen, & Mou, 2020). In addition, information which includes the presence of groundwater, degree of saturation, and grain size may be necessary to evaluate a potential soil dynamic problem and consequently challenge the analysis accuracy requirements (Jia, 2018; Li, Nie, Yue, Leng, & Guo, 2021; Yang et al., 2020).

Cyclic loads like earthquakes comprise of seismic ground motions whose characteristics are significantly affected by site conditions such as the local soil geotechnical properties and topography. Moreover, the intensity of seismic ground motions are affected by the distance from the motion source, fault size, and released strain energy in rock and local geology (Fardis, 2010; Towhata, 2008; Yang et al., 2020). These seismic ground motions can result in catastrophic events that entail economic losses, loss of human life, and environmental destruction. In a seismic environment, the loads imposed on the foundation from a super-structure can greatly exceed the static vertical loads leading to uplift, creating horizontal forces and possibly moments at the foundation level (Jia, 2018; Seymour, 2018; Mawer et al., 2017). This arises the need for the consideration of dynamic soil behavior of the specific geological hazards during the seismic vulnerability assessment of an existing structure or during the design stage.

The seismic design of foundations depends on the dynamic bearing capacity, dynamic settlements and liquefaction susceptibility of the soil, which are all induced through earthquake ground motions that trigger the dynamic soil behavior (Jia, 2018). This phenomenon can cause permanent deformation when the stress variations cause shear or tensile strength to be surpassed. Loose, saturated cohesionless soils contract as the soil particles are rearranged when subjected to earthquake motions. Soil is said to experience a significant reduction in its shear strength when its pore pressure increase is enough to reduce the effective stress to nearly zero (Towhata, 2008). In dense, saturated, cohesionless soils, large shear displacements may not occur. The temporary occurrence of excess pore water ratios of 100% is accompanied by the development of limited strains, resulting in progressive and incremental lateral movements. Whether or not the soil around the foundation ultimately experiences a significant reduction in its shear strength. When sufficient

reduction occurs, over an adequate extent, large deformations can consequently yield due to pore water dissipation after an earthquake-induced ground motion (Fardis, 2010; Jia, 2018; Towhata, 2008).

In the laboratory, the dynamic soil behavior under earthquake ground motions can be evaluated and simulated using the cyclic Triaxial test, simple shear test, torsional shear test, and resonant column test to obtain a wide range of dynamic soil properties with respect to the modulus and damping ratio (Chowdhury et al., 2016; Fardis, 2010; Li et al., 2021; Seymour, 2018; Sun, Cai, Chu, Dong, & Wang, 2017; Whang, Stewart, & Bray, 2004).

Most geotechnical structures are surrounded by either unsaturated or partially saturated soils, and the degree and state of saturation can greatly impact their dynamic properties, such as shear modulus and damping ratio. Therefore, it is important to incorporate the degree of saturation in seismic analyses to ensure accurate seismic designs. Understanding the role of degree of saturation on cyclic properties for soil layers may help explain why certain geosystems behave a certain way during an earthquake. It is also essential to consider the local soil stratigraphy, water-table depth, and climatological setting to avoid over-conservative seismic designs (Mousavi, 2020).

Currently, there are various empirical methods used to estimate the soil behavior during earthquake ground motions (Chowdhury et al., 2016). However, many of these methods were developed for sands with limited seismic response properties, leaving a gap in understanding the mechanisms of partially saturated sands (Whang et al., 2004). As a result, these methods may not be universally applicable to all soils present in a seismic environment like Cape Town. Therefore, it is necessary to investigate the local soil properties and their dynamic behavior under cyclic earthquake loading.

1.2 Research Problem

Cape Town is located within a region of high seismicity within South Africa per SANS 10160-4: 2017, and the Milnerton Faultline underlies it. SANS 10160-4: 2017 focuses on the geotechnical seismic parameters of four (4) ground types concerning rock, very dense sand, or very stiff clay, dense or medium dense sand or gravel or stiff clay and loose to medium cohesionless soils. These parameters include shear wave velocity ($v_{s,30}$), N-SPT value and undrained shear strength. However, the seismic standard is silent on shear modulus and damping ratio models for the respective soils that should accompany the ground response analyses during the development of the normalised design response spectra. Owing to the minimal guidance by SANS 10160-4:2017 on the dynamic properties of soil types like Cape Flats Sand, this has prompted the adoption of estimated dynamic properties that include the shear modulus and damping ratio from correlations like Menq (2003); Oztoprak & Bolton (2013); EPRI (1993); Seed et al., (1984); Ishibashi & Zhang (1993); Vucetic & Dobry (1991); Seed & Idriss (1970). These correlations may be overly conservative owing to the limited assumptions such as the type of soils used, simplified approximate earthquake site response and dependency of the void ratio for a given relative density

of soil, soil plasticity, confining pressure, and state of saturation. In addition, limited research has been conducted on evaluating dynamic tests on Cape Flat Sands within South Africa. This necessitated a rigorous approach to understand further and investigate the dynamic soil behaviour of Cape Flat Sands under cyclic earthquake loading. In addition, the mean water table within the Cape Flats is 2m in winter and 3m in summer (Fouche, 2021; Fouché & Day, 2022). This further necessitates the need to evaluate the dynamic soil behaviour under varying states of saturation.

1.3 Research Questions

The research questions for this study included;

a) What were the laboratory classification properties of the Cape Flat Sands?
b) Which dynamic laboratory tests simulated cyclic earthquake loading and what were the key parameters being sought?
c) Which key dynamic soil properties are important for correlations and which software were adopted to achieve this?
d) How could the dynamic soil test results obtained from this study be demonstrated in a geotechnical engineering project?

1.4 Research Objectives

The main objective in this research was to investigate the dynamic soil behavior of Cape Flat Sands under earthquake cyclic loading.

1.4.1 Specific Objectives

a) Establishing the physical characteristics of Cape Flat Sands,
b) Evaluating the dynamic characteristics of Cape Flat Sands under cyclic earthquake loading,
c) Developing correlations between the investigated dynamic soil properties under cyclic earthquake loading,
d) Demonstrating application of the results to a suitable geotechnical project.

1.5 Research Assumptions

The following research assumptions were adopted;

i. The soils used were representative of the Cape Flat sands,
ii. The relative density, degree of saturation, cyclic axial strain, effective confining pressure, and number of cycles influence the dynamic characteristics of the Cape Flat Sands,

iii. During the statistical analysis, the observations are independent such that the residuals follow a multivariate normal probability distribution with means equal to zero and the variance-covariance matrices of each group of residuals are equal.

1.6 Scope and Limitations

This research involved the application of a constant effective confining pressure of 100 kPa, a constant number of cycles based on the seismic level (10 cycles), variation of relative density, variation of degree of saturation and cyclic axial strain of Cape Flat Sands using dynamic triaxial equipment from 0.005% - 1.0%.

The research activities were restricted to only cyclic triaxial laboratory tests (no in-situ tests), constant frequency, constant effective confining pressure, one type of soil (only sands) and shear strains ranging from 0.0001%-0.005% were outside the range of accuracy for the cyclic equipment.

1.7 Research Significance

This study sought to expand the current limited knowledge on the dynamic soil behavior of sands under cyclic earthquake loading, particularly in earthquake-prone regions within Southern Africa. To meet this challenge, it was necessary to identify potential ground conditions for any geotechnical infrastructure under which dynamic properties within these regions could be evaluated. The study sought to assess dynamic conditions for ground conditions under varying saturation states (dry, partially saturated, and fully saturated), relative densities (loose, medium dense, and dense), and shear strains (small to large strains) to enhance knowledge in this field.

Furthermore, estimating pre-failure dynamic response was crucial in meeting the increasing need for seismic design and analysis based on performance. To carry out such an analysis, it was essential to have a reliable comprehension of dynamic shear modulus, damping, and pore-pressure generation in a three-phase medium with varying ground conditions previously mentioned.

Additionally, this study aimed to enhance guidance on the dependability and reliability of dynamic soil models used for forecasting dynamic properties, such as shear modulus/normalized shear modulus and damping ratio.

This study sought to provide a basis for updating local and regional seismic codes for the site response analysis, which relies on dynamic soil properties. This would help create long-lasting foundation designs for geotechnical engineering, which can support civil infrastructure during earthquakes. By developing effective seismic designs, the impact of natural disasters such as earthquakes on civil infrastructure could be minimized, thereby reducing the risk of building collapse, amongst other risks.

1.8 Research Framework

The research framework for this proposed research study was presented in Figure 1-1.

1.9 Organization of the Thesis

The research was split up into five (5) chapter presented below;

Chapter 1	**-Introduction:** This chapter presents the research background, research problem, research objectives, research framework, research assumptions and research location,
Chapter 2	**-Literature Review:** This chapter provides knowledge on site response analysis, seismic assessment of South Africa, dynamic properties of sands, Cape Flat Sands, Past research in the world over and in South Africa,
Chapter 3	**-Methodology:** This chapter provides the experimental program, laboratory tests carried out and the test standards followed, approach for regression analysis, development of correlations and their statistical MANOVA, and procedure for demonstrating the applicability of the results obtained to geotechnical engineering.
Chapter 4	**-Results and Discussion:** This chapter presents the physical and dynamic properties of Cape Flat Sands, a discussion of the effects of saturation to cyclic properties and their respective comparison to past literature, development of correlations between the cyclic properties, MANOVA analysis, presentation of the quality control assurance mitigation strategy and demonstration of the applicability of the results to geotechnical engineering through ground response, free vibration and earthquake analysis of a five-storied building with a basement
Chapter 5	**-Conclusions:** This chapter presents a summary and closure of the research objectives in line with the results and finding obtained to give an overall view and evident appreciation of the research project.

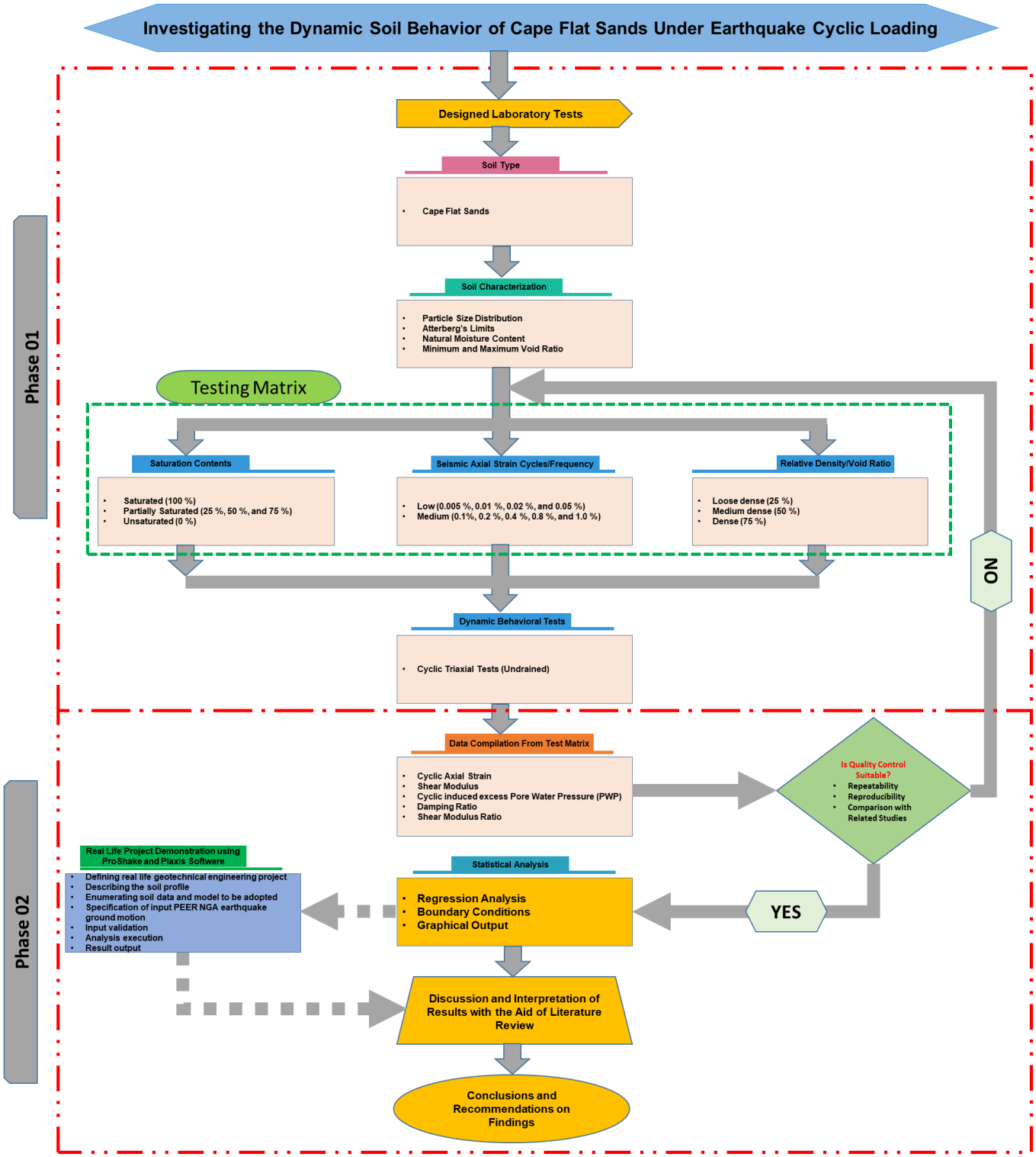

Figure 1-1: Research framework

2 Literature review

2.1 Site Response Analysis

Earthquake loads on structures are different from loads generated by wind, waves, current, and ice. They are induced by ground accelerations transferred to the foundation of the structures (Jia, 2018; Ye & Lu, 2022). Four primary factors determine the earthquake ground excitation: the seismic source, transmission of the excitation, local geotechnical effects on soil motion, and soil structure interactions (SSI) during the earthquake events (Jia, 2018; Pinzón, Mánica, Pujades, & Alva, 2020; Ye & Lu, 2022). The level of ground shaking is influenced by the fault-rupture mechanism, source-to-site distance, and local soil effects. Additionally, the dynamic and vibration characteristics of structures strongly influence the seismic loading applied to them (Jia, 2018).

When seismic waves move away from a fault rupture, they spread out and are partially absorbed by the media they travel through. This results in a reduction in seismic energy as the distance between the source and the site increases. Assuming the transmission media has isotropically elastic characteristics, the effects of the nature and length of the intermediate path from the fault to a site at bedrock or rock outcrop can be estimated using attenuation relationships or ground motion prediction equations (GMPEs) (Jia, 2017; Jia, 2018; López-Castañeda & Reinoso, 2021). After reaching the bedrock or rock outcrop, the seismic wave continues through soil media before arriving at the ground surface or structural foundations, as shown in Figure 2-1 (Khanbabazadeh, Iyisan, & Ozaslan, 2022; Pinzón et al., 2020).

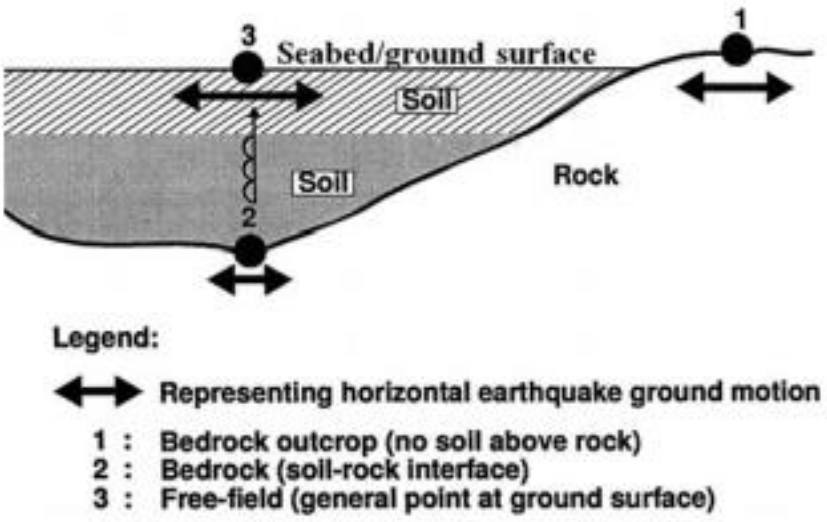

Figure 2-1: Illustration of seismic wave transmission from the bedrock [2] to the ground surface/seabed [3] (Jia, 2018)

The soil media will work as a filter to tune the energy and frequency of the seismic wave. This attenuation process usually eliminates high-frequency motion. It filters the signal into a narrow-

frequency motion at the seabed, with amplification at and around the resonance period of the soil column at the site, known as the site period, as illustrated in Figure 2-2 (Jia, 2018; Khanbabazadeh et al., 2022; SW-AJA, 1971).

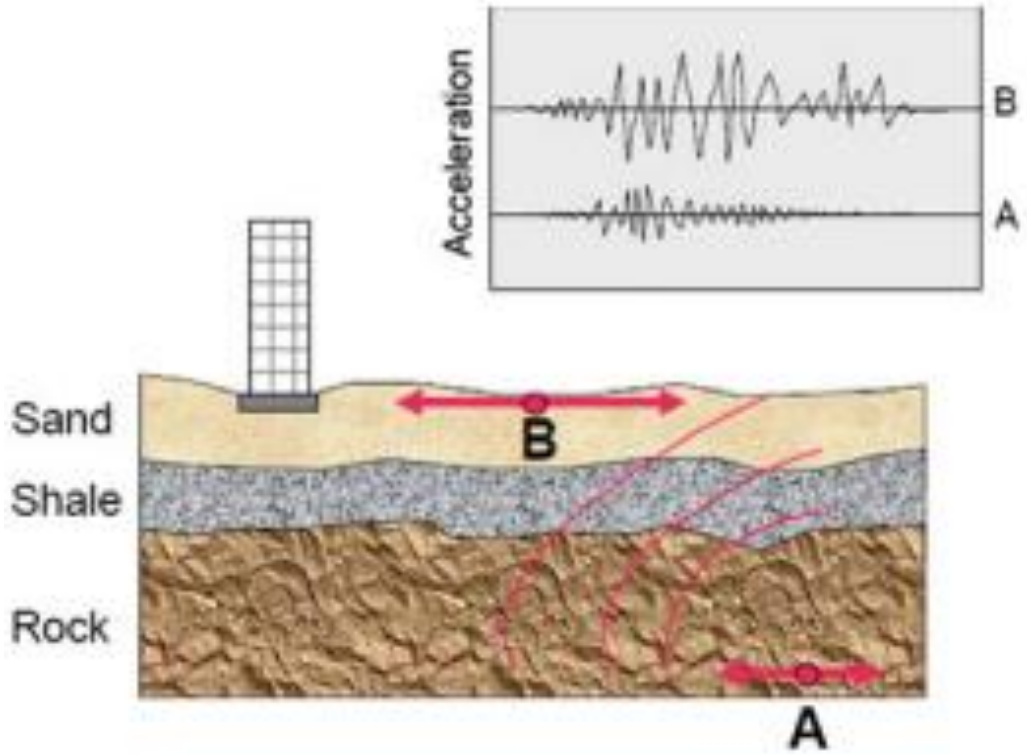

Figure 2-2: Transmission of a seismic wave through soil layers with attenuation of seismic wave in both energy (represented by motion amplitude) and frequency content (Jia, 2018)

2.1.1 Site Period

The soil can affect the frequency and magnitude of ground motions by acting as a filter for bedrock movements. If the soil is dense/stiff, the ground motions will be short, while loose/soft soil will cause longer ground motions (Jia, 2018; López-Castañeda & Reinoso, 2021).

2.1.2 Peak Ground Acceleration (PGA)

When it comes to providing information for geotechnical and structural engineers, PGA (peak ground motion acceleration) is more directly useful than magnitude (section 2.1.3.2) or intensity (Section 2.1.3.1). Figure 2-3 shows PGA and it is particularly helpful for geotechnical and structural engineers constructing a design spectrum (Jia, 2018).

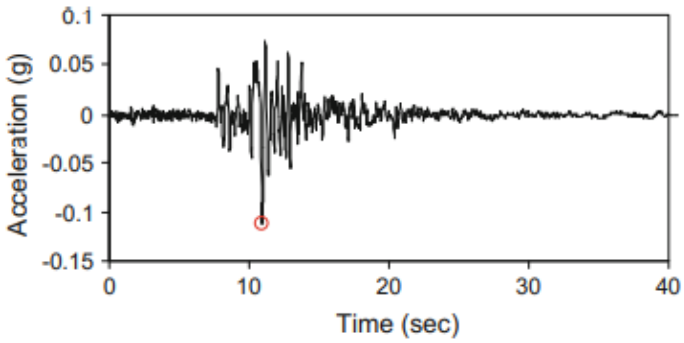

Figure 2-3: Recorded ground motions with a PGA of 0.11g (Jia, 2018)

Although PGA is a reliable measure for assessing ground motion intensity, it can also be used in conjunction with earthquake time history, power spectrum, or design spectrum to determine the frequency content of the ground motion (Jia, 2018). Figure 2-4 displays the recorded ground motion data, including acceleration, velocity, and displacement time series, which suggests that PGA is associated with high-frequency signals, the peak ground velocity (PGV) with intermediate-frequency motions, and the peak ground displacement (PGD) with low-frequency motions (Jia, 2018).

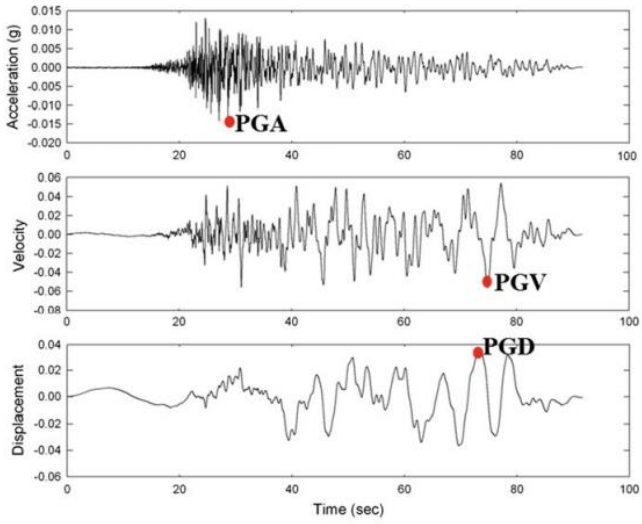

Figure 2-4: Recorded acceleration, velocity, and displacement time histories (Jia, 2018)

2.1.3 Measuring Earthquakes

2.1.3.1 Intensity

Intensity is a non-instrumental perceptibility measure of damage to structures and ground surface effects to earthquake shaking to establish earthquake size. This subjective measure has led to several worldwide intensity scales that include; Mercalli-Cancani-Seiberg (MCS), Modified

Mercalli (MM), Medvedev-Sponheuer-Karnik (MSK), European Macroseismic Scale (EMS) and Japanese Meteorological Agency (JMA) (Amr & Luigi, 2008).

2.1.3.2 Magnitude

Magnitude is a quantitative measure of earthquake size and fault dimensions based on the maximum amplitude of body or surface seismic waves. Several magnitude scales have been proposed over the years, and the most common include Local (Richter) magnitude (M_L), Body wave magnitude (M_b), Surface wave magnitude (M_s) and Moment magnitude (M_w) (Amr & Luigi, 2008). The specific properties of the above magnitude scales can be summarized in Table 2-1.

Table 2-1: Properties of major earthquake scales

Scale type	Author	Earthquake size	Earthquake depth	Epicenter distance (km)	Reference parameter	Applicability	Saturation
M_L	Richter (1935)	Small	Shallow	< 600	Wave amplitude	Regional (California)	✓
M_b	Gutenberg and Richter (1956)	Small to medium	Deep	>1000	Wave amplitude (P-waves)	Worldwide	✓
M_S	Richter and Gutenberg (1936)	Large	Shallow	>2000	Wave amplitude (LR-waves)	Worldwide	✓
M_W	Kanamori (1977)	All	All	All	Seismic moment	Worldwide	n.a.
	n.a.	Not applicable					
	✓	Saturation occurs					

2.1.3.3 Earthquake Records

There are three main approaches to obtaining earthquake ground motion records for advanced analyses in geotechnical engineering, and these include (Amr & Luigi, 2008);

i. Natural records of earthquakes have been compiled over the past decade and are available as strong motion data like the Pacific Earthquake Engineering Research Center (PEER) (Bommer & Acevedo, 2004).
ii. Artificial records through generating random signals (random vibration theory) that fit a target spectrum with a certain degree of approximation. A comparison of the natural and an equivalent set of artificial records is presented in Figure 2-5.
iii. Mathematical formulation-based records adopted from mathematical source models to generate time series that look like earthquake-strong motion owing to advancements in earthquake geophysics and wave propagation modelling.

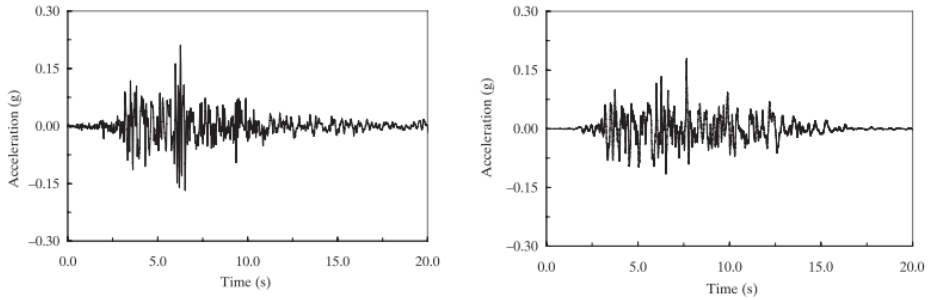

Figure 2-5: Natural record (left) at Westmorland Brawley, N45W (California, 1981) and relative artificial record generated (right) (Amr & Luigi, 2008)

2.1.4 Effects of Earthquakes

Earthquakes can cause several devastating direct and indirect effects on life and livelihood, as summarized in Figure 2-6.

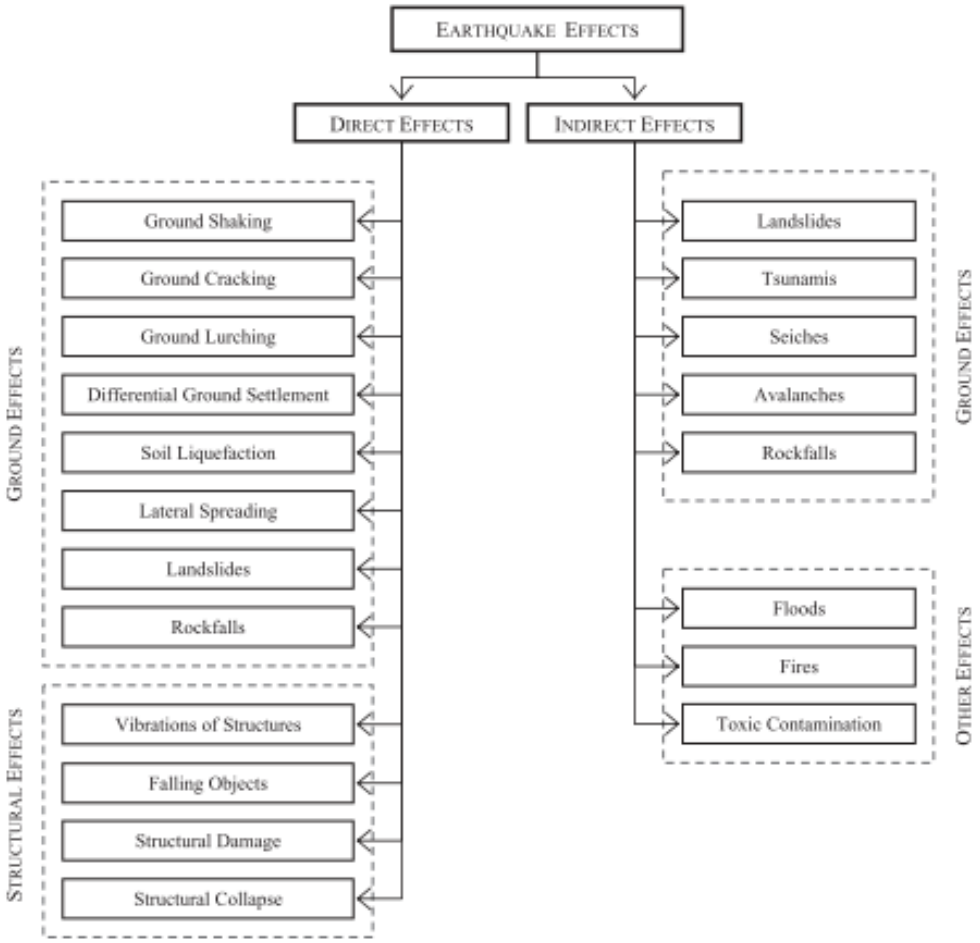

Figure 2-6: Direct and indirect earthquake effects (Amr & Luigi, 2008)

2.2 Seismic Assessment of South Africa

South Africa is located within a 'stable continental region' (SCR), distant from active tectonic plates and continental rifts (Johnson & Kanter 1990). This does not rule out the phenomena of large earthquakes; however, they are far less frequent than the tectonically active regions such as Italy, Japan, and the western USA, owing to their return periods being in centuries or millennia. The relative comparison of the highly prone earthquake regions in South Africa compared to the African continent is presented in Appendix 1. Nevertheless, South Africans cannot afford to be complacent in an unexpected occurrence neither should they neglect its danger. A moderate-sized earthquake with a shallow focus occurring close to a town can be devastating, especially if the buildings are not designed to be earthquake-resistant, the terrain is steep and prone to landslides, or the soil is thick and prone to amplification and liquefaction (Durrheim, 2015; Durrheim & Manzunzu, 2018).

Seismicity in South Africa arises from both natural sources (plate tectonic forces, buoyant uplift of the continent after erosion) and human-induced sources (rock failure caused by mining-induced stresses, slip on faults caused by changes in load and pore fluid pressure during the filling of reservoirs, and vibrations produced by blasting for open pit mining, civil excavation and the disposal of expired munitions) (Durrheim & Manzunzu, 2018). Most earthquakes are induced by deep-level mining for gold and platinum and are thus restricted to the mining districts. On the other hand, between 40 and 60 tremors occur monthly, focused primarily in the gold-mining areas of Gauteng, North West Province and the Free State (Wium, 2006). Over eight damaging earthquakes ($5.0 < M_L < 6.3$) have occurred in South Africa during the last 120 years, of which five had an unequivocal tectonic origin, while three were in mining districts (Durrheim & Manzunzu, 2018). Thus, a potentially damaging earthquake (say $5.0 < M_L < 6.5$) occurs somewhere in South Africa, on average, every 10-20 years, with structural damage being limited to a 100 km radius from the epicenter (Durrheim & Manzunzu, 2018). Three of these earthquakes caused deaths: the toll of the 1969 Ceres-Tulbagh earthquake is reported as nine; two underground workers died as a result of the 2005 Stilfontein earthquake; and a collapsed garden wall killed one person during the 2014 Orkney earthquake (Durrheim & Manzunzu, 2018).

More significant tectonic earthquakes ($6.5 < M_L < 8.0$) are rare in stable regions but may occur both on faults with a recent (100s - 10,000s years) history of earthquake activity, and in areas, with no known precursory activity as thus such events could therefore take place anywhere (Durrheim & Manzunzu, 2018). Therefore, the locations of historical earthquakes cannot be taken as reliable indicators of areas where large earthquakes will occur. Three damaging $M_L > 6$ tectonic earthquakes have happened in the last 120 years: in the Western Cape (M_L 6.3, 1969), northern KwaZulu- Natal (M_L 6.3, 1932), and the southern Free State (M_L 6.2, 1912) (Durrheim & Manzunzu, 2018). The most significant earthquakes ($M_L \geq 5.0$) in South Africa are summarized in Table 2-2;

Table 2-2: Significant earthquakes ($M_L \geq 5.0$) in South Africa since 1900

Date	Region	Depth (km)	Magnitude, M_L	Source
5/8/1909	Northern Zoutpansberg	-	5.0	(Wood, 1913)
21/10/1910	Near Philipstown	-	5.0	(Wood, 1913)
20/02/1912	Koffiefontein	-	6.2	(Wood, 1913)
31/12/1932	Off Cape St Lucia	-	6.3	(Krige & Venter 1933)
8/11/1952	Southwestern Botswana region		5.2	(Midzi et al., 2020a)
9/29/1969	Cape Province (Ceres-Tulbagh)	32	6.3	NGDC/WDS, 2022
10/5/1969	Tulbagh	-	5.8	NGDC/WDS, 2022
11/9/1969	Cape Fold Belt East	-	5.2-7.2	(Midzi et al., 2020a)
12/8/1976	Near Welkom	25	5.2	NGDC/WDS, 2022;
7/21/1997	Avgold's Hartebeestfontein Mine	49	5.0	NGDC/WDS, 2022
9/3/2005	Near Stilfontein	-	5.3	(Durrheim et al., 2006)
23/02/2006	Machaze district, Mozambique*	-	7.0	(Saunders et al., 2010)
8/5/2014	Orkney	38	5.5	(Midzi et al., 2015b)
3/4/2017	Central Botswana*	-	5.5	(Midzi et al 2018a)
3/4/2017	Zoetfontein fault region	-	6.5	(Midzi et al., 2020a)
*Occurred out of South Africa but was felt as far as Johannesburg and Gauteng				

2.2.1 Potentially Active Faults in South Africa

Manzunzu et al., (2019) compiled a map of potentially active faults during the Quaternary (2.588±0.005 million years ago to the present), as presented in Figure 2-7. Only two of these faults (Kango (Figure 2-8) and Bosbokpoort) have palaeoseismological evidence of large earthquakes of magnitude exceeding $M_L \geq 7$ that caused surface ruptures. The location of recorded earthquakes in Southern Africa from 1811-2014 is presented in Figure 2-9.

Identifying actual seismicity sources in South Africa has been challenging owing to their relatively small magnitudes, non-surface rupture and sparsely distributed seismic stations, which make it challenging to associate events with known mapped faults (Midzi et al., 2020b; Saunders et al., 2016). New identification methods like focal mechanisms in Figure 2-10 and stress field data (Meghraoui et al., 2016) are helpful in the characterization of faults and delineation of seismic source zones.

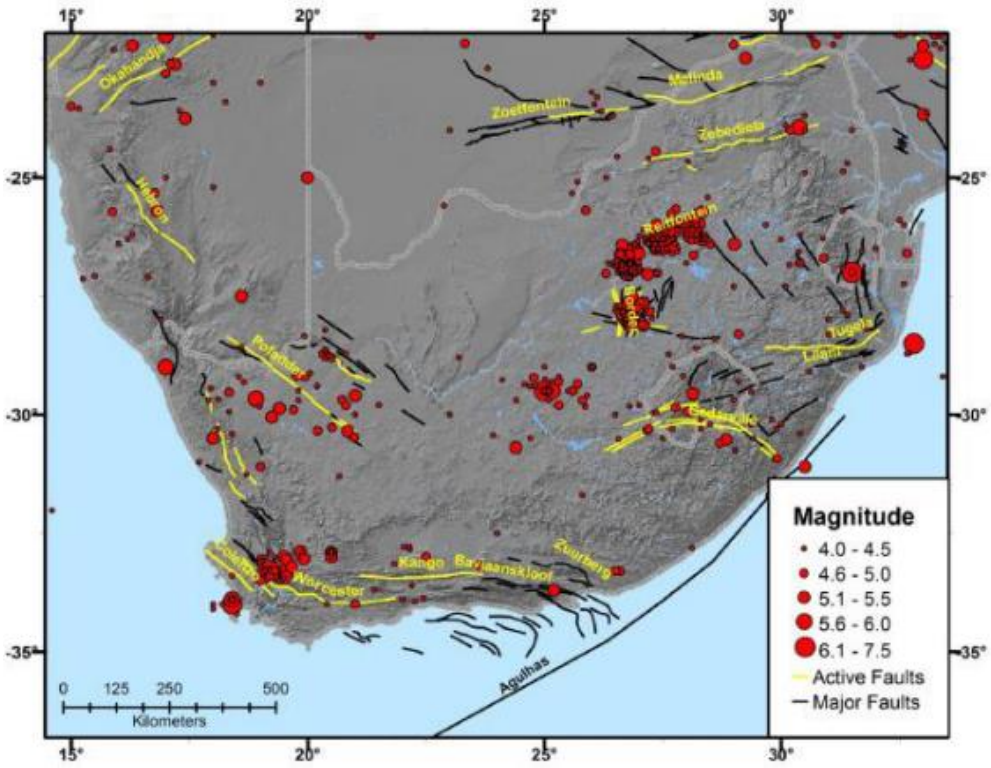

Figure 2-7: Major faults of southern Africa, Faults potentially active during the Quaternary (2.588 ± 0.005 million years ago to the present) are shown in yellow. The red circles comprehend earthquake magnitudes in southern Africa that exceeds 4.0 (Manzunzu et al., 2019)

Figure 2-8: The Kango fault showing part of an 84 km long and 2m high fault scarp produced by an Mw 7.4 event about 10600 years ago (Midzi & Goedhart, 2009)

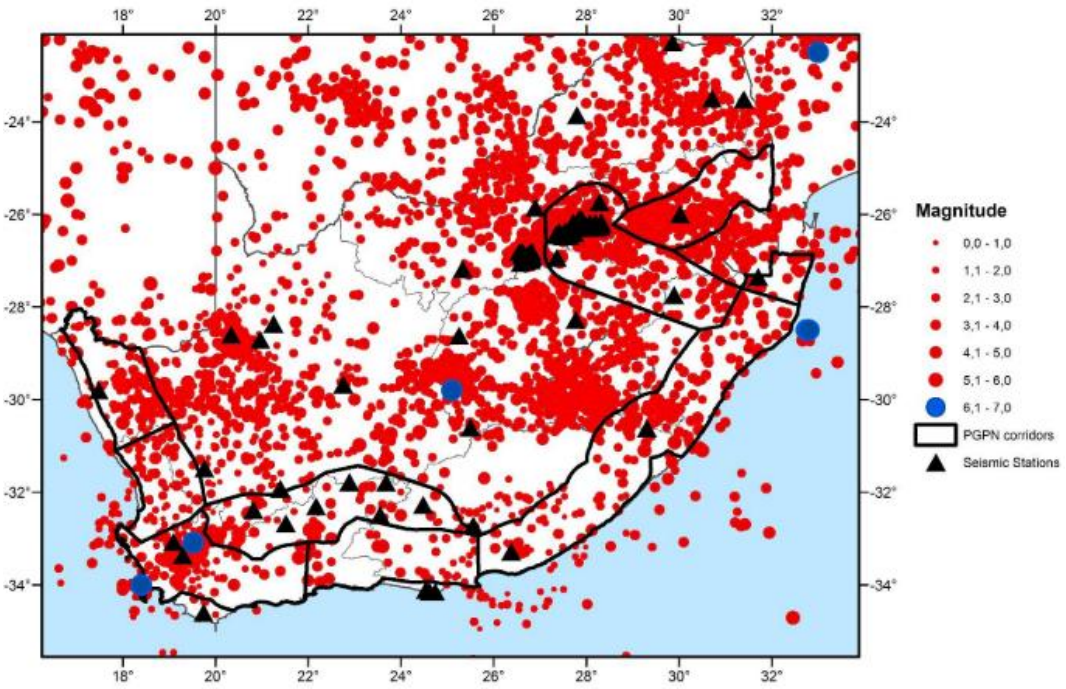

Figure 2-9: Location of recorded earthquakes in southern Africa from 1811-2014. Triangles mark the position of the stations that comprise the South African Standard Seismograph Network (SANSN) (Durrheim & Manzunzu, 2018)

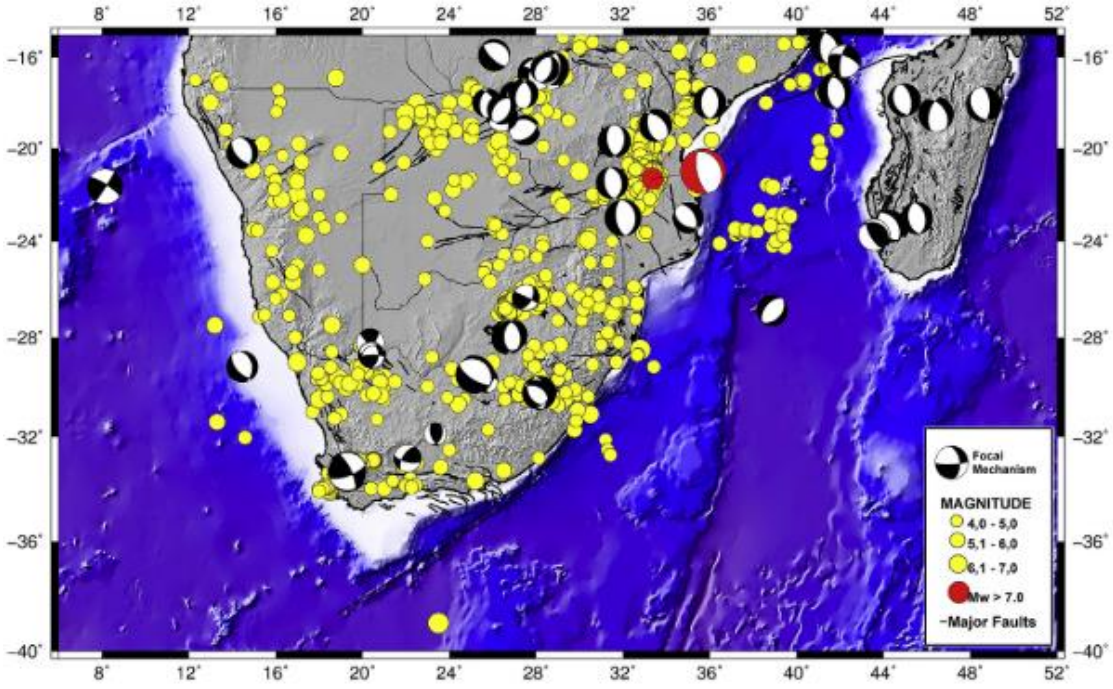

Figure 2-10: A seismotectonic map of southern Africa combining available information used in the identification of seismic sources (Midzi et al., 2020b)

2.2.2 South African Seismic Maps

2.2.2.1 Parametric-Historic Method Hazard Map

The South African National Standard seismic hazard map and hazard zones according to SANS 10160-4, 2017 is displayed in Figure 2-11. This map was created using the parametric historic procedure, which combines the "deductive" and "historic" approaches. The data covers the period from 1620 to December 2000 and includes both natural and mining-induced seismicity (Kijko & Graham 1998; 1999; Kijko, 2003). The map shows the computed 10% probability of exceedance in 50 years, with a return period of 475 years, and the nominal peak ground acceleration expressed in g (9.98 m/s^2) is presented in Figure 2-12.

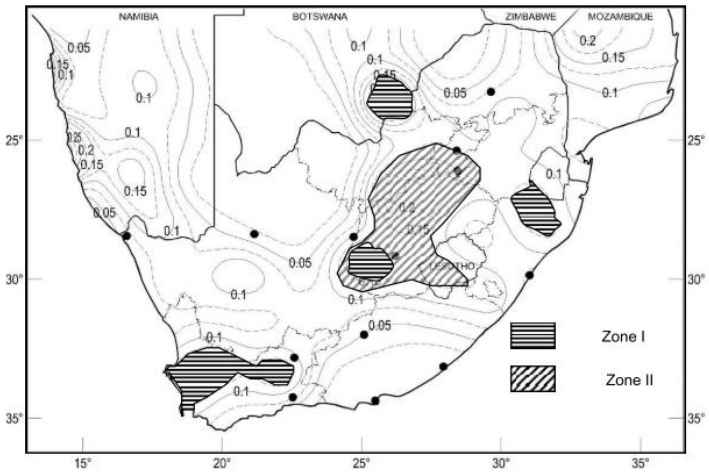

Figure 2-11: South African National Standard seismic hazard map (SANS 10160-4, 2017; Kijko & Graham 1998; 1999)

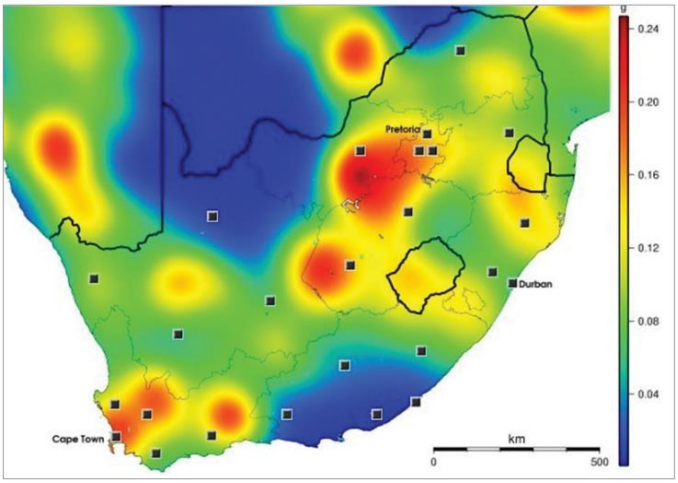

Figure 2-12: South African seismic hazard map: Nominal peak ground acceleration in g (gravity acceleration with a probability of exceedance of 10% in 50 years (Kijko, 2003)

2.2.2.2 Probabilistic Seismic Hazard Assessment (PSHA) Method

The Council of Geoscience recently conducted a comprehensive earthquake PSHA risk assessment in South Africa. This assessment utilized an updated earthquake catalogue with more reliable seismicity and geological data. The catalogue was compiled by systematically combining historical and instrumental events (Midzi et al., 2018; 2020).

Due to the lack of strong ground motion data in South Africa, including the absence of Ground Motion Prediction Equations (GMPEs), two published models [Akkar et al., (2014) and Boore & Atkinson (2008)] from regions with similar tectonics, such as North America (Canada), were selected for use in the PSHA calculations. The maps in Figure 2-13, Figure 2-14 and Figure 2-15 depict the distribution of acceleration at two periods (0.15s [short period] and 2.0s [long period]) computed for a 10% probability of exceedance in 50 years.

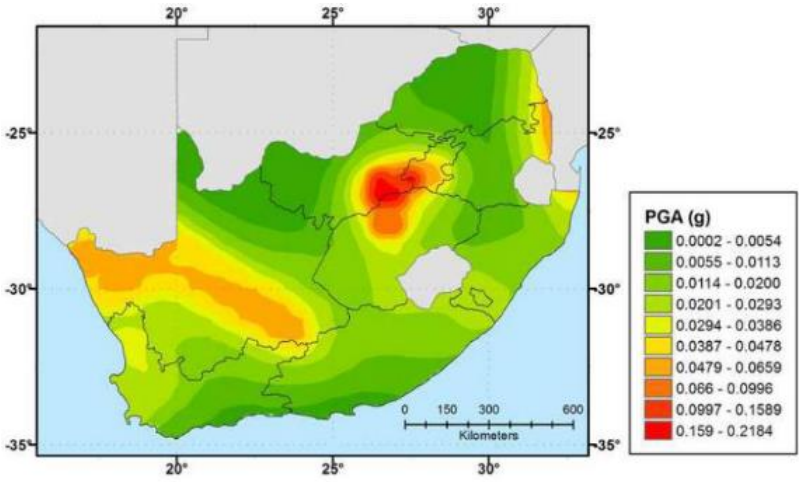

Figure 2-13: Distribution of mean PGA in South Africa (Midzi et al., 2020b)

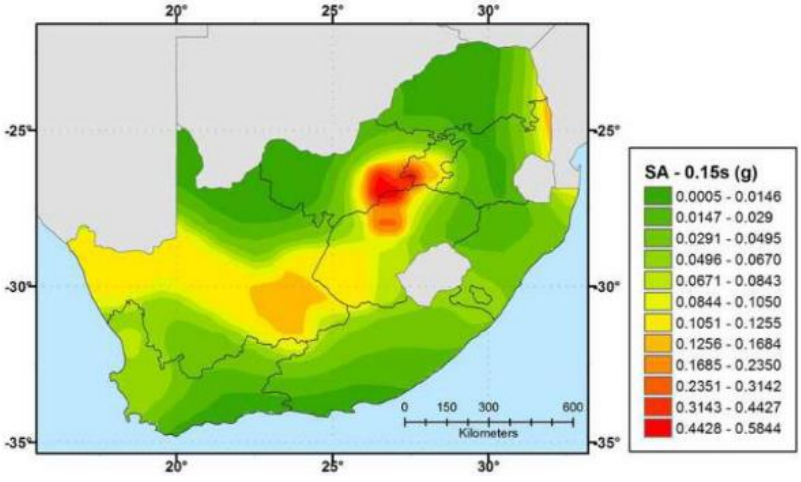

Figure 2-14: Distribution of spectral acceleration (period of 0.15s) in South Africa (Midzi et al., 2020b)

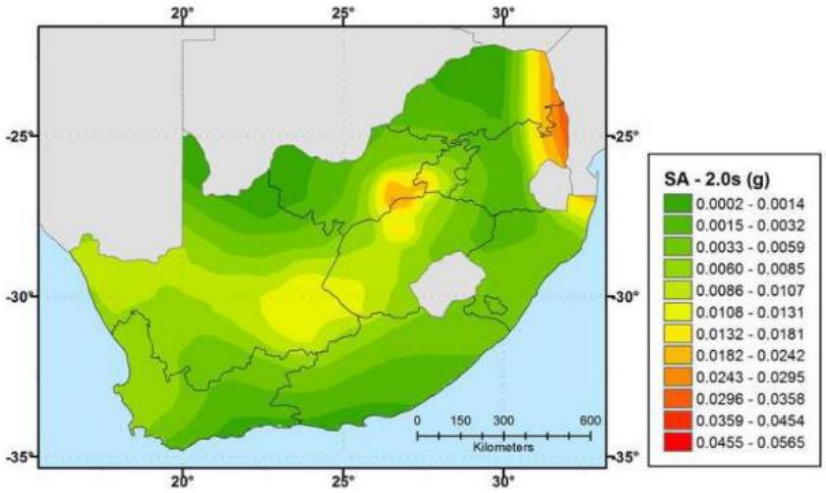

Figure 2-15: Distribution of spectral acceleration (period of 2s) South Africa (Midzi et al., 2020b)

2.2.2.3 Comparison Between the Existing Seismic Hazard Maps

Two different methods were used to produce seismic hazard maps, one by Midzi et al., (2018) using the PSHA method (Figure 2-13) and the other by Kijko & Graham (1998, 1999) using the parametric-historic method (Figure 2-11). While both methods agree that areas with PGAs > 0.1g have a 10% chance of exceedance in 50 years in gold mining districts, they differ in their assessment of tectonic seismicity hazard. The parametric-historic method gives more weight to regions with recorded large earthquakes in the last century (such as southern Free State, Western Cape, and northern KwaZulu-Natal), while the PSHA method places more emphasis on regions with elevated seismicity (such as Northern Cape) using both seismic and non-seismic data. It's worth noting that the parametric-historic method relies solely on seismic data, while the PSHA method uses both seismic and non-seismic data to define seismic source zones (Midzi et al., 2020b).

2.2.3 Seismic design with SANS 10160-4-2017

2.2.3.1 Ground Types

For civil engineering developments within seismic regions, SANS 10160-4: 2017 recommends geophysical and geotechnical investigations to identify the ground conditions according to the types given in Table 2-3. However, the most unfavorable of the four types is recommended when the site conditions still need to be fully known or if the site investigations need to enable profiles to be used.

Table 2-3: Ground types (SANS 10160-4, 2017)

Ground type	Description of stratigraphic profile	Parameters	
		$v_{s,30}$ (m/s)	N_{SPT} (blows/ 30cm)
1	Rock or other rock-like geological formation, including at most 5m of weaker material at the surface	>800	-
2	Deposits of very dense sand, gravel, or very stiff clay, at least several tens of meters in thickness, characterized by a gradual increase of mechanical properties with depth	360-800	>50
3	Depth deposits of dense or medium-dense sand, gravel, or stiff clay with thickness from several tens to hundreds of meters.	180-360	15-50
4	Deposits of loose to medium cohesionless soil (with or without some soft cohesive layers) or of predominantly soft to firm cohesive soil.	<180	<15
$v_{s,30}$	The average value of propagation of S-waves in the upper 30m of the soil profile at shear strains of 10^{-5} or less		
N_{SPT}	The standard penetration test blow count		
c_u	The undrained shear strength of soil		

2.2.3.2 An Essential Representation of Seismic Action

The earthquake motion at a given point on the surface is represented by an elastic ground acceleration response spectrum called the elastic response spectrum (SANS 10160-4, 2017). The normalized design spectra according to the ground condition types presented in Table 2-3 are illustrated in Figure 2-16 for 5% damping.

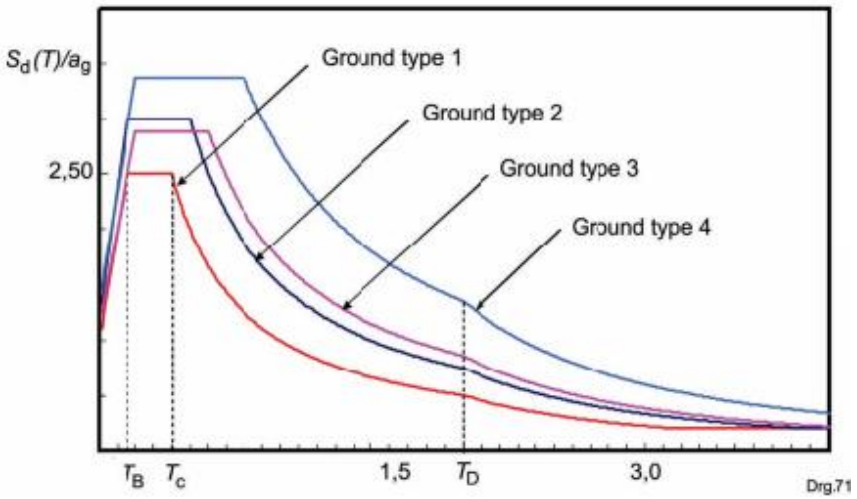

Figure 2-16: Normalized design response spectra, S_d (T)/a_g for 5% damping and q = 1.0 (SANS 10160-4, 2017)

2.2.3.3 Structural Analysis and Modelling

According to SANS 10160-4 (2017), when designing buildings to withstand earthquakes, the model of the building should reflect the distribution of stiffness and mass. This ensures that important deformation shapes and inertia forces are accounted for during seismic activity. The three main structural systems used in earthquake-resistant design are the bearing wall system, the building frame system, and the moment resisting frame. These systems provide support for gravity loads and resistance to lateral seismic force.

A linear elastic structural model can calculate the impact of seismic forces. For buildings that are not significantly affected by higher modes of vibration, the equivalent static lateral force procedure can be used. This procedure is considered satisfactory if the fundamental period of vibration (T) is $T \leq 4T_C$ or $T \leq 2.0$ s. If a building does not meet this requirement, specialized literature should be consulted for rigorous analysis methods such as the response spectrum method and time history analysis (SANS 10160-4, 2017). Figure 2-18 illustrates how buildings behave during earthquake loading.

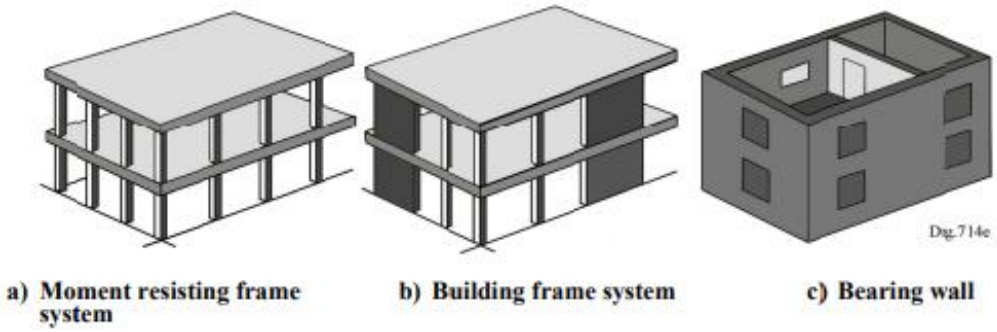

Figure 2-17: The structural system (SANS 10160-4, 2017)

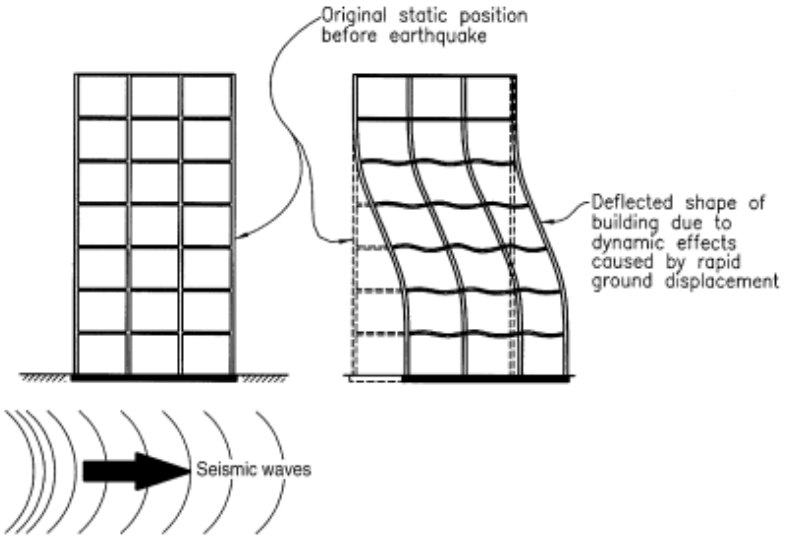

Figure 2-18: Behavior of a building during earthquakes (Taranath, 2004)

2.2.4 Minimum Standard on Ground Vibrations in South Africa

Earthquakes, noise, mine blasts, air-blast, and fly rocks near surface structures all create ground vibrations (Milev et al., 2016). The level of damage that these vibrations can cause to buildings is most closely linked to the Peak Particle Velocity (PPV). Humans can feel ground motion with PPVs as low as 0.8mm/s, while buildings may experience cosmetic damage at PPVs of 10mm/s at frequencies of 10 Hz. Severe structural damage may occur when PPVs exceed 200 mm/s. The methods used to record and analyze vibrations produced by earthquakes and mine blasts are similar, but with some significant differences outlined in Table 2-4. This means that the relationships and conclusions drawn in earthquake engineering may not necessarily apply to mine blasting (JKMRC, 1996). Table 2-5 shows the safe limits of ground vibration for various engineered structures, while Table 2-6 provides a summary of vibration limits for civil and engineering structures.

Table 2-4: Comparison of blast-induced and earthquake ground vibrations

Parameter	Typical opencast blast	Damaging Earthquake (M>6)
Frequency (Hz)	5-200	0.1-5
Duration (sec)	0.5-5	10s of seconds to minutes
Displacement (mm)	0.001-2	100s of mm
Peak velocity (mm/s)	0.1-1000	Up to 1000
Peak acceleration (m/s^2)	0.01-100	Seldom >10

Table 2-5: Vibration amplitudes for structures and equipment (Rorke, 2011)

Type of Structure	Type of Damage	PPV at which damage starts (mm/s)
Rigidly mounted mercury switches	Trip out	12.7
Concrete blocks (like floor slabs)	Hairline cracks in concrete	203
Cased drill holes	Horizontal offset	381
Mechanical equipment (like pumps and compressors)	Shaft misalignment	1016
Prefabricated metal buildings on concrete pad foundations	Cracked floor, building twisted and distorted	1524

Table 2-6: Vibration limits for civil infrastructure used in South Africa (Blast Management and Consulting, 2017)

Structure Description	Ground Vibration Limit (mm/s)
National roads	150
Electrical lines (Pylons)	75

Table 2-6: Vibration limits for civil infrastructure used in South Africa (Blast Management and Consulting, 2017)

Structure Description	Ground Vibration Limit (mm/s)
Railway	150
Transformers	25
Water wells	50
Telecoms tower	50
Telecom relay tower	10 (Rorke, 2011)
General houses of proper construction	25
Houses of lesser proper construction	12.5
Rural building-Mud houses	6
Conveyors	200 (Rorke, 2011)
Pipelines (Water and Transnet)	50 (Rorke, 2011)

2.3 Dynamic and Cyclic Properties of Soils

2.3.1 Soil Stiffness and Damping

2.3.1.1 Equivalent Linear Soil Models

When subjected to cyclic loads, the soil's shear stress-strain relationship beneath the ground and away from nearby structures shows a hysteresis loop, as depicted in Figure 2-19. The loop's shape can be defined by its parameters, such as inclination, breadth, shear modulus, and damping, or by the path it follows (Jia, 2018; Mojtahedzadeh, Ghalandarzadeh, & Motamed, 2022).

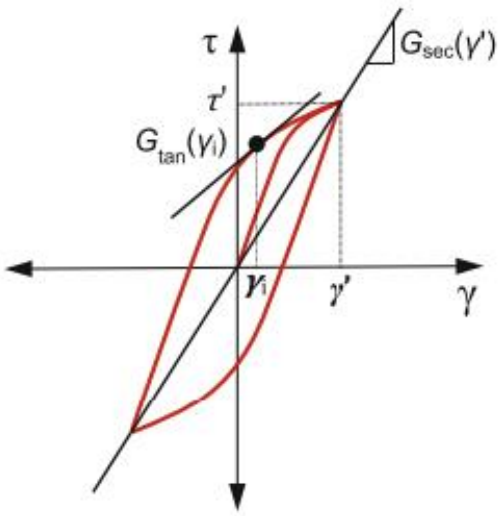

Figure 2-19: Secant shear modulus G_{sec} and tangent shear modulus G_{tan} in a hysteresis loop (τ' and γ' are shear stress and shear strain, respectively) (Jia, 2018)

Additionally, the tangent shear modulus (G_{tan}) in Figure 2-19 varies along the hysteresis loop's path under cyclic loads. At low shear strain amplitudes, the tangent shear modulus is high, and vice versa. However, the average value of the tangent shear modulus over the entire loop can be approximated as the secant shear modulus G_{sec} in Equation 2-1 (Jia, 2018):

$$G_{sec} = \frac{\tau'}{\gamma'} \qquad \text{Equation 2-1}$$

The secant shear stiffness is greatly affected by the amplitude of shear strain and decreases as the shear strain increases. The hysteresis loops of cyclic strain amplitudes form a backbone shape shown in Figure 2-20, which depicts the locus of points corresponding to their tips. At zero strain, the shear modulus reaches its maximum value G_{max}. To describe the secant shear stiffness degradation of soils, an equivalent linear model typically adopts the modulus ratio $G_{sec} = G_{max}$ (also written as $G = G_{max}$). This results in a modulus reduction curve (also known as normalized shear modulus) as shown in Figure 2-21, which conveys the same information as the backbone curve (Figure 2-20) (Jia, 2018).

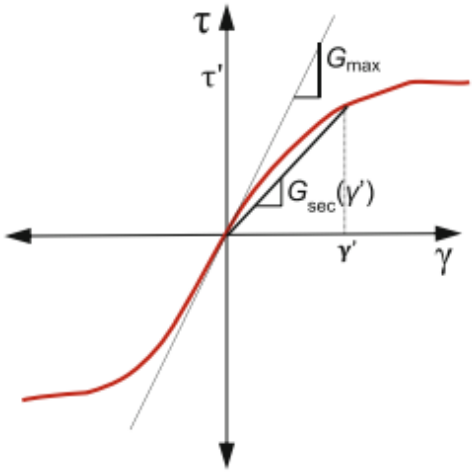

Figure 2-20: Modulus reduction curve represented by a backbone curve showing the secant shear modulus, G_{sec}, and maximum shear modulus G_{max} (Jia, 2018)

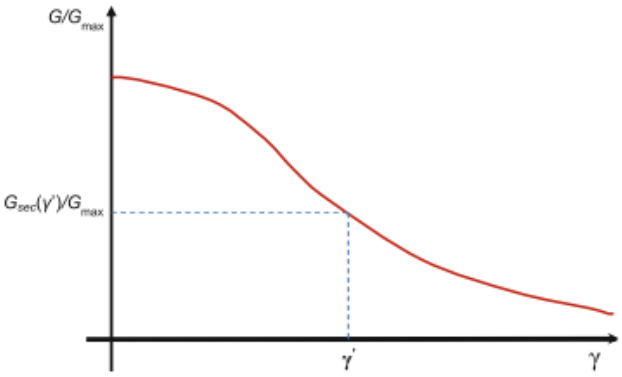

Figure 2-21: Normalized shear modulus reduction curve (Jia, 2018)

2.3.1.2 Dynamic Soil Properties and Strain Thresholds

The stress-strain relationship of soil behavior at various strains is illustrated in Figure 2-22 by Atkinson & Sallfors (1991) and Vucetic (1992). During the very small strain regime, the stiffness modulus remains constant, and the soil exhibits elastic behavior where the stiffness modulus varies nonlinearly with strain. The soil stiffness decreases as it approaches failure in the large strain regime.

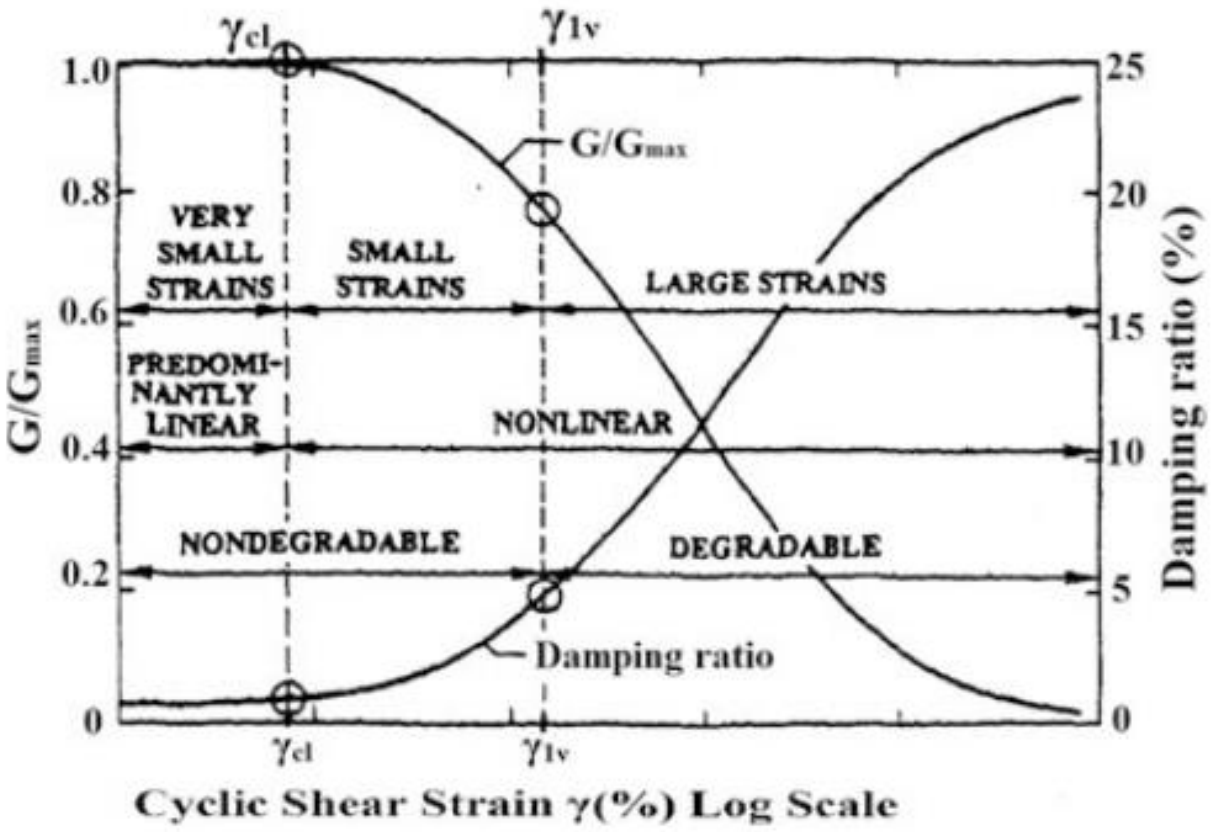

Figure 2-22: Curves of secant modulus reduction and damping at varied cyclic shear strain (Vucetic, 1992), where γ_{c1} and γ_{1v} are the linear thresholds shear strain and the volumetric cyclic threshold shear strain, respectively.

Additionally, there are two important strain values to consider: the volumetric cyclic threshold shear strain (γ1v) and the large strain threshold (γtd) (Vucetic & Dobry, 1991). The γ1v is the strain level below which the structure of soils remains unchanged, but beyond which irreversible changes occur in the soil skeleton, leading to volume change and pore-water pressure generation as illustrated in Figure 2-22. For sands, the γ1v is 0.01%, while for clay, it can be ten times larger. The γtd, on the other hand, is the critical level of cyclic loading above which decisive destructuring of soil specimen occurs (Díaz-Rodríguez, 1989; 2001). Below this threshold, the soil behaves almost elastically. These strain values are important in determining soil stiffness and damping, which is typically done by measuring the shear wave velocity, soil stiffness, and soil damping at different shear strains. Figure 2-23 shows the normalized stiffness degradation curve, which is commonly used in geotechnical engineering projects that involve small-strain and large-strain regimes (Jia, 2018).

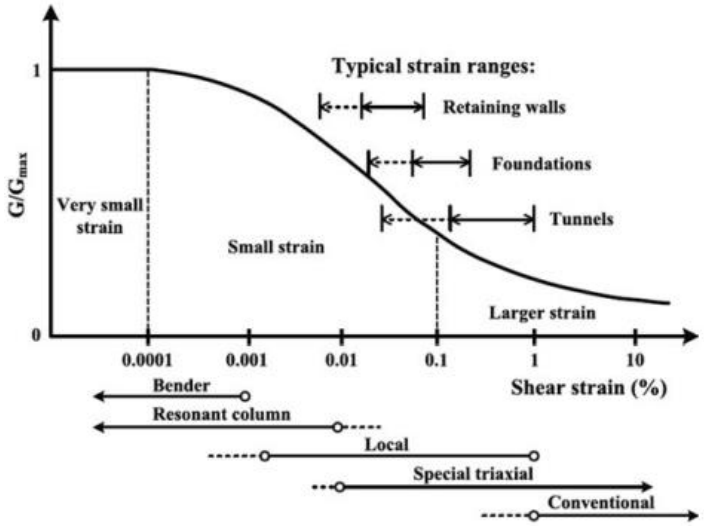

Figure 2-23: Normalized stiffness degradation curve with corresponding geotechnical applications (Likitlersuang et al., 2013)

2.3.1.3 Stiffness Modeling

To suit dynamic stiffness modelling, two important factors to consider are the shear modulus and damping ratio (Mojtahedzadeh et al., 2022). The stiffness of soil can be influenced by various factors such as soil type, cyclic shear strain level, plasticity index, mean effective confining stress, loading history, frequency of loading, number of loading cycles, over-consolidation ratio, void ratio, degree of saturation, and grain characteristics (Jia, 2018).

a) Modulus Reduction Curve

The modulus reduction curve plays a critical role in the evaluation of numerous dynamic geotechnical engineering problems (Rohilla & Sebastian, 2023).

To date, there have been various hyperbolic soil models proposed by well-known researchers (Vucetic, 1992; Hardin & Drnevich, 1972; Pyke, 1993; Stokoe et al., 1999). Hardin & Drnevich (1972) suggested that a hyperbolic curve that asymptotes to the maximum shear stress can represent the stress-strain relationship of soil. The normalized modulus reduction curve can be expressed as Equation 2-2:

$$\frac{G}{G_{max}} = \frac{1}{1 + \frac{\gamma}{\gamma_r}} \qquad \text{Equation 2-2}$$

Where;

- G = shear modulus at shear strain γ (%),
- $\gamma_r = \frac{\tau_{max}}{G_{max}}$ is the reference strain,

Hardin & Drnevich (1972) further modified Equation *2-2* to Equation 2-3;

$$\gamma_h = \frac{\gamma}{\gamma_r}\left[1 + a.\exp\left(-b.\left(\frac{\gamma}{\gamma_r}\right)\right)\right] \quad \text{Equation 2-3}$$

Where; a and b are coefficients that adjust the shape of the stress–strain curve for different soil types, number of cycles, and loading frequencies.

In Equation 2-3 by Hardin & Drnevich (1972), only one curve-fitting variable (reference strain γ_r) is involved, making it difficult to fit experimental data. Thus, to remedy this, Stokoe et al., (1999) and Darendeli (2001) proposed that modulus reduction curves can be established by fitting the experimental data using Equation 2-4 below:

$$\frac{G}{G_{max}} = \frac{1}{1 + \left(\frac{\gamma}{\gamma_r}\right)^{\alpha}} \quad \text{Equation 2-4}$$

Where; α is a curvature parameter (α = 1.0 corresponds to a standard hyperbolic backbone curve) and can generally be taken as 0.92; γ_r is called the pseudo-reference strain, corresponding to the shear strain when $G/G_{max} = 0.5$.

Menq (2003) conducted tests on several coarse sandy (D_{50} greater than 0.3 mm) and gravelly soils. The results showed that the modulus reduction behavior can be described by a modified hyperbolic model, which uses the coefficient of uniformity as presented in Equation 2-5.

$$\frac{G}{G_{max}} = \frac{1}{1 + \left(\frac{\gamma}{\gamma_r}\right)^{a}} \quad \text{Equation 2-5}$$

Where;

- $\gamma_r = 0.12\ x\ C_u^{-0.6}\left(\frac{P'}{P_a}\right)^{0.5C_u^{-0.15}}$ Equation 2-6
- $a = 0.86 + 0.1\ x\ log\left(\frac{P'}{P_a}\right)$ Equation 2-7
- C_u = coefficient of uniformity

Oztoprak & Bolton (2013) compiled a large number of data reported in literature for modulus reduction of different non-plastic soils and developed the following Equation 2-8;

$$\frac{G}{G_{max}} = \frac{1}{1 + \left(\frac{\gamma - \gamma_e}{\gamma_r}\right)^{a}} \quad \text{Equation 2-8}$$

Where;

- $\gamma_r = 0.01\ x\ C_u^{-0.3}\left(\frac{P'}{P_{atm}}\right) + 0.08\ e\ D_r$ Equation 2-9
- $a = C_u^{-0.075}$ Equation 2-10
- $\gamma_e = 0.0002 + 0.012\gamma_r$ Equation 2-11

- C_u = coefficient of uniformity

The Electric Power Research Institute (EPRI) (1993) model was based on data from three earthquakes: the 1979 Coyote Lake earthquake, the 1984 Morgan Hill earthquake, and the 1989 Loma Prieta earthquake, specifically to address the effects of earthquakes on soil. The model provides modulus reduction and damping curves for cohesionless soils in the range of gravelly sands to low plasticity silts or sandy clays, as shown in Figure 2-24.

Ishibashi & Zhang (1993) came up with equations that take into account the plasticity index and the effective confining pressure to determine the soil's shear modulus. Figure 2-24 shows the curve for modulus reduction for soil with a plasticity index of 0 (which means it is non-plastic).

Seed et al., (1984) came up with modulus reduction curves for coarse-grained soils. These curves are based on the average behavior observed in 12-inch diameter cyclic triaxial tests conducted on four different types of coarse-grained soils, as depicted in Figure 2-24.

Seed & Idriss (1970) created the first widely used method for reducing modulus in sand. Their research presented a range of behaviors for modulus reduction, with upper, lower, and average bounds outlined in Figure 2-24.

In 1991, Vucetic & Dobry demonstrated the impact of soil plasticity on modulus behavior. They created various modulus reduction and damping curves based on plasticity index. Figure 2-24 displays the modulus reduction curve for non-plasticity (Plasticity Index, PI = 0).

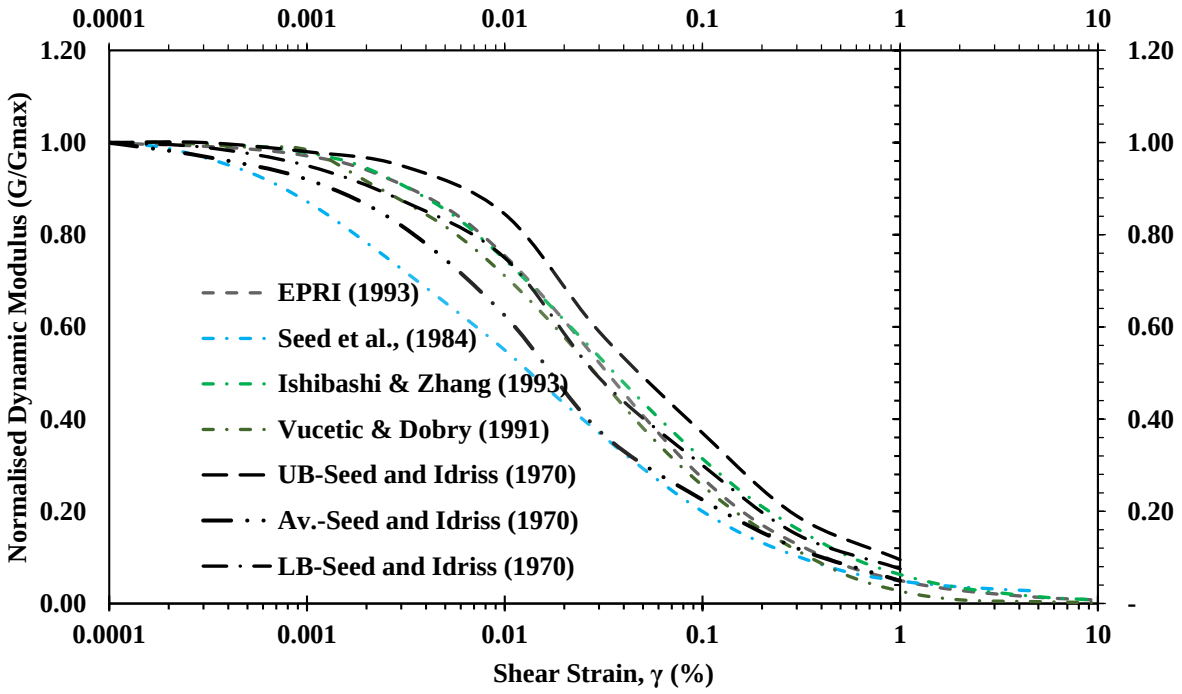

Figure 2-24: Modulus reduction curves for different scholars (EPRI, 1993; Seed et al., 1984; Ishibashi & Zhang, 1993; Vucetic & Dobry, 1991; Seed & Idriss, 1970)

b) Damping Modeling

The damping ratio provides a measure of the energy absorbing characteristics of a soil (SW-AJA, 1972; Mog & Anbazhagan, 2022). In geotechnical engineering, soil damping is specified by relating it to the strain level or G/G_{max}. Hardin & Drnevich (1972) developed an approximate shape for the material damping curve presented in Equation 2-12:

$$\frac{\lambda}{\lambda_{max}} = \frac{\gamma/\gamma_r}{1+(\gamma/\gamma_r)} = 1 - \frac{G}{G_{max}} \qquad \text{Equation 2-12}$$

Where;

λ_{max} is the maximum damping ratio of the soil, which depends on soil type, confining pressure, number, and frequency of cyclic loadings.

Seed & Idriss (1970) gathered all the data available on sands and created empirical equations based on previous research. Their study presented the upper and lower limits of damping ratio, which are shown in Figure 2-25.

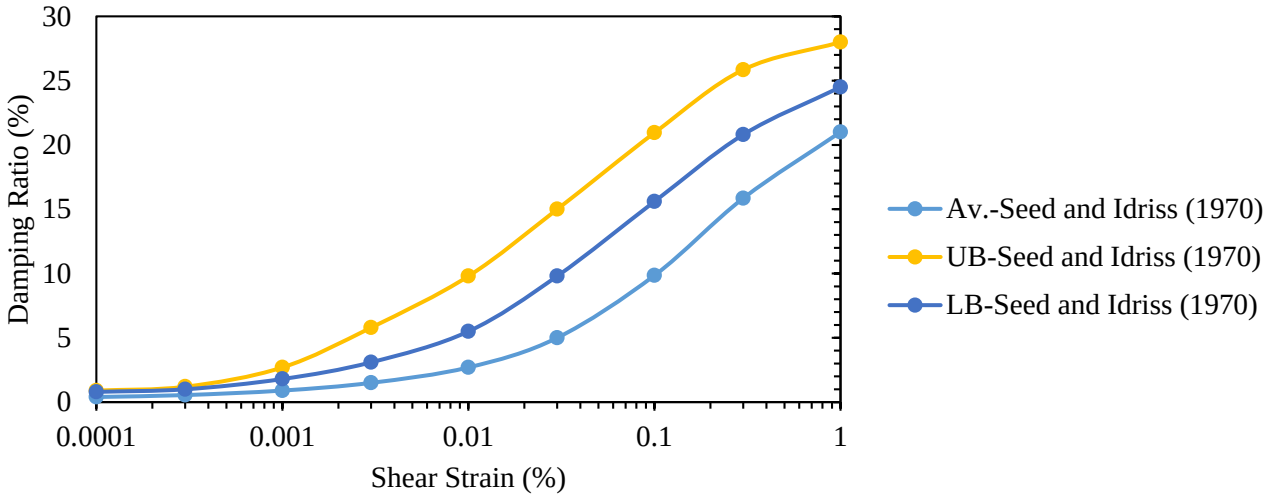

Figure 2-25: Upper, lower, and average damping ratio bounds (Seed & Idriss, 1970)

c) Damping Ratio Versus G/G_{max} modeling

Various equations have been suggested to forecast the normalized shear modulus and damping ratio under different strains (Mojtahedzadeh et al., 2022).

The following models are well-known for predicting the normalized shear modulus (G/G_{max}) based on damping ratio as depicted in Table 2-7.

Table 2-7: Showing models for predicting normalized shear modulus from damping ratio

No	Scholar	Model	
1	Ishibashi & Zhang (1993)	$\lambda = \left(\frac{0.333\left(1+e^{-0.0145I_P^{1.3}}\right)}{2}\right) x \left[0.586\left(\frac{G}{G_{max}}\right)^2 - 1.547\left(\frac{G}{G_{max}}\right) + 1\right]$	Equation 2-13
2	Menq (2003)	$\lambda = b\left(\frac{G}{G_{max}}\right)^{0.1} x\, \lambda_{masing} + \lambda_{min}$	Equation 2-14
3	Michaelides et al., (1998)	$\lambda = 2 + [18 - 0.08(I_p - 15)]x\left[1 - \left(\frac{G}{G_{max}}\right)\right]$	Equation 2-15
4	Park & Stewart (2001)	$\lambda = 17.83\left[0.56\left(\frac{G}{G_{max}}\right)^2 - 1.39\left(\frac{G}{G_{max}}\right) + 1\right]$	Equation 2-16
5	Zhang et al., (2005)	$\lambda = 10.6\left(\frac{G}{G_{max}}\right)^2 - 31.6\left(\frac{G}{G_{max}}\right) + 21 + \left[(0.008I_P + 0.82)\left(\frac{\sigma_0'}{P_a}\right)^{-0.5k}\right]$	Equation 2-17

Where;

- λ = damping ratio
- I_p = Plasticity Index
- σ'_0 = effective confining pressure
- f = exponent constant
- N = number of cycles
- C_u = coefficient of uniformity
- D_{50} = median size

• $\lambda_{min} = 0.55\ x\ C_u^{0.1}\ x\ D_{50}^{-0.3}\ x\ \left(\frac{P'}{P_a}\right)^{-0.08}$	Equation 2-18
• $b = 0.6329 - 0.0057\ x\ ln(N)$	Equation 2-19
• $\lambda_{Masing,\ a=1} = \frac{100}{\pi}\left[4\frac{\gamma - \gamma_r\, ln\left(\frac{\gamma+\gamma_r}{\gamma_r}\right)}{\frac{\gamma^2}{\gamma+\gamma_r}} - 2\right]$	Equation 2-20
• $\lambda_{Masing} = c_1\lambda_{Masing,\ a=1} + c_2{\lambda_{Masing,\ a=1}}^2 + c_3{\lambda_{Masing,\ a=1}}^3$	Equation 2-21
• $c_1 = -1.1143a^2 + 1.8618a + 0.2523$	Equation 2-22
• $c_2 = 0.0805a^2 - 0.071a + 0.0095$	Equation 2-23
• $c_3 = -0.0005a^2 + 0.0002a + 0.0003$	Equation 2-24
• a obtained from Oztaprak and Bolton's (2013) model see Equation 2-10	

2.3.2 Interpretation of the Influence of Shear Strain Amplitude on Shear Modulus and Damping Ratio

When it comes to sand and gravelly soils, their dynamic properties are not linear, indicating that the shear modulus and damping ratio change depending on the strain amplitude. The extent of non-linearity varies based on the discreteness of the material. Discreteness refers to how the particles of the soil are separated from one another. Here are some examples to highlight this concept (Towhata, 2008**;** Hardin & Drnevich, 1972):

1. In sand and gravel without fines, particles are not bonded together; However, they are highly discrete due to contact and friction resulting in more significant non-linearity compared to clay.
2. The magnitude of effective stress in sand and gravel affects its nonlinearity. Higher stress generates more interaction among grains, reducing discreteness, and decreasing non-linearity. Conversely, sand and gravel under lower effective stress exhibit more non-linearity.

The above phenomena are illustrated in more detail in Figure 2-26 and Figure 2-27.

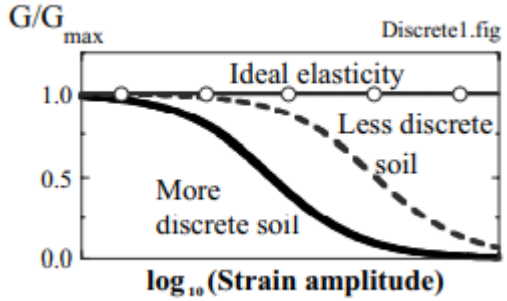

Figure 2-26: Effects of discreteness of soils on non-linearity in terms of variation of shear modulus with strain amplitude (Towhata, 2008)

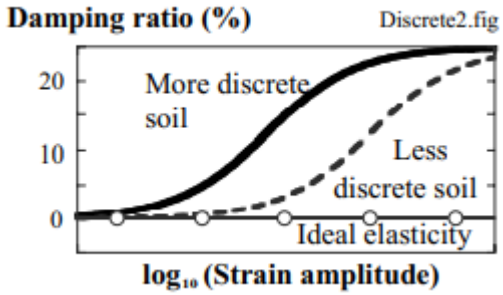

Figure 2-27: Effect of discreteness of soils on non-linearity in terms of variation of damping ratio with strain amplitude (Towhata, 2008)

2.3.3 Factors Affecting Modulus and Damping of Sand

Some researchers have investigated the cyclic deformations of soils and identified several factors that impact the shear modulus and damping ratio. These factors include strain amplitude, effective stress, density or void ratio, and anisotropic consolidation as summarized in Table 2-8 and Table 2-9 (Jia, 2018; Towhata, 2008).

The damping ratio of soil is not dependent on loading frequency, meaning that laboratory tests to determine the damping of sand can be performed at a relatively low frequency (~0.1 Hz) using a pneumatic-controlled device. This device is less expensive than hydraulic ones that can operate at higher frequencies experienced during earthquakes. Additionally, while void ratio and anisotropic

consolidation do not significantly affect the damping ratio of sand, over-consolidation is not an essential factor either (Towhata, 2008).

In Figure 2-28, the cyclic drained test conducted on Toyoura sand indicates that as the number of cycles increases, the modulus increases while the area of stress-strain loop decreases. The effective stress and isotropic consolidation state remain unchanged, with only a slight decrease in void ratio. However, the variations in modulus and damping are significant, which is commonly observed during laboratory testing. Therefore, G and γ values reported in literature mostly come from the 10th or 15th cycles and may not be suitable for the first few cycles or analyzing smaller magnitude earthquakes with fewer cycles (Towhata, 2008).

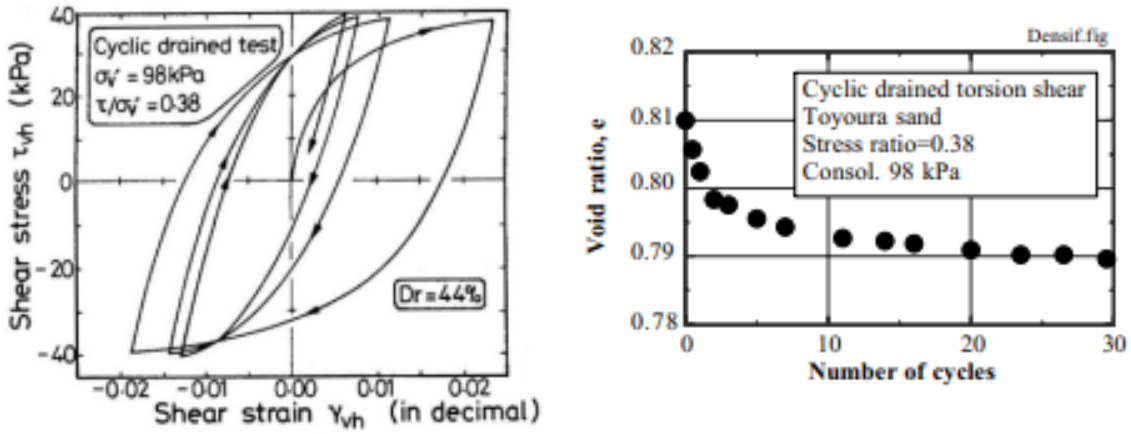

Figure 2-28: Cyclic deformation of sand in drained test (Towhata et al., 1985)

Table 2-8: Parameters that control non-linear soil behavior and their influence regarding the shear modulus and damping ratio (Hardin & Drnevich, 1972)

Parameters	Impact on shear modulus	Impact on material damping
	Clean sands	
Strain amplitude	***	***
Mean effective confining pressure	***	***
Void ratio	***	***
Number of loading cycles	+	***
Degree of saturation	*	**
Over Consolidation Ratio (OCR)	*	*
Effective strength envelope	**	**
Octahedral shear stress	**	**
Frequency of loading (above 0.1 Hz)	*	*
Other time effects (thixotropy)	*	*

Table 2-8: Parameters that control non-linear soil behavior and their influence regarding the shear modulus and damping ratio (Hardin & Drnevich, 1972)

Parameters			Impact on shear modulus	Impact on material damping
			Clean sands	
Grain characteristics, size, shape, gradation,			*	*
Soil structure			*	*
Volume changes due to shearing strain below 0.5%			-	-
Notes	***	Very important		
	**	Less important		
	*	Relatively unimportant		
+		Relatively unimportant except for saturated sand		
-		unknown		

Table 2-9: Parameters that control non-linear behavior and their influence on the normalized modulus reduction and damping ratio curves (Darendeli, 2001)

Parameters	Impact on normalized shear modulus reduction curve	Implications for material damping curve
	Clean sands	
Strain amplitude	***	***
Mean effective confining pressure	***	***
Soil type and plasticity	***	***
Number of loading cycles	*+	***++
Frequency of loading (above 1 Hz)	*	**
Over Consolidation Ratio (OCR)	*	*
Void ratio	*	*
Degree of saturation	*	*
Grain characteristics, size, shape, gradation, mineralogy	*	*

***	Very important
**	Important
*	Less important
+	On competent soils included in the study by Darendeli (2001)
++	Soil type dependent

2.3.4 Small Strain Shear Modulus of Sand

The shear modulus, G = G_{max}, is a crucial parameter in soil analysis, particularly at small strain amplitudes of 10^{-6} (≡ 0.0001%) or less (Kaya, Erken, & Cilsalar, 2021; Mojtahedzadeh et al., 2022; Yan, Wang, Yang, Lai, & Chen, 2022). It is best determined by measuring the shear wave velocity (V_s) as presented in Equation 2-25;

$$V_s = \sqrt{G_{max}/\rho} \qquad \text{Equation 2-25}$$

Where;

ρ is the soil density.

When that's not feasible (i.e., using Equation 2-6), SPT-N is commonly used (Towhata, 2008). However, field investigations of Vs or N are impossible for unconstructed earth structures. In such cases, G_{max} can be estimated by either collecting disturbed soil samples from the project site and conducting cyclic tests in the laboratory, or by using an empirical formula like Equation 2-26 and Equation 2-27 from Richart et al., (1970) if shear wave velocity measurements are unavailable.

$$G_{max} = 700\frac{(2.17-e)^2}{1+e}(p')^{0.5}\ for\ round\ sand \qquad \text{Equation 2-26}$$

$$G_{max} = 330\frac{(2.97-e)^2}{1+e}(p')^{0.5}\ for\ angular\ sand \qquad \text{Equation 2-27}$$

Where;

- kgf = kg as force
- 1kgf/cm^2 = 98 kN/m^2 = 98 kPa

Where "e" stands for the void ratio of sand and the effective mean principal stress of P' is defined by $P' = (\sigma'_1 + \sigma'_2 + \sigma'_3)/3$.

From laboratory tests, it can also be suggested that the maximum shear modulus may be calculated as given in Equation 2-28:

$$G_{max} = 625.F(e).(OCR)^k.{p_a}^{1-n}.(\sigma'_m)^n \qquad \text{Equation 2-28}$$

where;

- F(e) is a function of void ratio e, and it may be taken as 1/(0.3 + 0.7e^2) (Hardin, 1978) or 1/e$^{1/3}$ (Jamiolkowski et al., 1991);
- σ'$_m$ the mean principal effective stress; k is an over-consolidation ratio exponent related to plasticity index (I_p) as shown in Table 2-10; p_a = 100 kPa is the atmospheric pressure with the same unit as σ'$_m$ and G_{max};
- n is the stress component and is usually taken as 0.5 but can be computed for individual soils at different effective confining pressures (Kramer, 1996).

Table 2-10: Over-consolidation ratio exponent k varied with I_p (Hardin & Drnevich, 1972))

I_p (%)	k
0	0.00
20	0.18
40	0.30
60	0.41
80	0.48
≥100	0.50

By adopting F(e) = 1/(0.3 + 0.7e^2) proposed by Hardin (1978) and assuming that the soil is normally consolidated (OCR = 1), Equation 2-28 above can be rewritten as Equation 2-29 below:

$$G_{max} = 625.(p_a.\sigma'_m)^{0.5}/(0.3 + 0.7e^2) \quad \text{Equation 2-29}$$

Based on the effective octahedral stress σ'_m, and the void ratio e, Harding & Drnevich (1972) also proposed another maximum shear modulus calculation as Equation 2-30;

$$G_{max} = 3230.(\sigma'_{oct})^{0.5}(2.793 - e)^2/(1 + e) \quad \text{Equation 2-30}$$

Earlier, in 1970, Seed & Idriss (1970) proposed a calculation of maximum shear modulus given in Equation 2-31:

$$G_{max} = 22.K_{2.max}.(p_a.\sigma'_m)^{0.5} \quad \text{Equation 2-31}$$

Where;

- $K_{2;\,max}$ is determined by the relative density to water D_r and void ratio e, as shown in Table 2-11.

Table 2-11: $K_{2,\,max}$ as a function of relative density to water D_r and void ratio, e (Seed & Idriss, 1970)

e	$K_{2,\,max}$	D_r (%)	$K_{2,\,max}$
0.4	70	30	34
0.5	60	40	40
0.6	51	45	43
0.7	44	60	52
0.8	39	75	59
0.9	34	90	70

2.3.5 Effects of Strain Amplitude on Shear Modulus

At small strain (< 10^{-5}), a stress–strain loop is reduced to a nearly straight line: an elastic behavior. The secant modulus of $G = \tau/\gamma$ decreases as the strain amplitude increases. Nevertheless, it is a convention to study the effects of strain-non-linearity separately from such factors as effective stress and density given in Equation 2-32 (Towhata, 2008):

$$G = G_{max}\,(function\ of\ \sigma', e, etc.)\ x\ \left(\frac{G}{G_{max}}\right) \qquad \text{Equation 2-32}$$

Thus, the effect of strain is indicated by G/G_{max}; G_{max} is also frequently designated by G_o and can be used interchangeably. Figure 2-29, Kokusho (1987) compares G/G_{max} measured on laboratory-reconstituted samples of clean sand under drained conditions. Since G varies with the number of cycles, Figure 2-29 shows G in the 10^{th} – 20^{th} cycles. Figure 2-29 indicates the following;

1. G/G_{max} decreases as the strain amplitude increases,
2. The reduction of G/G_{max} is less significant when the effective stress is higher,
3. Nevertheless, most sands exhibit similar G/G_{max} curves irrespective of different testing conditions.

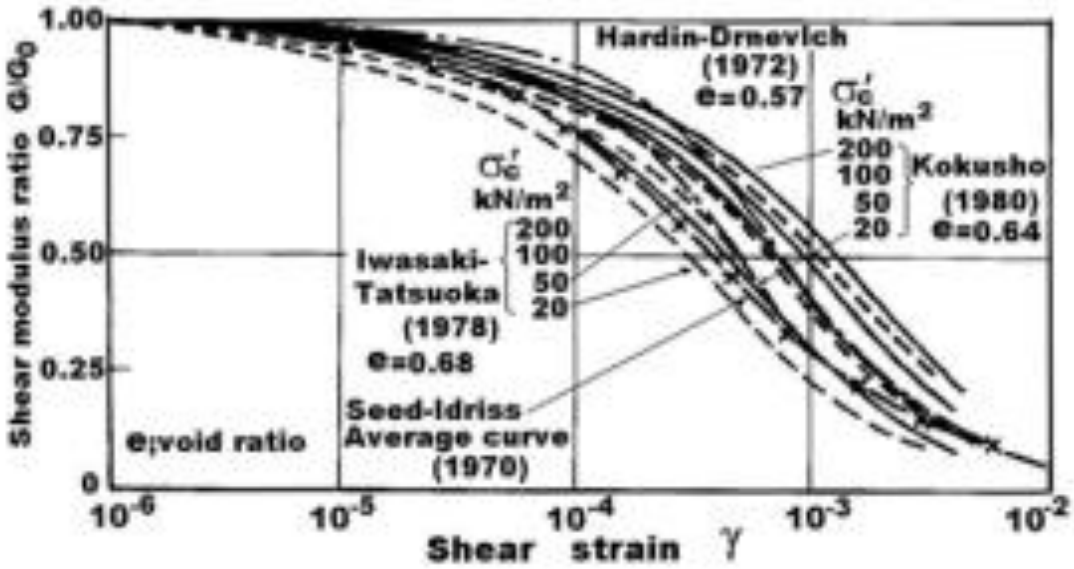

Figure 2-29: G/G_{max} of reconstituted clean sands (Kokusho, 1987)

2.3.6 Influence of Effective Stress on Shear Modulus of Sand

Figure 2-29 demonstrates that G/G_{max} is affected by effective stress to some extent. However, the more important effect of the effective stress occurs in G_{max} at a small strain amplitude. Chung et al., (1984) performed resonant column tests on clean sand for which their specimens were isotropically consolidated under effective stress of σ'_3'as presented in Figure 2-30.

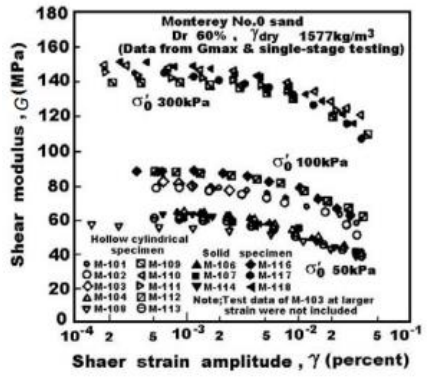

Figure 2-30: Effects of effective stress on G (Chung et al., 1984)

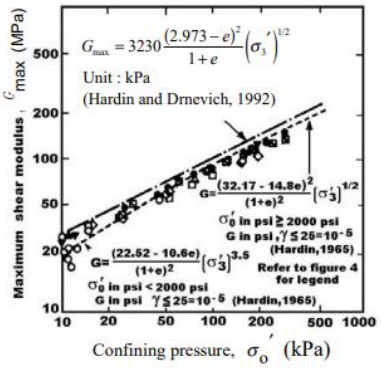

Figure 2-31: Variations of G_{max} with effective stress (Chung et al., 1984)

Figure 2-31 illustrates the variation of G_{max} with the effective stress, and this shows that;

i. G_{max} increases in proportion to $\sigma'_3{}^{0.5}$,
ii. The effects of void ratio, e, on G_{max} is approximated by an empirical formula of $(2.97-e)^2/(1+e)$.

2.3.7 Damping Ratio of Sand

In section 2.3.1, it was shown that the shape of a hysteresis stress-strain loop of sand changes with the number of loading cycles during drained cyclic shear. As the cycles increase, the secant shear modulus increases, and the area of the loops decreases. As a result, the damping ratio decreases with the progress of cyclic loading. Therefore, laboratory tests report the damping ratio in the 10^{th}-20^{th} cycles without considering the initial few cycles (Towhata, 2008).

2.3.8 Cyclic Loading Behavior of Saturated Sands

2.3.8.1 Drained Cyclic Loading

For a wide range of relative densities, drained cyclic loading combined with shear stress reversal causes densification or net contraction (Chaneva, Kluger, Moon, Lowe, & Orense, 2023). Figure 2-32 (Youd, 1972) illustrates the progressive net contraction of a sand sample under strain-controlled, drained, cyclic loading. The test sample experienced a gradual oscillating decrease in the void ratio (contraction) and a gradual increase in the void ratio (dilation), with an overall accumulation of contractive strains. The sample contracted from point A to point B due to the initial shear loading, and additional shear led to incremental dilation from point B to point C. This led to the sample being looser at point C than point A. At the onset of shear reversals, the sample incrementally contracted to point D (a denser state) and then transformed to incremental dilation to point E. This alternated for every cycle, resulting in a balanced accumulation of net strains leading to a progressively denser state (smaller void ratio per loading cycle).

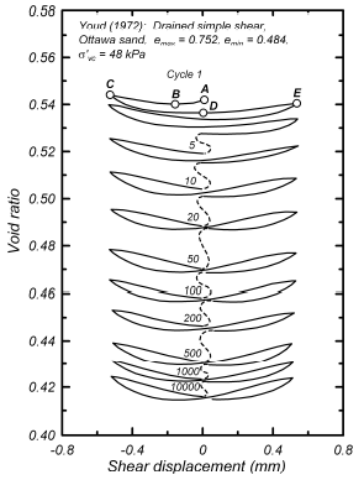

Figure 2-32: Change in void ratio with cyclic shear displacement for a drained simple shear loading (Youd, 1972)

2.3.8.2 Undrained Cyclic Loading

Figure 2-33 illustrates how the sand matrix contracts and rearranges its particles under undrained cyclic loadings, transferring normal stresses from the sand particles to the pore water. Drained cyclic loading results in a plastic volumetric contraction of the sand skeleton, leading to the stress path from point A to point B. However, undrained, saturated conditions counterbalance the plastic volumetric strain through the expansion of the skeleton due to the stress path from point B to C. Eventually, the cyclic loading breaks apart the load-bearing contacts among sand particles, causing the sand grains or skeleton to carry zero normal stress ($\sigma' = 0$), while the pore water takes the entire normal stress ($u = \sigma$) (Idriss & Boulanger, 2008).

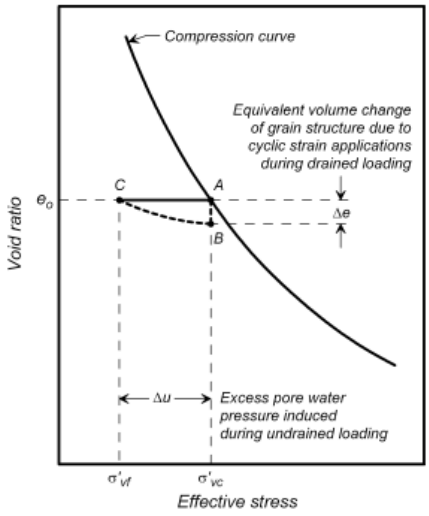

Figure 2-33: Mechanisms of pore pressure generation during cyclic loading (Idriss & Boulanger, 2008)

The cyclic undrained loading behavior is shown in Figure 2-34 through the results of an anisotropically consolidated undrained (ACU) cyclic triaxial test on medium-dense clean sand with uniform sinusoidal stress loading. Excess pore water pressure (Δu) generated during undrained cyclic triaxial loading is normalized by the minor effective consolidation stress (σ'_{3c}), yielding the excess pore water pressure ratio (r_u) term expressed in Equation 2-33 (Idriss & Boulanger, 2008);

$$r_u = \frac{\Delta u}{\sigma'_{3c}} \qquad \text{Equation 2-33}$$

The standard cyclic triaxial test keeps the minor principal total stress constant, so the maximum possible value for r_u is 1.0 (or 100%), which occurs when $\Delta u = \sigma'_{3c}$ and $\sigma'_3 = 0$ (Idriss & Boulanger, 2008).

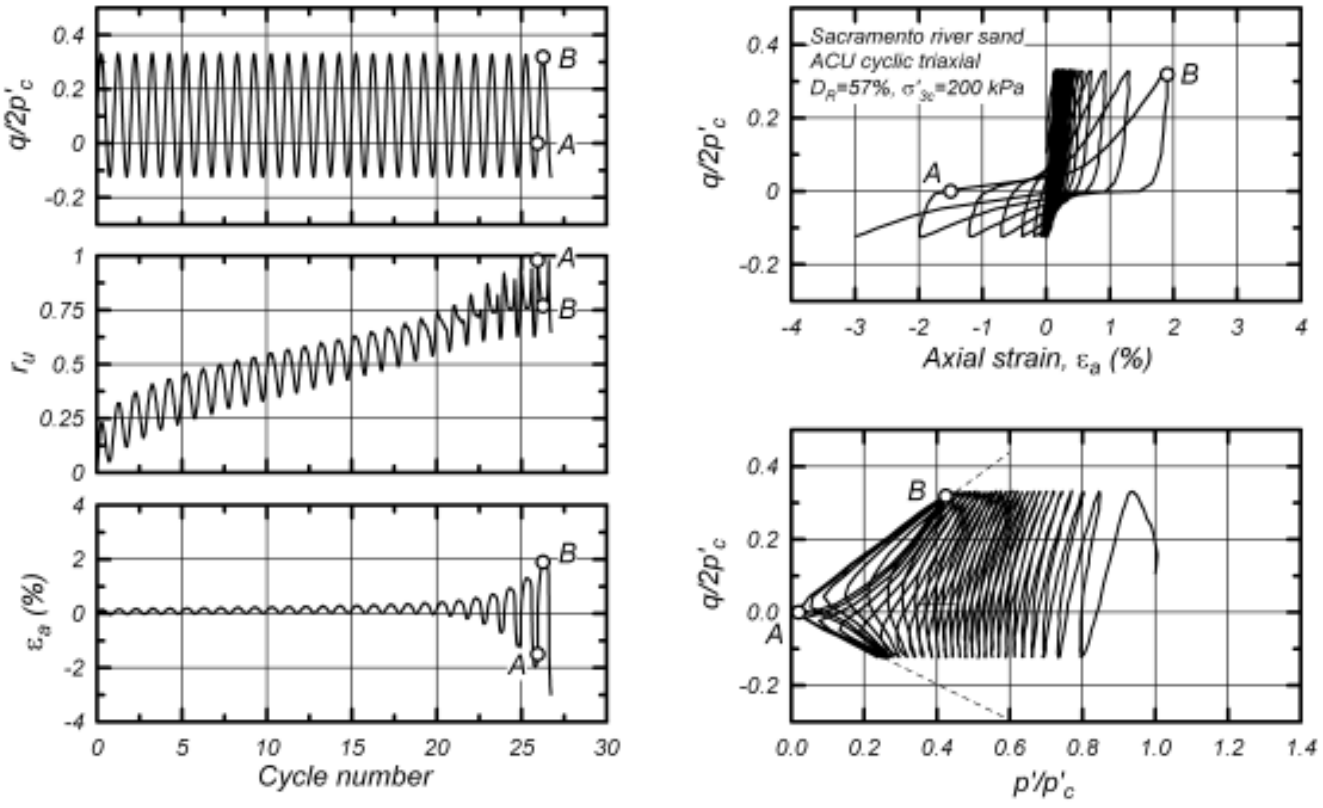

Figure 2-34: Response of Sacramento Rover sand to undrained cyclic triaxial loading (Boulanger & Truman, 1996)

The condition known as "initial liquefaction," or r_u = 1.0, can also be referred to as "excess pore pressure ratio of 100%." However, it's important to note that the term "liquefaction" has been used in various contexts in literature. It's also possible for r_u values to exceed 100% if mean total stress increases, which can occur in field, centrifuge, or numerical model loading conditions. In these

cases, it's more useful to focus on effective stress values rather than excess pore pressure ratios (Idriss & Boulanger, 2008).

2.3.9 Strain-Based Evaluations of Undrained Cyclic Loading Behavior

To evaluate the behavior of saturated sands under cyclic loading, strain-based approaches can be used. Research has shown that generating excess pore pressures is more closely related to imposed shear strains rather than shear stresses. However, estimating induced shear strains requires calculating induced shear stresses and soil shear moduli, which makes strain-based approaches less practical (Idriss & Boulanger, 2008). Therefore, a stress-based approach is commonly used in practice; Figure 2-35 shows this approach.

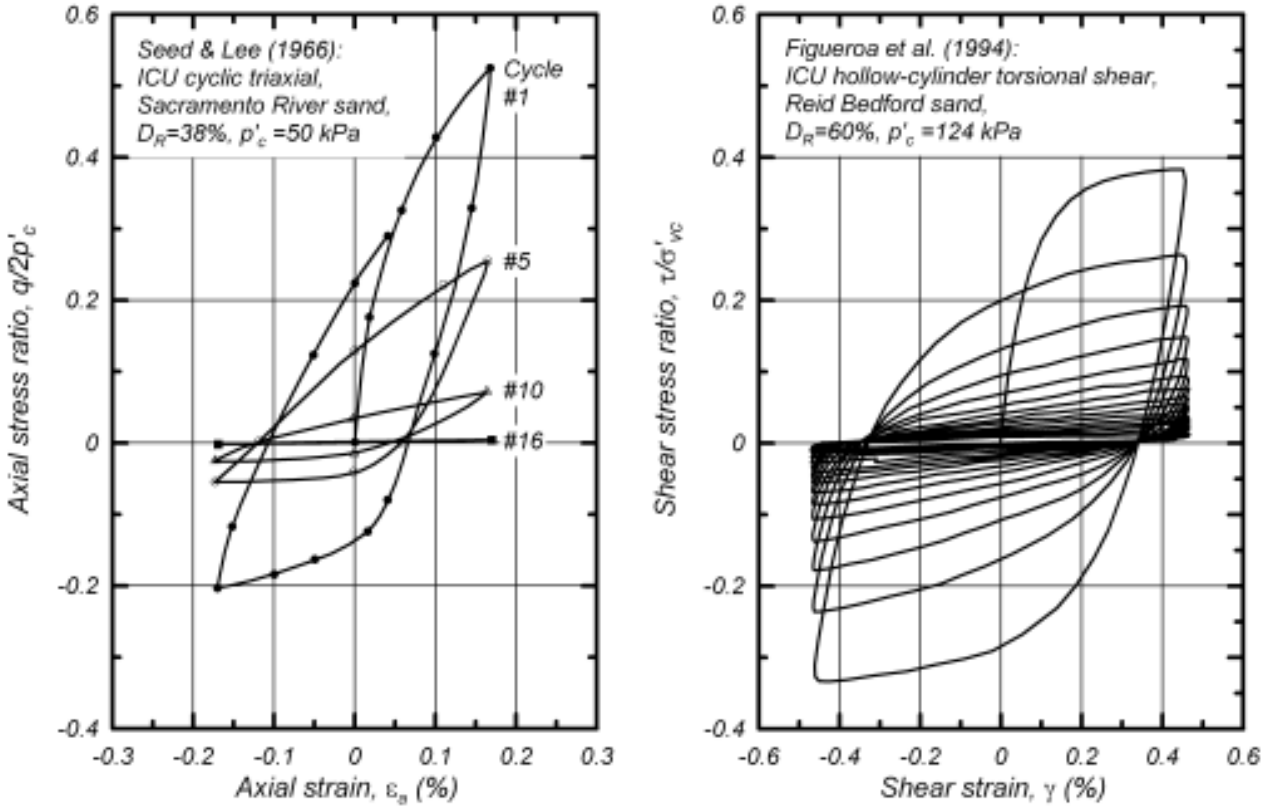

Figure 2-35: Stress-strain response of sand in strain-controlled cyclic undrained loading in a triaxial test (Seed & Lee. 1966) and a torsional shear test (Figueroa et al., 1994)

In triaxial tests, cyclic loading with an axial strain amplitude of 0.17% caused the specimen to gradually soften, resulting in a decrease in mobilized shear stress with each cycle of loading as r_u progressively increased to 100% in about 16 cycles. Stress-controlled tests, on the other hand, cause an increase in strain with each cycle, leading to a dilative tendency.

According to Dobry (1985), when looking at various types of sand, densities, and stress levels, the amount of r_u generated over a certain number of cycles at different shear strain amplitudes is relatively consistent. The accompanying Figure 2-36 demonstrates that if a shear strain amplitude of 0.3-1.0% is maintained for ten (10) cycles, r_u will reach 100%. The volumetric cyclic threshold shear strain, or the point at which there is no potential for volumetric strains or pore water pressure generation, typically falls around 0.01-0.02% for sand as illustrated in Figure 2-36 (Ladd et al., 1989; Hsu & Vucetic, 2004).

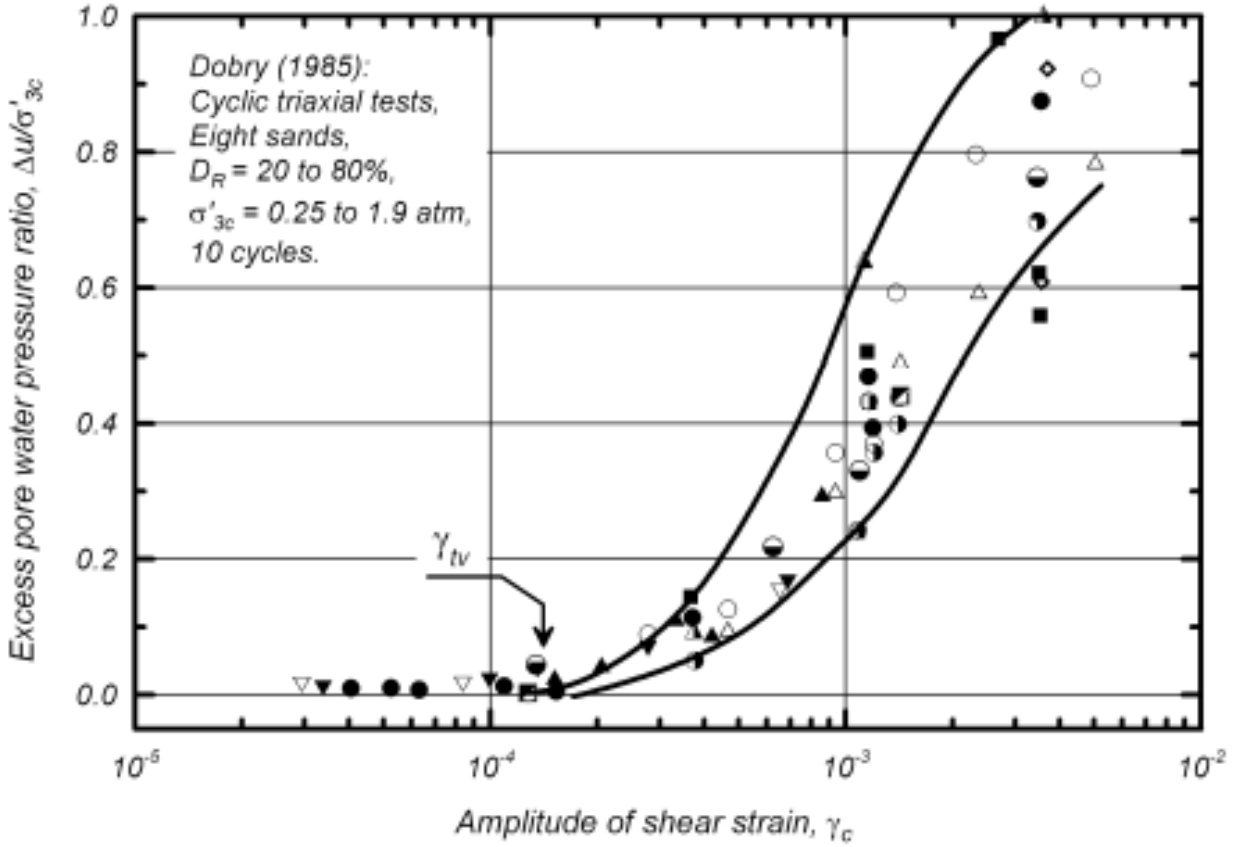

Figure 2-36: Excess pore water pressure generation versus shear strain amplitude in strain-controlled cyclic undrained triaxial tests on sand (Dobry, 1985)

2.3.10 Degree of Saturation and Skempton's B Value

The subsoil is partially saturated (see Figure 2-37), and cyclic laboratory tests make a lot of effort to attain a great extent of saturation in a specimen. To achieve a high level of saturation in a specimen during cyclic laboratory testing, Skempton's B value is used instead of the degree of saturation, Sr. This is because the B value is a more sensitive index when a specimen is almost completely saturated, as shown in Figure 2-38 (Towhata, 2008). To ensure satisfactory saturation, the minimum acceptable value of B in cyclic laboratory tests is 0.95-0.99. If the saturation is not

satisfactory, the back pressure is raised to higher values to dissolve pore gas into the water, and the remaining size of bubbles is compressed and decreases further (Kaya et al., 2021).

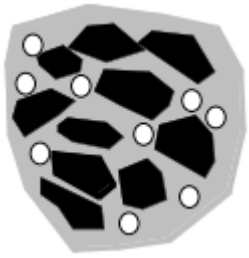

Figure 2-37: Soil element consisting of particles, pore water and air bubbles (Towhata, 2008)

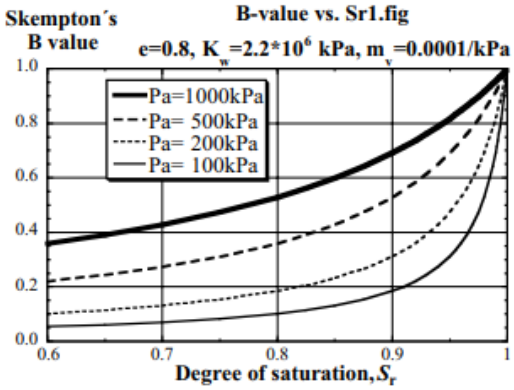

Figure 2-38: Example calculation of Skempton's B value varying with the degree of saturation (Towhata, 2008)

2.3.11 Relative Density and Poisson's Ratio of Sands

The relative density of clean fine, medium, and coarse-size sands is illustrated in Table 2-12 for the relative measure of corrected SPT-N blows/300mm and frictional angle. This table provides a range of values for different coarse-grained soil descriptions with respect to an equivalent relative density. These ranges of relative density can be used to prepare laboratory samples based on a given description such as loose, medium dense, or dense soils, as required. From these laboratory samples, correlations can be calculated, like the equivalent corrected SPT-N blows for a given fine sand, medium sand, or coarse-grained sand and its frictional angle, to suit geotechnical design analysis (Look, 2007).

Table 2-12: Strength from SPT on clean fine, medium and coarse-size sands only (Look, 2007)

Description	Relative Density, D_r (%)	Corrected SPT-N (blows/300 mm)			Frictional Angle, ^{0}
		Fine Sand	Medium Sand	Coarse Sand	
V. Loose	<15	≤3	≤3	≤3	<28
Loose	15-35	3-7	3-8	3-8	28-30
Medium Dense	35-65	7-23	8-25	8-27	30-40
Dense	65-85	23-40	25-43	27-47	40-45
Very Dense	>85	>40	>43	>47	45-50
-	100	55	60	65	50

Kumar & Madhusudhan, (2012) conducted tests using bender and extender elements to examine the impact of relative density and confining pressure on Poisson's ratio. These tests were carried out at an effective confining pressure of 100 kPa and five different relative densities ranging from 38.25% to 83.37%. The results, presented in Figure 2-39, show that an increase in degree of saturation leads to a higher magnitude of Poisson's ratio.

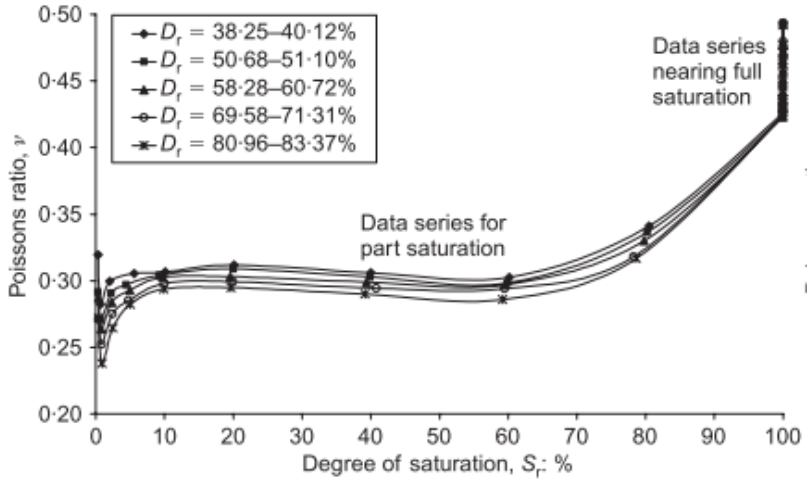

Figure 2-39: Variation of Poisson's ratio with degree of saturation at different relative densities for effective confining pressures of: (a) σ'_3 = 100 kPa (J. Kumar & Madhusudhan, 2012)

2.3.12 Laboratory Techniques for Evaluation of the Dynamic Response of Unsaturated and Partially Saturated Soils

The most common methods include the following;

2.3.12.1 Wet Compaction Technique

This approach utilizes soil compaction at varying saturation levels using the three-phase mass-volume relationship for a given relative degree of compaction. Complete saturation is then ensured by percolating the sample with carbon dioxide and applying back pressure in incremental steps, while checking the pore pressure parameter (B-value) to dissolve entrapped air such that B > 0.95 (Chen, Olson, Banerjee, Dewoolkar, & Dubief, 2022; Jafarzadeh & Sadeghi, 2012; Liu, Qin, & Yang, 2023; Mojtahedzadeh et al., 2022; Mousavi, 2020; Sze & Yang, 2014; Zhu et al., 2021).

2.3.12.2 Suction Control Through Tensiometric Technique

Once full saturation (B > 0.95) is achieved, tensiometric suction control is applied to desaturate the specimen in small incremental steps until the target saturation level is reached. The suction level and degree of saturation are measured and to provide the Soil Water Retention Curve

[SWRC]. The pressure differential transducer measures the contrast between the water and air pressure until equilibrium is reached to give a good matric suction (Mousavi, 2020).

2.3.12.3 Other Suction Control Techniques for unsaturated and Partially Saturated Soils

The approaches include; the MIPS technique, axis-translation technique, osmotic technique, humidity control technique, hanging water column, and vapor equilibrium techniques (Lu & Likos, 2004; Mousavi, 2020; Murray & Sivakumar, 2010; Ng & Menzies, 2007). These techniques are coupled with the following suction measurement instruments; pressure plates, tensiometers and suction probes, thermal conductivity sensors, electrical conductivity sensors, filter paper contact, thermocouple psychrometers, transistor psychrometers, chilled mirror psychrometers, filter paper non-contact, electrical conductivity of pore water extracted using pore fluid squeezer (Fredlund & Rahardjo, 1993; Fredlund, Rahardjo, & Fredlund, 2012; Murray & Sivakumar, 2010; Ng & Menzies, 2007).

2.3.13 Equivalent Number of Cycles for a Given Earthquake Magnitude

Seed & Idriss (1971) developed an equivalent number of cycles for a given earthquake magnitude to enable replicate cyclic laboratory tests at controlled conditions, as presented in Table 2-13. These stress cycles provide guidance for interpreting cyclic data to aid in seismic design for civil engineering project's seismic design.

Table 2-13: Equivalent number of cycles (Seed & Idriss, 1971)

Earthquake magnitude (Richter scale)	Number of significant stress cycles
7.0	10
7.5	20
8.0	30

2.3.14 Soil Liquefaction

When buildings are exposed to earthquakes, the soil around their foundations can lose its ability to resist shear stress. This can lead to catastrophic events, such as the failure of foundations and the collapse of entire structures (Chavan & Babu, 2023). While proper drainage can prevent water pressure buildup under static loading, cyclic loading can cause loose saturated sand to settle, break down the soil structure, and compress (Manzoor, Pandya, & Sachan, 2023; Sharika & Kumari, 2023). The brief duration of the shaking does not allow water to dissipate, resulting in increased water pressure that reduces effective stress and shear resistance (Al Tarhouni & Hawlader, 2023; Seyedi-Viand & Eseller-Bayat, 2022). This happens because loose particles in sand tend to compact more tightly under repeated loading, increasing pore-water pressure that cannot be

dissipated under undrained or partially drained conditions (Asadi, Orense, Asadi, & Pender, 2022; Gobbi, Reiffsteck, Lenti, d'Avila, & Semblat, 2022; Jia, 2018; Zhang, Gong, Wu, Li, & Zhao, 2023).

Figure 2-40, shows how pore-water pressure and shear stress-strain behavior change over time during undrained cyclic loading with constant shear stress. This loading creates a pore pressure that has two components: a permanent component called "u_p" and a cyclic component called "u_{cy}." Each load cycle adds an incremental pore pressure, which reduces the effective stresses in the soil and causes increased average, permanent, and cyclic shear strains over time (Li, Liu, & Nan, 2022). Eventually, the stress path reaches the failure envelope, as shown in Figure 2-41 (Liu et al., 2023; Manzoor et al., 2023). Figure 2-42 displays the excess pore-water pressures under different consolidation ratios ($k_c = \sigma_1/\sigma_3$, where σ_1 and σ_3 are the maximum principal stress and confining pressure), measured by the stress-controlled torsional shear test method. For cases without liquefaction occurrence, the number of load cycles required to induce liquefaction (N_f) is defined as the load cycles corresponding to deformation/strain of 5%. The number of loading cycles leading to liquefaction failure in saturated sand is highly influenced by the ratios and phase between the axial and horizontal dynamic stress (Andersen, 2015; Orang & Motamed, 2021; Stark, MacRobert, & Hayter, 2021; Zhang et al., 2023).

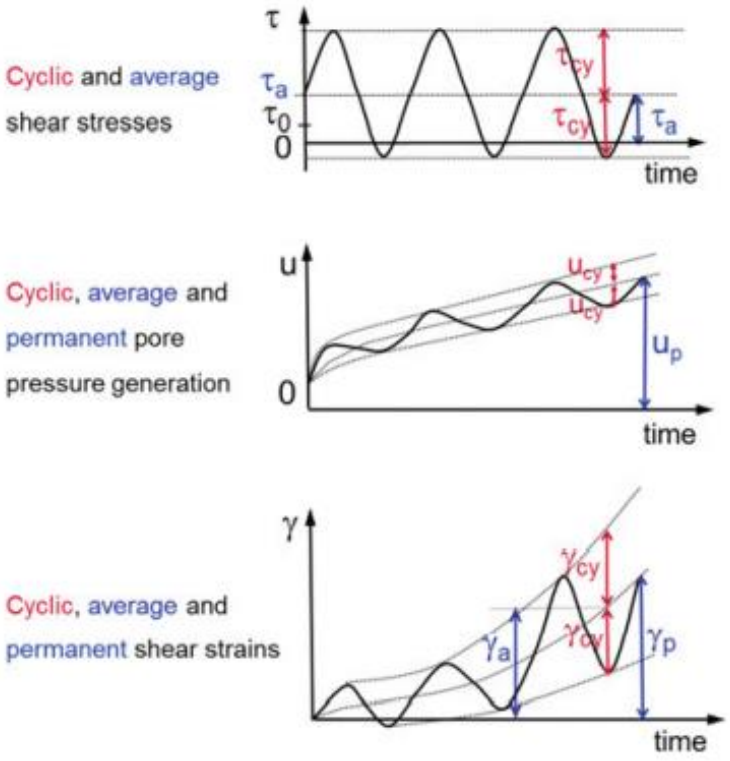

Figure 2-40: Pore pressure and shear strain as functions of time under undrained cyclic loading (Andersen, 2015)

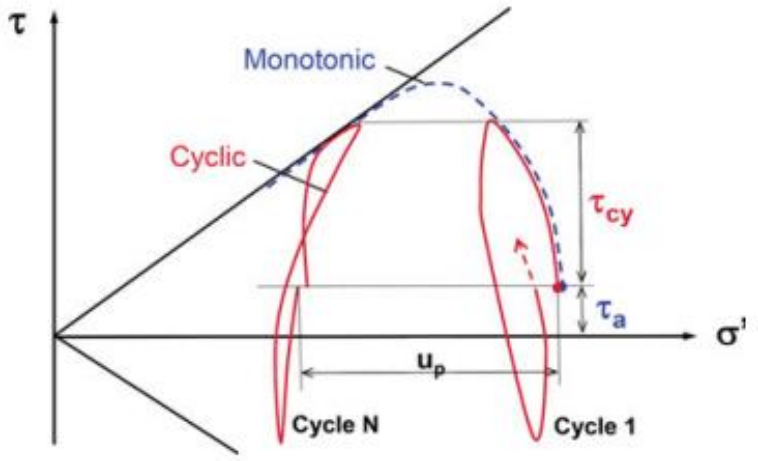

Figure 2-41: Development of effective stress for undrained tests in a contactant soil from monotonic to cyclic loading. In each load cycle, a single amplitude shear stress τ_{cyc} around a constant shear stress τ_a can be defined (Andersen, 2015)

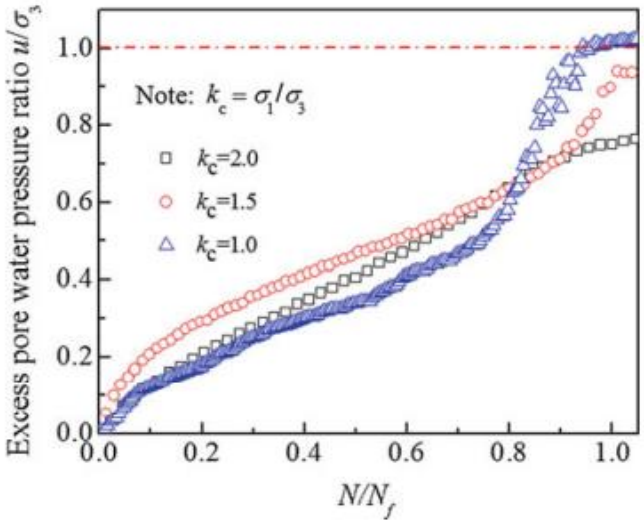

Figure 2-42: Excess pore-water pressure under different consolidation ratios (k_c), measured by the stress-controlled torsional shear test method (Andersen, 2015)

2.4 Cape Flat Sands

The Cape Flats is in the Western Cape in South Africa, as illustrated in Figure 2-43. It predominantly consists of a low-lying, sand-covered expanse linking the southwestern Cape mainland with the mountainous Cape Peninsula. Muizenberg, Bellville and Eerste River railway lines. The Cape Flats covers approximately 460 km^2, mostly made up of whitish transported Quaternary sands. The Quaternary age sediments sit on top of Neogene deposits, which rest on a basement of Precambrian and Paleozoic rocks (Fouche, 2021; Fouché & Day, 2022).

Figure 2-43: Geological map of the Cape Flats (Theron, 1990)

The Cape Flats is a coastal area with an elevation of around 30 meters above sea level. It is characterized by a dune system and wetlands made up of sand depressions and saturated soils. The sand in this area is light-colored and poorly graded, with a considerable variation in its properties. The ten year average groundwater level in the area is around 2m and 3m in winter and summer, respectively (Fouche, 2021; Fouché & Day, 2022). Fouche (2021) and Fouche & Day (2022) conducted various classification tests, including grading, soil classification, California Bearing Ratio, corrosivity, and erodibility tests, as well as characterizing tests such as collapsibility, hydraulic capacity, shear strength, liquefaction potential, and compressibility. The data collected from these tests were used to create an entire Cape Flats database, which includes both previous and new soil investigations. Most of the data were from a shallow soil profile of 0-3m below ground level, although some SPT/JKMRC profiles were up to 20-43m deep.

From the 16 CPTu profiles in the Cape Flat sands, Fouche (2021) reported that the liquefaction potential of the Cape Flats sands demonstrated a predominance of dilative sands. However, there are also contractive soils present that are vulnerable to losing strength and turning into liquid during shear. Ground failures caused by soil liquefaction are expected to exhibit limited deformation during cyclic loading. In a region with a typical seismic activity of moment magnitude 6.0 and PGA of 0.15g, there is generally a resistance to liquefaction during earthquakes. Fouche (2021) also mentioned the use of dynamic triaxial testing, but it was only limited to determining the resilient modulus through a multi-stage (4 stages) approach that involved different stress magnitudes for different cycles (0-1500) and confinement pressure (50-150 kPa).

The liquefaction potential of the Cape Flat sands was evaluated in the laboratory using a modified vibration table fitted with an accelerometer and mobile measuring device application (Schoeman, 2018). To prepare the 72 samples, a combination of air pluviation technique and compaction using

a hammer drill for loose and compacted states was used with uniformly graded sand, well-graded sands, and gap-graded sands at various moisture contents. Bricks with an approximate pressure of 1 kPa each were used to simulate foundations at different pressures. The vibrating table was used to simulate an acceleration of 0.15g (M_w = 6) and 0.25g (M_w = 8.0) until liquefaction occurred or for 60 - 120 seconds. The results showed that sands compacted at higher densities were more resistant to liquefaction, with fine sand demonstrating more resistance to liquefaction than medium-sized sands. Poorly graded sands showed an increased susceptibility to liquefaction compared to well-graded sands. Samples that contracted during shear had large settlements during liquefaction, while those with high liquefaction resistance exhibited dilatant properties.

2.5 Past Research

2.5.1 Past Research in the World

Tanaka, Kokusho, Tohma, & Kudo (1994) evaluated the cyclic properties of four gravelly and sandy soils (fines content of 2.0-8.1% with maximum grain sizes of 40-200mm) due to an earthquake using undrained cyclic Triaxial tests. The cyclic tests were performed at varying relative densities (40 - 90%), cyclic cycles (0 - 225 cycles), and axial strain (0 - 10%). In this study, the analysis of the gravelly and sandy soils revealed the dependency of the volume change characteristics on the maximum shear strain, relative density, and difference between void ratio (minimum and maximum), which resulted in a rough (poor) estimate in the calculation of the residual settlement when compared with the large-scale shaking table tests.

Ramadan (2007) evaluated the earthquake-induced loads to dry cohesionless deposits using 18 different clean sands and eight silty sands. The sands were selected to span a range of material gradations, particle sizes and shapes. The soils were prepared using varying relative densities (D_r = 45, 60 and 80%) and subjected to cyclic simple shear tests. These tests revealed variability of the determination of the vertical strains by up to three times when prepared at the same relative density, while the vertical strains decreased with increasing secant shear modulus by up to a factor of three times.

Stamatopoulos et al., (2004) assessed the performance of cyclic tests on three different soil densities (loose, medium, and dense), two Over Consolidated Ratio (OCR) values (OCR = 1 and OCR = 3) on saturated/unsaturated Greek sand (with non plastic fines content of 11%) and using the direct cyclic simple device under constant volume with cyclic cycles ranging from 0 - 55 cycles. The results of the volumetric strain obtained in this study showed reasonable agreement (for OCR = 1) and cases of disagreement (for OCR = 3%) being observed when compared to the predictions using Tokimatsu-Seed and Ishihara-Yoshimine evaluation methods.

Ghayoomi et al., (2015) reported that several methods used to determine volumetric strains primarily focused on the behaviour of sands in dry or saturated conditions leaving no knowledge

of the basic understanding on the behaviour of partially saturated sands. The research study utilized numerical models using Geostudio software to develop an equivalent approach that expresses the effective stress in the saturated sands and pore water pressure generation during cyclic loading as the most practical means of analysis due to their interrelationships with dynamic properties. Despite this developed numerical model, their study showed that the equivalent linear approach could not adequately predict the dynamic soil behaviour of partially saturated sand under earthquake load.

Kaya & Erken (2015) evaluated the cyclic behaviour of soils (sands, silts, and clays) using the cyclic Triaxial tests with a failure criterion being 5% of the axial strain. The study evaluated soils with natural water contents of 29 - 50%, fines content of 39 - 98% and Plasticity Index of 0 - 22% using up to 150 cycles. In sands, the failure limit of double amplitude shear strain of 5% was obtained with an increasing cyclic stress ratio. Large axial strains were observed within non-plastic fine-grained soils, while axial strain and pore water pressure reduction was observed with increasing plasticity indices at the end of the tests. The soils with Plasticity Index PI = 15 - 16% were observed to have lower strength than the soils of high plasticity, while the dynamic sand strength was 45% lower than the high plasticity soils. The research study further indicated that the fines content and plasticity index influenced the induced pore water pressure. The normally consolidated and overconsolidated soils showed a critical deformation level of $\varepsilon_{crit} = \pm 0.50\%$ and $\varepsilon_{crit} = \pm 1.0\%$ respectively. The static strength exposed to excessive axial strain during the cyclic loading was observed to decrease such that for a given number of N = 20 cycles at plasticity indices of NP, 16%, 30% and 40%, the reduction in deviator stresses was 27%, 40%, 53%, and 65% respectively. The soils demonstrated softening behaviour with $PI \leq 30\%$ and low consistency index ($I \leq 0.433$).

Whang et al., (2004) evaluated the seismic compression property using the cyclic simple shear laboratory test on four soils of fines content of 40-54% having a Plasticity Index, PI = 2 - 15% using a range of dry densities and degree of saturation levels. This study demonstrated the susceptibility of seismic compression to decrease with increasing density and decreasing amplitude of shear strain. In addition, the degree of saturation was noticed to impact the behaviour of soils with high plasticity (PI ~ 15%) while insignificant for the low plasticity soils (PI = 2%) with over-saturation levels of greater than 54%. The study further compared the results of the soils with clean sands, where they reported a decrease for an equivalent proportional behaviour of the seismic compression potential. The study generally showed agreement with previous scholars in which the seismic compression susceptibility of soils with fines increased with a decrease in relative compaction while showing an increase in the shear strain amplitude. The study shows the need to improve/modify the existing analysis procedures of seismic compression (like Tokimatsu & Seed 1987) for soils having fines considering the development of the equations using only clean and uniform sands.

Sayedmasoud (2020) evaluated the impact of the state and degree of saturation on the dynamic properties of silty sands using the wet compaction method. The saturation states were varied to include 35%, 50%, 65% and 80% with shear strain cycles of 0.025%, 0.1%, 0.2% and 0.4%, respectively, at a relative density of $D_r = 55 \pm 5\%$ using the undrained cyclic Direct Simple Shear (DSS) equipment. The fines content of the silty sands also varied from 0%, 10% and 20%, respectively. The shear modulus at 80% saturation content generally decreased with shear strain amplitude. At shear strains of 0.025% and 0.4%, the G/G_{dry} curve versus the saturation contents generally increased non-linearly to a peak value at 35% saturation content and, after that, fell below its original value at 80% saturation content. At 0.025% and 0.4% shear strains, the $D/_{Ddry}$ curve versus saturation content generally forms a minimum value at 35% saturation content and, after that, increases to about its original value. In addition, the wet compacted samples demonstrated varying volumetric behaviour than the unsaturated ones, especially at high saturation contents, and this was attributed to the soil structure dynamics during compaction.

2.5.2 Past Research in South Africa

Haas & Solms (2017) reported that certain regions in the Western Cape Province of South Africa are susceptible to moderate-intensity earthquakes of up to 0.15g, with recent research indicating up to 0.25g. Despite this, no available time histories are present; thus, in their evaluation of analyzing infrastructure using limited acceleration time history analysis, the scholars used an equivalent Chi-Chi earthquake (which occurred in Taiwan in 1999) time history since its detailed acceleration, velocity and time displacement records were readily available.

Haas & Kolf (2014) reported the susceptibility of moderate seismic activity with a peak ground acceleration of between 0.1g and 0.15g in the southern parts of the Western Cape. Thus, the scholars adopted the following six different earthquake data sets ($M_w = 5.77$ - 7.60 and PGA of 0.079 - 0.100g) with a broad range of responses to develop an acceleration response spectrum with a 5% viscous damping ratio for the evaluation of a three-storey unreinforced masonry (URM) low-cost residential buildings in Stellenbosch, Western Cape Town to high excitation frequencies. The results showed that the Chalfant Valley earthquake with PGA 0.095g led to a disproportionate response compared with the other earthquakes.

Haas & Marsh (2017) evaluated the safety and economic threat of low-income URM structures in the Cape Flats, a southwestern region of the Western Cape Province of South Africa, to moderate seismic activity, given that a number of these structures were constructed before the first codified provision for seismicity in SABS 0160 (1989). The structures consisted of 3 to 5-storey URM apartment buildings with plan dimensions of approximately 50m by 8m. Using the dynamic cyclic loading induced by a shaking table in 0.5Hz increments for 30 seconds and a constant horizontal displacement of 5mm to the base, the different wall size openings of 10%, 20% and 30% for the URM structures were evaluated. The experimental results indicated that the solid walls could

sustain higher frequencies at lower failure displacements. Thus, the walls become less stiff as the failure frequencies are reduced, increasing the in-plane failure displacement.

Kafodya & Okonta (2021) evaluated the cyclic and post-cyclic shear behaviour of natural fibre-reinforced soils by conducting undrained cyclic triaxial tests with sisal fibres of 25mm lengths at varying dosage levels of 0.25%, 0.5% and 1% with respect to the shear modulus, damping ratio, permanent strain, cumulative strain, and liquefaction potential. The tests also included the post-cyclic shear tests to evaluate the effects of fibre inclusion on the post-cyclic energy absorbing capacity, toughness, and static energy ratio. The study demonstrated that sisal fibres increased shear modulus to a limiting content of 0.5%, beyond which the modulus reduced. In contrast, the fibres increased the damping ratio due to their enhanced resistance to deformation. Both reinforced and unreinforced soil types exhibited high resistance to liquefaction. However, increasing the fibre content increased the post-cyclic energy absorbing capacity, toughness, and static energy ratio for the composite soil.

Studies concerning the liquefaction potential of the Cape Flat sands with respect to the CPTu and vibrating table (Fouche, 2021; Fouché & Day, 2022; Schoeman, 2018) are presented in Section 2.4.

2.5.3 Summary

Several research in South Africa has been related to seismic hazard and risk assessment (Brandt, 2011; Durrheim & Manzunzu, 2018; IAEA, 2002; Kijko, Smit, & Coolwijk, 2015; Liebenberg, Smit, Coetzee, & Kijko, 2017; Midzi et al., 2020a; OCHA, 2007; Ramirez, 2015; Worku, 2014), ground motion prediction and experimental response spectra (Cichowicz, 2012), acceleration time history analysis (Haas & Solms, 2017), and seismic analysis of URM buildings (Haas & Kolf, 2014; Haas & Marsh, 2017).

Several worldwide research have been performed in dry or fully saturated conditions with little fundamental understanding on the impact of the degree of saturation and state of saturation on the dynamic properties of sands. Furthermore, there is scarce research that has been carried out on the dynamic properties of soils in South Africa; these are related to cyclic and post-cyclic shear behaviors of natural fibre-reinforced soil (Kafodya & Okonta, 2021) and the effect of increased axle loading on the behaviour of heavily overconsolidated railway foundation material (Mpye & Gräbe, 2021). Several soil characterization tests have been carried out on Cape Flat Sands with little or no cyclic properties being evaluated. This study investigates the dynamic soil behaviour of Cape Flat sands under cyclic earthquake loads varying moisture/saturation contents, seismic strain cycles and relative density/void ratio for the localized soils within Cape Town in South Africa.

3 Methodology

3.1 Experimental Program

The laboratory test matrix for this research design is presented in Figure 3-1 for the Cape Flat sands, varying relative density, range of seismic cyclic strain and saturation states (from unsaturated-partially saturated-saturated).

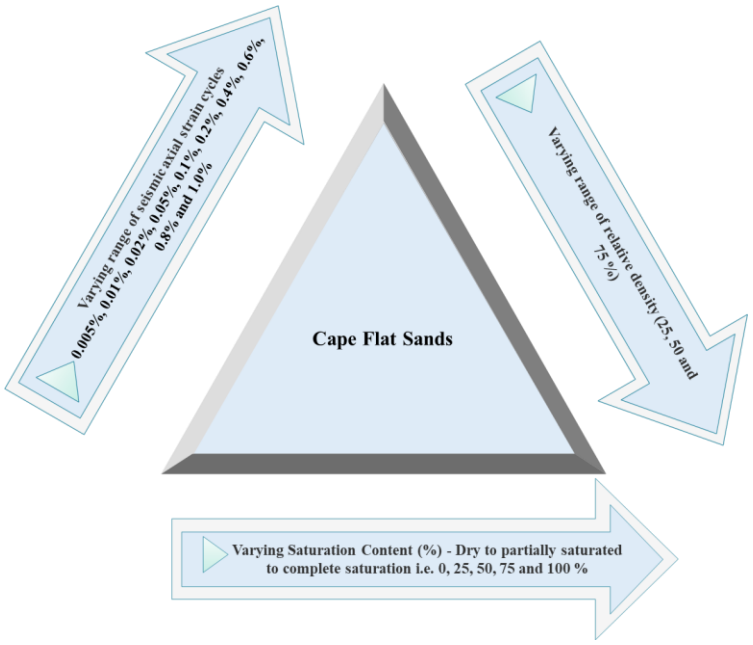

Figure 3-1: Testing matrix

3.1.1 Relative Density (D_r)

Using relative densities in Table 2-12, the D_r was selected as an average to reflect the loose dense (25%), medium dense (50%) and dense states (75%).

3.1.2 Saturation Contents (SAT)

Saturation contents of 0, 25, 50, 75 and 100% were selected to reflect the varying states from dry to partially saturated to saturated.

3.1.3 Cyclic Axial Strain Cycles (ε_a)

Cyclic axial strain cycles were carried out for 30 cycles and a period (T) of 2s (0.5 Hz), with each axial strain being varied from 0.005%, 0.01%, 0.02%, 0.05%, 0.1%, 0.2%, 0.4%, 0.6%, 0.8% and 1.0%. These cyclic axial strains were varied to reflect the small, medium, and large strains.

3.1.3.1 Cyclic Shear Strain (γ)

The cyclic shear strain was calculated using the relationship in Equation 3-1 (Gu, Gu, Cai, Wang, & Ling, 2017; Kaya et al., 2021);

$$\gamma = \varepsilon_a(1 + \mu) \qquad \text{Equation 3-1}$$

Where;

- γ = cyclic shear strain,
- ε_a = cyclic axial strain executed for 30 cycles and a period of two (2) seconds for each test,
- μ = Poisson's ratio obtained using the relative density in Section 2.3.11 and Figure 2-39 as presented in Table 3-1.

Table 3-1: Adopted Poisson's ratio (Kumar & Madhusudhan, 2012)

Relative Density (%)		Poisson's ratio (See section 1.1.1)				
		Degree of saturation (%)				
		0	25	50	75	100
Loose Dense	25	0.340	0.315	0.305	0.320	0.400
Medium Dense	50	0.285	0.310	0.300	0.305	0.400
Dense	75	0.275	0.295	0.290	0.300	0.400

3.2 Laboratory Tests

The following laboratory tests were carried out on Cape Flat sands, readily available within the laboratory for the soil classification and dynamic tests, as presented in Table 3-2. Table 3-2 also shows the test standards that were adopted during this research study.

Table 3-2: Laboratory tests standards and test parameters to be obtained

Laboratory Tests	Test Standards
Atterberg's Limits	ASTM D4318-17e1
Particle Size Distribution by wet sieving	ASTM D6913/D6913M-17
Specific gravity	ASTM D854-14
Minimum index density	ASTM D4254-16
Maximum index density	ASTM D4253-16e1
Classification of Soils for Engineering Purposes (Unified Soil Classification System)	ASTM D2487-17
Cyclic Triaxial Tests	ASTM D5311/D5311M-13

3.2.1 Plastic Limit

The Plastic Limit test was conducted on Cape Flats sand, following the guidelines in ASTM D4318 - 17e1. The dry preparation method was adopted in which the sample was oven dried at 60^0 degrees for 24 hours, then manually sieved through 425µm (No. 40) for testing. About 30g of the moist portion that had a consistency of around 10 drops using the Casagrande equipment was set aside. The sample was then rolled between the palms of the hands and a glass plate with enough pressure to form threads of approximately 3.2mm within 2 minutes. The moisture content of the sample was then determined and reported as the Plastic Limit (PL). Following the test standard, where the PL could not be performed, the PI was reported as non-plastic (NP).

3.2.2 Particle Size Distribution by Wet Sieving

This test was conducted per ASTM D6913/6913M-17 using method A, involving the single sieve-set sieving. In this approach, the bulk sand sample was oven dried at 105 ± 5^0C for 24 hours. Using the cone and quartering sampling technique, two representative oven-dried samples of about 1.5kg were obtained and accurately weighed. Each sample was then submerged in water for an hour and then wet sieved using 75µm protected by the 300µm sieve in the presence of running water. The washed sample was then oven-dried at 105 ± 5^0C for 24 hours.

The oven-dry samples were then mechanically sieved through a nest of sieves in descending order comprising 6.70, 4.75, 2.00, 1.18, 0.600, 0.425, 0.300, 0.212, 0.150 and 0.075 mm, respectively, with a pan at the bottom and lid at the top. The sample mass retained in each sieve was weighed and recorded, and the results were tabulated to give the percentage finer. This was repeated for the second sample, and then a semi-logarithmic graph of the sieve aperture against the percentage finer was plotted.

3.2.3 Specific Gravity

This test was conducted following ASTM D854-14 for soils passing through a sieve 4.75mm (No. 4) using the water pycnometer method. In this approach, the sands passing 4.75 mm were oven dried in a thermostatically controlled oven for 24 hours at 105 ± 5^0C to method B. About 60g of the oven-dried sand was transferred to a 250 ml pycnometer of known weight, after which the new weight of the pycnometer and sand was determined. Distilled water was added to the sand to make a slurry whilst the water level reached halfway through the pycnometer's main body. All soils adhering to the sides of the pycnometer were rinsed into the slurry.

The soil slurry in the pycnometer was then de-aired continuously using a vacuum (see Figure 3-2) for 2 hours and then left to cool overnight. The pycnometer containing the slurry was then filled with water to the required mark. The new weight of the pycnometer with the slurry and water was determined and recorded. The contents of the pycnometer were emptied, rinsed, and then filled

with water to the mark; this weight was then read and recorded. Caution was taken to ensure the same weighing scale was used during this test.

The specific gravity was calculated from Equation 3-2;

$$G_{s,t} = \frac{M_s}{\left(M_{\rho w,t} - \left(M_{\rho ws,t} - M_s\right)\right)} \qquad \text{Equation 3-2}$$

Where;

- $G_{s,t}$ = the specific gravity of soil solids at the test temperature,
- M_s = the density of the oven-dry soil solids (g),
- $M_{\rho ws,t}$ = the mass of pycnometer, water, and soil solids at the test temperature, (T_t), g,
- The specific gravity at 20^0C was calculated from Equation 3-3;

$$G_{s,20^0c} = K.G_{s,t} \qquad \text{Equation 3-3}$$

Where;

- K = temperature coefficient of water.

Figure 3-2: Vacuum apparatus for specific gravity

3.2.4 Index density and Index Void Ratio

3.2.4.1 Minimum Index Density

This test was conducted following ASTM D4254-16 using method C for inverting a graduated cylinder. In this method, the oven-dry mass (105 ± 5^0C for 24 hours) of sand passing 2.00 mm (No. 10) sieve was cone and quartered to obtain a representative sample of about 1.5 kg. 1000 ± 1g of sand was weighed and then transferred to a 2000 mL graduated cylinder. The top of this cylinder was stoppered, tipped upside down and returned to its original vertical position. The

volume (V_g) occupied by the sand within the graduated cylinder was read and recorded. This procedure was repeated thrice until the minimum index density/unit weight was within 2%.

The minimum index density was calculated from Equation 3-4;

$$\rho_{dmin,n} = \frac{M_s}{V_g} \qquad \text{Equation 3-4}$$

Where;

- $P_{dmin,\ n}$ = minimum index density for a given trial (Mg/m^3)
- M_s = mass of oven-dry soil (g)
- V_g = volume occupied by sand

3.2.4.2 Maximum Index Density

This test was conducted per ASTM D4253-16e1 using method 1A. In this method, oven-dried samples were cone and quartered to obtain a representative even sample of about 11kg with little segregation as possible. Using a scoop, the sand is filled into the assembled maximum index density mould (of known volume and weight). The sides of the mould were struck using a rubber hammer to ensure settlement of the sand whilst allowing the surcharge base plate to be placed within the position quickly. This approach also confirmed that there was no surge of air from the mould after the initiation of vibration. The surcharge base plate was then transferred to the soil surface and jolted firmly in contact with the soil, followed by the removal of the plate handle. The mould was transferred to the vibrating table (60 Hz) for 8 minutes.

The surcharge base plate was removed from the mould; the mould was removed from the vibratory table whilst preventing any fines that could have been collected on the surface of the surcharge base plate and rim of the mould from entering the mould. The mass of the mould and sand was then obtained using a weighing scale. This process was repeated till the value of the maximum index density/unit weight was consistent within 2%.

The maximum index density was calculated from Equation 3-5;

$$\rho_{dmax,n} = \frac{M_s}{V} \qquad \text{Equation 3-5}$$

Where;

- $P_{dmax,\ n}$ = maximum index density for a given trial (Mg/m^3)
- M_s = mass of oven-dry soil (g)
- V = volume occupied by sand

The set of equipment for the maximum index test is presented in Figure 3-3;

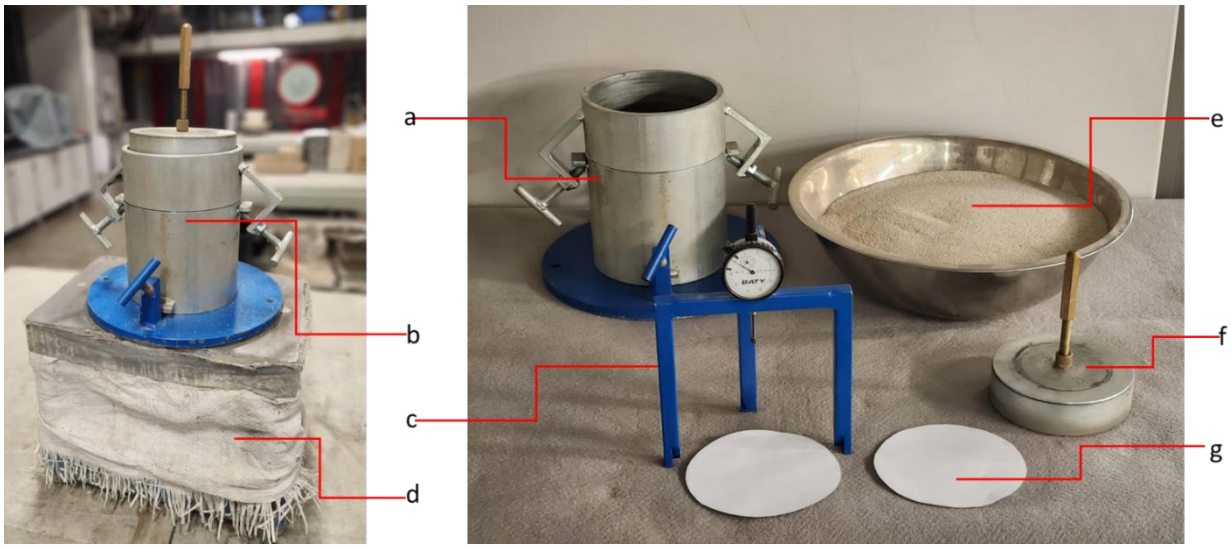

Figure 3-3: Test set for maximum index void ratio

a Maximum index density mold
b Assembled mold
c Dial gauge + stand
d Vibrating table
e Oven-dried sand
f Surcharge base plate and spacer disc
g Filter paper

3.2.4.3 Minimum Index Void Ratio

The minimum index void ratio was calculated from Equation 3-6;

$$e_{min} = \frac{\rho_w \, G_{20^0C}}{\rho_{d,max}} - 1 \qquad \text{Equation 3-6}$$

Where;

- e_{min} = maximum index void ratio
- ρ_w = density of water at 20^0C
- G_{20^0C} = specific gravity at 20^0C

3.2.4.4 Maximum Index Void Ratio

The maximum index void ratio was calculated from Equation 3-7;

$$e_{max} = \frac{\rho_w \, G_{20^0C}}{\rho_{d,min}} - 1 \qquad \text{Equation 3-7}$$

Where;

- e_{max} = maximum index void ratio
- ρ_w = density of water at 20^0C

- G_{20^0C} = specific gravity at 20^0C

3.2.5 Cyclic Triaxial Tests

This test was conducted by ASTM D5311/D5311M-13 using a triaxial cell for specimen dimensions of diameter 50mm and height 100mm.

3.2.5.1 Test Equipment

During the testing process, several components were utilized, including a LoadTrac-II load frame, two FlowTrac-II flow pumps, a Linear Electro-Mechanical Actuator (LEMA), a Cyclic-RM unit, a cyclic triaxial test chamber, and a computer with a Geo-Net card. Test data was displayed on the LCD front panels of both the LoadTrac-II and the FlowTrac-II in real time.

The LoadTrac-II was responsible for providing the static vertical force through its vertical stepper motor, while the linear electro-mechanical actuator provided the cyclic component of vertical force. This vertical system used a high-speed, precision micro stepper motor with a constant rate of displacement capacity ranging from 0.00003 to 15 mm per minute. The FlowTrac-II flow pump was equipped with a high-speed, precision micro stepper motor to synchronize confining pressure to an accuracy of 0.35 kPa and volume to the cell or specimen to within 0.001 cc. The system also included output and supply valve controls from the cell or sample that were automatically maintained using an in-built microprocessor (Geocomp, 2019).

The Cyclic-RM unit uses its own Central Processing Unit (CPU) to synchronize signals from externally mounted displacement and pressure sensors. It also includes an E/P controller that regulates the air pressure in the triaxial cell. The CYCLIC7N v3.0 software automates the synchronization process and runs through all testing phases until completion. The software automatically analyzes and stores data using its built-in report capability algorithm (Geocomp, 2019).

3.2.5.2 Sample Preparation

Two porous stones were used to initiate the test set up; the first stone was placed at the bottom cap of the triaxial cell, followed by a filter paper. Using a stretching technique, the membrane was transferred to the bottom cap using a membrane catcher. After that, an O-ring was lowered over the membrane and placed over the bottom groove. Then, the triaxial split vacuum mould was clamped around the membrane and then applied a vacuum through the tubing supplied to the split vacuum mould. At the top of the triaxial split vacuum mould, an O-ring was used to stretch and hold the membrane in place. Finally, the sand sample was remoulded using the modified pluviation technique described below;

a) Pluviation Technique

The void ratio, e, equivalent relative density, D_r, and equivalent water content, w, were calculated using the three-phase mass-volume relationships. Equation 3-8 was used to calculate e, Equation 3-9 was used to calculate D_r, and Equation 3-10 was used to calculate w for a specific saturation content, S_r. These calculations were done for oven dry weights and the known volume of the triaxial split mould. The desired mass of de-aired water was also calculated to achieve the desired degree of saturation.

$$e = \left(\frac{G_s \gamma_w}{\gamma_d}\right) - 1 \qquad \text{Equation 3-8}$$

$$D_r = \left(\frac{e_{max} - e}{e_{max} - e_{min}}\right) x100 \qquad \text{Equation 3-9}$$

$$w = \left(\frac{eS_r}{G_s}\right) \qquad \text{Equation 3-10}$$

Where;

- G_s = specific gravity obtained from Equation 3-3,
- γ_d = dry density,
- e_{min} = minimum void ratio obtained from Equation 3-6,
- e_{max} = maximum void ratio obtained from Equation 3-7,
- γ_w = unit weight of water,

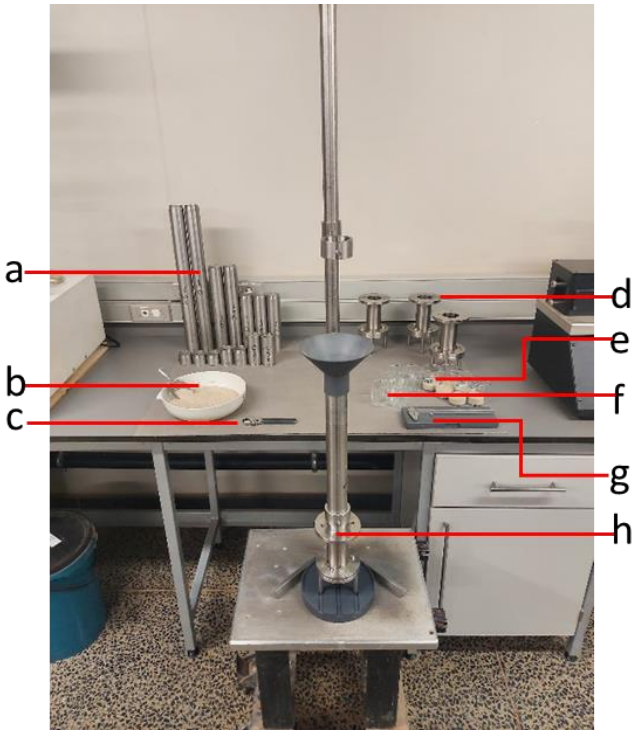

Figure 3-4: Test set for sample preparation by pluviation

a Pluviation tubing of varying lengths
b Oven-dried sand
c Spanner
d Calibration triaxial molds dia. 100mm, height =200 mm
e 6 proportions of weighed sand in beakers
f 6 proportions of weighed water in beakers
g vernier callipers
h Assembled set for pluviation

The required mass of sand and water for the respective D_r and S_r were then divided into six equal portions.

To achieve a specific degree of relative density, the modified moist pluviation technique involved pouring oven-dried sand in six layers from a funnel and tubing into the triaxial mould from a calibrated height. The dry sand was first transferred to achieve the given saturation contents, followed by sprinkling its equivalent amount of water till the required height of 100mm was attained from all six proportions. For preparing dense samples, the split mould was gently tamped 1-3 times after three layers of pluviation (Chavan, Sitharam, & Anbazhagan, 2021; Madhusudhan & Kumar, 2013; Monkol & Yamamuro, 2010; Xubin, 2007; Thevanayagam, 1998). Various trials were conducted using the equipment sets in Figure 3-4 and Figure 3-5 to ensure quality control during the actual tests.

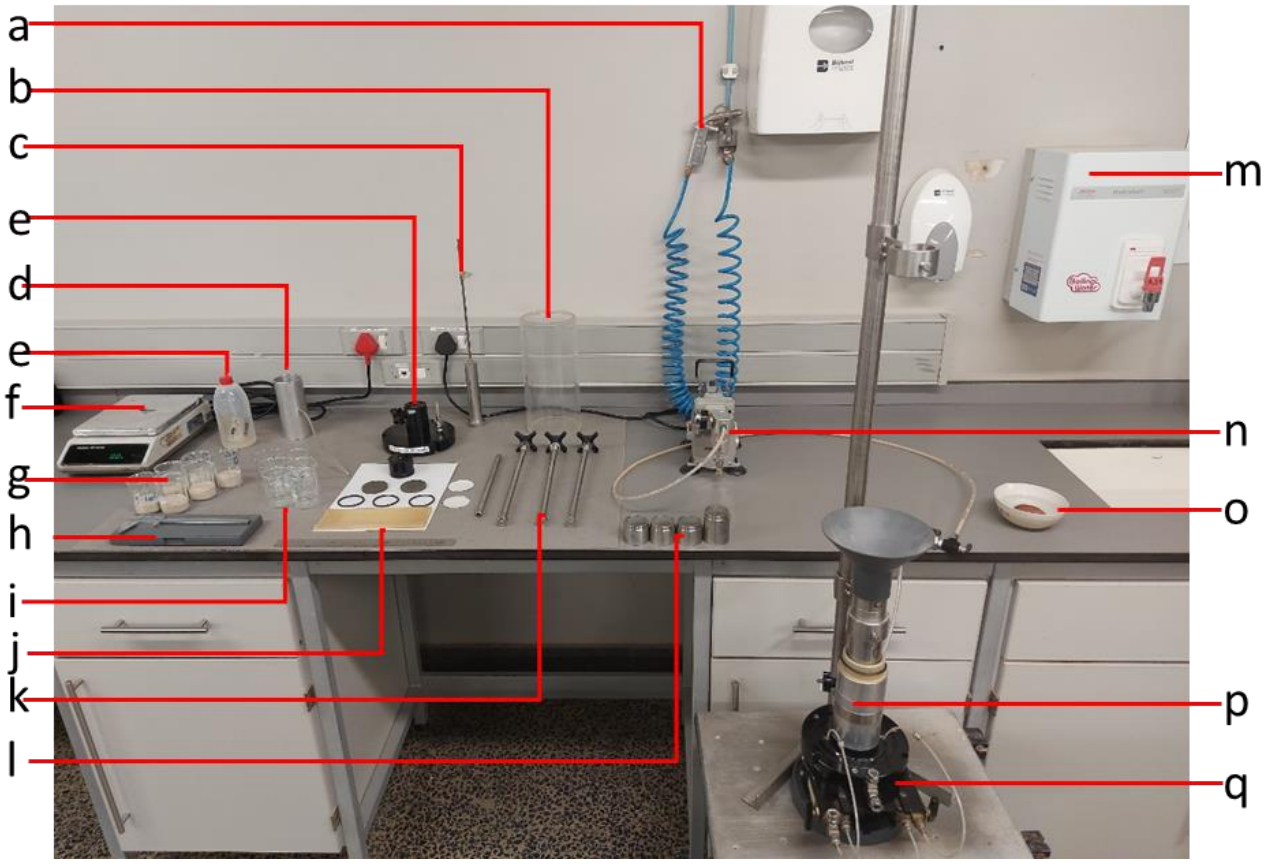

Figure 3-5: General test set for sample preparation for cyclic triaxial

a Compressed air gun
b Cell wall cylinder
c Tamping rod
d Membrane catcher
e Distilled water bottle
f Weighing scale
g 6 proportions of weighed sand in beakers
h Vernier calipers
i 6 proportions of weighed water in beakers
j Membrane + O-rings + Porous stones
k Tie-rod knob
l Pluviation tubing of varying lengths
m Hot water heater
n Vacuum pump
o Porous stone in hot water
p Triaxial split mold assemble + membrane
q Cell base

b) Triaxial Cell and Specimen Set-up

To confine the sample, the vacuum was released, and the membrane was held in place by an O-ring. A filter paper was placed on top of the sample, followed by a top cap. Two O-rings were added to the top grooves and the top drain tubing was clamped onto the top cap using bolts and tightened without disturbing the sample. The diameter and height of the remoulded specimen were measured at four locations using a vernier caliper. The piston was then attached to the top cap and the triaxial cylindrical chamber was inserted. The cell top, chamber posts, post knobs and piston locks were assembled and tightened to ensure the triaxial chamber was watertight.

c) Pressurizing the Triaxial Cell

To prepare for the test, water was added to the cylindrical chamber until the top of the membrane was submerged. The cell bleed port was left open to avoid pressure build-up. Care was taken to avoid bubbles that could affect the accuracy of the results or skew the data. After filling, the cell was checked for any leaks that might have occurred during the process.

3.2.5.3 Sample Pre-Saturation with Carbon dioxide (CO_2)

After ensuring that there were no leaks from the pressurizing stage, the next step was initiated began. CO_2 was gradually released from the bottom to the top of the specimen for 20 minutes at a pressure of 20kPa, as illustrated in Figure 3-6. This allowed the air inside the sample to be displaced, paving the way for successful saturation stages. Following this, the triaxial cell was cautiously moved to the LoadTrac-II platen.

Figure 3-6: Set up for pre-saturation with carbon dioxide

a Hot water heater
b Compressed air gun
c Partially filled cell with water
d Carbon dioxide bubbling in water
e Carbon dioxide gas cylinder

3.2.5.4 Test Assembly on the Cyclic Triaxial Test Frame

To prepare for the cyclic triaxial test, the LoadTrac-II's platen was lowered to 40mm above its lowest position using the load frame keypad. Then, a pair of 10mm maximum displacement traducers were connected with a bracket and placed over the triaxial cell's piston, ensuring that the transducer shafts were halfway into the transducer body. The triaxial cell was centered onto the platen and secured with C-clamps, and the coupling assembly was connected to the load cell, making sure it was not more than 38mm above the top of the test cell piston. Next, the cell water FlowTrac-II and sample FlowTrac-II were filled to 90% and 50%, respectively, with de-aired water using the keypad on its front panel. The tubing was then bled to remove air bubbles before connecting the tubing fittings to the triaxial cell in their respective order, including the cell water, sample water, EP pressure regulator, air supply, external sample pressure regulator, and external

EP pressure regulator from the sample water FlowTrac-II, cell water FlowTrac-II, and Cyclic-RM. Refer to Figure 3-7 for the schematic of the cyclic triaxial test.

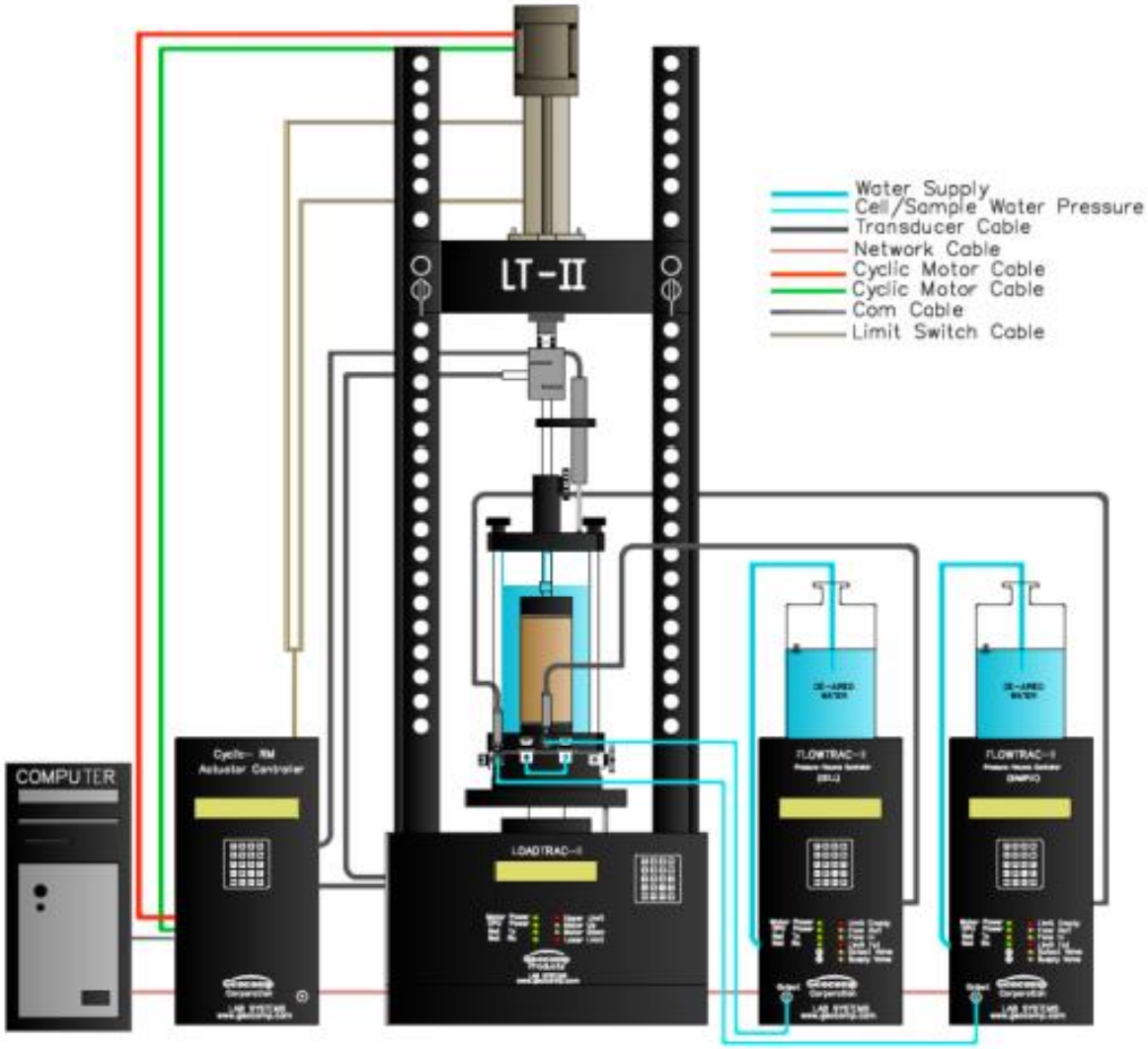

Figure 3-7: Schematic for the cyclic Triaxial test (Geocomp, 2019)

3.2.5.5 Commencing the Cyclic Test

The cyclic equipment includes a powerful data acquisition system that can collect experimental data in real-time with accuracy by using the Cyclic7N v3.0 software template. The software template file was named according to thequation 2-9e relative density (DR), degree of saturation (SAT), and cyclic axial strain (STR) using the code DR-XX-SAT-XXX-STR-XXX given in Appendix 2. For instance, DR-25-SAT-000-STR-0.1 was used for a test sample with 25% relative density, 0% degree of saturation, and 0.1% axial strain. Figure 3-9 presents the completed tabs of the software;

a) Zeroing/Calibrating

The system monitor displaying the real-time-current status of the different elements within the system is used to zero the test using the calibration summary menu before commencing the test.

b) Project

The was utilized to enter general information for this research project.

c) Specimen

This tab was used to enter physical parameters for the specimen like average diameter, average height, sample mass, and specific gravity.

d) Read Table

This tab was used to control the data acquisition frequency from the transducers and sensors during the test.

e) Test parameters

This tab was used to select the parameters that control the test and those used in the data reduction after the completion of the test.

f) Initialization

This tab was used to evaluate leaks within the membrane by inducing preliminary vertical, horizontal, and sample pressures for a given time.

g) Saturation

This stage was conducted to ensure all voids within the specimen were filled with water without necessarily allowing the sample to swell. Specified conditions were predetermined to enable an incremental increase in cell and sample pressure to achieve the minimum Skempton's B (saturation ratio) parameter value of 0.95.

h) Consolidation

This stage consolidated the sample after the saturation stage to an effective stress of 100 kPa for a minimum of 30 minutes.

i) Cyclic Axial Table

The cyclic strain method was adopted using the strain control approach with a cycle period of two (2) seconds.

j) Running the test

To initiate the test, the menu tab was run, for which subsequent prompts were followed to initialize the flow pumps, positioning the platen, and unlocking the piston respectively. The test then commenced by automatically executed each stage as presented above. Graphs were used to monitor the test in real-time until completion.

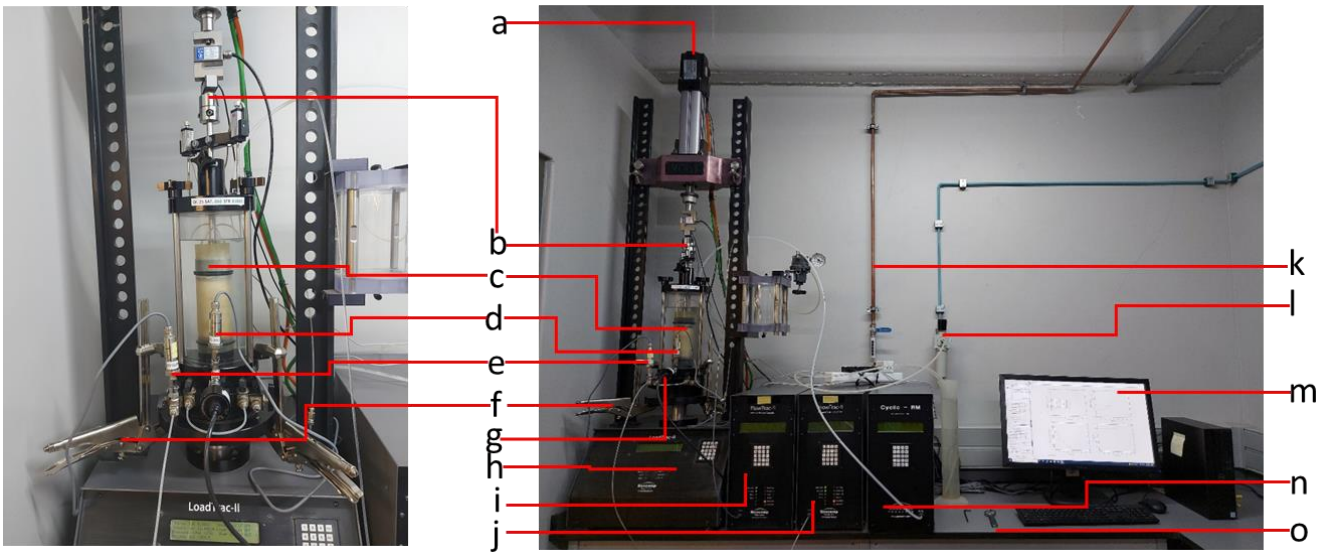

Figure 3-8: Test set up for running the cyclic triaxial test

a LEMA
b Coupling
c Top specimen
d external EP pressure regulator
e external sample pressure regulator
f C Clamps
g EP Pressure
h Load Trac II
i Sample water Flow Trac II
j Cell water Flow Trac II
k Water inlet
l Pressure regulator
m Computer set + Monitor
n Cyclic RM -Actuator Controller
o Spanner

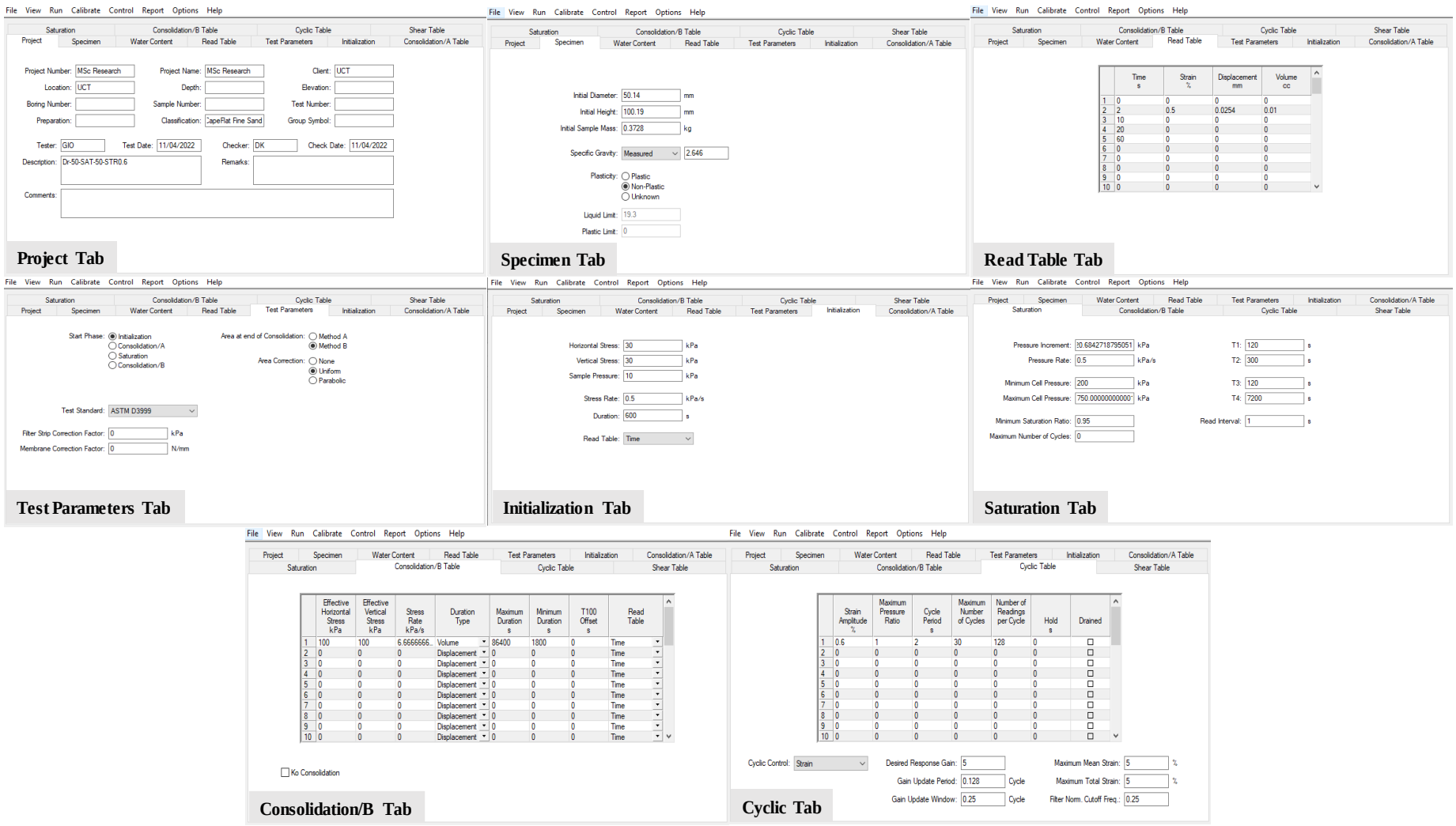

Figure 3-9: General settings fulfilled within the Cyclic7N software Template

3.2.5.6 Ending the Cyclic Test

After the cyclic phase ended, the software automatically stopped all data acquisitions and saved the test data; this was shown by the "test finished" window. Next, the cell chamber was depressurized, and the piston was locked while the coupler was loosened. The linear actuator was raised to its highest position, and the C-clamps were dismantled followed by the removal of the transducer bracket. Then, the respective cell water and sample water valves on the triaxial cell were closed, while the output valve was opened and the supply valve of the FlowTracs were closed. The tubing fittings from the sample water FlowTrac-II, cell water FlowTrac-II, EP pressure regulator, air supply, external sample pressure regulator, and external EP pressure regulator were disconnected from the triaxial cell. The test cell was then removed from the load frame and transferred to the sink. To release the pressure, a nipple was inserted into the quick-connect coupling on the cell top. The knobs at the top of the posts were loosened and disassembled, followed by the piston and the top of the triaxial cell. The cylindrical chamber was removed, and then the tubing was subsequently removed. The specimen was transferred from the base of the triaxial cell to a sample tray where the O-rings at the sample's top and bottom were removed, including the membrane and porous stones. The sample contents transferred to the tray were used to determine the moisture content after the test.

3.3 Correlations Between the Soil Properties

3.4 Regression Analysis

These were developed using the data obtained from the cyclic properties. The results of the tests were studied with the help of the IBM SPSS Statistics version 26.0.0.0 software program and the ASTM E2586-19. The correlations were made using Spearman's rho and were considered significant at a level of 0.05 (2-tailed) due to their significance, regardless of the distribution of variables (Norusis, 2004).

3.5 Multivariate Analysis of Variance (MANOVA)

To determine the factors and their interactions that had a significant impact on the shear modulus, damping ratio, and excess pore water pressure ratio (PWPR), MANOVA was conducted using IBM SPSS version 26.0.0.0. The analysis considered three factors: relative density (DR), saturation content (SAT), and cyclic axial strain (STR), each with varying levels. Two statistical models (Intercept + STR + DR + SAT + DR*SAT and Intercept + SAT + DR + STR + DR * STR) were carried out to analyze the data obtained at a significance level of $\alpha = 0.05$. The analysis was based on Pillai's trace, Wilks' lambda, Hotelling's trace, and Roy's largest root. Aspects related to confining pressure, period, and number of cycles were excluded since the tests were conducted under identical conditions, resulting in zero degrees of freedom (d_f). The MANOVA assumes that observations are independent, and the residuals follow a multivariate normal probability

distribution with means equal to zero and the variance-covariance matrices of each group of residuals are equal (Baecher & Christian, 2003; George & Mallery, 2019).

The hypotheses for the comparison of independent groups within the two models at $\alpha = 0.05$ were (Baecher & Christian, 2003; George & Mallery, 2019):

- H_o: means of all shear modulus or damping ratio or PWPR at given DR, SAT and STR were equal,
- H_a: means of all shear modulus or damping ratio or PWPR at given DR, SAT and STR were not equal,

Where;

- k = the number of independent comparison groups,
- H_o = hypothesis for equality of means,
- H_a = hypothesis for unequality of means

3.6 Repeatability

Achieving reliable results in a research project relies on the precision and repeatability of test results. To ensure this, calibrated equipment was used, and testing procedures and methods were carefully selected to guarantee reproducibility of test samples. The use of fully automated cyclic triaxial testing required meticulous sample preparation to ensure consistent sample quality. This allowed independent test results to be obtained using the same method on identical specimens, in the same laboratory, and by the same operator (ASTM E29, 2013; Gu et al., 2017; Wanatowski & Chu, 2008).

Considering that ten (10) axial strain levels (0.005%, 0.01%, 0.02%, 0.05%, 0.1%, 0.2%, 0.4%, 0.6%, 0.8%, 1.0%) were being carried out for the same relative density and saturation contents; a quality control chart monitored the respective masses of soil and water, masses, and back pressure to identify a possible outlier owing to the sample preparation process. Where the quality control chart limits were not met, the given test was repeated to confirm the reliability of cyclic results. Other techniques utilized to ensure repeatability included regular checks on the testing equipment, intermediate checks on the measuring equipment, replicate tests, re-tests, spot checks, good book-keeping records and review of the results obtained with existing literature (ASTM E1329, 2010; ASTM E178, 2021; ASTM E29, 2013).

In addition, the precision limits for a given test result that was calculated using the arithmetic of two other test results were adopted under the guidance of ASTM D4460-97 and ASTM E2586-19. Similarly, the significant digits reported for the given test data were adhered to using ASTM E29-13 and ASTM D6026-21.

3.7 Data collection and analysis of the laboratory results

i. The results were suitably analyzed using appropriate excel worksheets designed to carry out the data analysis for the test standards.
ii. The results from the customized templates were statistically evaluated using Microsoft Excel and SPSS statistical tools to obtain correlations and regression properties.
iii. The report document was prepared using the Microsoft office applications like MS Word, Excel, PowerPoint, Edraw and MS-Paint applications for illustrations, visual aid, and representation of the analyzed data.

3.8 Applicability of Test Results to Applications in Geotechnical Engineering

This was conducted by using two software programs, ProShake version 2.0.1.14 and Plaxis 2D version 20.2.0.83, for ground response analysis and free vibration and earthquake analysis of a building respectively.

3.8.1 Ground Response Analysis

3.8.1.1 Soil Profile and Equivalent Soil Model

An extract of a soil profile from the Cape Flats region (see Figure 2-43) was obtained from Kantey & Templer (Pty) Ltd (2018), along the R300. The detailed soil profile for Borehole number 3 (BH03) that has a water table of 2.45m can be found in Appendix 7A. The SPT results from BH03 in Appendix 7A were analyzed according to Burt's (2007) methodology to obtain the corrected SPT (N_{corr}), relative density (D_r), and angle of internal friction (φ), which is presented in Appendix 7B. The model was created based on the soil profile to account for the partial saturation effect at 2.00-2.45 m, as shown in Table 3-3.

Table 3-3: Soil profile

Depth (m)	Soil Consistency	Saturation State	Sample code
0.00-2.00	Medium Dense	Dry	DR050-SAT-000
2.00-2.45	Loose Dense	Partially Saturated	DR025-SAT-075
2.45-3.00	Loose Dense	Saturated	DR025-SAT-100
3.00-7.00	Medium Dense	Saturated	DR050-SAT-100
7.00-15.00	Dense-Very Dense	Saturated	DR075-SAT-100
15.00-20.00	Rock (Residual Malmesbury)	Saturated	-

3.8.1.2 Equivalent Soil Material Properties

The material properties of the soils are presented in Appendix 7D and 7C; the sources of the material properties included;

- Table 3-3 displays the results of this study, including bulk density, maximum shear modulus at small strain, shear strain, shear modulus reduction curve (G/Gmax), and damping ratio, which were used as input parameters,
- Reference manual (EduPro Civil Systems, 2017; Meyyappan, 2019; Noguera, 2016).

3.8.1.3 Equivalent Seismicity Properties

Since there is a lack of strong seismic ground motion data in South Africa, specifically in Cape Town, an "AT2 file" was obtained from the PEER NGA ground motion database (PEER, 2022). This file represents an equivalent tectonic plate in North America with M_w = 6.9 and PGA 0.174g (see Section 2.2.2.2). This seismicity equivalence was arrived at after conducting a literature review on the magnitudes of earthquakes that occurred in Cape Town during the Quartenary period presented in Sections 2.2.1. Table 3-4 summarizes the ground motion parameters for this seismicity record identified as Nahanni, Canada (1985)-RSN 497 on the PEER NGA database.

Table 3-4: Ground motion seismic properties for Nahanni, Canada (1985)-RSN 497

Ground motion record name	NS3 360
Digitization Interval (seconds)	0.0025
Number of data points	3819
Magnitude	6.8
Arias Intensity (m/s)	0.229
Bracketed Duration (s)	5.918
PGA (g)	0.174
PGV (cm/s)	0.030
Peak Displacement (m)	0.004
RMS Acceleration (g)	0.048
Predominant Period (s)	26.988
Mean Frequency (Hz)	7.070
Epicentral Distance (km)	22.4
Focal Distance (km)	23.8
Rupture Distance (km)	5.3

The acceleration time history, velocity time history, displacement time history, husid plot of acceleration, Fourier amplitude spectrum and response spectrum for Nahanni, Canada (1985)-RSN 497 earthquake record is presented in Figure 3-10.

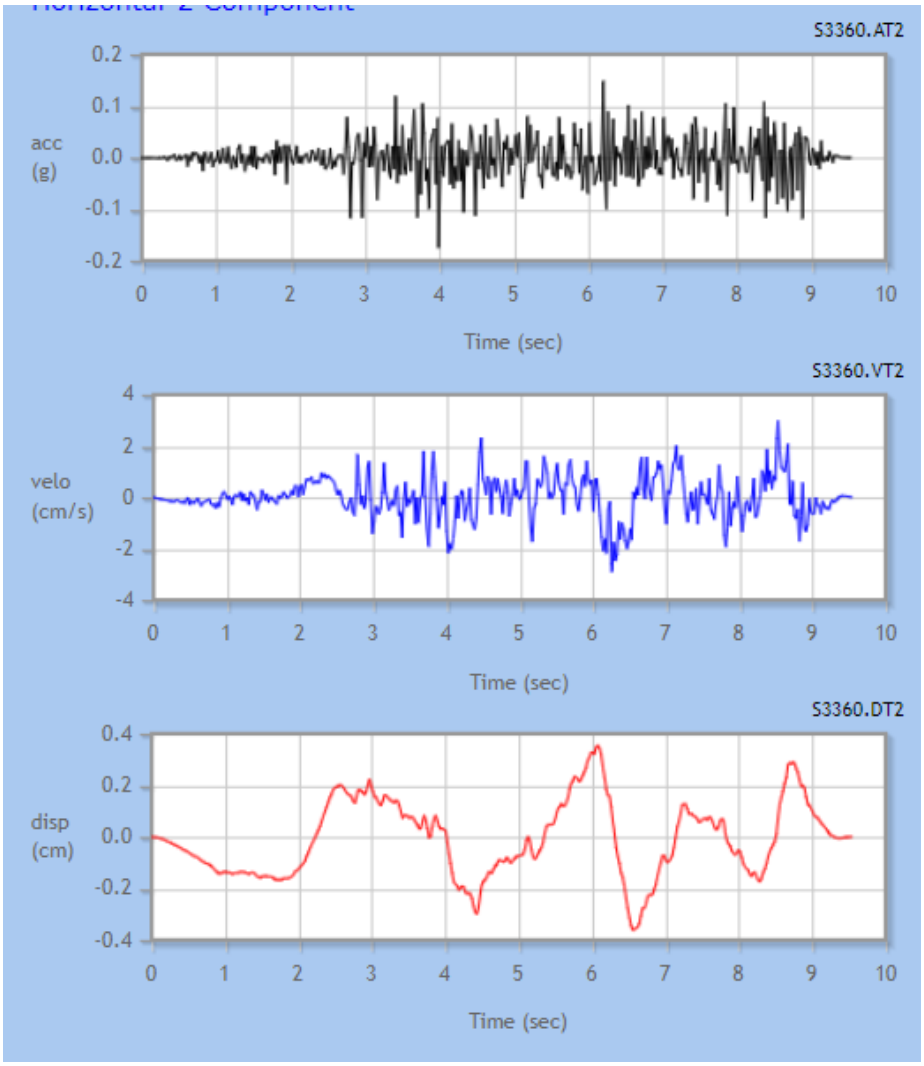

Figure 3-10: Ground motion parameters for RSN 497-Nahanni-Canada (1985) Earthquake with respect to time history of acceleration, velocity, and displacement - [PEER, 2022]

3.8.1.4 Software Analysis

ProShake 2.0-version 2.0.1.14 software (Figure 3-11) was used to develop the ground response analysis to demonstrate the applicability of the results derived from this study using its inbuilt input manager, solution manager and output manager, respectively. The software utilizes the Equivalent Linear (EQL) analysis to show non-linear behavior in soil, representing the total stress of soil behavior and its visco-elastic concept (EduPro Civil Systems, 2017; Meyyappan, 2019; Noguera, 2016).

The soil profile, soil properties (like modulus reduction and damping curve) and ground motion (Nahanni, Canada [1985] - RSN 497) were input into the input manager tab, followed by the analysis in the solutions manager. The ground response analysis was obtained as an output in the

output manager tab. T The output included plots of time histories with respect to acceleration, velocity, shear stress, peak acceleration, arias intensity, predominant period, and depth plots, among others (EduPro Civil Systems, 2017; Meyyappan, 2019; Prathima, 2009).

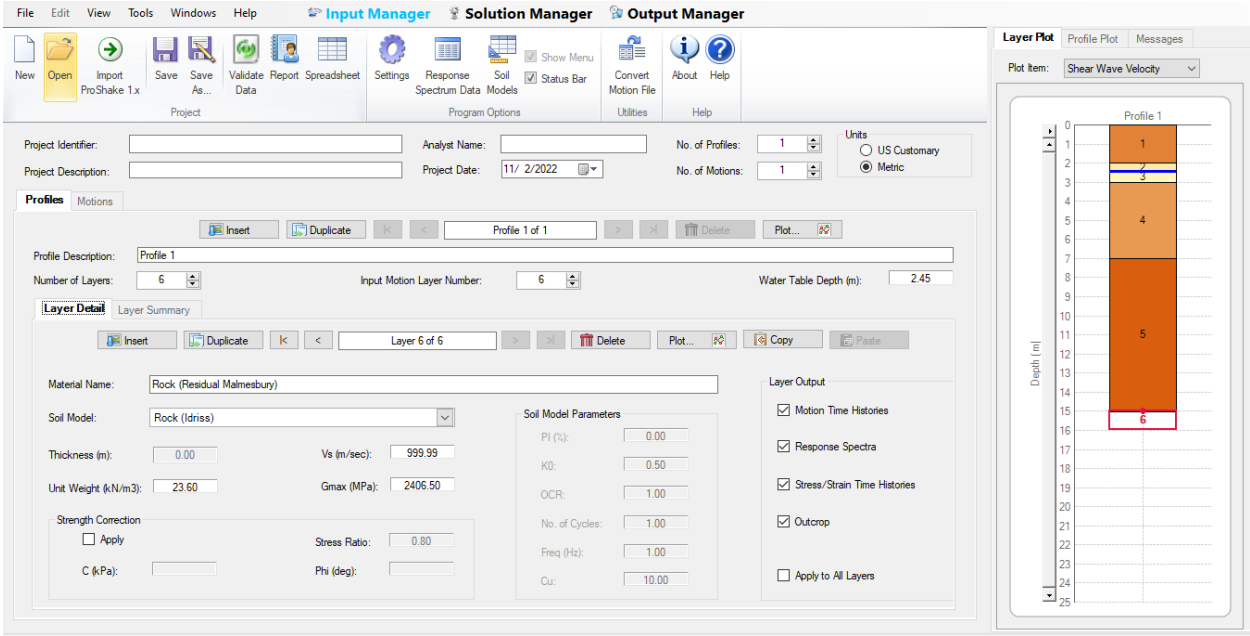

Figure 3-11: ProShake 2.0- version 2.0.1.13 software

3.8.2 Free Vibration and Earthquake Analysis of a Five-Storied Building

The free vibration and earthquake analysis of a five-storied structure was simulated using Plaxis 2D software (version 20.2.0.83).

3.8.2.1 Equivalent Soil Material Properties

The material input properties for the soils in the profile are presented in Appendix 7D; the sources of the material properties include;

- The results from this study using the sample codes presented in Table 3-3,
- The empirical formula for sands derived from SPT (Brinkgreve, Engin, & Engin, 2010),
- Plaxis scientific manual and reference manual (Plaxis, 2020b, 2020a).

3.8.2.2 Equivalent Seismicity Properties

The ".AT2" file obtained from the PEER NGA ground motion database (see Section 3.8.1.3) was converted to a".smc" file which was then used as an input motion in the Plaxis 2D software (PEER, 2022; Plaxis, 2020b; Onur, Tuncan, & Tuncan, 2016).

3.8.2.3 Storey Building

A 5 storied building with a basement was considered in applying the results from this study to demonstrate free vibration and earthquake evaluation of a structural building.

3.8.2.4 Software Analysis

The demonstration of the applicability of the results derived from this study was adopted using Plaxis 2D software (version 20.2.0.83). Plaxis 2D was utilised to execute dynamic calculations by modelling the hysteretic behaviour of Cape Flat Sand using the hardening soil model having small strain stiffness.

a) Stratigraphy

The stratigraphy was adopted in the model to 15m depth using Table 3-3 as illustrated in Figure 3-12.

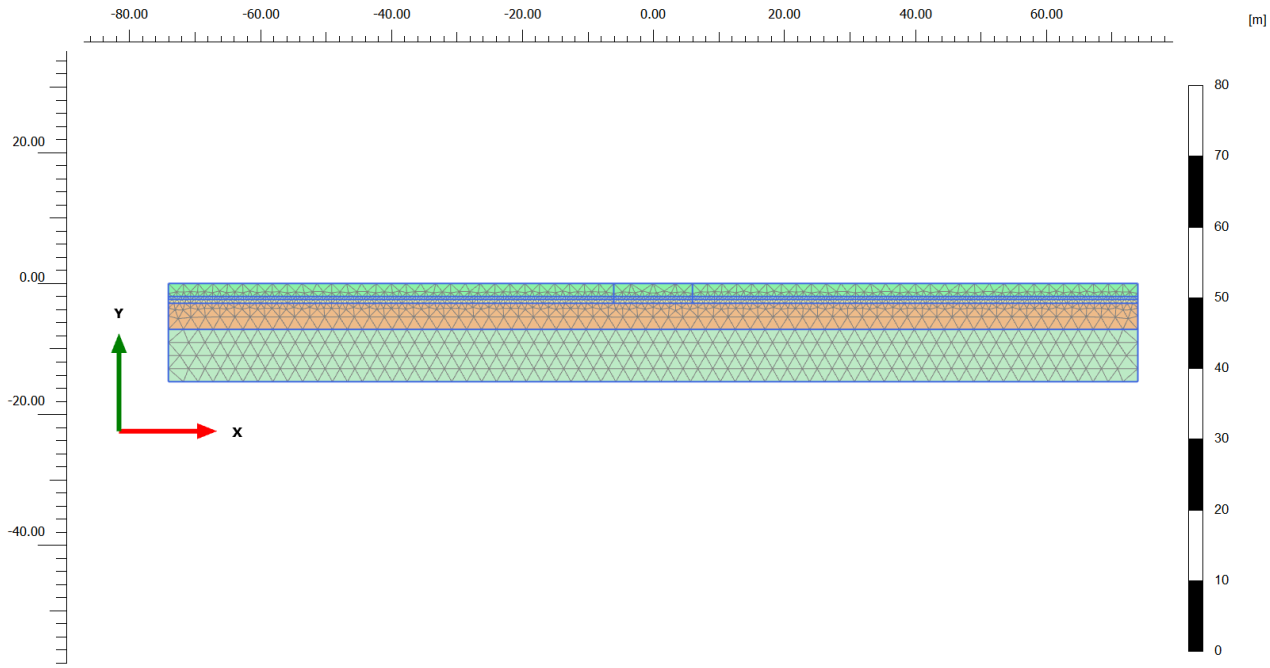

Figure 3-12: Meshed stratigraphy in Plaxis 2D

b) Material Data Sets

The material data sets for the soil stratigraphy, building (basement and superstructure) and node-to-node anchor are presented in Appendix 7C.

c) Earthquake/Dynamic Loads

This was simulated by adopting a dynamic point load (10 kN) as a driving force at the top left corner of the building. At the same time, the earthquake was modelled by creating a prescribed

displacement at 15m, which was the rock's surface (residual Malmesbury). The dynamic displacement of the prescribed displacement was defined by adopting a strong motion CD-ROM (.smc file) file for ground motion record NS3360 (RSN 497) from Nahanni, Canada (1985) records (Plaxis, 2020b, 2020a).

d) Performing dynamic calculation

Interfaces were created on the boundary, followed by the generation of the medium coarse mesh; the dynamic calculations were then generated by adopting the following phases (Plaxis, 2020b, 2020a);

- Initial conditions phase
- Phase 01-Simulation of building construction
- Phase 02-Dynamic excitation loading
- Phase 03-Free vibration analysis
- Phase 04-Earthquake analysis

After generating the four (4) phases (see Figure 3-13), the analysis was executed, and the output of the dynamic calculation was then used for the evaluation of the free vibration analysis of the building.

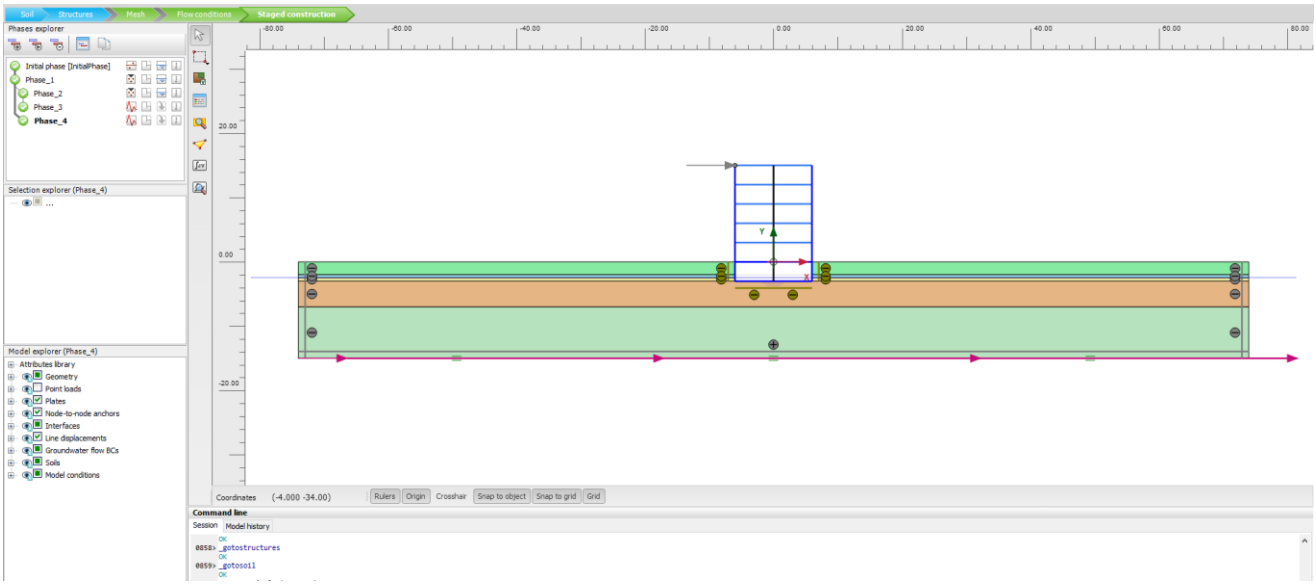

Figure 3-13: Soil stratigraphy and phases for the dynamic calculation

4 Results and Discussions

4.1 Introduction

This section covers information about the physical properties of Cape Flat sands, including particle size distribution, specific gravity, Atterberg's Limits, and minimum and maximum void ratios. The cyclic triaxial properties are also discussed, which include dynamic shear modulus, damping ratio, and Excess Pore Pressure Ratio at a constant confining pressure of 100 kPa. The discussion delves into varying relative density (25%, 50%, and 75%), degree of saturation (0%, 25%, 50%, 75%, and 100%), and cyclic axial strain (ranging from 0.005% to 1.0%). Shear strain was derived from the axial strain and Poisson's ratio, and the data presented provides a solid basis for discussing the results. The study results were utilized to showcase the practical application of earthquake time series equivalents in a real-life geotechnical project.

4.2 Physical Properties of Cape Flat Sand

The physical properties of Cape Flat Sand, including particle size distribution properties, degree of roundness, specific gravity, minimum and maximum void ratio, and Atterberg's limits, are provided in Table 4-1. Figure 4-1 shows the grain size distribution of the sand from two riffled samples, with an average of medium-sized sand fraction and 0.72% silts. The sand was classified as poorly graded sand (SP) due to a coefficient of uniformity (C_u) of 2.30 and a coefficient of curvature (C_c) of 1.15 in accordance to ASTM D2487-17. The average D_{50} and D_{90} were 0.40 mm and 0.85 mm, respectively. The sand was angular, non-plastic (NP), with a specific gravity of 2.646, minimum void ratio of 0.391, maximum void ratio of 0.377, minimum density of 1578 kg/m^3, and maximum density of 1902 kg/m^3.

Table 4-1: Summary of the Cape Flat Sand physical properties

	Test Parameter	Value	Units
Particle Size Distribution Properties	Coarse sand fraction (2.00 - 0.63 mm)	20	%
	Medium sand fraction (0.63 - 0.20 mm)	70	%
	Fine sand fraction (0.20 - 0.063 mm)	9.28	%
	Silty fraction (< 0.075 mm)	0.72	%
	D_{10}	0.200	mm
	D_{30}	0.325	mm
	D_{50}	0.400	mm
	D_{60}	0.460	mm
	D_{90}	0.850	mm
	C_u	2.30	-

Table 4-1: Summary of the Cape Flat Sand physical properties

Test Parameter		Value	Units
	C_c	1.15	-
	Soil Classification	Poorly graded clean sand (SP)	
	Degree of Roundness	Angular	-
	Specific Gravity	2.646	-
	Minimum void ratio, e_{min}	0.391	-
	Maximum void ratio, e_{max}	0.677	-
	Minimum Density	1577.5	kg/m^3
	Maximum Density	1902.19	kg/m^3
Atterberg's Limits	Plastic Limit (PL)	NP	%
	Plasticity Index (PI)	NP	%

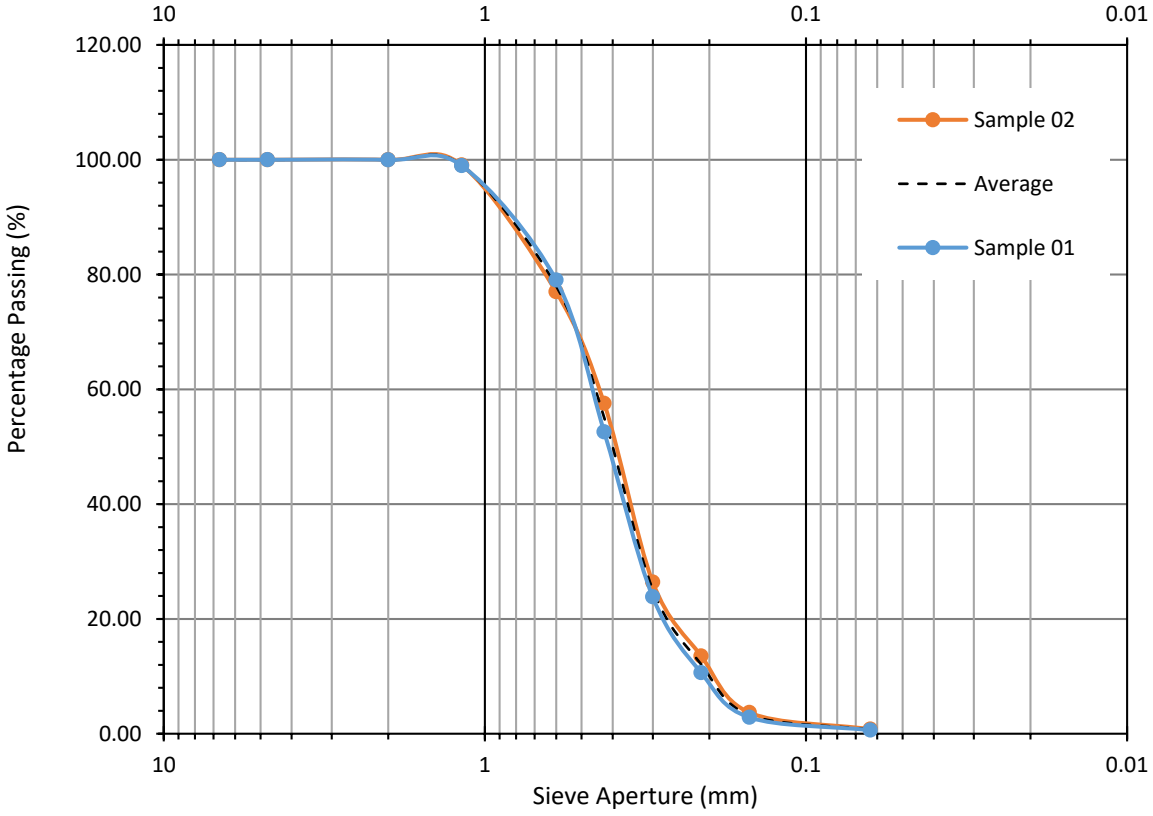

Figure 4-1: Particle Size Distribution Graph for the Cape Flat Sand

4.3 Dynamic Properties of Cape Flat Sands

4.3.1 Test Data from the Cyclic Triaxial Test

The test data for the cyclic triaxial test was generated by the Cyclic7N v3.0 software. This data was extracted from different phases of the test, including initialization, saturation, consolidation, and cyclic stages as illustrated in Appendix 3.

The results of an undrained cyclic triaxial test carried out with test number DR-75-SAT-000-STR-0.6 are presented in Figure 4-2. The test involved continuous two-way cyclic loading of compression and extension to replicate dynamic conditions (Karakan, Sezer, & Tanrinian, 2019). The shear stress curve starts at 0 kPa and increases to 90 kPa in the first cycle; it then decreases to 60 kPa between cycles 1-15 and remains constant at 60 kPa until cycle 30. The axial strain curve showed a constant cyclic strain amplitude of 0.6% throughout all 30 cycles. This indicates that there is a noticeable reduction in shear stress with an increasing number of cycles, but this reduction becomes less notable after a few loading cycles, depending on the strain level (Kumar, Krishna, & Dey, 2017). The graph of shear stress versus axial strain further demonstrated this behavior and was represented as a hysteresis stress loop in Figure 4-3.

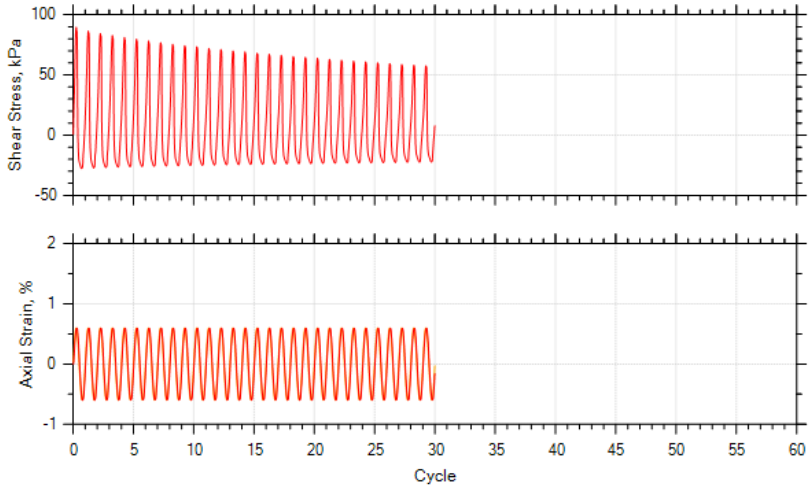

Figure 4-2: Cyclic test data for 30 cycles (DR-75-SAT-000-STR-0.6)

When sandy soil is repeatedly loaded and unloaded, it experiences a phenomenon called hysteresis, which causes damping due to non-linear frictional effects (Figure 4-3). This occurs as mineral particles slide over each other, resulting in less energy being released during unloading than the energy stored during loading. The degree of movement of individual soil particles affects the amount of energy absorbed, with greater movement resulting in higher damping (SW-AJA, 1972). Figure 4-3 shows the hysteresis stress loops for test number DR-75-SAT-000 at different axial strains (0.005%, 0.01%, 0.02%, 0.05%, 0.1%, 0.2%, 0.4%, 0.6%, 0.8% and 1.0%). The loops illustrate the behavior of shear stress versus axial strain, generally showing a decrease in shear stress with an increase in cycles (N) until it reaches a constant level. This is highlighted in stress cycles at N = 5, N = 10, N = 15, N = 20, and N = 25 cycles within all the stress hysteresis loops.

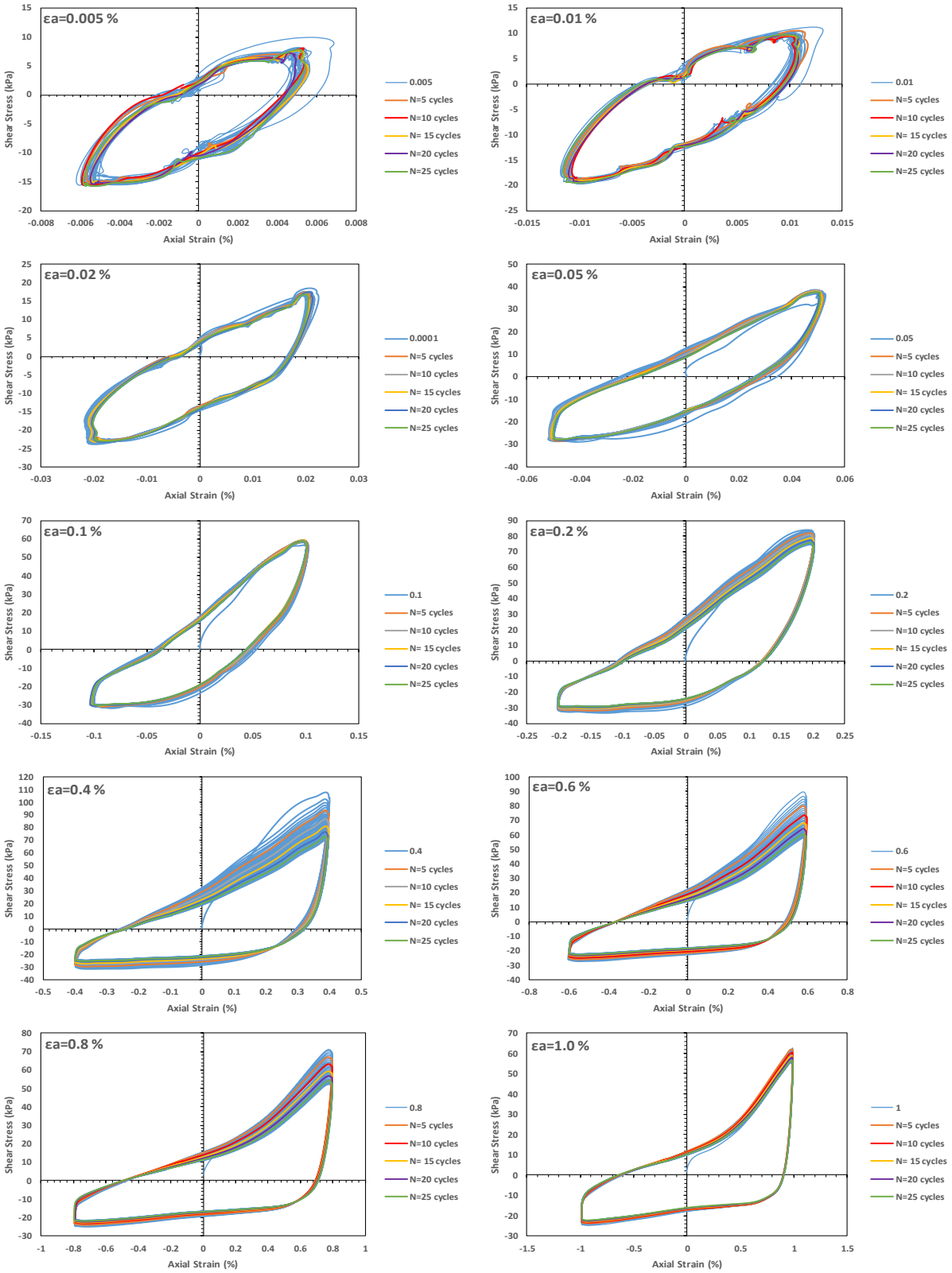

Figure 4-3: Hysteresis loops for axial strains of 0.005%- 1.0% (DR-75-SAT-000)

4.3.2 Shear Modulus

The relationship between shear modulus and shear strain for D_r at 25%, 50%, and 75% over ten cycles (N) is shown in Figure 4-4, Figure 4-5 and Figure 4-6. The results indicate that shear modulus values were highest in specimens with D_r = 75%, followed by D_r = 50% and D_r = 25%. This suggests that an increase in relative density leads to an increase in shear modulus, indicating that relative density has an outstanding impact on shear modulus (Mog & Anbazhagan, 2019). This is likely due to the dense interparticle arrangement in high relative densities like D_r = 75%, which leads to greater stiffness and lower void ratios (Dutta, 2015; Kakavand & Naeini, 2019).

It was noted that the shear modulus levels converged between shear strains of 0.7% - 1.5%. At relative densities, Dr, of 25%, 50%, and 75%, the shear modulus curve was higher for 25% saturation content compared to 0% saturation content for all shear strains that exceeded 0.01%. Generally, for shear strains greater than 1%, the shear modulus at all relative densities reached a range of 3223 - 5745 kPa, with each curve ultimately converging to a constant shear modulus.

It has been observed that the shear modulus of all graphs decreases non-linearly as the shear strain [γ] increases due to the loss of stiffness in the respective specimen (Hardin & Drnevich, 1972). It is evident that the shear modulus is dependent on the shear strain and relative density (SW-AJA, 1972). Furthermore, the higher the relative density, the higher the shear modulus. This was because an increase in relative density led to denser packing of soil grains and therefore increased soil stiffness. As the shear strain increases, the interparticle arrangement of the grains within the specimen breaks down, resulting in a reduction in stiffness and consequently diminishing the value of the shear modulus (Dutta, 2015).

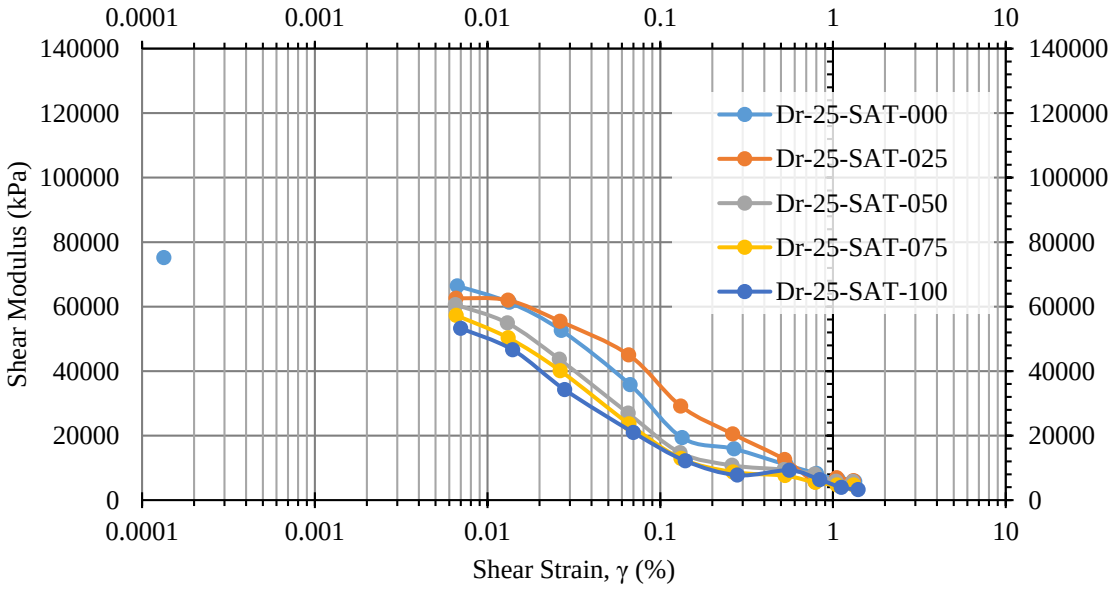

Figure 4-4: Variation of Shear Modulus with Shear Strain at D_r = 25%

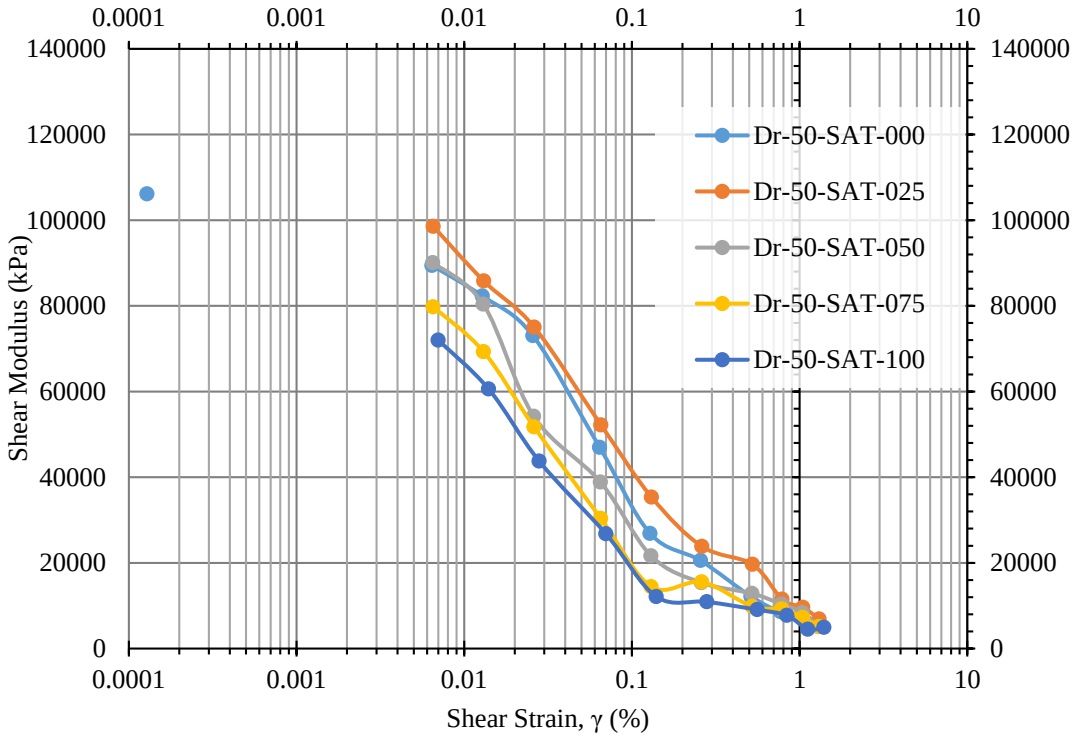

Figure 4-5: Variation of Shear Modulus with Shear Strain at D_r = 50%

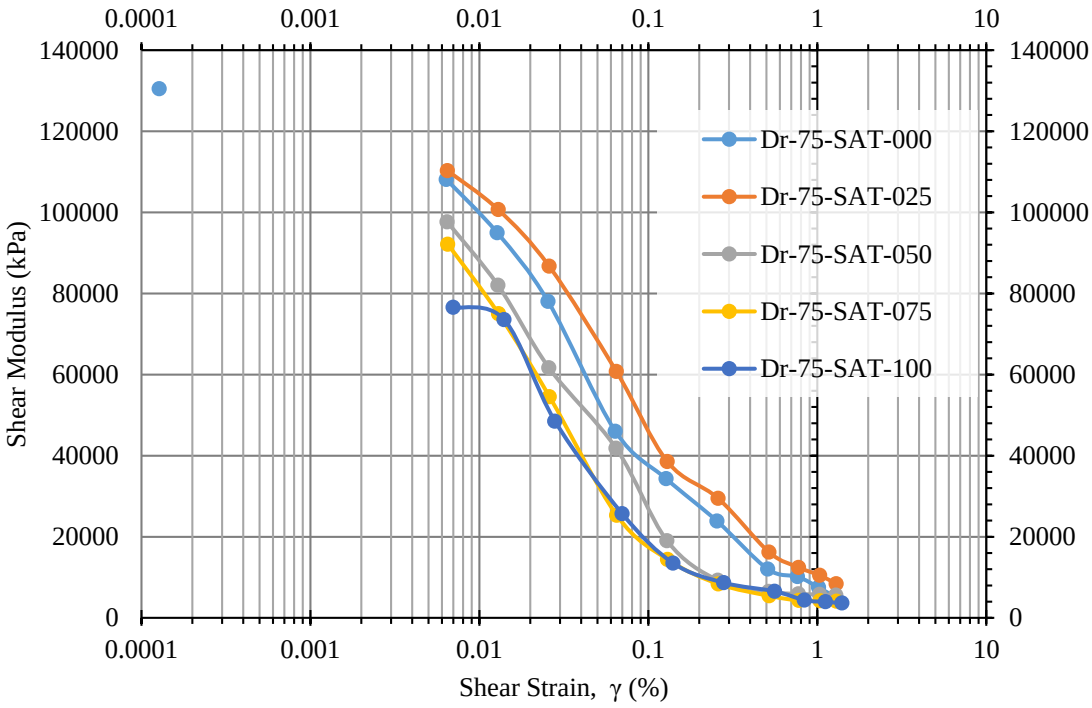

Figure 4-6: Variation of Shear Modulus with Shear Strain at D_r = 75%

The dynamic shear modulus at small strain was estimated from empirical correlations by Seed & Idris (1970) for all three relative densities owing to the conservative approach. However, Table 4-2 compares these estimates with those from Hardin & Drnevich (1972), Richard et al., (1970), and Hardin (1972). The adopted maximum shear modulus for D_r = 25%, 50%, and 75% were 75,173 kPa, 106,127 kPa, and 130,447, respectively.

Table 4-2: Estimation of shear modulus at small strains

Scholars	Maximum Shear Modulus (G_{max}) at given Relative Density (D_r), kPa		
	25 %	50 %	75 %
Seed & Idris, (1970)	75,173	106,127	130,447
Hardin & Drnevich, (1972)	96,237	107,427	119,938
Richard et al., (1970)	112,582	125,077	139,021
Hardin, (1972)	112,803	125,694	139,649

The normalized dynamic/shear modulus at D_r 25%, 50% and 75% is synthesized in Figure 4-7, Figure 4-8 and Figure 4-9, respectively. Generally, the normalized dynamic/shear modulus increased as relative density decreased, with D_r = 25% having a higher normalized dynamic/shear modulus than D_r = 75%. However, the pattern of shear modulus curves in Figure 4-4, Figure 4-5 and Figure 4-6 was similar to the normalized dynamic/shear modulus in Figure 4-7, Figure 4-8 and Figure 4-9. At higher shear strain levels, the scatter of the normalized dynamic modulus decreased (Mog & Anbazhagan, 2019).

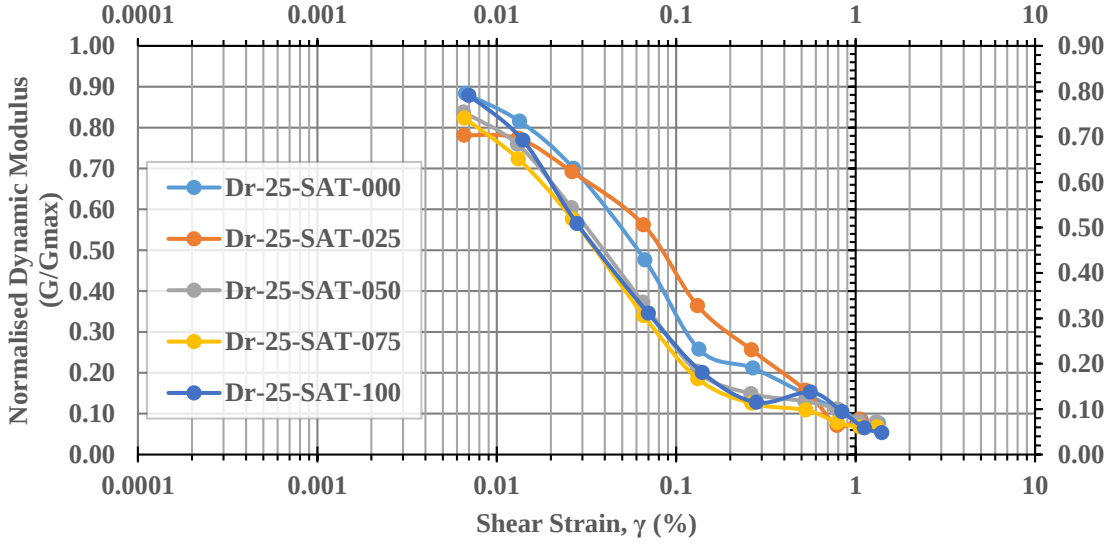

Figure 4-7: Variation of normalized shear modulus with shear strain at D_r = 25%

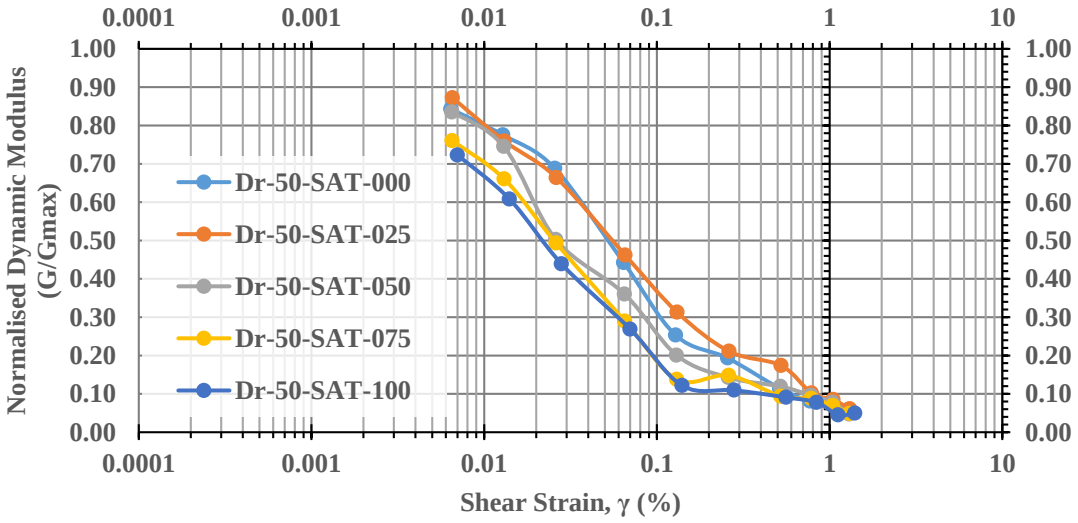

Figure 4-8: Variation of normalized shear modulus with shear strain at D_r = 50%

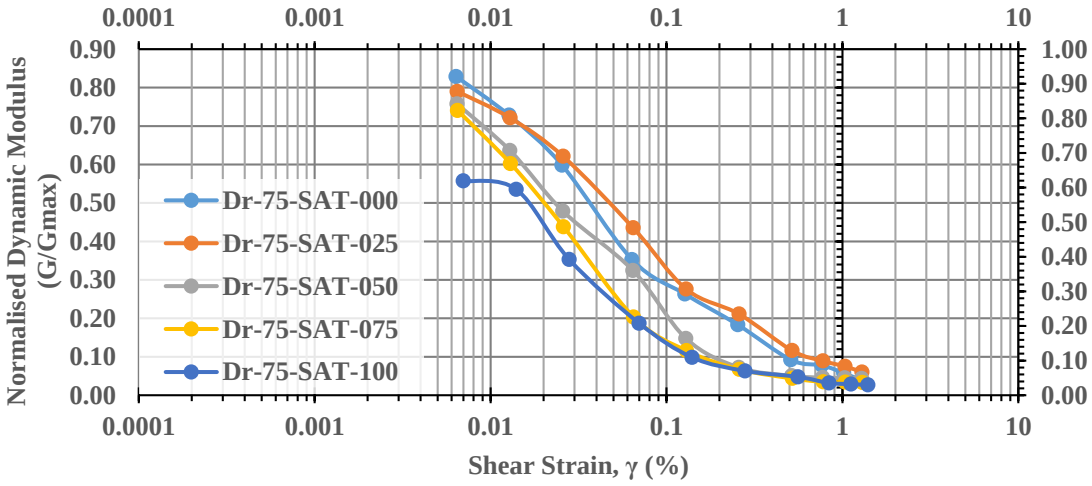

Figure 4-9: Variation of normalized shear modulus with shear strain at D_r = 75%

A common way to show how the shear modulus changes in response to shear strain in soil dynamics is by using normalized shear modulus curves. These curves are further used in Section 4.7.1 to analyze site response or estimate amplification. The normalized dynamic/shear modulus was calculated using the modulus reduction curves shown in Figure 4-7, Figure 4-8 and Figure 4-9. These curves were used to derive the curves on the left side of Figure 4-10, which were obtained from the studies of Stokoe et al., (1999) and Darendeli (2001). Table 4-3 (Section 4.5.1) shows the Pseudo-reference strain (γ_t) for G/G_{max} = 0.5 and curvature parameter (a) for each set of curves at the respective relative densities and saturation contents. These curves closely fit and match the test data obtained from this research study. At 0.1 - 0.3% shear strains, the results from this study for curves D_r = 25 and D_r = 50% at saturation contents of 75% and 100% fall below the corresponding fitting curves.

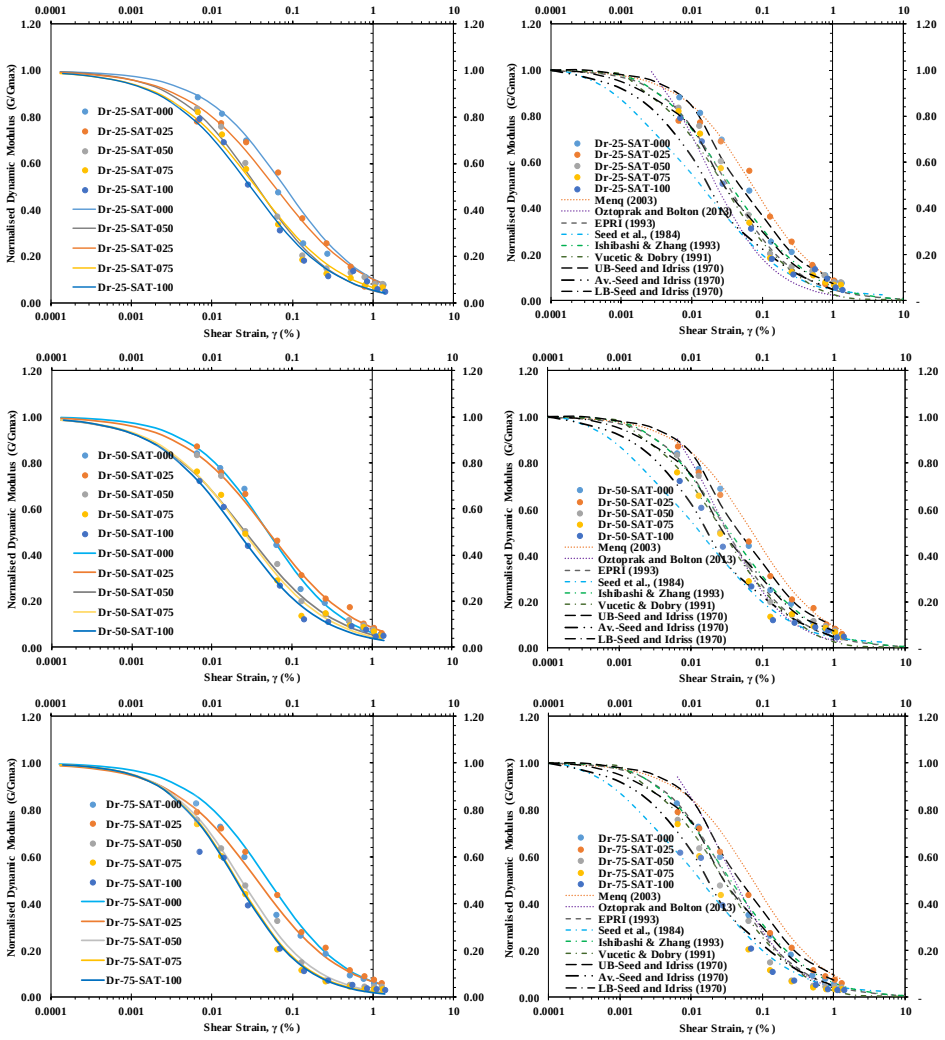

Figure 4-10: Curve fitting with Stokoe et al., (1999); Darendeli (2001) [left] and several scholars [right]

Several scholars' curves based on sand literature were fitted over the test data on the right side of Figure 4-10. These curves generally fit within the non-linear elastic range and non-linear range with shear strain (γ) of 0.005 - 0.01% and more remarkable than 0.01%, respectively. For D_r = 25%, the test data fit within the upper and lower bound curves by Seed & Idriss (1970). EPRI (1993), Ishibashi & Zhang (1993), and Vucetic & Dobry (1991) curves also had good agreement within the results. However, the results were below the Menq (2003) curve and above the Oztoprak & Bolton (2013) and Seed et al., (1984) curves, despite having a similar shape. For D_r = 50%, the curves fit the test data such that the results were generally between the Menq (2003) and Seed et al., (1984) curves. Some test data plotted above and below the upper and lower bounds, respectively, by Seed & Idris (1970). Only the data Dr-50-SAT-075 and Dr-50-SAT-100 plotted below the Seed et al., (1984) curve at a shear strain of 0.15%. For D_r = 75%, the results fit within

the upper bound by Seed & Idris (1970) and Seed et al., (1984) curves. The data plots from Dr-75-SAT-075 and Dr-75-SAT-100 were marked below the Seed et al., (1984) curve from 0.06-1.5% shear strains. Although each of the established modulus reduction models were developed based on the dynamic testing of a specific soil, adopting any model to determine the dynamic response of different soils may be incorrect. This illustrates that the dynamic properties of each soil should be judiciously determined before its application for any practical geotechnical engineering problems (Kumar et al., 2017).

4.3.3 Damping Ratio

Generally, in contrast to the dynamic/shear modulus at ten (10) cycles, the damping ratio tends to increase when the shear strain [γ] ranges from 0.005% to 1.5%, as presented in Figure 4-11 (Hardin & Drnevich, 1972; Dutta, 2015). The increase in damping ratio is due to the greater mobility of the sand particles during the cyclic tests, which results in a loss of energy (Dutta, 2015).

The low damping ratio during low shear strain range can be attributed to the specimens' equivalent higher shear modulus. However, the damping ratio increases to 19.7-23.5%, 18.7-22.8%, and 16.6-20.6% for Dr = 25%, Dr = 50% and Dr = 75%, respectively. As the relative density of sand increases, the damping ratio decreases slightly, meaning that loose sand (D_r = 25%) has a higher damping ratio under the same strain than dense sand (D_r = 75%) (Dutta, 2015; Kakavand & Naeini, 2019; Mog & Anbazhagan, 2019).

The damping ratios obtained by Seed & Idris (1970) on sand samples subjected to same confining pressure was superimposed over the test data. The damping ratio curves obtained from this study for shear strains of 0.005-0.1% were mostly between the upper bound curve by Seed & Idris (1970) and the average curve by Seed and Idris (1970) for all relative densities. However, for shear strains beyond 0.1%, the damping ratio curves from this study were between the average curve by Seed & Idris (1970) and the lower bound curve by Seed & Idris (1970) for D_r = 25%. For D_r = 50%, only two curves (SAT-000 and SAT-025) were below the lower bound curve by Seed and Idris (1970), while at D_r = 75%, all curves (at given saturation contents) were below the lower bound curve by Seed and Idris (1970). At shear strains of 0.02-0.06% and 0.01-0.06%, respectively, the damping ratio curve for DR-25-SAT-100 and DR-50-SAT-100 crossed above the upper boundary by Seed & Idris (1970). At D_r = 25%, D_r = 50%, and D_r = 75%, the damping ratios demonstrated a relative peaking behavior between shear strains of 0.7-1.5%, as seen in studies by Kumar et al., (2017). Therefore, for D_r = 25% and D_r = 50%, for a given strain, the damping ratio generally fits within the approximate upper and lower bound relationships by Seed & Idris (1970), and the average relationship is likely to provide values of damping ratio with sufficient accuracy, as shown in Figure 4-11. It is worth noting that the studies by Seed & Idris (1970) are limited to shear strains of 1.0%.

Based on the present observation, there is a prominent decrease in damping ratio beyond a value of γ = 0.7%. This finding differs greatly from traditional estimates obtained through extrapolation.

Therefore, it is not advisable to assume that damping ratios for $\gamma \leq 0.7\%$ can be used for $\gamma > 0.7\%$. For this reason, it is recommended to create a new functional variation of the damping ratio to effectively use it in a wider range of geotechnical engineering applications that involve varying shear strains. It is crucial to create a practical and effective functional variation of damping ratio that can be used with software such as Flac, Shake, and Proshake (Kumar et al., 2017; Mog & Anbazhagan, 2019). Additionally, the site-specific dynamic shear modulus reduction curves from this study can be used for site response studies and amplification estimation, as demonstrated in section 4.8.1.

Figure 4-11 shows that there were two distinct ranges: non-linear elastic and non-linear. This was such that the non-linear elastic range was observed with a shear strain (γ) of 0.005 - 0.01%, while the non-linear range was observed with a shear strain greater than 0.01% and these findings align with Menq's (2003) curves.

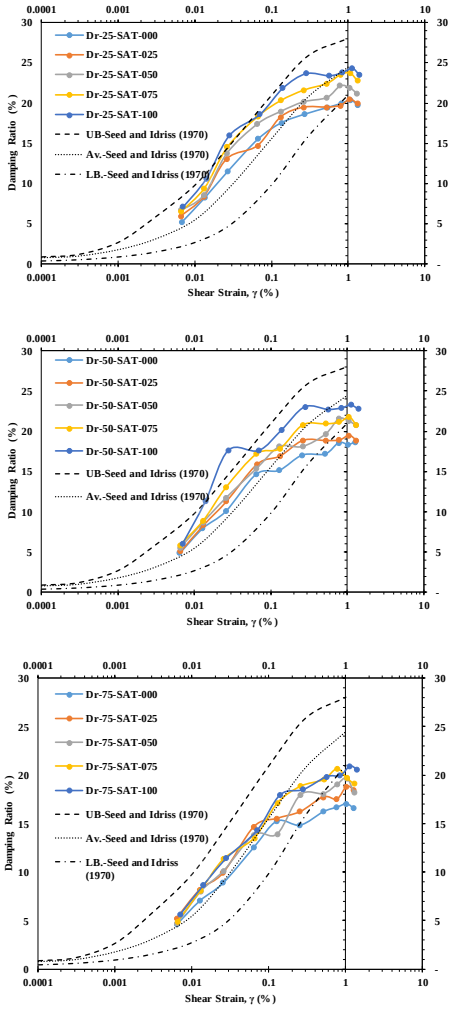

Figure 4-11: Variation of damping ratio with shear strain including comparison with Seed & Idris (1970)

4.3.4 Excess Pore Pressure Ratio

A sample time history of excess pore pressure ratio from the cyclic triaxial test is displayed in Figure 4-12. It shows the progression of EPWP (r_u) for DR-25-SAT-000 with the number of cycles at 0.1%, 0.8%, and 1.0% axial strains, including their maximum, minimum, and average values. The graph reveals that the r_u progression steadily increased until accumulating plastic strain after 30 cycles. Although the plastic strain builds up quickly, the PWP generation remains stable. It's worth noting that the sample did not undergo excessive deformations that could lead to a complete loss of strength (Sze & Yang, 2014).

The analysis of r_u in this study was based on data from 10 cycles, as indicated in Figure 4-12. Results indicated that axial strains of 1.0% led to higher excess pore pressure generation compared to strains of 0.1% and 0.8%. Figure 4-13 provides a summary of r_u for DR-25-SAT-000 at each cycle, based on the given axial strain. When axial strains range from 0.005% to 0.01%, r_u is close to zero. For strains of 0.05% to 0.4%, r_u increases rapidly in the first few cycles, followed by a slight rate of increase until 30 cycles while for strains greater than 0.4%, r_u increases with each cycle.

Based on Figure 4-14, Figure 4-15 and Figure 4-16, the excess pore pressure ratio (r_u) increased non-linearly with shear strain at all relative densities. The excess pore pressure remained constant between shear strains of 0.005-0.02%, then moderately increased between 0.02-0.6% with sharp increases above 0.6%. This occurred because the soil matrix contracted, causing particle arrangement to transfer and distribute normal stresses to the pore water (Idriss & Boulanger, 2008). Pore pressure generated during cyclic loading reduces effective stress, which affects soil shear stiffness and shear stress development (Kumar, Krishna, & Dey, 2017; Mousavi, 2020).

It can further be inferred that the excess pore pressure ratio (r_u) increases as the degree of saturation increases. This confirms that saturated soil responds more softly to undrained cyclic loading due to excess pore pressure generation. When the soil is dry, the r_u decreases as the relative density increases. For example, at shear strains > 1%, the r_u values were 0.57, 0.38, and 0.36 at D_r = 25%, D_r = 50%, and D_r = 75%, respectively. On the other hand, an increase in saturation content at D_r = 25%, 50%, and 75% results in an increase of r_u to 0.62 - 0.67, 0.45 - 0.84, and 0.46 - 0.91, respectively, at shear strains > 1%, as shown in Figure 4-14, Figure 4-15 and Figure 4-16. These results demonstrate the correlation between induced shear strain and pore water generation. However, the r_u value of 1.0, which indicates liquefaction, was not observed in any of the relative densities and saturation contents examined. While cyclic tests on sands that are controlled by strain are useful in studying excess pore pressure generation, the lower pore pressures generated do not necessarily indicate a lower potential for liquefaction during a seismic event (Mousavi, 2020).

The study's outcomes were compared to the upper and lower bound curves from Dobry's (1985) research, which utilized seven different sands as presented in Figure 4-17. The results were generally found to fall beneath Dobry's (1985) lower bound curve and were thus non-narrow banded. For all relative densities and saturation contents assessed, the results from this study marginally fit with the curves between shear strains of 0.005% - 0.03%. This suggests that the upper and lower bounds above 0.03% shear strains do not capture most of the test data points. The findings also suggest that there is a shear strain level below which no excess pore pressure is generated. The threshold shear strain level, also known as γ_{tv}, is typically between 0.006 - 0.01%; this aligns with the findings of previous studies by Ladd et al., (1989) and Hsu & Vucetic (2004), who reported γ_{tv} to be between 0.01-0.02%.

The level of induced shear strain has a major impact on excess pore pressure in sands, as shown in Figure 4-14, Figure 4-15 and Figure 4-16. Based on experimental data in Figure 4-17, higher induced shear strain levels are expected in D_r = 75% compared to D_r = 25% and D_r = 50% under the same cyclic stress amplitudes. This is because low relative densities result in a reduction in shear modulus during cyclic loading in undrained conditions due to the generation of pore pressure. Higher induced shear strain amplitudes result in greater excess pore pressure during cyclic loading and more reduction in effective stress, as indicated by studies conducted by Jafarzadeh & Sadeghi (2012) and Mousavi & Ghayoomi (2020).

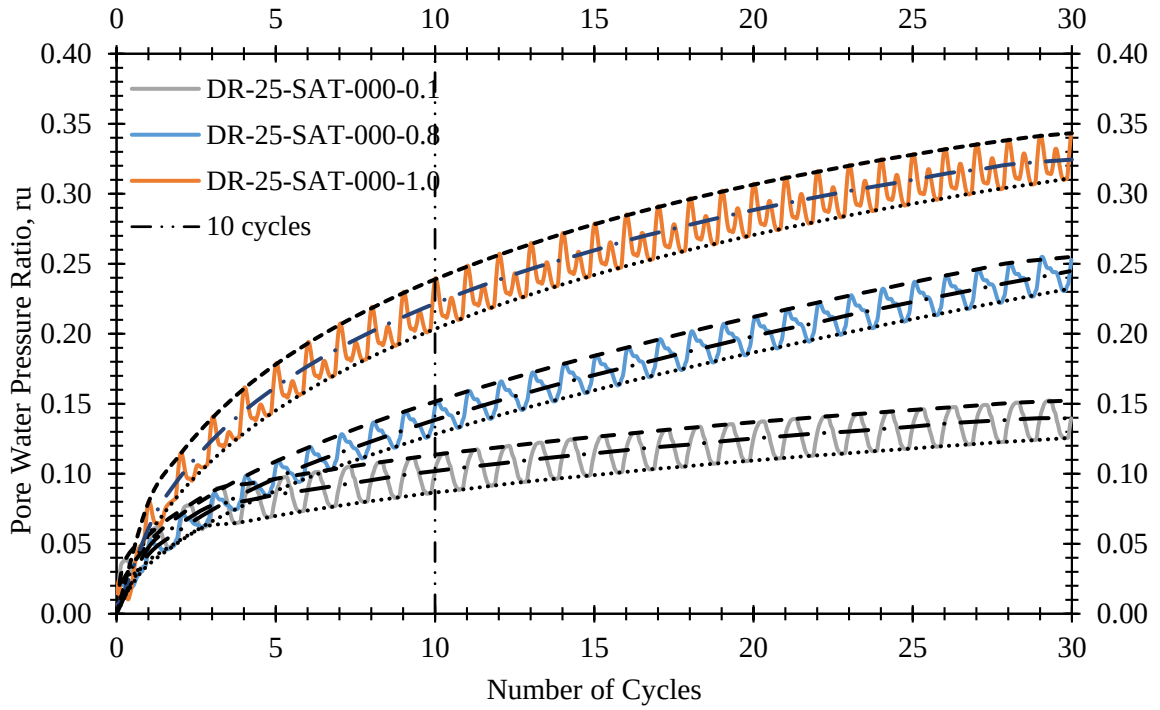

Figure 4-12: Continuous Pore Water Pressure Ratio (PWPR), r_u data recording for DR-25-SAT-000 during the cyclic test

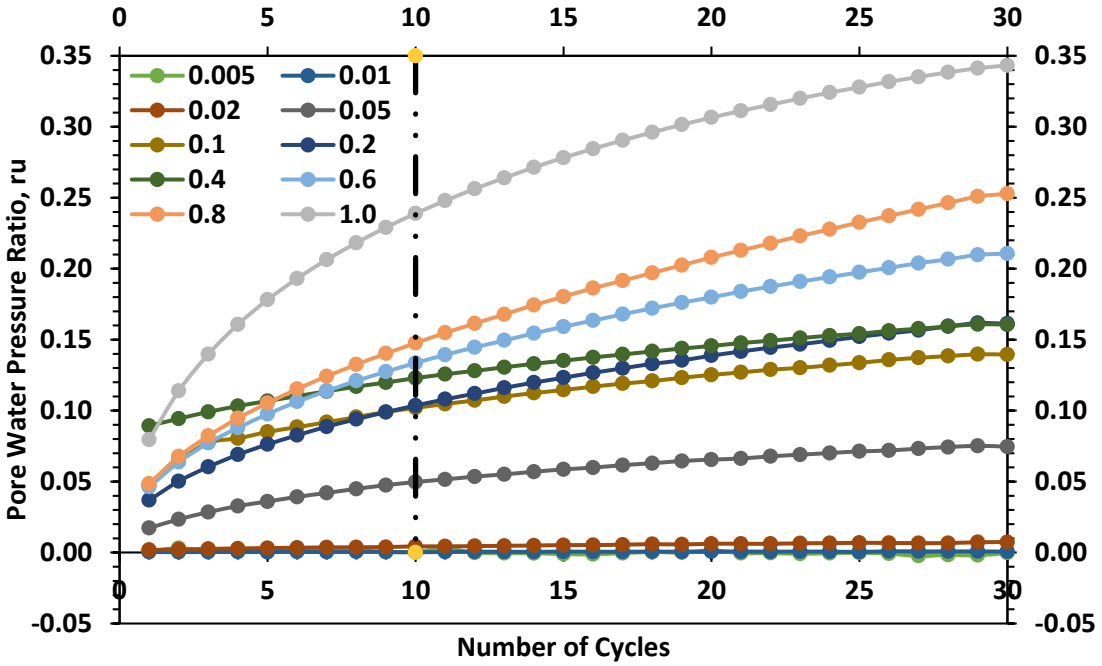

Figure 4-13: Summary of PWPR, r_u for DR-25-SAT-000 at every cycle

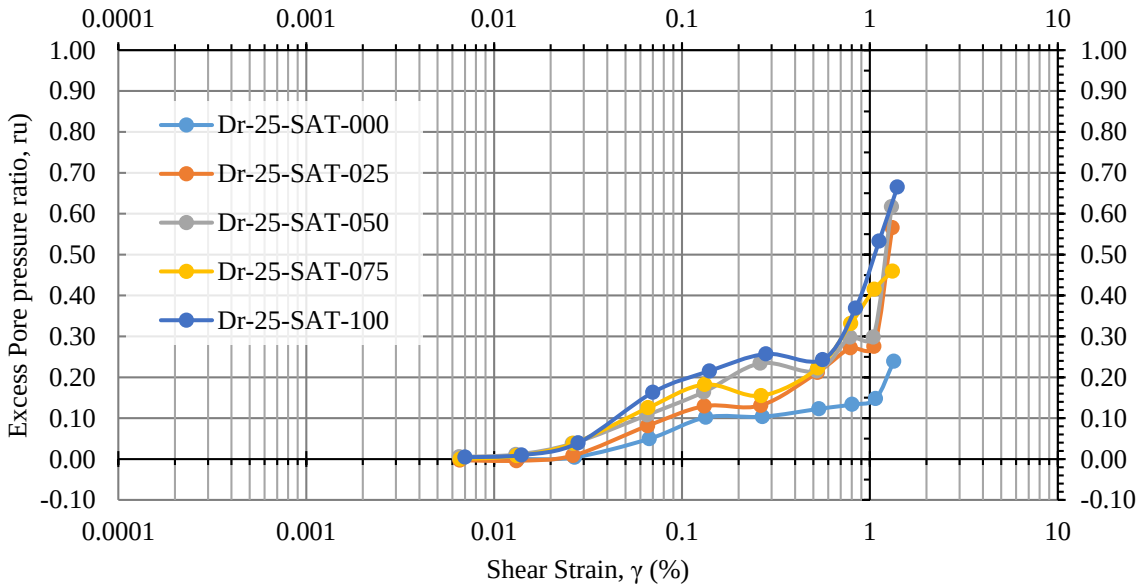

Figure 4-14: Variation of Excess Pore Water Pressure with Shear Strain at D_r = 25%

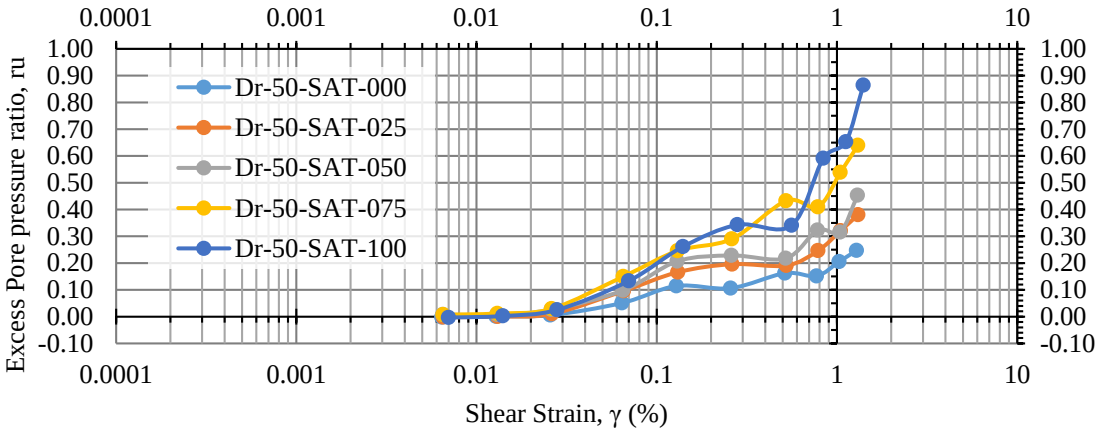

Figure 4-15: Variation of Excess Pore Water Pressure with Shear Strain at D_r = 50%

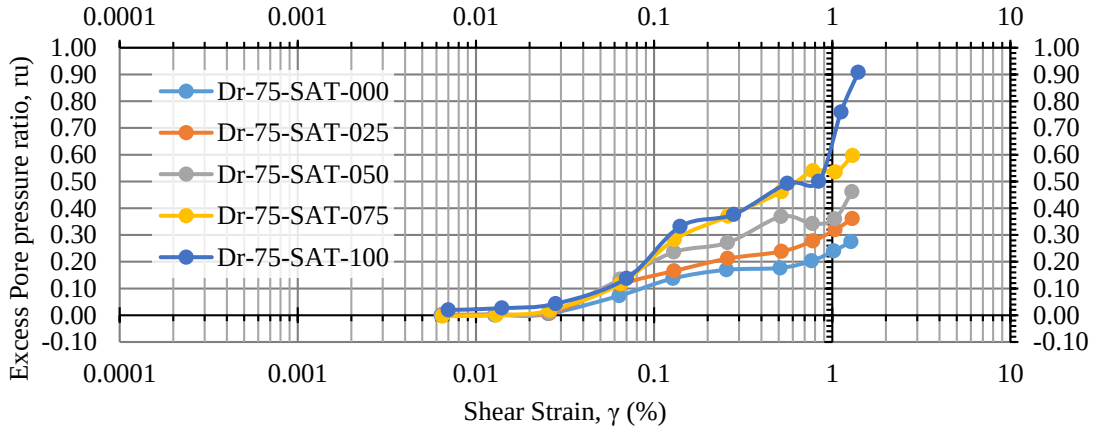

Figure 4-16: Variation of Excess Pore Water Pressure with Shear Strain at D_r = 75%

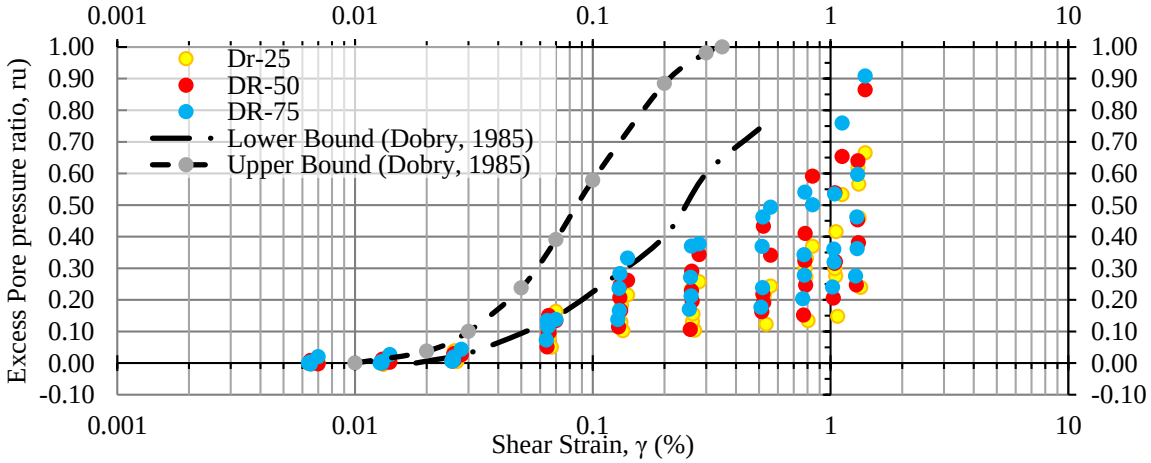

Figure 4-17: Comparison of the variation of Excess Pore Water Pressure with shear strain at all relative densities with Dobry (1985)

4.4 Effect of Saturation Content on Dynamic Properties of Cape Flat Sands

This study aimed to examine how saturation affects the dynamic properties of sand. To perform this, cyclic tests were conducted at different saturation levels - 0%, 25%, 50%, 75%, and 100% - and relative densities of 25%, 50%, and 75%. By testing the sand in dry, partially saturated, and fully saturated states, the study aimed to gain a comprehensive understanding of its dynamic properties.

4.4.1 Shear Modulus

The impact of saturation content on shear modulus at different axial strains is shown in Figure 4-18, Figure 4-19 and Figure 4-20. These figures depict the results at D_r values of 25%, 50%, and 75%, respectively.

The shear modulus of sand was found to peak at around 25% saturation content and then decrease as the saturation content increased. Peaks in the shear modulus curves were typically seen with axial strains ranging from 0.005% to 0.4%. However, for axial strains above 0.4%, the shear modulus remained nearly constant regardless of the saturation content for all relative densities. It's worth noting that the shear modulus of fully dry sand (0% saturation) and fully saturated sand (100% saturation) was almost the same, except for axial strains under 0.4%. While the shear modulus displayed a clear trend with the degree of saturation, a unique relationship was not established (Khosravi, Ghayoomi, McCartney, & Ko, 2010). The results also revealed a decrease in the shear modulus of partially saturated sands with an increase in the initial degree of saturation (Chakrabortty, Roshan, & Das, 2020).

For D_r = 25% at axial strains 0.005%, with an increasing saturation content, the shear modulus decreased by 6-20% with no peak. However, when the axial strain increased to between 0.01-0.4%, the shear modulus increased by 1-51% with the most highest increase happening at 0.1% axial strain. Beyond 25% saturation content, the shear modulus generally decreased by 10-51%, with a remarkable decrease shown at 0.2% axial strain. Above 0.4% axial strain, the shear modulus remained relatively constant for all saturation contents.

For D_r = 50%, the shear modulus with a saturation content of 25% typically increases by 3-62% for all axial strains. The major increase is seen at 0.4% axial strain. However, when saturation content exceeds 25%, the shear modulus decreases by 2-55% for all axial strains.

For D_r = 75%, an increase of shear modulus by 2 - 64% was observed at 25% saturation content at all axial strains. However, for saturation contents greater than 25%, a reduction of 9 - 64% in shear modulus was demonstrated with an axial strain of 0.1%, indicating the major decrease.

When the saturation content is at 0%, the shear modulus generally increases by 4-39% and 9-77% for D_r = 50% and 75%, respectively, compared to D_r = 25%. At 100% saturation content, the shear

modulus increases by 14-53% and 14-44% for D_r = 50% and 75%, respectively, at all axial strains (0.005-1.0%). It is worth noting that most studies on soil shear modulus and degree of saturation have mainly focused on the small-strain shear modulus of unsaturated soils (Mousavi, 2020).

The optimum saturation content for this study was derived by regression analysis, as presented in Section 4.5.3.

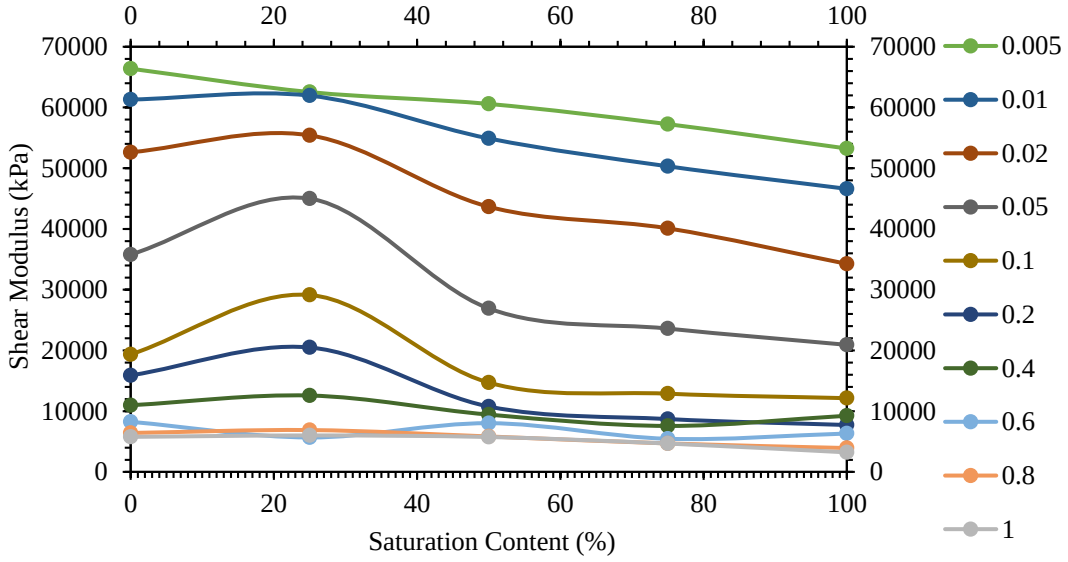

Figure 4-18: Variation of shear modulus with saturation Content at D_r = 25%

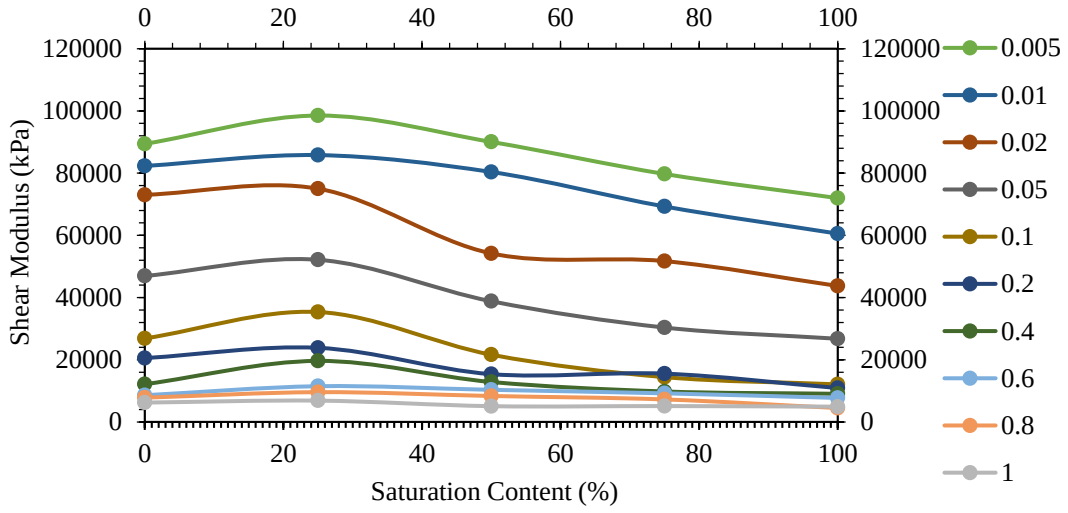

Figure 4-19: Variation of shear modulus with saturation content at D_r = 50%

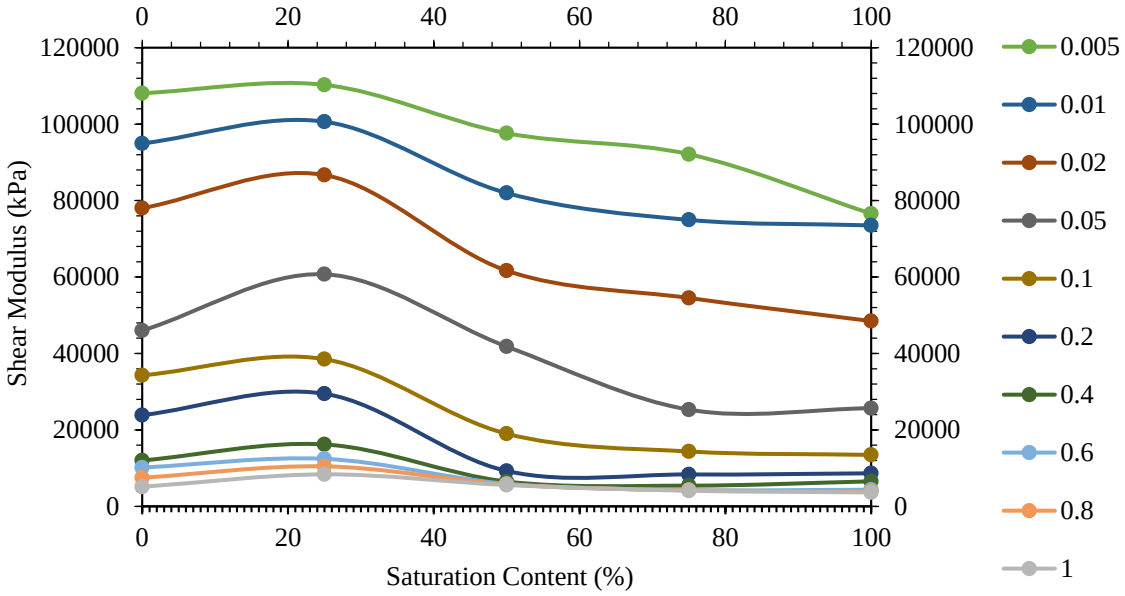

Figure 4-20: Variation of shear modulus with saturation Content at D_r = 75%

4.4.2 Damping Ratio

The soil's damping ratio is a crucial dynamic property that indicates how much energy is lost in each cycle as the loading progresses. The effects of saturation content on damping at different axial strains are shown in Figure 4-21, Figure 4-22 and Figure 4-23 for D_r = 25%, 50%, and 75%. At all axial strains until full saturation, an increase in saturation content led to a marginal increase in damping ratio by 1.9-4.5%, 1.1-5.6%, and 1.0-4.0% for D_r = 25%, D_r = 50%, and D_r = 75%, respectively. This means that fully/nearly saturated samples had consistently higher damping ratio values than dry samples, which is consistent with previous research by Seed & Idriss (1970). Softening of the soil due to pore pressure generation resulted in an increase in damping ratio for specimens with high saturation.

The damping ratios were generally lower for low axial strains (0.005 - 0.1%) compared to higher axial strains. As the relative density (D_r) increased, the damping ratios were observed to decrease for any given axial strain and saturation content. At 100% saturation content, the damping ratio marginally decreased by 0.0-1.7% and 1.5-4.5% for D_r = 50% and D_r = 70% respectively at all axial strains. For D_r = 50% and D_r = 75%, the damping ratio marginally decreased by 0.2-2.4% and 2.4-3.8%, respectively, when compared to D_r = 25% at 0% saturation content. This is comparable to 0.4 - 0.6% and 0.5 - 1.0% for (Dutta, 2015) and (Kumar & Madhusudhan, 2012), respectively.

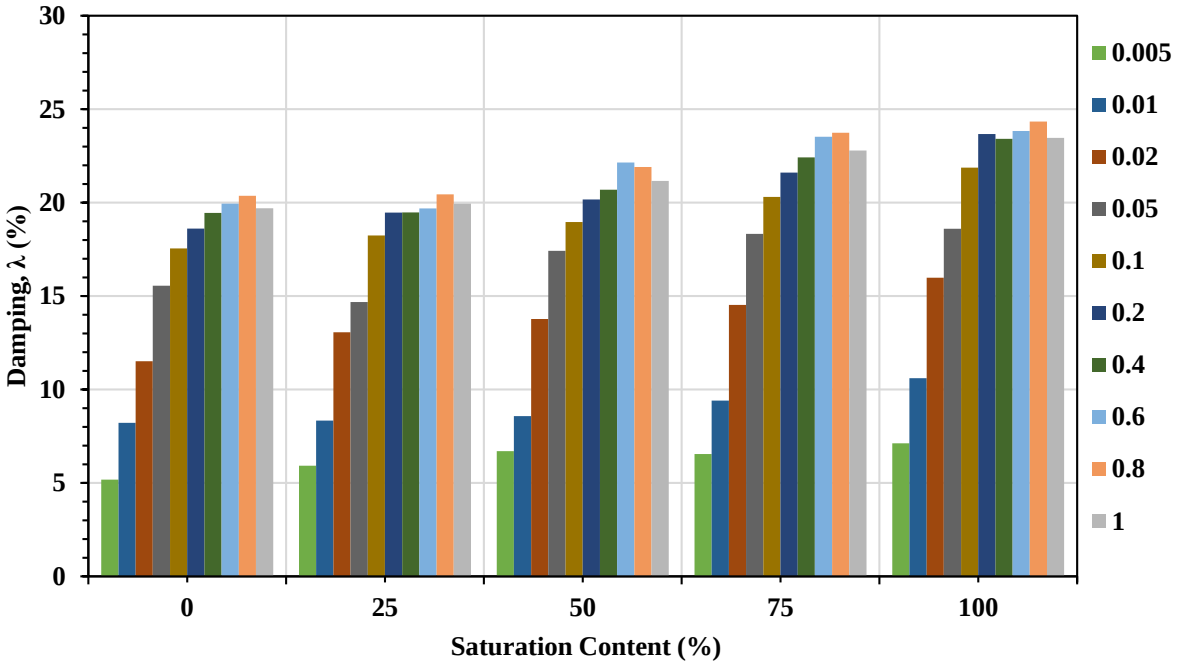

Figure 4-21: Variation of damping ratio with saturation content at D_r = 25%

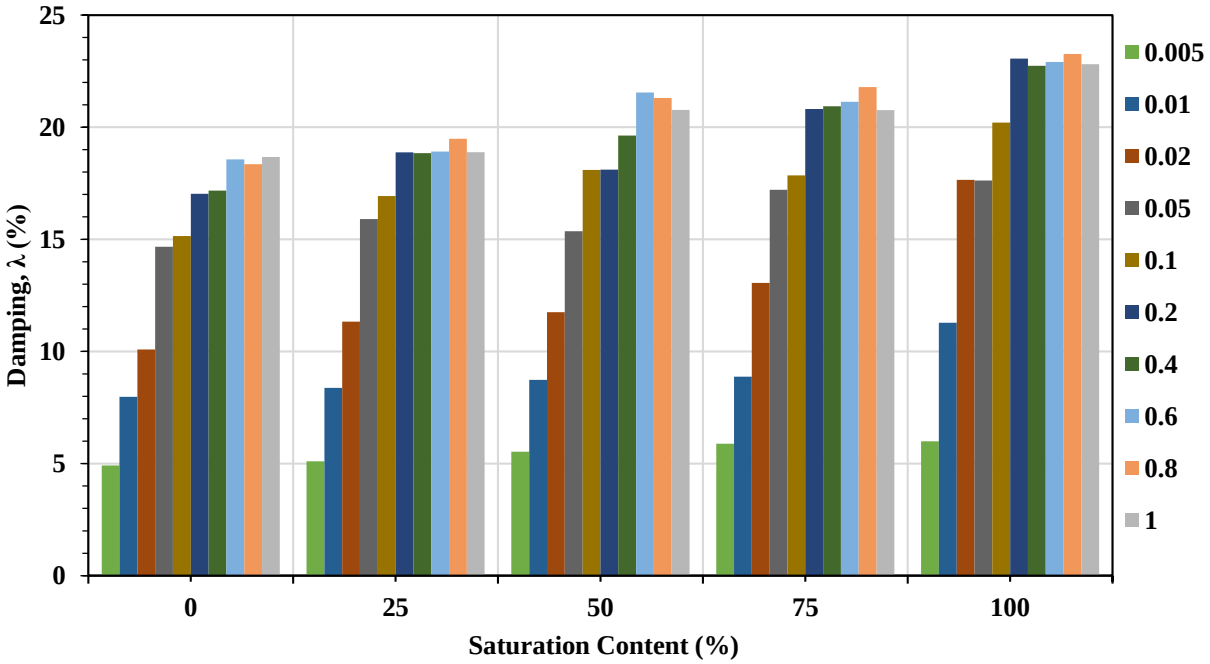

Figure 4-22: Variation of damping ratio with saturation content at D_r = 50%

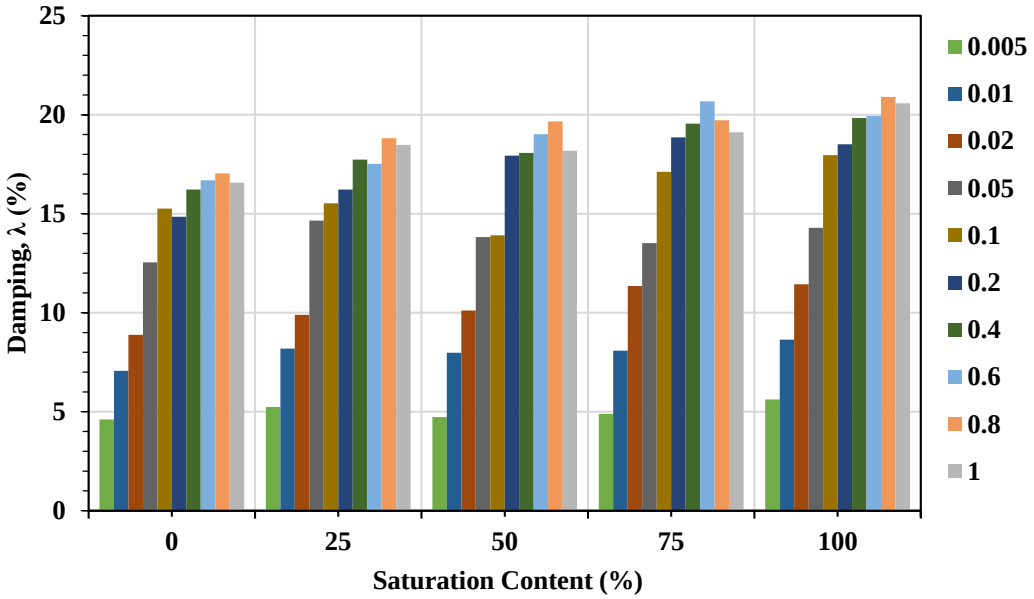

Figure 4-23: Variation of damping ratio with saturation content at D_r = 75%

4.5 Development of Correlations and MANOVA for the Dynamic Properties of Cape Flat Sands

4.5.1 Dynamic Shear Modulus Ratio (G/G_{max})

Correlations for this study were developed by adapting the general equations for Stokoe et al., (1999) & Darendeli (2001), Menq (2003) and Oztoprak & Bolton (2013) to curve fit the data obtained with respect to Figure 4-10. According to Stokoe et al., (1999) & Darendeli (2001), the pseudo-reference strain (γ_t) generally decreased with an increase in saturation content, while the curvature parameter (a) did not show a clear pattern. Table 4-3 shows that for Dr = 25%, Dr = 50%, and Dr = 75%, γ_t ranged from 0.03-0.08, 0.02-0.05, and 0.02-0.05 respectively, while a ranged from 0.78-0.88, 0.78-0.83, and 0.81-0.99.

Considering Menq (2003) was generally adapted for a given coefficient of curvature (C_u) and D_{50}; in addition, other parameters like the Reference strain, (γ_r) and Curvature Parameter (a) were determined as 0.073 and 0.860 respectively, for all relative densities, including its variation with saturation content as presented in Table 4-3. Oztoprak and Bolton's (2013) curve parameters were as follows: for D_r = 25%, D_r = 50%, and D_r = 75%, the Reference strain (γ_r) was 0.018, 0.029, and 0.036, respectively, with a constant curvature Parameter (a) of 0.939 at all relative densities, and γ_e values of 0.0026, 0.0037, and 0.0045, respectively, which increased with an increase in D_r.

Table 4-3: Curve fitting parameters obtained for selected scholars

Test Phase	Stokoe et al., (1999); Darendeli (2001)		Menq (2003)		Oztoprak & Bolton (2013)		
	Pseudo-reference strain, γ_t for G/G_{max} = 0.5	Curvature Parameter, a	Reference strain, γ_r	Curvature Parameter, a	Reference strain, γ_r	Curvature Parameter, a	γ_e
DR-25-SAT-000	0.080	0.8568	0.0725	0.8596	0.0198	0.9394	0.0026
DR-25-SAT-025	0.060	0.7788					
DR-25-SAT-050	0.036	0.8752					
DR-25-SAT-075	0.035	0.7966					
DR-25-SAT-100	0.030	0.8164					
DR-50-SAT-000	0.050	0.9031			0.0291	0.9394	0.0037
DR-50-SAT-025	0.051	0.7914					
DR-50-SAT-050	0.026	0.7752					
DR-50-SAT-075	0.025	0.8190					
DR-50-SAT-100	0.021	0.8333					
DR-75-SAT-000	0.050	0.8780			0.0355	0.9394	0.0045
DR-75-SAT-025	0.036	0.8102					
DR-75-SAT-050	0.023	0.9574					
DR-75-SAT-075	0.021	0.9910					
DR-75-SAT-100	0.020	0.9922					

4.5.2 Damping Ratio and Dynamic Shear Modulus Ratio (G/G_{max})

Table 4-4 and Figure 4-24 display the linear and quadratic equations derived from plotting the damping ratio against the dynamic shear modulus ratio. These equations were fitted to Equation 4-1 and Equation 4-2, respectively.

The equations developed for D_r values of 25%, 50%, and 75% had a coefficient of determination, R^2, greater than 0.90 for both linear and quadratic models. The combined equation for all results in this study had an R^2 greater than 0.84, indicating a strong relationship between λ predicted by G/G_{max} as a goodness of fit for the two models (Norusis, 2004). The findings of this study's linear equations, both individually and combined, closely matched those of Okur & Ansal's (2007) study.

$$\lambda = m + n\left(\frac{G}{G_{max}}\right) \qquad \text{Equation 4-1}$$

$$\lambda = p\left(\frac{G}{G_{max}}\right)^2 + q\left(\frac{G}{G_{max}}\right) + r \qquad \text{Equation 4-2}$$

Where;
- λ = damping ratio
- m and n = fitting parameters for the linear equation
- p, q, and r = fitting parameters for the quadratic equation

Table 4-4: Linear and quadratic curve fitting parameters

D_r (%)	Linear equation			D_r (%)	Quadratic Equation			
	m	n	R^2		p	q	r	R^2
25	-19.234	23.776	0.93	25	-13.304	-7.7556	22.473	0.95
50	-18.988	22.19	0.92	50	-6.9814	-13.145	21.564	0.92
75	-18.322	19.527	0.94	75	3.65	-21.07	19.756	0.94
Combined	-18.281	21.646	0.84	Combined	-6.7135	-12.777	21.089	0.85
(Okur & Ansal, 2007)	-18.114	20.033	0.96					
(Zhao et al., 2021)	0.38	-0.34	0.95					

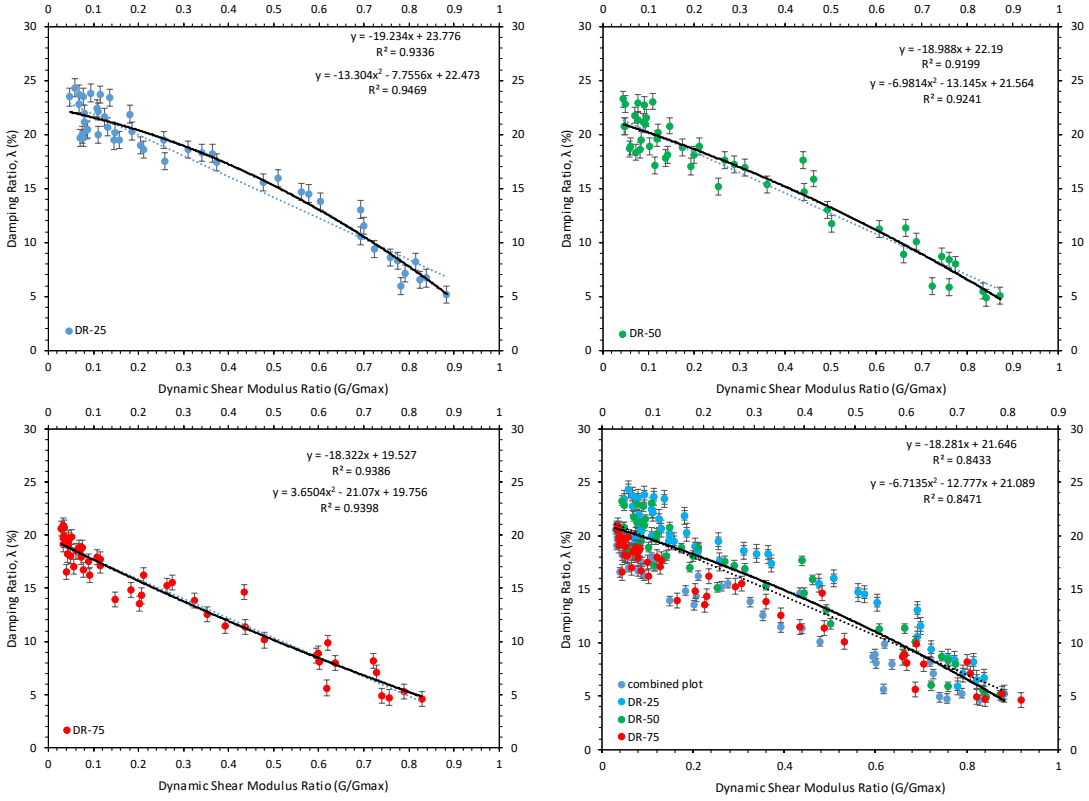

Figure 4-24: Linear and quadratic correlations developed from this study

Furthermore, five correlations from past scholars were superimposed over the combined test data, as presented in Figure 4-25. Overall, the predictions of λ by Menq (2003) and Park & Stewart (2001) provided upper and lower bounds for all test data values of G/G_{max}. However, some of Menq's (2003) predictions were below the lower bound of Park & Stewart's (2001). For λ at D_r = 75%, Michaelides et al., (1998) and Park & Stewart (2001) defined upper and lower bounds for all G/G_{max} values. The predicted λ values from Ishibashi & Zhang (1993) were valid for G/G_{max} ranging from 0.35 to 0.90, while the expected λ values from Zhang et al., (2005) were valid for G/G_{max} ranging from 0.02 to 0.40.

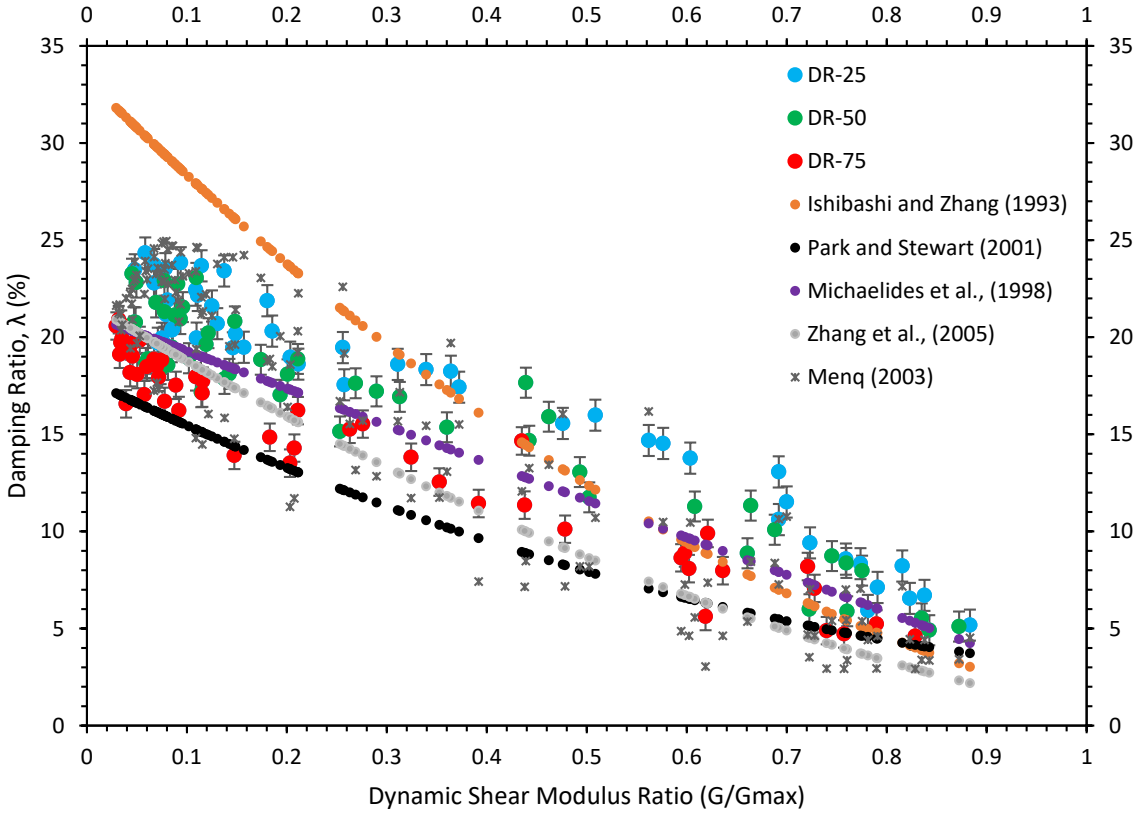

Figure 4-25: Damping ratio versus dynamic shear modulus ratio

4.5.3 Shear Modulus with Saturation Content

Through regression analysis using quartic equations, the optimal saturation content was obtained for the shear modulus versus saturation content curves in Figure 4-18, Figure 4-19 and Figure 4-20. Different linear, quadratic, and cubic equations were analyzed for regression, and the quartic equation yielded the highest R^2 value of close to 1. These equations are represented in Figure 4-26, Figure 4-27 and Figure 4-28, including standard error bars. An R^2 value of 1 indicates that the predicted model matches the observed results, so all results would fall along the regression line

(Norusis, 2004). At the optimum degree of saturation ($S_{r\ opt}$), the shear modulus reaches its maximum magnitude (Madhusudhan, 2011).

Overall, the optimum saturation content ($S_{r,\ opt}$) varied with respect to D_r and cyclic axial strain as presented in Table 4-5. The $S_{r\ opt}$ for D_r = 25%, 50%, and 75% at different cyclic axial strains ranged from 12.1 - 29.1%, 11.6 - 23.6% and 11.9 - 18.5%, respectively. This analysis showed that higher relative density, such as D_r = 75%, resulted in lower $S_{r,\ opt}$ compared to D_r = 50% and D_r = 25%. Other studies, including Wu et al., (1984), Qian et al., (1993), Kumar & Madhusudhan (2012), and Mousavi (2020), found the shear modulus peaked at a saturation content ($S_{r,\ opt}$) of 5%, 3.6% - 18%, 0.69% - 0.92%, and 35%, respectively. Therefore, the $S_{r\ opt}$ in this study fell within the range of peak saturation contents from Qian et al.'s (1993) study.

Some scholars have reported a decrease in the shear modulus with an increase in the saturation content. Conversely, some scholars have also reported a peak in the shear modulus with a decrease till the shear modulus approached the value similar to 0% saturation content (Qian et al., 1993; Wu et al., 1984; Kumar & Madhusudhan, 2012).

Table 4-5: Constants derived for the quartic equation

D_r (%)	Cyclic Axial Strain	x^4	x^3	x^2	x	C	R^2	$S_{r,\ opt}$ (%)
		A	B	C	D	E		
25	0.005	0.0004	-0.0986	7.0574	-275.58	66397	1	-
	0.01	-0.0013	0.2968	-22.928	433.2	61307	1	12.1
	0.02	-0.0035	0.7752	-54.252	1039	52616	1	12.8
	0.05	-0.006	1.3467	-96.628	2036.1	35787	1	14.6
	0.1	-0.0052	1.1669	-84.328	1851.4	19349	1	15.5
	0.2	-0.0031	0.6925	-50.057	1050.3	15898	1	14.5
	0.4	-0.0004	0.12	-11.342	276.16	10974	1	15.9
	0.6	-0.0019	-0.3951	25.093	-513.45	8247.3	1	-
	0.8	-0.0001	0.0305	-3.0701	78.414	6407.7	1	16.6
	1.0	0.00008	-0.0154	0.407	7.5968	5769.8	1	29.1
50	0.005	-0.0012	0.3493	-34.952	1038.4	89424	1	20.6
	0.01	0.0005	-0.0423	-6.1871	312.88	82292	1	22.0
	0.02	-0.0069	1.4773	-98.713	1731.8	73015	1	11.6
	0.05	-0.0025	0.6257	-50.82	1127.6	46953	1	14.8
	0.1	-0.0032	0.7907	-62.92	1468.8	26862	1	16.2
	0.2	-0.0036	0.758	-50.489	976.86	20529	1	13.3
	0.4	-0.0021	0.5029	-40.088	1020.5	12146	1	18.5

Table 4-5: Constants derived for the quartic equation

D_r (%)	Cyclic Axial Strain	x^4	x^3	x^2	x	C	R^2	$S_{r,\,opt}$ (%)
		A	B	C	D	E		
	0.6	-0.0005	0.1167	-9.9111	299.36	8595.9	1	23.6
	0.8	-0.0005	0.112	-8.5122	222.14	7821.5	1	20.0
	1.0	-0.0007	0.1475	-10.054	195.25	6251.4	1	13.2
75	0.005	-0.0042	0.8609	-58.153	1068.3	108076	1	12.3
	0.01	-0.0045	1.0563	-79.083	1614.4	94957	1	13.7
	0.02	-0.0073	1.6443	-118.38	2392.6	78010	1	13.7
	0.05	-0.0023	0.729	-71.539	1957.8	45994	1	18.5
	0.1	-0.0053	1.2082	-86.389	1656.7	34296	1	11.9
	0.2	-0.0067	1.4902	-102.94	1970.9	23861	1	12.9
	0.4	-0.0031	0.7041	-50.391	1035.6	12004	1	14.1
	0.6	-0.0018	0.4178	-30.464	619.63	10151	1	13.8
	0.8	-0.0013	0.3173	-24.027	542.33	7496.9	1	15.8
	1.0	-0.0008	0.201	-16.361	426.57	5113.7	1	-

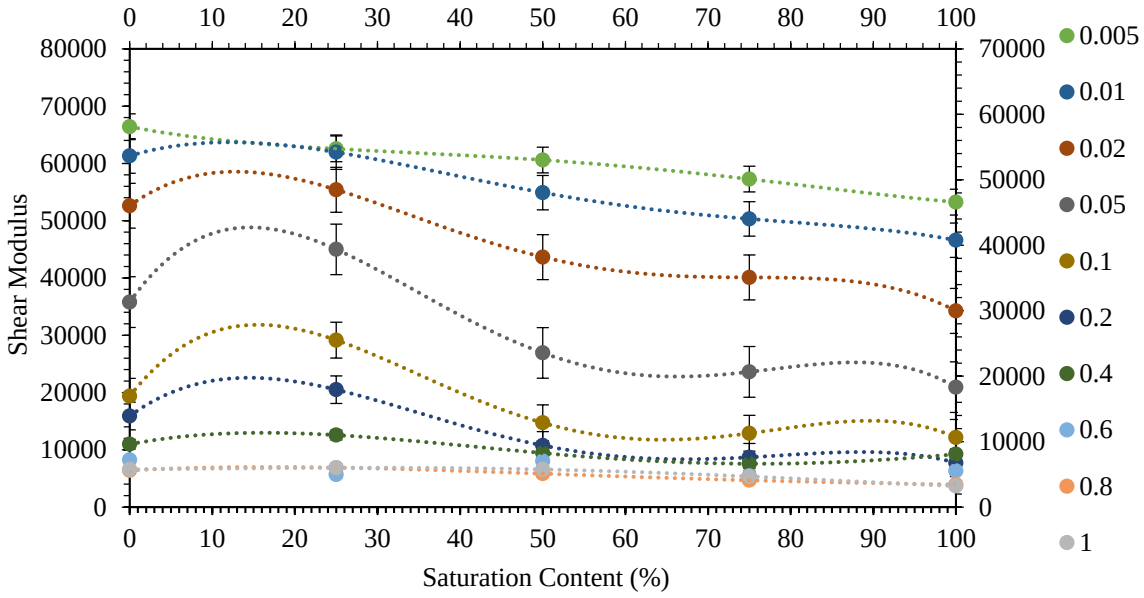

Figure 4-26: Variation of shear modulus with saturation content at D_r = 25%

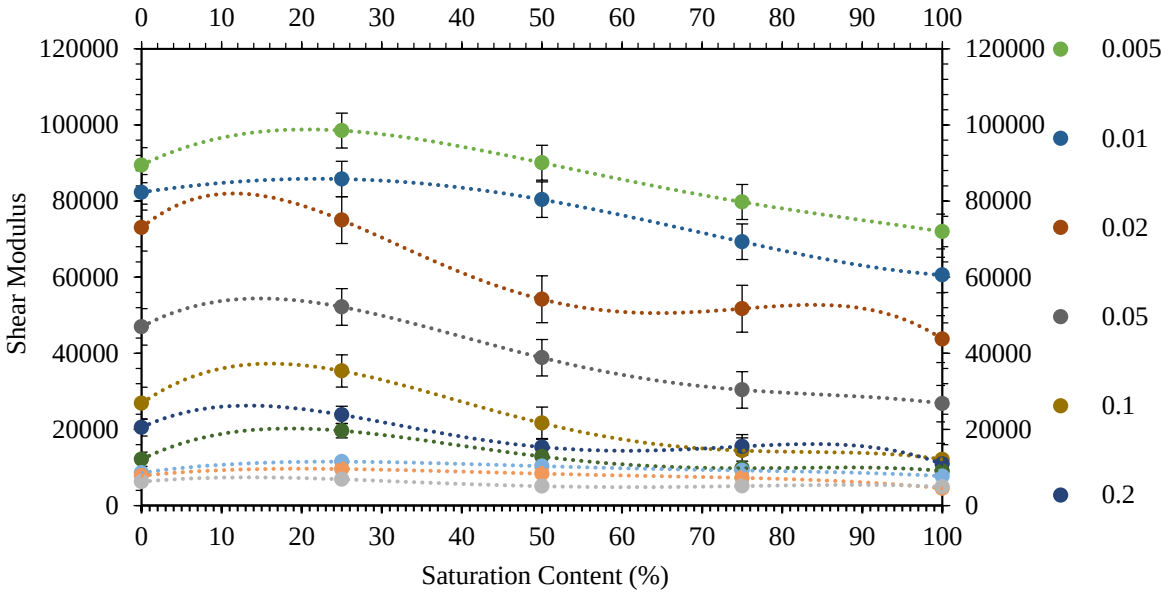

Figure 4-27: Variation of shear modulus with saturation content at D_r = 50%

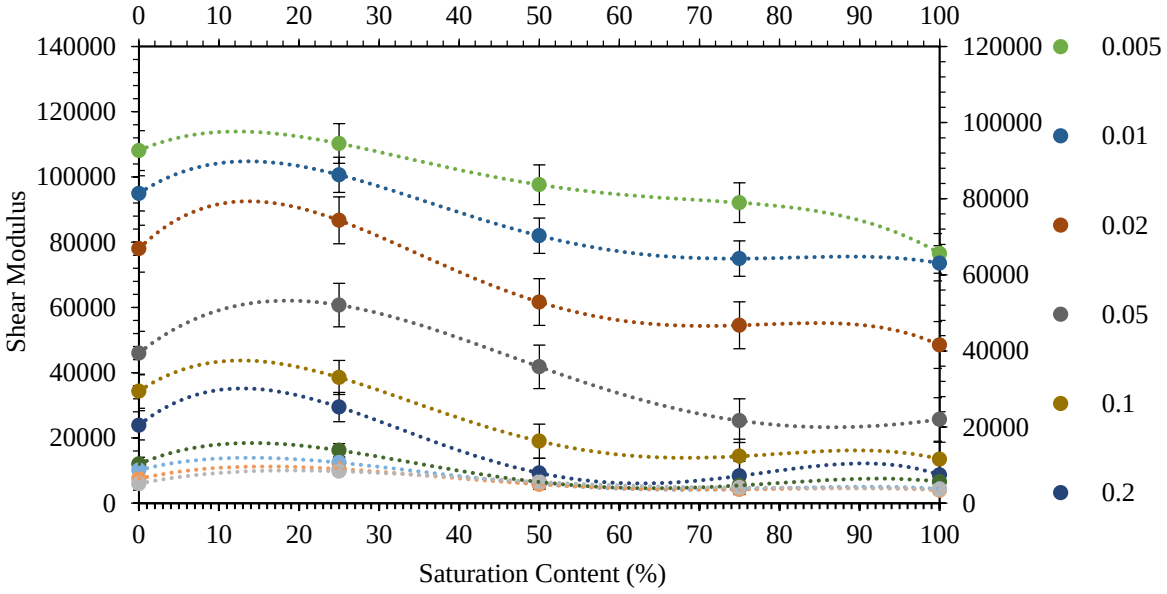

Figure 4-28: Variation of shear modulus with saturation content at D_r = 75%

4.5.4 Multivariate Analysis of Variance (MANOVA)

The results from Table 4-6, Table 4-7, Table 4-8 and Table 4-9 showed that the primary factors analyzed in the MANOVA tests for both models were significant, including evaluations using Pillai's trace, Wilks' lambda, Hotelling's trace, and Roy's largest root. Most of the factors had p-values less than 0.05, indicating no evidence to reject the null hypothesis of equality of means. This aligns with the graphs concerning shear modulus, damping ratio, and PWPR earlier presented,

as well as the F-critical value (F > 1). Furthermore, Table 2-8 and Table 2-9 demonstrated that the strain amplitude (STR), void ratio/relative density (DR), and degree of saturation (SAT) were significant parameters influencing the non-linear behavior of soils. Other factors, such as mean effective confining pressure, number of cycles, and frequency/period, could not be evaluated as they were kept constant for all tests and their respective degrees of freedom would be zero (0).

If the p-value is less than 0.05, it means there is no enough evidence to reject the null hypothesis and accept the alternative hypothesis. This indicates that there is no significant difference between the variances. This is further supported by the F_{crit} value being F < 1. These findings mainly applied to the two-way mean interactions, which showed that the main factors were sufficient for shear modulus or damping ratio or PWPR strength and their respective combinations. In model 1, this was observed for Dr * SAT, where Pillai's trace [p = 0.478], Wilks' lambda [p = 0.998], Hotelling's trace [p = 0.588] were seen in Table 4-6. These findings were reflected in the two-way effect in the shear modulus [p = 0.998], damping ratio [p = 0.998], and PWPR [p = 0.588] as shown in Table 4-8. However, in model 2, the two-way effect for Dr * STR was only greater than 0.05 for PWPR [p = 0.869].

The plots of the predicted, observed and residuals for the respective tests, the main factor and two-way interactions were evaluated to check for linearity and equality of variances, as presented in Figure 4-29. From the residual plots, it was deduced that the residuals did not follow a particular pattern, indicating that these errors were random and independent and, thus, did not influence the relationship between the predicted and observed values. Some of these factors could have been the room temperature and environmental factors (Baecher & Christian, 2003; George & Mallery, 2019).

Table 4-6: Model 1 multivariate tests[a]

Effect		Value	F	Hypothesis df	Error df	Sig. (p-value)
Intercept	Pillai's Trace	0.988	3639.616[b]	3.000	132.000	0.000
	Wilks' Lambda	0.012	3639.616[b]	3.000	132.000	0.000
	Hotelling's Trace	82.719	3639.616[b]	3.000	132.000	0.000
	Roy's Largest Root	82.719	3639.616[b]	3.000	132.000	0.000
STR	Pillai's Trace	0.775	151.699[b]	3.000	132.000	0.000
	Wilks' Lambda	0.225	151.699[b]	3.000	132.000	0.000
	Hotelling's Trace	3.448	151.699[b]	3.000	132.000	0.000
	Roy's Largest Root	3.448	151.699[b]	3.000	132.000	0.000
DR	Pillai's Trace	0.305	7.975	6.000	266.000	0.000
	Wilks' Lambda	0.709	8.273[b]	6.000	264.000	0.000
	Hotelling's Trace	0.392	8.567	6.000	262.000	0.000

Table 4-6: Model 1 multivariate tests[a]

Effect		Value	F	Hypothesis df	Error df	Sig. (p-value)
	Roy's Largest Root	0.336	14.891[c]	3.000	133.000	0.000
SAT	Pillai's Trace	0.464	6.129	12.000	402.000	0.000
	Wilks' Lambda	0.566	6.991	12.000	349.531	0.000
	Hotelling's Trace	0.714	7.772	12.000	392.000	0.000
	Roy's Largest Root	0.63	21.095[c]	4.000	134.000	0.000
DR * SAT	Pillai's Trace	0.167	0.99	24.000	402.000	0.478
	Wilks' Lambda	0.835	1.022	24.000	383.441	0.437
	Hotelling's Trace	0.193	1.053	24.000	392.000	0.397
	Roy's Largest Root	0.173	2.903[c]	8.000	134.000	0.005

Note:

a. Design: Intercept + STR + DR + SAT + DR * SAT
b. Exact statistic
c. The statistic is an upper bound on F that yields a lower bound on the significance level

Table 4-7: Model 2 multivariate tests[a]

	Effect	Value	F	Hypothesis df	Error df	Sig. p-value)
Intercept	Pillai's Trace	0.993	5351.863[b]	3.000	117.000	0.000
	Wilks' Lambda	0.007	5351.863[b]	3.000	117.000	0.000
	Hotelling's Trace	137.227	5351.863[b]	3.000	117.000	0.000
	Roy's Largest Root	137.227	5351.863[b]	3.000	117.000	0.000
SAT	Pillai's Trace	0.89	314.470[b]	3.000	117.000	0.000
	Wilks' Lambda	0.11	314.470[b]	3.000	117.000	0.000
	Hotelling's Trace	8.063	314.470[b]	3.000	117.000	0.000
	Roy's Largest Root	8.063	314.470[b]	3.000	117.000	0.000
DR	Pillai's Trace	0.928	34.032	6.000	236.000	0.000
	Wilks' Lambda	0.164	57.221[b]	6.000	234.000	0.000
	Hotelling's Trace	4.527	87.521	6.000	232.000	0.000
	Roy's Largest Root	4.4	173.052[c]	3.000	118.000	0.000
STR	Pillai's Trace	1.703	17.361	27.000	357.000	0.000
	Wilks' Lambda	0.003	85.919	27.000	342.343	0.000
	Hotelling's Trace	133.141	570.371	27.000	347.000	0.000
	Roy's Largest Root	131.246	1735.364[c]	9.000	119.000	0.000
	Pillai's Trace	0.802	2.414	54.000	357.000	0.000

Table 4-7: Model 2 multivariate tests[a]

Effect		Value	F	Hypothesis df	Error df	Sig. p-value)
DR * STR	Wilks' Lambda	0.308	3.135	54.000	349.430	0.000
	Hotelling's Trace	1.896	4.062	54.000	347.000	0.000
	Roy's Largest Root	1.701	11.243[c]	18.000	119.000	0.000

Note:

a. Design: Intercept + SAT + DR + STR + DR * STR
b. Exact statistic
c. The statistic is an upper bound on F that yields a lower bound on the significance level.

Table 4-8: Model 1 tests of between-subjects effects

Source	Dependent Variable	Type III Sum of Squares	df	Mean Square	F	Sig. p-value)
Corrected Model	Shear Modulus	71893926185.458[a]	15	4792928412	11.606	0.000
	Damping Ratio	2446.884[b]	15	163.126	10.908	0.000
	PWPR	4.640[c]	15	0.309	35.231	0.000
Intercept	Shear Modulus	2.04435E+11	1	2.04435E+11	495.028	0.000
	Damping Ratio	13003.37	1	13003.37	869.483	0.000
	PWPR	0.311	1	0.311	35.451	0.000
STR	Shear Modulus	62963721869	9	62963721869	152.463	0.000
	Damping Ratio	1995.056	9	1995.056	133.401	0.000
	PWPR	3.776	9	3.776	430.081	0.000
DR	Shear Modulus	3261816613	2	1630908306	3.949	0.022
	Damping Ratio	191.827	2	95.914	6.413	0.002
	PWPR	0.073	2	0.036	4.152	0.018
SAT	Shear Modulus	5249533666	4	1312383417	3.178	0.016
	Damping Ratio	244.035	4	61.009	4.079	0.004
	PWPR	0.733	4	0.183	20.886	0.000
DR * SAT	Shear Modulus	418854037.5	8	52356754.69	0.127	0.998
	Damping Ratio	15.966	8	1.996	0.133	0.998
	PWPR	0.057	8	0.007	0.818	0.588
Error	Shear Modulus	55338958906	110	412977305.3		
	Damping Ratio	2004.01	110	14.955		
	PWPR	1.176	110	0.009		
Total	Shear Modulus	2.7433E+11	150			
	Damping Ratio	42881.941	150			

Table 4-8: Model 1 tests of between-subjects effects

Source	Dependent Variable	Type III Sum of Squares	df	Mean Square	F	Sig. p-value)
	PWPR	12.296	150			
Corrected Total	Shear Modulus	1.27233E+11	149			
	Damping Ratio	4450.894	149			
	PWPR	5.816	149			

Note:

a. R Squared = .565 (Adjusted R Squared = .516)

b. R Squared = .550 (Adjusted R Squared = .499)

c. R Squared = .798 (Adjusted R Squared = .775)

Table 4-9: Tests of between-subjects effects

Source	**Dependent Variable**	**Type III Sum of Squares**	**df**	**Mean Square**	**F**	**Sig. p-value)**
Corrected Model	Shear Modulus	123129755945.077[a]	30	4104325198	119.035	0.000
	Damping Ratio	4374.698[b]	30	145.823	227.740	0.000
	PWPR	5.046[c]	30	0.168	26.000	0.000
Intercept	Shear Modulus	75359092378	1	75359092378	2185.584	0.000
	Damping Ratio	10094.405	1	10094.405	15764.954	0.000
	PWPR	0.596	1	0.596	92.151	0.000
SAT	Shear Modulus	4226846381	4	4226846381	122.588	0.000
	Damping Ratio	242.388	4	242.388	378.550	0.000
	PWPR	0.73	4	0.73	112.845	0.000
DR	Shear Modulus	3261816613	2	1630908306	47.300	0.000
	Damping Ratio	191.827	2	95.914	149.793	0.000
	PWPR	0.073	2	0.036	5.634	0.005
STR	Shear Modulus	1.11312E+11	9	12367973128	358.699	0.000
	Damping Ratio	3920.397	9	435.6	680.298	0.000
	PWPR	4.17	9	0.463	71.616	0.000
DR * STR	Shear Modulus	4329334802	18	240518600.1	6.976	0.000
	Damping Ratio	20.085	18	1.116	1.743	0.041
	PWPR	0.073	18	0.004	0.630	0.869
Error	Shear Modulus	4103129147	92	34480076.86		
	Damping Ratio	76.196	92	0.64		

Table 4-9: Tests of between-subjects effects

Source	Dependent Variable	Type III Sum of Squares	df	Mean Square	F	Sig. p-value)
	PWPR	0.77	92	0.006		
Total	Shear Modulus	2.7433E+11	150			
	Damping Ratio	42881.941	150			
	PWPR	12.296	150			
Corrected Total	Shear Modulus	1.27233E+11	149			
	Damping Ratio	4450.894	149			
	PWPR	5.816	149			

Note:

a. R Squared = .968 (Adjusted R Squared = .960)
b. R Squared = .983 (Adjusted R Squared = .979)
c. R Squared = .868 (Adjusted R Squared = .834)

Figure 4-29: Residual plots for statistical model 1 and model 2

4.6 Summary of Key Results on Cyclic Properties of Cape Flat Sands

4.6.1 Shear Modulus

When the relative density is greater, the shear modulus is also higher. Moreover, an increase in relative density causes the shear modulus to increase as well, demonstrating that relative density has a significant effect on shear modulus. It has been noticed that the shear modulus of all graphs decreases in a nonlinear manner as the shear strain increases because of the loss of stiffness in the specimen.

By using quartic equations in regression analysis, the optimal saturation content was determined with a high R^2 value close to 1. The optimum saturation content ($S_{r,\,opt}$) varied based on Dr and cyclic axial strain such that for D_r values of 25%, 50%, and 75%, $S_{r\,opt}$ ranged from 12.1% to 29.1%, 11.6% to 23.6%, and 11.9% to 18.5% at different cyclic axial strains. It was found that higher relative density, such as D_r = 75%, resulted in lower $S_{r,\,opt}$ compared to D_r = 50% and D_r = 25%.

4.6.2 Normalised shear modulus

The curve for the normalized shear modulus was similar to that of the shear modulus. In general, as relative density decreased, the normalized dynamic/shear modulus increased. At higher levels of shear strain, the scatter of the normalized dynamic modulus decreased. These curves are useful for analyzing site response or estimating amplification.

Various scholars have developed normalized shear modulus models, but fitting them to different soil data sets has shown that using any single model to determine the dynamic response of different soils may be inaccurate. This emphasizes the importance of carefully determining the dynamic properties of each soil before applying it to any practical geotechnical engineering problems.

4.6.3 Damping Ratio

As the shear strain increases, the damping ratio also tends to increase non-linearly. During the low shear strain range, the damping ratio is low due to the specimens' higher shear modulus. However, the damping ratios at all relative densities (D_r = 25%, D_r = 50%, and D_r = 75%) showed a relative peaking behavior between shear strains of 0.7-1.5%. This observation is different from traditional estimates obtained by extrapolation. Therefore, it is not recommended to assume that damping ratios for $\gamma \leq 0.7\%$ can be used for $\gamma > 0.7\%$. To effectively use the damping ratio in a wider range of geotechnical engineering applications that involve varying shear strains, it is advisable to create a new functional variation.

When sand is more tightly packed, its damping ratio decreases. This means that sand with a lower relative density (D_r = 25%) has a higher damping ratio under the same amount of strain compared to sand with a higher relative density (Dr = 75%).

Typically, for a given shear strain, the damping ratio tends to fall within the established upper and lower bounds as outlined by Seed & Idris (1970) for D_r = 25% and D_r = 50%. It has been observed that the average relationship accurately provides values for the damping ratio.

There were two types of ranges observed: non-linear elastic and non-linear; The non-linear elastic range was observed at a shear strain (γ) of 0.005 - 0.01%, while the non-linear range was observed at a shear strain greater than 0.01%.

Increasing saturation content resulted in a slight increase in damping ratio at all axial strains up until full saturation. This indicates that fully or nearly saturated samples consistently had higher damping ratio values than dry samples. However, as the relative density (D_r) increased, the damping ratios decreased for any given axial strain and saturation content.

4.6.4 Excess Pore Pressure Ratio

At all relative densities, the ratio of excess pore pressure (r_u) increased in a non-linear manner as shear strain increased. The excess pore pressure stayed the same between shear strains of 0.005-0.02%, then increased moderately between 0.02-0.6% before sharply increasing above 0.6%. These findings show that there is a connection between the amount of shear strain and the generation of pore water.

As the degree of saturation increases, the excess pore pressure ratio (r_u) also increases. This means that soil that is fully saturated responds more gently to undrained cyclic loading because of excess pore pressure creation. Conversely, when soil is dry, the r_u decreases as the relative density increases.

This study found that excess pore pressure is not generated when the shear strain level is between 0.006% and 0.01%. However, for all other shear strains, the Excess Pore Pressure Ratio was observed to be lower than the lower bound curves by Dobry (1985), except for 0.05-0.03% shear strains. This indicates that the upper and lower bounds for shear strains above 0.03% do not accurately capture most of the test data points.

When the relative density is low, the excess pore pressure generated is also low. This occurs because undrained cyclic loading causes a decrease in shear modulus, which in turn creates pore pressure; low relative densities contribute to this phenomenon.

4.6.5 Development of correlations and MANOVA for the dynamic properties of Cape Flat Sands

4.6.5.1 Damping Ratio and Dynamic Shear Modulus Ratio

The equations created for D_r values of 25%, 50%, and 75% produced a high coefficient of determination, R^2, above 0.90 for both linear and quadratic models. The overall equation for all results in this study showed an R^2 above 0.84, demonstrating a strong correlation between damping ratio (λ) predicted by Dynamic Shear Modulus Ratio (G/G_{max}) and the accuracy of the two models.

After superimposing five correlation models from past scholars onto the combined test data, it is clear that no model is accurate for determining the dynamic response of different soils, regardless of their relative densities.

The MANOVA tests found significant results for the primary factors analyzed. Most of these factors had p-values less than 0.05, which means that there is no evidence to reject the null hypothesis of equality of means. This indicates that the strain amplitude (STR), void ratio/relative density (DR), and degree of saturation (SAT) are important parameters that influence the non-linear behavior of soils. The F_{crit} value also supports this finding with $F < 1$.

Based on the residual plots, it appears that the errors are random and independent, meaning they do not affect the relationship between the predicted and observed values. Possible factors that could have contributed to these errors include room temperature and other environmental factors.

4.7 Repeatability

Repeatability tests were demonstrated with DR-75-SAT-000-STR-0.6 being replicated twice, as presented in Figure 4-30 concerning shear stress and cyclic axial strain versus cycles. The results show reasonable handling, precision and accuracy of the data output as seen by both cyclic loci produced by both tests. This is further emphasized by the quality control charts of the triaxial specimen masses and back pressure illustrated in Figure 4-31. Figure 4-31 demonstrates that the masses of the triaxial specimen and back pressure for DR-75-SAT-000 for all the ten (10) cyclic axial strains (0.005%, 0.01%, 0.02%, 0.05%, 0.1%, 0.2%, 0.4%, 0.6%, 0.8% and 1.0%) was within twice the limits of the standard deviation (2S) thus indicating a reliable degree of uniformity between the ten specimens prepared and consequently the consistent output of the cyclic results with great accuracy and precision. The control limits adopted were such that warning limits were twice the standard deviation (2S) and alarm limits thrice the standard deviation (3S) (Baecher & Christian, 2003; George & Mallery, 2019). This ensured that all the ten (10) samples evaluated at the respective cyclic axial strains had the same relative density (D_r = 75%), degree of saturation (SAT = 0%) and the back pressure after the completion of the saturation stage was generally invariable. The detailed quality control chart for DR-75-SAT-000-STR-0.6 is presented in Appendix 5.

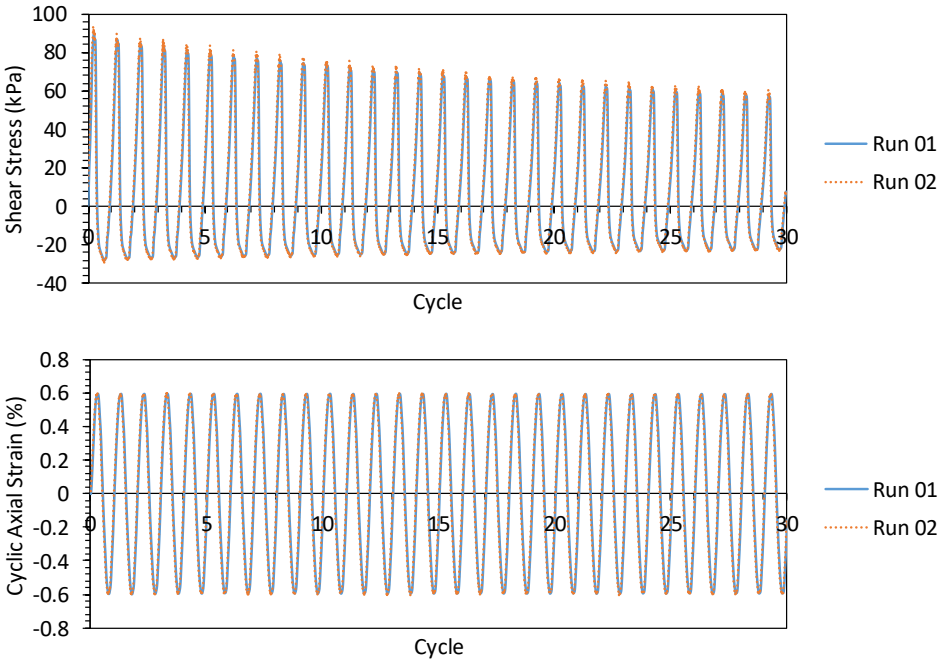

Figure 4-30: Repeatability tests for DR-75-SAT-000-STR-0.6

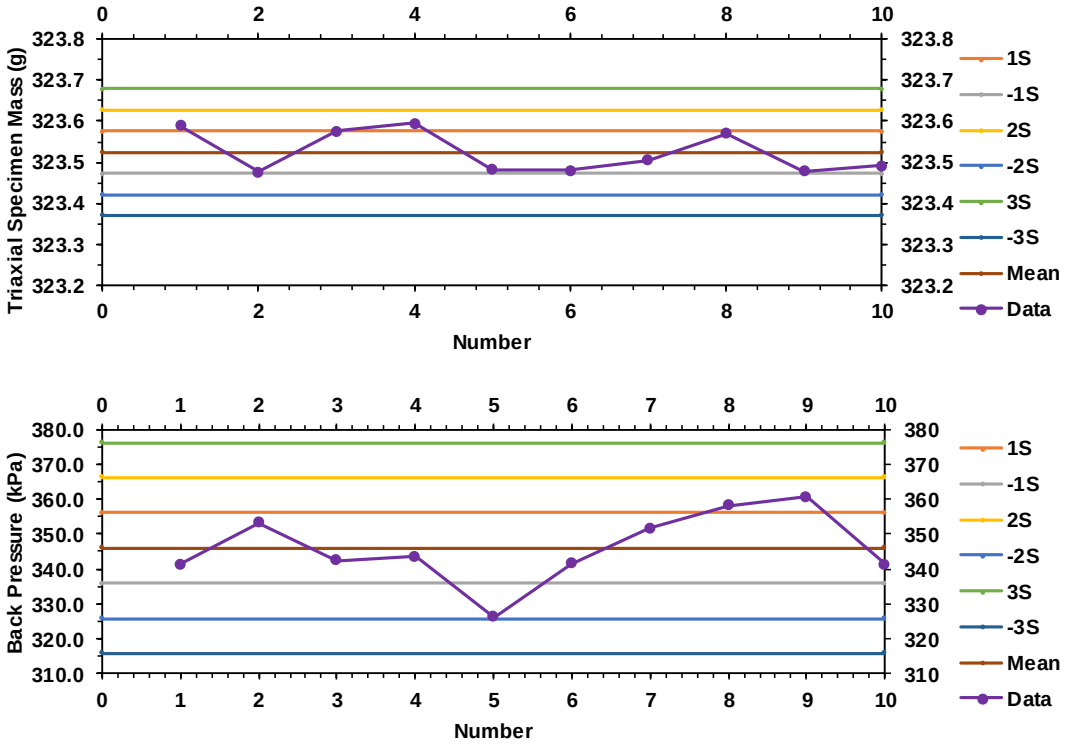

Figure 4-31: Quality control chart for triaxial specimen mass and back pressure for D_r-75-SAT-000

4.8 Demonstration of the Applicability of Test Results to Applications in Geotechnical Engineering

4.8.1 Ground Response Analysis

ProShake software (version 2.0.1.14) was used to conduct an equivalent linear analysis of the ground response for which the results are summarized in Table 4-10. Figure 4-32 displays the ground motions (including acceleration time history, acceleration Fourier spectrum, and spectral acceleration) for each of the six soil layers. Figure 4-33 shows how shear strain and stress time history vary with response spectra at 5% damping in Figure 4-34 for each layer of soil.

The results showed that when the ground motion of 0.174g was applied to the rock (Layer 6), it took about 1.1 times quicker to reach the 2nd - 4th layers with 0.182 - 0.192g. The ground motion advanced through the rock with a peak velocity of 0.030m/s, rapidly increased by 1.5 times within the top five (5) layers 0.042 - 0.045 m/s). Similarly, the peak displacement rapidly escalated 1.25 times from 0.004 m at layer 6 (rock) to 0.005m within the first 4 layers. The arias intensity at the rock increased from 0.333 m/s to 0.340 - 0.382m/s (~1.69 times), within the 2nd - 4th layers; The arias intensity of the top layer was 0.274m/s, indicating its relative stability against landslides coupled with its subsequent five (5) layers (Meyyappan, 2019). The predominant period of 0.126s decreased by 20% to 0.110s for all five layers. This predominant period of 0.110s corresponded to the maximum value of the Fourier amplitude spectrum that could be used to guide the structural engineers against structural distress and damage arising from this ground motion (Meyyappan, 2019; Noguera, 2016).

The peak velocity gives a measure of hazard to storied buildings by governing the ground response at intermediate periods. The peak velocity is generally 42 - 45mm/s which was within the limits of the vibration amplitudes for a storied building with respect to Table 2-5 (203 - 1524 mm/s at which damage commences). Based on the information presented in Table 2-6, it appears that the peak velocity resulting from the earthquake ground motion may not be appropriate for certain structures, such as transformers, homes with varying levels of construction quality, and rural mud houses that may be present in the area. These types of civil engineering infrastructure could potentially fail during an earthquake, as illustrated by the direct effects (structural and ground effects) shown in Figure 2-6. Additionally, the response spectrum could be utilized in detailed structural analysis and design with the bracketed duration of 6.278 - 7.170s being used for further computation of elastic and inelastic response (Meyyappan, 2019; Prathima, 2009).

Table 4-10: Summary of the results from the ground response analysis

Parameter	Layer No						Mean	Median	Standard Deviation
	1	2	3	4	5	6			
Peak Acceleration (g)	0.159	0.187	0.192	0.182	0.205	0.174	0.183	0.183	0.014
Peak Velocity (m/s)	0.042	0.044	0.045	0.043	0.043	0.030	0.041	0.041	0.005
Peak Displacement (m)	0.005	0.005	0.005	0.005	0.004	0.004	0.004	0.004	0.000
RMS Acceleration (g)	0.052	0.060	0.061	0.058	0.063	0.048	0.057	0.057	0.006

Table 4-10: Summary of the results from the ground response analysis

Parameter	Layer No						Mean	Median	Standard Deviation
	1	2	3	4	5	6			
Arias Intensity (m/s)	0.274	0.365	0.382	0.340	0.407	0.229	0.333	0.327	0.062
Cumulative Absolute Velocity (g-sec)	0.297	0.344	0.351	0.331	0.362	0.268	0.326	0.324	0.033
Response Spectrum Intensity (g^2)	0.274	0.365	0.382	0.340	0.407	0.229	0.335	0.333	0.037
Predominant Period (s)	0.110	0.110	0.110	0.110	0.110	0.126	0.113	0.113	0.006
Mean Frequency (Hz)	16.42	17.27	17.44	17.73	20.15	26.99	19.33	19.04	3.61
Bracketed Duration (s)	6.278	6.280	6.370	6.280	7.170	7.0707.	6.575	6.563	0.388
Spectral Acceleration at 1.0 second (g)	0.030	0.030	0.030	0.030	0.030	0.025	0.029	0.029	0.002

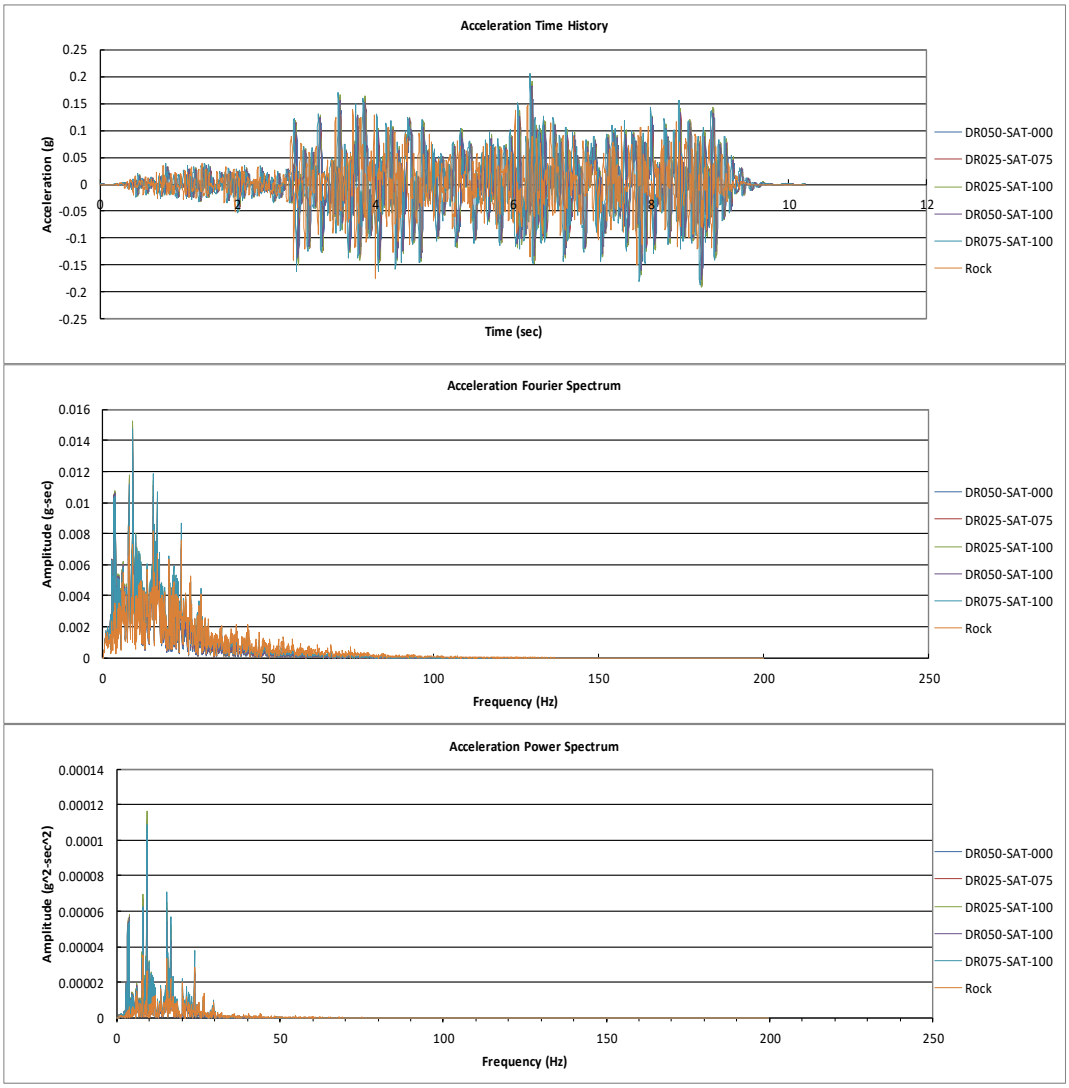

Figure 4-32: Ground motions for the Soil Profile

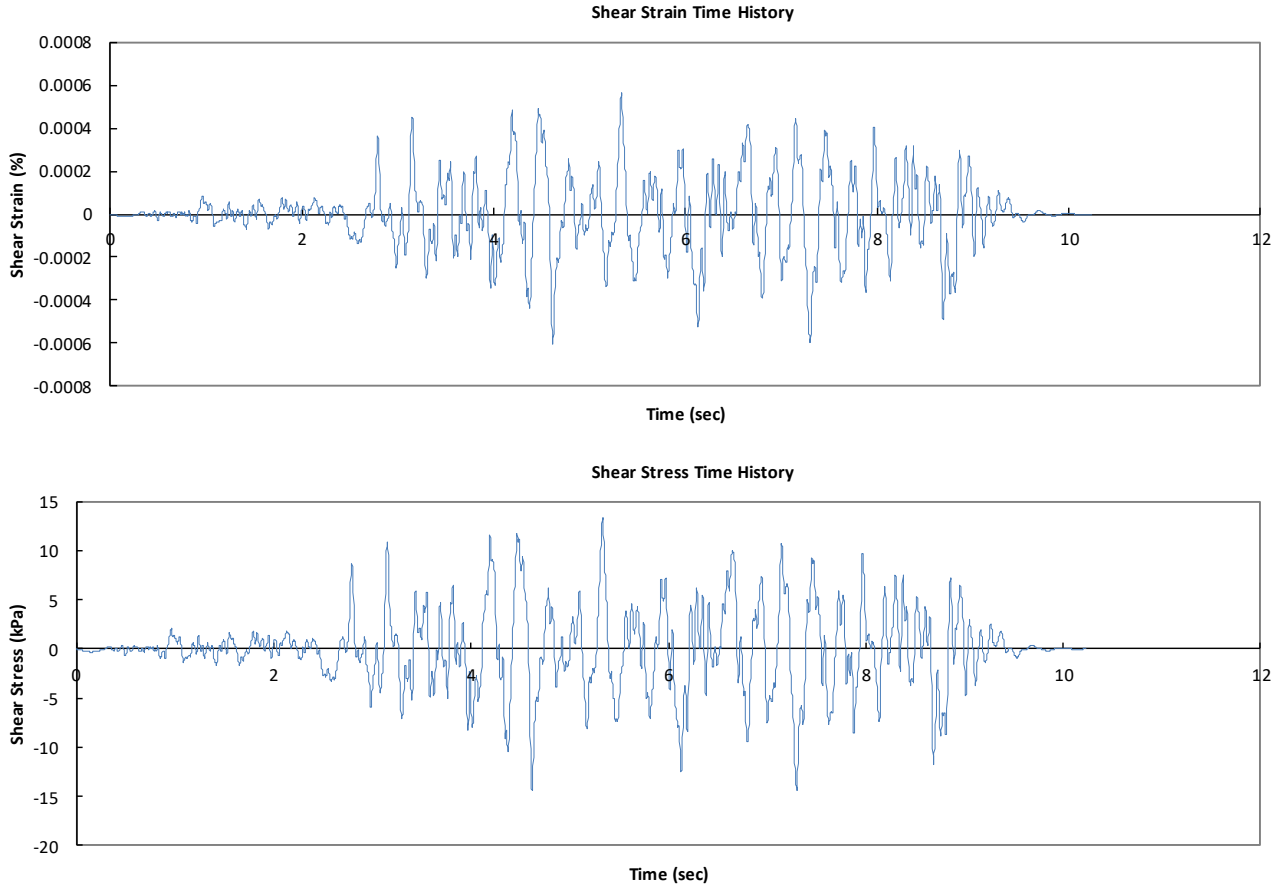

Figure 4-33: Shear strain and stress time history

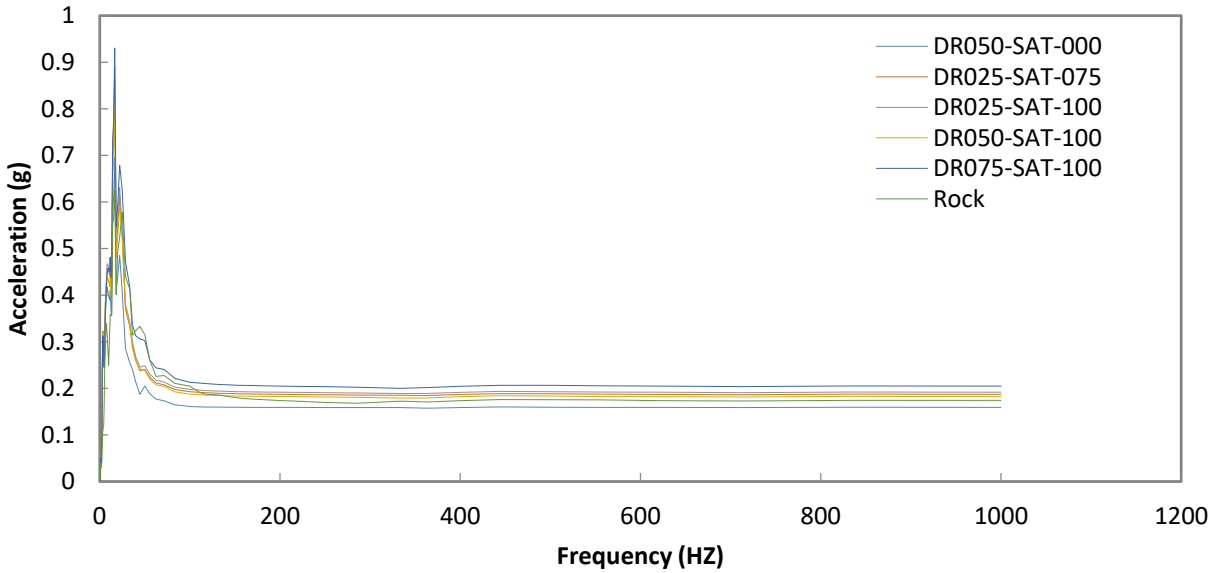

Figure 4-34: Spectral acceleration for the soil profile

In Figure 4-35, depth plots specific to the site were shown for acceleration, displacement, velocity, and effective shear strain profiles. These plots revealed a noteworthy change at a depth of 2.45m, which corresponded to the water table depth, suggesting that the ground response was affected by the presence of the water table. Furthermore, the plots indicated that there were proportional changes in the depth plots based on the soil strata's relative density and partial or full saturation states.

The effective shear strain ranged from 0.002-0.011% indicating that this was a small strain geotechnical problem that could be evaluated in Plaxis 2D for dynamic calculations, free vibration analysis and earthquake analysis with respect to Figure 2-23 (see Section 2.3.1.2). The peak shear strain (0.011%) occurred at 11m, while the minimum acceleration (0.104g) occurred at 2.45m, with the maximum acceleration (0.159g) occurring at the surface. Structural building codes like SANS 10160-4:2017 utilizes this maximum acceleration (0.159g) and spectral acceleration (Figure 4-34) to identify the magnitude of the horizontal force that can be withstood by a structure (Meyyappan, 2019; Noguera, 2016; Prathima, 2009).

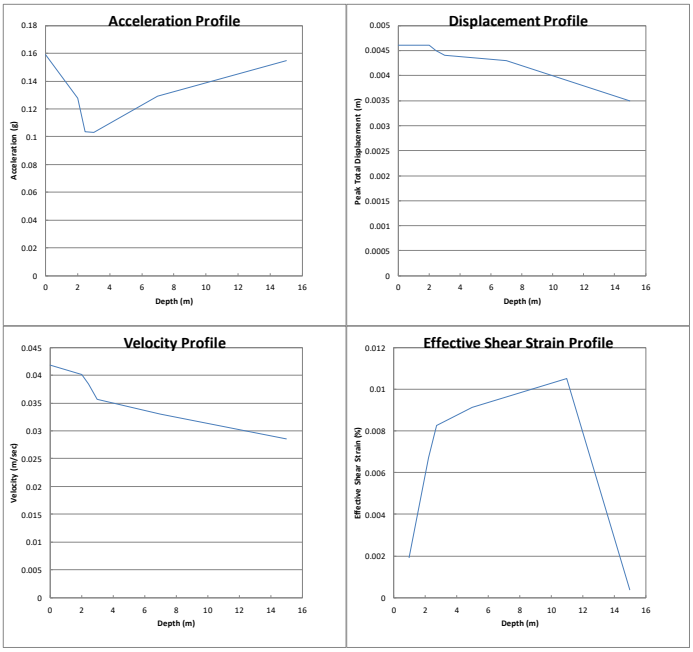

Figure 4-35: Acceleration, displacement, velocity, and effective shear strain profile with depth

4.8.2 Free Vibration and Earthquake Analysis of a Five-Storied Building

The time history displacement in Figure 4-36 showed that the vibration of the building from its top induced an immediate displacement of 6.4 mm at 0 seconds (dynamic time) which slowly decayed over 5 seconds (dynamic time) owing to damping of the soil and the building. The frequency spectrum and spectral acceleration illustrated a dominant frequency of 0.8 Hz and acceleration of 0.047g during this dynamic ground motion.

The dominant frequency of 0.8 Hz (from the frequency spectrum Figure 4-36) obtained from Plaxis 2D analysis was equivalent to a period of 1.25s; this demonstrated an amplification from 0.110s (predominant period in Table 4-10) at the surface soils to about 11.36 times at the building top during an earthquake. This led to a displacement of 6.4mm at 0 seconds (time history displacement Figure 4-36) and equivalent variation of properties in the spectral acceleration and arias intensity. If the structure was designed in such a way that the natural period of the structure does not coincide with the predominant period of the earthquake ground motion it would mitigate the damage of the structures due to dynamic loading (Meyyappan, 2019; Prathima, 2009). With respect to SANS 10160-4: 2017, the satisfaction requirement was $T \leq 2.0$s (Section 2.2.3.2) which indicated that the structural linear model had a period of vibration less than 2.0s in such a way that T was 1.25s $\leq$ 2.0s.

Figure 4-37 illustrates that the dynamic ground motion yields maximum deformation of 24.96 mm, 6.83 mm, 1.26 mm, and 0.43 mm with respect to Phase 01, Phase 02, Phase 03, and Phase 04, respectively, giving a total seismic displacement of 33.48 mm. This overall settlement would guide the geotechnical and structural engineer to obtain suitable foundation dimensions or ground improvement methods to ensure that the overall settlement is within the tolerable limits of say 25 mm during the design stage (Das, 1999, 2016; Geotechnical Engineering Office, 2006).

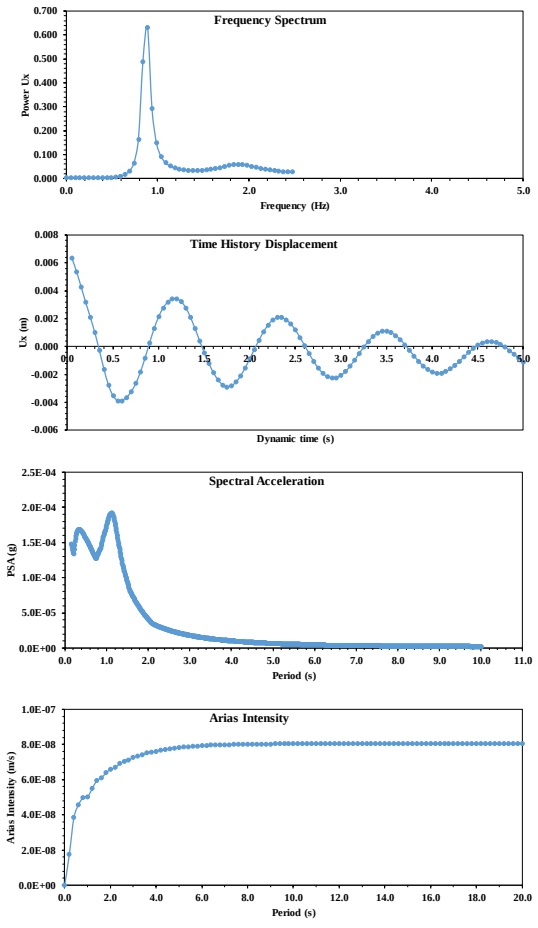

Figure 4-36: Results of the free vibration and earthquake analysis of the building

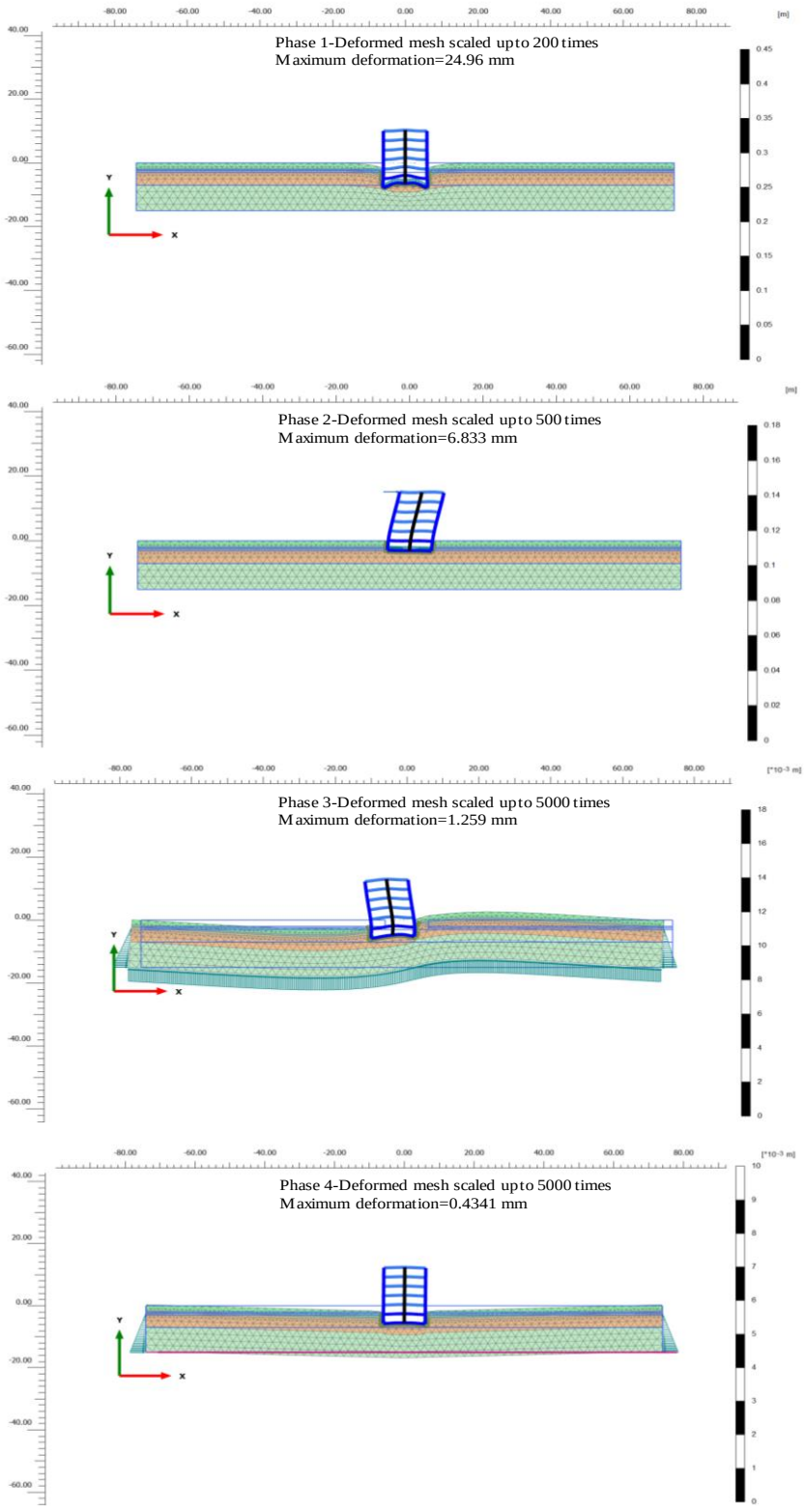

Figure 4-37: Output of the results using Plaxis 2D for all respective phased

4.9 Summary of Key Results on Demonstration of the Applicability of the Test Results to Applications in Geotechnical Engineering

4.9.1 Ground Response Analysis

An equivalent linear analysis of the ground response was conducted using ProShake software. The analysis revealed amplification of various parameters such as peak acceleration, peak velocity, peak displacement, RMS acceleration, Arias intensity, cumulative absolute velocity, response spectrum intensity, predominant period, mean frequency, bracketed duration, and spectral acceleration. These changes were observed from the rock layer to the top sandy layer.

In addition, depth plots for acceleration, displacement, velocity, and effective shear strain profiles that were specific to the site were created. These plots showed a significant change at a depth of 2.45m, which is the same depth as the water table. This suggests that the ground's response was influenced by the presence of the water table.

4.9.2 Free Vibration and Earthquake Analysis of a Five-Storied Building

To analyze the free vibration and earthquake effects on a five-storied building, Plaxis 2D was utilized. The time history displacement revealed that the vibration from the top of the building caused an initial displacement of 6.4mm at 0 seconds, which gradually decreased over 5 seconds due to soil and building dampening. Additionally, the equivalent frequency spectrum, spectral acceleration, time history displacement, and arias intensity were calculated. These parameters assist the structural engineer in preventing structural damage caused by dynamic loading.

During the dynamic ground motion, there was a deformation of 33.48 mm. This information can be used by geotechnical and structural engineers to determine the appropriate foundation dimensions or ground improvement methods. The goal is to keep the settlement within tolerable limits, which are typically around 25 mm during the design stage.

5 Conclusions and Recommendations

5.1 Introduction

This research study delved into the dynamic soil behaviour of Cape Flats sand under earthquake cyclic loading, utilizing the cyclic triaxial equipment. Cape Flats sand was specifically chosen due to its abundant presence in Cape Town's seismically sensitive zone. An elaborate laboratory testing program was established to assess the Cape Flat sand cyclic properties. The program involved varying the axial strains, relative densities, and saturation content. The cyclic properties obtained were utilized to carry out ground response analysis, free vibration analysis, and earthquake analysis of a five-story building.

5.2 Conclusions

Cape Flats is a coastal area in the Western Cape that predominantly consists of a saturated low-lying sand-covered expanse linking the southwestern Cape mainland with the mountainous Cape Peninsula. In this study, the Cape Flat sand was generally characterised as poorly graded sand (SP) in accordance with the Unified Soil Classification System. The sand grains were angular with a median size of 0.4mm and 70% medium grained sand sized fraction. Its specific gravity, minimum and maximum void ratios were 2.646, 0.391 and 0.677, respectively.

When performing cyclic triaxial tests on sands, their dynamic properties were measured through dynamic shear modulus, damping ratio, and excess pore pressure ratio (r_u). The dynamic shear modulus indicated the soil stiffness in shear, the damping ratio stipulated how much energy was dissipated during cyclic loading, and the excess pore pressure ratio designated the ratio of excess pore pressure to effective confining pressure. The study found that as the shear strain increased, the shear and normalized shear modulus decreased non-linearly. Furthermore, an increase in relative density led to increased shear modulus. As the shear strain reached higher levels in this study, the scatter of the normalized dynamic modulus decreased remarkably and remained relatively constant. Regression analysis showed that the shear modulus reached its peak at an optimal saturation content ($S_{r,\,opt}$). For D_r values of 25%, 50%, and 75%, the $S_{r\,opt}$ values were 12.1 - 29.1%, 11.6 - 23.6%, and 11.9 - 18.5%, respectively. The results also showed that the shear modulus decreased in partially saturated sands as the degree of saturation increased. As the relative density increased, the damping ratio was observed to decrease. Additionally, an increase in shear strain typically led to an increase in the damping ratio until $\gamma = 0.7$, beyond which a peaking behaviour was observed at all relative densities. This implied that correlations for damping ratios with shear strain for $\gamma \leq 0.7\%$ could not be applied to $\gamma > 0.7\%$. Furthermore, increased saturation content resulted in a slight increase in damping ratio until full saturation was achieved, implying that fully or partially saturated samples consistently have higher damping ratio values than dry samples. Finally, for any given saturation content, an increase in relative density (D_r) decreased

damping ratios. The excess pore pressure ratio (r_u) increased non-linearly with shear strain at all relative densities. Pore pressure was generated when the sand was cyclically loaded, which diminished effective stress and consequently affected soil shear stiffness and shear stress development. It can also be concluded that the excess pore pressure ratio (r_u) increased as the degree of saturation increased. Additionally, this study suggested a threshold shear strain (γ_{tv}) level below which no excess pore pressure was generated; this level was found to be γ_{tv} = 0.006 - 0.01%.

Regression models were developed using experimental data and theoretical analysis to establish a link between the damping ratio (λ) and normalized shear modulus (G/G_{max}). The equations, including linear and quadratic terms, produced an R^2 value of over 0.84 for all the combined study's findings, indicating a strong correlation between λ and G/G_{max} as a measure of accuracy and goodness of fit. In addition, five correlations from past scholars were superimposed over the combined data set, and some scatter was observed. However, it is essential to note that while each of these five models was created based on dynamic testing of a specific sandy soil, adopting any model to determine the dynamic response of different sandy soils may not be accurate. This highlights the importance of carefully determining the dynamic properties of each soil before applying it to any practical geotechnical engineering project. Furthermore, the statistical plots of the predicted and residuals of all combined data sets from MANOVA showed that the residuals were random and independent.

A ground response and free vibration analysis of a five-storied building were carried out using ProShake software and Plaxis 2D software. This was achieved using normalized shear modulus and damping ratio with shear strain curves against a soil profile obtained along the R300 road in the Cape Flats region. A water table underlay this soil profile at 2.45m depth, enabling varying saturation states to be adopted. The above software used the Nahanni (1985)-RSN497 ground motion adopted from the PEER NGA ground database. This ground motion from North America was adopted owing to its equivalent tectonic plate to Cape Town with earthquake magnitude M_w = 6.9. The ground response analysis obtained a site-specific peak acceleration, peak velocity, peak displacement, arias intensity, predominant period, and bracketed durations for all the adopted soil profile layers. In addition, a site-specific depth plot for acceleration, velocity, displacement, and effective shear strain profile was obtained. The free vibration and earthquake analysis, the site-specific frequency spectrum, time history displacement, spectral acceleration, arias intensity and total seismic displacement during an earthquake event was obtained. The total seismic settlement of the building was 33.5mm, which would guide the geotechnical and structural engineer to provide ground improvement methods or foundation dimensions to limit this settlement to tolerable limits of about 25mm during the design stage. The above results of the ground response analysis, free vibration and earthquake analysis showed that the different saturation states (SAT), relative density (D_r) and equivalent dynamic properties influenced the behaviour of the ground motion parameters for each respective sandy layer.

5.3 Recommendation for Future Study

The research study was conducted at a constant effective confining pressure of 100kPa, with constant frequency (0.5Hz) for all test combinations. The mean effective confining pressure and loading frequency influence the dynamic properties of sand, as presented in Table 2-8 and Table 2-9 (Darendeli, 2001).

The maximum shear modulus (G_{max}) was obtained through correlations by Seed & Idriss (1970); Adopting a very small strain (0.0001%) cyclic equipment like the Piezoelectric bender element and resonant column equipment would increase the reliability for obtaining the maximum shear modulus under cyclic conditions. This equipment would also facilitate the study of the cyclic shear strains from 0.0001% - 0.05%, which was a limitation for the cyclic triaxial equipment used in this study (Jones, 2013; J. Kumar & Madhusudhan, 2010; Pan, Yuan, Zhao, Tong, & Yang, 2022; Varghese, Senthen, Boominathan, & Banerjee, 2019).

The study focused on the cyclic properties of Cape Flat Sands; however, Cape Town is characterized by several soils that include clays. Thus, evaluating the cyclic properties of clays would also give the dynamic behaviour of fine-grained soils whose OCR, plasticity and amount of fines influence the cyclic shear modulus and damping properties. It becomes necessary to ensure that seismic responses for both sands and clays are well understood and studied in detail to suit adequate seismic designs (Towhata, 2008; Whang, Stewart, & Bray, 2004; Martindale & Basu, 2011; Hardin and Drnevich, 1972).

Owing to the absence of ground motion data within South Africa, the seismic ground response, free vibration and earthquake analysis was carried out for a soil profile along R300 within the Cape Flats Region using an equivalent ground motion in North America (Nahanni, NS3360-RSN497) (Midzi et al., 2020b). Thus, adopting different soil profiles and several ground motions from the PEER database would give a detailed ground response analysis under various earthquakes, including worse-case scenarios like the Kobe earthquake (Amr & Luigi, 2008). Asakereh & Tajabadipour (2018) reported the study of 12 ground motions from the PEER database with various parameters like frequency, PGA (0.001g-0.8g and PGV during their study of the analysis of local site effects on seismic ground response under multiple earthquakes.

SANS 10160-4 (2017) focuses on the geotechnical seismic parameters of four (4) ground types concerning rock, very dense sand or very stiff clay, dense or medium dense sand or gravel or stiff clay and loose to medium cohesionless soils. These parameters include shear wave velocity ($v_{s,30}$), N-SPT value and undrained shear strength. However, the seismic standard is silent on shear modulus and damping ratio models for the respective soils that should accompany the ground response analyses during the development of the normalized design response spectra. Therefore, SANS 10160-4 (2017) should be improved to adopt cyclic properties for South African soils by coordinating wide-scale research with research institutions in the country.

References

Al Tarhouni, M. A., & Hawlader, B. (2023). Drained cyclic behaviour and state-dependent stress–dilatancy relationship of sand in direct simple shear tests. *Soil Dynamics and Earthquake Engineering*, *168*. https://doi.org/10.1016/j.soildyn.2023.107801

Amr, S. E., & Luigi, D. S. (2008). *Fundamentals of Earthquake Engineering*. *Engineering Geology* (Vol. 43). England: A John Wiley & Sons Limited Publication.

Andersen, K., H. (2015). *Cyclic soil parameters for offshore foundation design*. In: Meyer V (ed) The 3rd ISSMGE McClelland lecture, in frontiers in offshore geotechnics III, CRC Press, Boca Raton

Asadi, M. B., Orense, R. P., Asadi, M. S., & Pender, M. J. (2022). A unified approach to link small-strain shear modulus and liquefaction resistance of pumiceous sand. *Soils and Foundations*, *62*(1). https://doi.org/10.1016/j.sandf.2021.101098

Asakereh, A., & Tajabadipour, M. (2018). Analysis of Local Site Effects on Seismic Ground Response Under Various Earthquakes. *AUT Journal of Civil Engineerng*, *2*(2), 227–240. https://doi.org/10.22060/ajce.2018.13696.5253

ASTM D2487. (2017). Standard Practice for Classification of Soils for Engineering Purposes (Unified Soil Classification System)". *Annual Book of ASTM Standards.*, 1–10. https://doi.org/10.1520/D2487-17E01.2

ASTM D4253. (2016). Standard Test Methods for Maximum Index Density and Unit Weight of Soils Using a Vibratory Table. *Annual Book of ASTM Standards.*, 14. https://doi.org/10.1520/D4253-16E01.1.3

ASTM D4254. (2016). *Standard Test Methods for Minimum Index Density and Unit Weight of Soils and Calculation of Relative Density*. *ASTM Standards*. https://doi.org/10.1520/D4254-16.2

ASTM D4318. (2017). Standard Test Methods for Liquid Limit, Plastic Limit, and Plasticity Index of Soils. *Annual Book of ASTM Standards.*, 20. https://doi.org/10.1520/D4318-17E01.

ASTM D4460. (1997). Standard Practice for Calculating Precision Limits Where Values are Calculated from Other Test Methods. *Annual Book of ASTM Standards.*, 3. https://doi.org/10.1520/D4460-97R15.2

ASTM D5311/D5311M. (2013). Standard test method for load controlled cyclic triaxial strength of soil. *Annual Book of ASTM Standards.*, 11. https://doi.org/10.1520/D5311

ASTM D6026. (2021). Standard Practice for Using Significant Digits and Data Records in Geotechnical Data. *Annual Book of ASTM Standards.*, 6. https://doi.org/10.1520/D6026-21.

ASTM D6913/D6913M. (2017). Standard Test Methods for Particle-Size Distribution (Gradation) of Soils Using Sieve Analysis. *Annual Book of ASTM Standards.*, 34. https://doi.org/10.1520/D6913

ASTM D854. (2014). Standard Test Methods for Specific Gravity of Soil Solids by Water Pycnometer. *Annual Book of ASTM Standards.*, 8. https://doi.org/10.1520/D0854-14.

ASTM E1329. (2010). Standard Practice for Verification and Use of Control Charts in Spectrochemical Analysis. *Annual Book of ASTM Standards.*, 12. https://doi.org/10.1520/E1329-10.2

ASTM E178. (2021). Standard Practice with dealing with outlying observations. *Annual Book of ASTM Standards*, 11. https://doi.org/10.1520/E0178-21.2

ASTM E2586. (2019). Standard Practice for Calculating and Using Basic Statistics. *Annual Book of ASTM Standards.*, 22. https://doi.org/10.1520/E2586-19E01.2

ASTM E29. (2013). Standard Practice for Using Significant Digits in Test Data to Determine Conformance with Specifications. *Annual Book of ASTM Standards.*, (Reapproved 2019), 5. https://doi.org/10.1520/E0029-13R19.2

Atkinson, J., H., & Sallfors, G. (1991). *Experimental determination of soil properties.* In: Proceedings of the 10th ECSMFE, vol 3, Florence, pp 915–956.

Baecher, G. B., & Christian, J. T. (2003). *Reliability and Statistics in Geotechnical Engineering*. Wiley-ISBN 0471498335.

Boorea, D., M., & Atkinson, G., A. (2008). *Ground Motion Prediction Equations for the Average Horizontal Component of PGA, PGV, and 5% Damped PSA at Spectral Periods between 0.01s and 10s*. Earthquake Spectra 24 (1).

Brandt, M. (2011). *Seismic Hazard in South Africa*. *Council for Geoscience* (Vol. 2011–0061). Cape Town.

Brinkgreve, R. B. J., Engin, E., & Engin, H. K. (2010). Validation of empirical formulas to derive model parameters for sands. In *Research*. https://doi.org/10.1201/b10551-25

Chakrabortty, P., Roshan, A. R., & Das, A. (2020). Evaluation of Dynamic Properties of Partially Saturated Sands Using Cyclic Triaxial Tests. *Indian Geotechnical Journal*, *50*(6), 948–962. https://doi.org/10.1007/s40098-020-00433-3

Chaneva, J., Kluger, M. O., Moon, V. G., Lowe, D. J., & Orense, R. P. (2023). Monotonic and cyclic undrained behaviour and liquefaction resistance of pumiceous, non-plastic sandy silt. *Soil Dynamics and Earthquake Engineering*, *168*(December 2022), 107825. https://doi.org/10.1016/j.soildyn.2023.107825

Chavan, D., & Babu, G. L. S. (2023). Site response analysis of liquefiable stratified ground comprising silt and sand : Numerical investigations. *Soil Dynamics and Earthquake Engineering*, *173*(February), 108098. https://doi.org/10.1016/j.soildyn.2023.108098

Chavan, D., Sitharam, T. G., & Anbazhagan, P. (2021). Failure Modes of Air Desaturated Sand in Undrained Cyclic Loading : A Systematic Experimental Investigation. *Indian Geotechnical Journal*, (1). https://doi.org/10.1007/s40098-021-00577-w

Chen, J., Olson, S. M., Banerjee, S., Dewoolkar, M. M., & Dubief, Y. (2022). Water content of moist-tamped nonplastic specimens for constant-volume direct simple shear testing. *Geotechnical Testing Journal*, *45*(2), 503–512. https://doi.org/10.1520/GTJ20210125

Chowdhury, I., Ghosh, A., & Dasgupta, S. P. (2016). Dynamic Soil Structure Interaction of Structures Resting on Soil Under Earthquake Motion. *Indian Geotechnical Journal*, *46*(1), 85–103. https://doi.org/10.1007/s40098-015-0153-7.

Cichowicz, A. (2012). *Ground Motion Prediction and Experimental Response Spectra*. *ResearchGate*. Project Number: SIM 11-02-01. Retrieved from https://www.researchgate.net/publication/312472292%0AGround

Darendeli, M., B. (2001). *Development of a new family of normalized modulus reduction and material damping curves.* PhD Thesis, Department of Civil Engineering, University of Texas, Austin.

Das, B. M. (1999). *Shallow Foundations: Bearing Capacity and Settlement*. (C. P. LLC, Ed.), *New York*. California,USA: CRC Press LLC.

Das, B. M. (2016). *Priciples of Foundation Engineering* (Eighth Edi). Boston,USA: Cengage Learning, Global Engineering.

Díaz-Rodríguez, J., A. (1989). *Behavior of Mexico City clay subjected to undrained repeated loading*. Can Geotech J 26(1):159–162.

Diaz-Rodriguez, J., A., & Santamarina, C. (2001). *Mexico City soil behavior at different strains: observation and physical interpretation*. J Geotech Geoenviron Eng 127(9):783–789.

Durrheim, R. J., & Manzunzu, B. (2018). *Strategic environmental assessment for gas pipeline development in south africa-Seismicity assessment report for stakeholder review*.

Dutta, T. T. (2015). *Dynamic Properties of Clean Sand and Expansive Clay fromResonant Column Studies*. Indian Institute of Technology Hyderabad.

EduPro Civil Systems. (2017). *ProShake- Ground Response Analysis Program Version 2.0 User's Manual*. Sammamish, Washington. Retrieved from http://www.proshake.com/index.html

EPRI. (1993). *Guidelines for Determining Design Basis Ground Motions*. Palo Alto, California, USA, Electric Power Research Institute. Report number: EPRI TR-102293.

Fardis, M. N. (Ed.). (2010). Advanced in performance-based earthquake engineering. In *Geotechnical, Geological and Earthquake Engineering* (p. 507). Springer Dordrecht Heidelberg London New York. https://doi.org/10.1007/978-90-481-8746-1

Fouche, N. (2021). *Geotechnical Characterisation of the Upper Quaternary Sands of the Cape Flats*. Stellenbosch University. Retrieved from https://scholar.sun.ac.za

Fouché, N., & Day, P. W. (2022). Geotechnical properties of Cape Flats sands. *Journal of the South African Institution of Civil Engineering*, *64*(2), 13–27. https://doi.org/ISSN 1021-2019

Fredlund, D. G., & Rahardjo, H. (1993). *Soil Mechanics for Unsaturated Soils*. *Soil Mechanics for Unsaturated Soils*. Alberta, Canada: A John Wiley & Sons Limited Publication. https://doi.org/10.1002/9780470172759

Fredlund, D. G., Rahardjo, H., & Fredlund, M. D. (2012). *Unsaturated Soil Mechanics in Engineering Practice* (ISBN 978-1). Hoboken, New Jersey: John Wiley & Sons, Inc.

Geocomp. (2019). *Cyclic Triaxial (CYCLIC7N) Software User's Manual V3.0. Control and Report Software for Fully Autimated Cyclic Triaxial Tests on LoadTrac-II/FlowTrac-II/Cyclic-RM and Linear Electro-Mechanical Actuator Systems Using Windows ® XP (SP3)/7/10*. Nagog Park, Geocomp Corporation, Acton, MA 01720 USA.

George, D., & Mallery, P. (2019). *IBM SPSS Statistics 26 Step by Step* (16th ed.). New York: Routledge-ISBN 9780429056765. https://doi.org/10.4324/9780429056765

Geotechnical Engineering Office. (2006). *Foundation Design and Construction*. *Geo Publication No. 1/2006*. Hon.

Ghayoomi, M., Khosravi, A., McCartney, J. S., & Ko, H.-Y. (2015). Challenges in Prediction of Earthquake-Induced Settlements of partially Saturated Sands, (303), 123–128. https://doi.org/10.1007/978-1-4614-7495-1_23

Gobbi, S., Reiffsteck, P., Lenti, L., d'Avila, M. P. S., & Semblat, J. F. (2022). Liquefaction triggering in silty sands: effects of non-plastic fines and mixture-packing conditions. *Acta Geotechnica*, *17*(2), 391–410. https://doi.org/10.1007/s11440-021-01262-1

Gu, C., Gu, Z., Cai, Y., Wang, J., & Ling, D.-S. (2017). Dynamic Modulus Characteristics of Saturated Clays Under Variable Confining Pressure. *Canadian Geotechnical Journal*, *54*(5), 729–735. https://doi.org/10.1139/cgj-2016-0441

Haas, T. N., & Kolf, T. Van Der. (2014). Seismic Analysis of URM Buildings in S . Africa. *International Scholarly and Scientific Research & Innovation*, *8*(12), 1267–1274. Retrieved from www.scholar.waser.org/1307-6892/9999942

Haas, T. N., & Marsh, R. (2017). The Effect Of Wall Opening Sizes On Unreinforced Masonry Subjected To Dynamic Loading. In *Proc. of the Fifth Intl. Conf. Advances in Civil, Structural and Mechanical Engineering - CSM* (pp. 59–63). https://doi.org/10.15224/ 978-1-63248-132-0-43

Haas, T. N., & Solms, M. N. (2017). Alternative Approach to Analysing Infrastructure Using Limited Acceleration Time History Analysis. *International Journal of Structural and Civil Engineering Research*, *6*(2), 144–148. https://doi.org/10.18178/ijscer.6.2.144-148

Hardin, B., O. (1978). *The nature of stress-strain behaviour of soils: measurement and parameter effects.* In: Proceedings of earthquake engineering and soil dynamics, ASCE Pasadena, CA, vol 1, pp 3–89.

Hardin, B., O., & Drnevich, V., P. (1972). *Shear modulus and damping in soils: design equations and curves.* J Soil Mech Found Div 98(SM7):667–692.

IAEA. (2002). *Evaluation of Seismic Hazards for Nuclear Power Plants*. A-1400 Vienna-Austria.

Idriss, I. M., & Boulanger, R. W. (2008). *Soil Liquefaction During Earthquakes*. *E*. California,USA: arthquake Engineering Research Institute (EERI). https://doi.org/10.1177/136218079700300202

Ishibashi, I. & Zhang, X. (1993) *Unified dynamic shear moduli and damping ratios of sand and clay*. Soils and Foundations, 33:1, 182-191

Jafarzadeh, F., & Sadeghi, H. (2012). Experimental study on dynamic properties of sand with emphasis on the degree of saturation. *Soil Dynamics and Earthquake Engineering*, *32*(1), 26–41. https://doi.org/10.1016/j.soildyn.2011.08.003

Jamiolkowski, M., Leroueil, S., & Lopresti, D., C., F. (1991). *Theme lecture: design parameters from theory to practice*. In: Proceedings of geo-coast 91, Yokohama, pp 1–4.

Jia, J. (2018). *Soil Dynamics and Foundation Modeling: Offshore and Earthquake Engineering*. Gewerbestrasse, Switzerland: Springer International Publishing AG 2018. https://doi.org/10.1007/978-3-319-40358-8.

Jones, K. C. (2013). *Dynamic Soil-Structure-Interaction Analysis of Structures in Dense Urban Environments*. University of California, Berkeley.

Kafodya, I., & Okonta, F. (2021). Cyclic and post-cyclic shear behaviours of natural fibre reinforced soil. *International Journal of Geotechnical Engineering*, *15*(9), 1145–1154. https://doi.org/10.1080/19386362.2019.1611720

Kakavand, M., & Naeini, S. A. (2019). Effect of Density on the Shear Modulus and Damping Ratio of Saturated Sand in Small Strain. *International Journal of Geotechnical and Geological Engineering*, *13*(12), 689–692, ISNI:0000000091950263, World Academy of S.

Kantey & Templer (Pty) Ltd. (2018). *Report on Geotechnical Investigation for the Proposed New Erica Road Bridge Over National Route R300, Kuils River*. Cape Town. Retrieved from https://www.ecoimpact.co.za/media/AppendixG6_Geotechnical_Investigation_R300_Bridge.pdf

Karakan, E., Sezer, A., & Tanrinian, N. (2019). Evaluation of effect of limited pore water pressure development on cyclic behavior of a nonplastic silt. *Soils and Foundations*, *59*, 1302–1312. https://doi.org/10.1016/j.sandf.2019.05.009

Kaya, Z., & Erken, A. (2015). Cyclic and post-cyclic monotonic behavior of Adapazari soils. *Soil Dynamics and Earthquake Engineering*, *77*, 83–96. https://doi.org/10.1016/j.soildyn.2015.05.003

Kaya, Z., Erken, A., & Cilsalar, H. (2021). Characterization of elastic and shear moduli of adapazari soils by dynamic triaxial tests and soil-structure interaction with site properties. *Soil Dynamics and Earthquake Engineering*, *151*. https://doi.org/10.1016/j.soildyn.2021.106966

Khanbabazadeh, H., Iyisan, R., & Ozaslan, B. (2022). 2D seismic response of shallow sandy basins

subjected to obliquely incident waves. *Soil Dynamics and Earthquake Engineering*, *153*, 107080. https://doi.org/10.1016/j.soildyn.2021.107080

Khosravi, A., Ghayoomi, M., McCartney, J., & Ko, H.-Y. (2010). Impact of Effective Stress on the Dynamic Shear Modulus of Unsaturated Sand, *41095*(February), 410–419. https://doi.org/10.1061/41095(365)38

Kijko, A., Smit, A., & Coolwijk, N. Van De. (2015). A scenario approach to estimate the maximum foreseeable loss for buildings due to an earthquake in Cape Town. *South African Actuarial Journal*, *15*, 1–30. Retrieved from http://dx.doi.org/10.4314/saaj.v15i1.1%0AA

Kijko, A., & Graham, G. (1998). *Parametric-historic Procedure for Probabilistic Seismic Hazard Analysis Part I: Estimation of Maximum Regional Magnitude.*

Kiptoo, D., Aschrafi, J., Kalumba, D., Lehn, J., Moormann, C. and Zannoni, E., 2017. "*Laboratory Investigation of a Geosynthetic Reinforced Pavement under Static and Dynamic Loading*", American Society for Testing and Materials (ASTM) Journal of Testing and Evaluation, Volume 45, Issue 1, Jan, https://doi.org/10.1520/JTE20160170. ISSN 0090-3973.

Kramer, S., L. (1996). *Geotechnical earthquake engineering*. Prentice Hall, Upper Saddle River, NJ.

Kumar, J., & Madhusudhan, B. N. (2010). Effect of relative density and confining pressure on Poisson ratio from bender and extender elements tests. *Geotechnique*, *60*(7), 561–567. https://doi.org/10.1680/geot.9.T.003

Kumar, J., & Madhusudhan, B. N. (2012). Dynamic properties of sand from dry to fully saturated states. *Geotechnique*, *62*(1), 45–54. Retrieved from http://dx.doi.org/10.1680/geot.10.P.042

Kumar, S. S., Krishna, A. M., & Dey, A. (2017). Evaluation of dynamic properties of sandy soil at high cyclic strains. *Soil Dynamics and Earthquake Engineering*, *99*, 157–167. https://doi.org/10.1016/j.soildyn.2017.05.016

Li, X., Liu, J., & Nan, J. (2022). Prediction of dynamic pore water pressure for calcareous sand mixed with fine-grained soil under cyclic loading. *Soil Dynamics and Earthquake Engineering*, *157*(February 2021), 107276. https://doi.org/10.1016/j.soildyn.2022.107276

Li, Y., Nie, R., Yue, Z., Leng, W., & Guo, Y. (2021). Dynamic Behaviors of Fine-grained Subgrade Soil Under Single-stage and Multi-stage Intermittent Cyclic Loading: Permanent Deformation and its Prediction Model. *Soil Dynamics and Earthquake Engineering*, *142*(106548), 12. https://doi.org/10.1016/j.soildyn.2020.106548

Liebenberg, K., Smit, A., Coetzee, S., & Kijko, A. (2017). A GIS approach to seismic risk assessment with an application to mining related seismicity in Johannesburg , South Africa. *Acta Geophysica*, *65*(4), 645–657. Retrieved from http://hdl.handle.net/2263/62820

Liu, X., Qin, Z., & Yang, J. (2023). Undrained cyclic behaviour of loess with initial shear stress: A focus on failure mode. *Soil Dynamics and Earthquake Engineering*, *171*(March), 107971. https://doi.org/10.1016/j.soildyn.2023.107971

Look, B. (2007). *Handbook of Geotechnical Investigation and Design Tables*. London, UK: Taylor and Francis Group.

López-Castañeda, A. S., & Reinoso, E. (2021). Strong-motion duration predictive models from subduction interface earthquakes recorded in the hill zone of the Valley of Mexico. *Soil Dynamics and Earthquake Engineering*, *144*, 106676. https://doi.org/10.1016/j.soildyn.2021.106676

Lu, N., & Likos, W. J. (2004). *Unsaturated Soil Mechanics*. New Jersey: John Wiley & Sons, Inc.

Madhusudhan, B. N., & Kumar, J. (2013). Damping of Sands for Varying Saturation. *Journal of Geotechnical and Geoenvironmental Engineering*, *Technical*(139), 1625–1630. https://doi.org/10.1061/(ASCE)GT.1943-5606.0000895.

Madhusudhan, B., N. (2011). "*Dynamic properties of dry to fully saturated states using resonant column and bender element tests*." Ph.D. thesis, Indian Institute of Science, Bangalore, India.

Manzoor, B., Pandya, S., & Sachan, A. (2023). *Liquefaction Susceptibility and Characterization of Rebound Response of Micaceous Sand*. *Transportation Infrastructure Geotechnology*. Springer US. https://doi.org/10.1007/s40515-023-00289-z

Martindale, H., and Basu, D. (2011). *Constitutive model for rate dependent behavior of clay, internal geotechnical report 2011-3*. Department of Civil and Environmental Engineering, University of Connecticut.

Matsui, T., Ohara, H., & Ito, T. (1980). *Cyclic stress-strain history and shear characteristics of clay*. ASCE J Geotech Eng 106(10):1101–1120.

Mawer, B., Kalumba, D, and Warren-Codrington C. J., 2017. "*Loading and Dynamic Response Considerations for the Design of Wind Turbine Foundations on South African Soils*", Geotechnical Engineering Journal of the SEAGS & AGSSEA, ISSN 0046-5828, Vol. 48, No. 3, September, pp 110-117.

Menq, F.-Y. (2003). *Dynamic Properties of Sandy and Gravelly Soils*. The University of Texas at Austin.

Meyyappan, P. L. (2019). Reliability on ProSHAKE 2 . 0 in the Assessment of One Dimensional Ground Response Analysis through Verification Example. *International Journal of Recent Technology and Engineering (IJRTE)*, *8*(4S2), 56–59, ISSN: 2277-3878. https://doi.org/10.35940/ijrte.D1014.1284S219

Michaelides, O.; Gazetas, G.; Bouckovalas, G.; Chrysikou, E. (1998). "*Approximate non-linear dynamic axial response of piles.*" Geotechnique, 48, 33–53.

Midzi, V., Manzunzu, B., Mulabisana, T., Zulu, B. S., Pule, T., & Myendeki, S. (2020a). Probabilistic seismic hazard maps for South Africa. *Journal of African Earth Sciences*, *162*, 103689. https://doi.org/10.1016/j.jafrearsci.2019.103689

Midzi, V., Manzunzu, B., Mulabisana, T., Zulu, B. S., Pule, T., & Myendeki, S. (2020b).

Probabilistic seismic hazard maps for South Africa. *Journal of African Earth Sciences*, *162*, 103689. https://doi.org/10.1016/j.jafrearsci.2019.103689

Mirshekari, M., and Ghayoomi, M. (2017). "*Centrifuge tests to assess seismic site response of partially saturated sand layers*." Soil Dynamics and Earthquake Engineering, Elsevier Ltd, 94, 254–265.

Mog, K., & Anbazhagan, P. (2019). Dynamic Properties of Surface Liquefied Site. In D. Choudhury (Ed.), *GeoMEact 2018 SUCI* (pp. 140–154). Switzerland: Springer International Publishing. https://doi.org/10.1007/978-3-030-01920-4

Mog, K., & Anbazhagan, P. (2022). Evaluation of the damping ratio of soils in a resonant column using different methods. *Soils and Foundations*, *62*(1). https://doi.org/10.1016/j.sandf.2021.101091

Mojtahedzadeh, N., Ghalandarzadeh, A., & Motamed, R. (2022). Experimental Evaluation of Dynamic Characteristics of Firouzkooh Sand Using Cyclic Triaxial and Bender Element Tests. *International Journal of Civil Engineering*, *20*(2), 125–138. https://doi.org/10.1007/s40999-021-00644-6

Monkol, M. M., & Yamamuro, J. A. (2010). Influence of Densification Method on Some Aspects of Undrained Silty Sand Behavior. In *International Conferences on recent Advances in Geotechnical Earthquake Engineering and Soil Dynamics and Symposium in Honor of Professor I.M. Idris* (p. Paper No. 1.34b). San Diego, California.

Mousavi, S. (2020). *Dynamic Performance of Partially Saturated and Unsaturated Soils*. University of New Hampshire.

Mousavi, S., and Ghayoomi, M. (2020). "*Liquefaction Mitigation of Sands with Non-Plastic Fines via Microbial Induced Partial Saturation*." Journal of Geotechnical and Geoenvironmental Engineering, Volume 147, Issue 2. doi.org/10.1061/(ASCE)GT.1943-5606.0002444

Mpye, G. D., & Gräbe, P. J. (2021). The effect of increased axle loading on the behavior of heavily overconsolidated railway foundation materials. *Transportation Geotechnics*, *27*, 100493. https://doi.org/10.1016/j.trgeo.2020.100493

Murray, E. J., & Sivakumar, V. (2010). *Unsaturated Soils: A Fundamental Interpretation of Soil Behaviour*. USA: A John Wiley & Sons Limited Publication.

Ng, C. W. W., & Menzies, B. (2007). *Advanced Unsaturated Soil Mechanics and Engineering*. London and New York: Taylor and Francis Group.

Noguera, S. M. (2016). *Assessment and mitigation of liquefaction seismic risk : numerical modeling of their effects on SSI*. Universite paris-Saclay. https://doi.org/English. NNT: 2016SACLC023, HAL Id: tel-01327934

OCHA. (2007). Earthquake Risk in Africa : Modified Mercalli Scale.

Okur, D. V., & Ansal, A. (2007). Stiffness degradation of natural fine grained soils during cyclic loading. *Soil Dynamics and Earthquake Engineering*, *27*, 843–854.

https://doi.org/10.1016/j.soildyn.2007.01.005

Onur, M. I., Tuncan, M., & Tuncan, A. (2016). Determination of Earthquake Effects on Sandy Soils for the City of Eskisehir, Turkey. *Disaster Science and Engineering*, *2*(2), 36–39. Retrieved from http://www.disasterengineering.com/issue/34560/381819

Orang, M. J., & Motamed, R. (2021). Shake Table Tests on a Shallow Foundation on Liquefiable Soils Supported on Helical Piles. *Pacific Earthquake Engineering Research Center (PEER), Report No.*

Oztoprak, S., & Bolton, M., D. (2013). *Stiffness of sands through a laboratory test data base*. Geotechnique 63, No. 1, 54-70 [http://dx.doi.org/10.1680/geot.10.).078]

Pan, K., Yuan, Z. H., Zhao, C. F., Tong, J. H., & Yang, Z. X. (2022). Undrained shear and stiffness degradation of intact marine clay under monotonic and cyclic loading. *Engineering Geology*, *297*(August 2021), 106502. https://doi.org/10.1016/j.enggeo.2021.106502

Pinzón, L. A., Mánica, M. A., Pujades, L. G., & Alva, R. E. (2020). Dynamic soil-structure interaction analyses considering directionality effects. *Soil Dynamics and Earthquake Engineering*, *130*. https://doi.org/10.1016/j.soildyn.2019.106009

Plaxis. (2020a). *Plaxis 2D- Scientific Manual-Connect Edition V20.03*.

Plaxis. (2020b). *Plaxis 2D-Reference Manual-Connect Edition V20.02*.

Prathima, A. (2009). *Dynamic behavior of unsaturated soils*. Louisiana State University and Agricultural and Mechanical College. https://doi.org/10.1201/noe0415380416.ch74

Pan, K., Yuan, Z. H., Zhao, C. F., Tong, J. H., & Yang, Z. X. (2022). Undrained shear and stiffness degradation of intact marine clay under monotonic and cyclic loading. *Engineering Geology*, *297*(August 2021), 106502. https://doi.org/10.1016/j.enggeo.2021.106502

Park, D., & Stewart, H., E., (2001): *Suggestion of empirical equations for damping ratio of plastic and non-plastic soils based on the previous studies,* Proceedings of the 4th International conference on recent advances in geotechnical earthquake engineering and soil dynamics, Paper no. 1.21, 1-6.

Plaxis. (2020a). *Plaxis 2D- Scientific Manual-Connect Edition V20.03*.

Plaxis. (2020b). *Plaxis 2D-Reference Manual-Connect Edition V20.02*.

Prathima, A. (2009). *Dynamic behavior of unsaturated soils*. *Poromechanics III - Biot Centennial (1905-2005)*. Louisiana State University and Agricultural and Mechanical College. https://doi.org/10.1201/noe0415380416.ch74

Pyke, R., M. (1993). *Modeling of dynamic soil properties, guidelines for determining design bases ground motions*. Appendix 7.A, Electric Power Research Institute, 7.A-1–7.A-90.

Qian, X., Gray, D., H., and Woods R., D., (1993). *"Voids and granulometry - effects on shear modulus of unsaturated sands."* Journal of Geotechnical Engineering ASCE 119(2), 295-314.

Ramadan, J. I. (2007). *Settlement of Dry Cohesionless Soil Deposits Under Earthquake Induced Loading*. *Journal of Chemical Information and Modeling*. University of Southern California.

Ramirez, J. E. . (2015). *Seismic Risk Evaluation for the eThekwini Municipality Area*. University of KwaZulu-Natal.

Rohilla, S., & Sebastian, R. (2023). Resonant column and cyclic torsional shear tests on Sutlej river sand subjected to the seismicity of Himalayan and Shivalik hill ranges: A case study. *Soil Dynamics and Earthquake Engineering*, *166*(December 2022), 107766. https://doi.org/10.1016/j.soildyn.2023.107766

SANS 10160-4. (2017). *South African National Standard - Basis of structural design and actions for buildings and industrial structures. Part 4: Sesismic actions and general requirements for buidlings*. Edition 2: SABS Standards Division. Retrieved from www.sabs.co.za

Schoeman, J. J. (2018). *The Liquefaction potential of soils on the Cape Flats established by means of empirical correlation by*. Stellenbosch University.

Seed, H., B., & Idriss, I., M. (1970). *Soil Moduli and Damping Factors for Dynamic Response Analyses*, Report EERC 70-10, Earthquake Engineering Research Center, Univer- sity of California, Berkeley.

Seed H., B., Wong, R., T., Idriss, I.,M., and Tokimatsu, K. (1984). *Moduli and Damping Factors for Dynamic Analyses of Cohesionless Soils*, Report No. UCB/EERC- 84/14, Earthquake Engineering Research Center, University of California, Berkeley, California.

Seyedi-Viand, S. M., & Eseller-Bayat, E. E. (2022). *Partial Saturation as a Liquefaction Countermeasure: A Review*. *Geotechnical and Geological Engineering* (Vol. 40). Springer International Publishing. https://doi.org/10.1007/s10706-021-01926-5

Seymour, S. (2018). *Numerical Modelling of Onshore Wind Turbine Gravity Foundations Susceptible To Cyclic Soil Degradation*. University of Cape Town. Retrieved from https://open.uct.ac.za/handle/11427/29415 on 27th February, 2021.

Sharika, S., & Kumari, S. D. A. (2023). An Experimental Study on Static and Cyclic Undrained Behaviour of Gangetic Sand. *Indian Geotechnical Journal*. https://doi.org/10.1007/s40098-023-00727-2

Stamatopoulos, C. A., Balla, L. N., & Stamatopoulos, A. C. (2004). Earthquake-Induced Settlement as a Result of Densification, Measured in Laboratory Tests. In *13th World Conference on earthquake Engineering* (pp. 1–15). Vancouver, B.C., Canada. Retrieved from Paper No. 3291

Stark, T. D., MacRobert, C. J., & Hayter, S. A. (2021). Liquefied Strength Ratio for Eight Laboratory-Tested Sandy Soils. *Journal of Geotechnical and Geoenvironmental Engineering*, *147*(2), 1–9. https://doi.org/10.1061/(asce)gt.1943-5606.0002450

Stokoe, K., H., Darendeli, M., B., Andrus, R., D., and Brown, L., T. (1999). *Dynamic soil properties: laboratory, field and correlation studies.* In: Proceedings of the 2nd international conference on earthquake geotechnical engineering, Lisbon, vol 3, pp 811–845.

Sun, Q., Cai, Y., Chu, J., Dong, Q., & Wang, J. (2017). Effect of Variable Confining Pressure on Cyclic Behaviour of Granular Soil Under Triaxial Tests. *Canadian Geotechnical Journal*, *54*(6), 768–777. https://doi.org/10.1139/cgj-2016-0439.

SW-AJA. (1971). *Soil Behavior Under Earthquake Loading Conditions-Interim Report No. 1*. Oak Ridge,Tennessee. SW-AJA-Shannon & Wilson, Inc and Agbabian-Jacobsen Associates. U.S. Atomic Energy Commission, Contract No. W-7405-eng-26.

Sze, H. Y., & Yang, J. (2014). Failure Modes of Sand in Undrained Cyclic Loading: Impact of Sample Preparation. *Journal of Geotechnical and Geoenvironmental Engineering*, *140*(1), 152–169. https://doi.org/10.1061/(asce)gt.1943-5606.0000971

Tanaka, Y., Kokusho, T., Tohma, J., & Kudo, K. (1994). Settlement Evaluation of Gravel and Sand Due to Earthquake. *CIMSTF*, *XIII*, 1025–1028. https://doi.org/New Delhi, India

Taranath, B. S. (2004). *Wind and Earthquake Resistant Buildings-Structural Analysis and Design*. (M. D. Meyer, Ed.), *Wind and Earthquake Resistant Buildings*. Los Angeles, California: Marcel Dekker. https://doi.org/10.1201/9780849338090

Towhata, I. (2008). *Geotechnical Earthquake Engineering*. (W. Wu & R. I. Borja, Eds.), *Springer Series in Geomechanics and Geoengineering*. Tokyo, Japan: Scientific Publishing Services Pvt. Ltd. https://doi.org/07/ 978-3-540-35783-4

Varghese, R., Senthen, A. M., Boominathan, A., & Banerjee, S. (2019). Cyclic and postcyclic behaviour of silts and silty sands from the Indo Gangetic Plain. *Soil Dynamics and Earthquake Engineering*, *125*, 105750. https://doi.org/10.1016/j.soildyn.2019.105750

Vucetic, M., and Dobry, R. (1991). *Effect of soil plasticity on cyclic response*. J Geotech Eng ASCE 117(1):89–107.

Vucetic, M. (1992). *Soil properties and seismic response.* In: Proceedings of the 10th world conference on earthquake engineering, Rotterdam.

Vucetic, M. (1994). *Cyclic threshold shear strains in soils.* ASCE J Geotech Eng 120:2208– 2228.

Wanatowski, D., & Chu, J. (2008). Effect of Specimen Preparation Method on the Stress-Strain Behavior of Sand in Plane-Strain Compression Tests Effect of Specimen Preparation Method on the Stress-Strain Behavior of Sand in Plane-Strain Compression Tests. *ResearchGate*, (244286). https://doi.org/10.1520/GTJ101307

Whang, D. H., Stewart, J. P., & Bray, J. D. (2004). Effect of compaction conditions on the seismic compression of compacted fill soils. *Geotechnical Testing Journal*, *27*(4), 371–379. https://doi.org/Paper ID GTJ11810

Wium, J. A. (2006). *Structural engineering to meet the challenges in South Africa*. (van der M.

Mattie, Ed.). Stellenbosch University Printers.

Worku, A. (2014). The Status of Basic Design Ground Motion Provisions in Seismic Design Codes of Sub- Saharan African Countries- A Critical Review. *Journal of the South African Institution of Civil Engineering*, *56*(1), 40–53.

Xubin, S. (2007). *Influence of Sample Preparation Methods and Interlocking on Sand Behaviour : An Experimental Investigation*. McMaster University.

Yan, K., Wang, Y., Yang, Z., Lai, X., & Chen, C. (2022). Experimental Study on Small-Strain Shear Modulus of Unsaturated Silty-Fine Sand. *Applied Sciences*, *12*(8743). Retrieved from https://doi.org/10.3390/app12178743

Yang, L., Luo, J., Chen, W., & Mou, Y. (2020). Amplification of Seismic Response in Poroviscoelastic Soil Layer. *Advances in Civil Engineering*, *8824445*(Hindawi), 1–12. https://doi.org/10.1155/2020/8824445.

Ye, J., & Lu, Q. (2022). Seismic dynamics of a pipeline shallowly buried in loosely deposited seabed foundation. *Ocean Engineering*, *243*, 110194. https://doi.org/10.1016/j.oceaneng.2021.110194

Zhang, S., Gong, W., Wu, Q., Li, T., & Zhao, X. (2023). Experimental studies on dynamic and static properties of sand during repeated liquefaction events. *Acta Geotechnica*, *2*. https://doi.org/10.1007/s11440-023-01819-2

Zhao, Y., Yang, Y., Ling, X., Gong, W., Li, G., & Su, L. (2021). Dynamic behavior of natural sand soils and fiber reinforced soils in heavy-haul railway embankment under multistage cyclic loading. *Transportation Geotechnics*, *28*, 100507. https://doi.org/10.1016/j.trgeo.2020.100507

Zhu, Z., Zhang, F., Dupla, J., Canou, J., Foerster, E., Paristech, P., … Paristech, P. (2021). *Assessment of tamping-based specimen preparation methods on static liquefaction of loose silty sand*.

Zhang, J., Andrus, R., D., and Juang, C., H. (2005). *Normalized shear modulus and material damping ratio relationships.* J Geotech Geoenviron Eng 131(4):453–464 ASCE.

6 Appendices

Appendix 1-Earthquake Risk Map in Africa

OCHA Regional Office for Central and East Africa

Earthquake Risk in Africa: Modified Mercalli Scale

Issued: December 2007

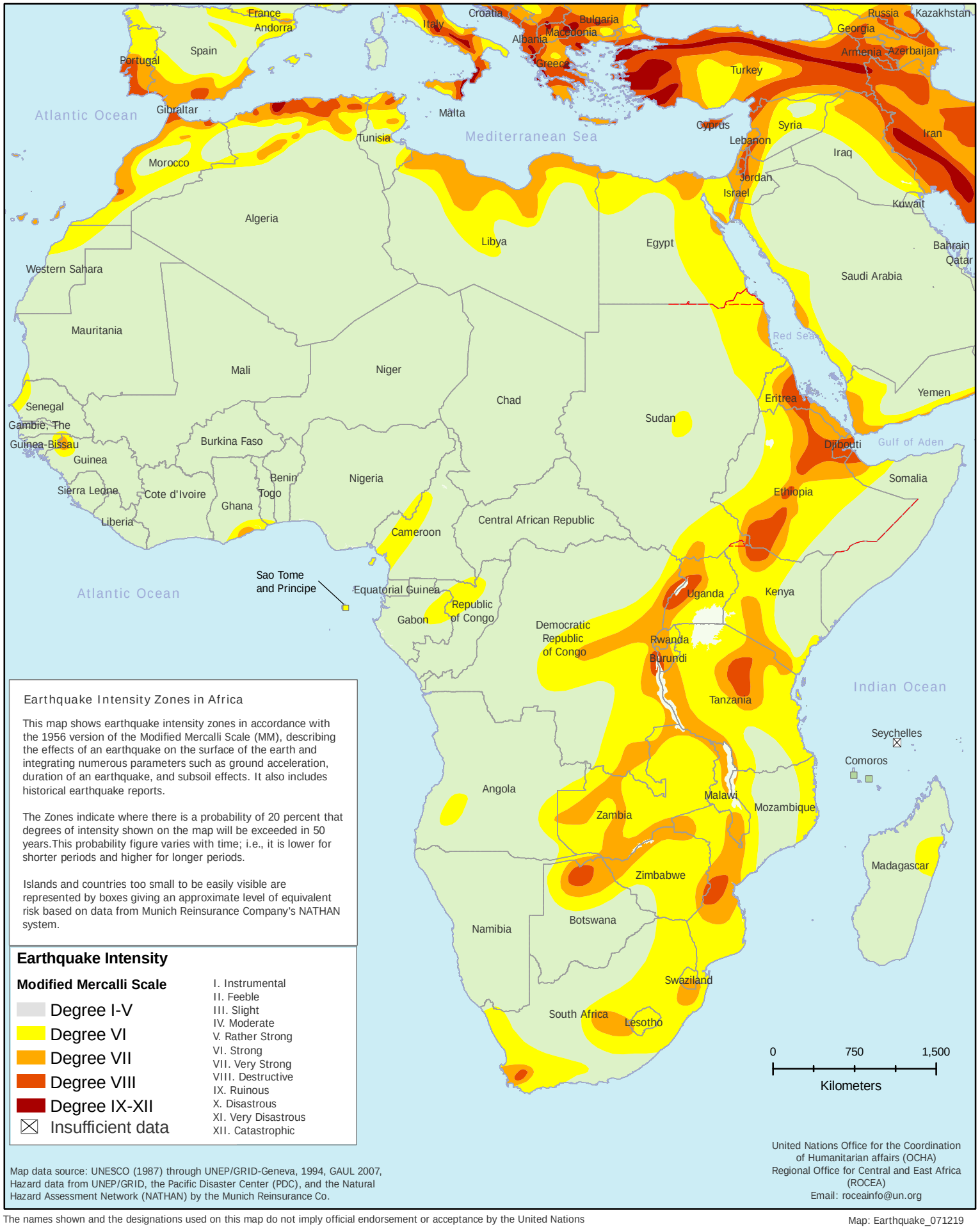

Earthquake Intensity Zones in Africa

This map shows earthquake intensity zones in accordance with the 1956 version of the Modified Mercalli Scale (MM), describing the effects of an earthquake on the surface of the earth and integrating numerous parameters such as ground acceleration, duration of an earthquake, and subsoil effects. It also includes historical earthquake reports.

The Zones indicate where there is a probability of 20 percent that degrees of intensity shown on the map will be exceeded in 50 years.This probability figure varies with time; i.e., it is lower for shorter periods and higher for longer periods.

Islands and countries too small to be easily visible are represented by boxes giving an approximate level of equivalent risk based on data from Munich Reinsurance Company's NATHAN system.

Earthquake Intensity

Modified Mercalli Scale

Degree I-V	I. Instrumental II. Feeble III. Slight IV. Moderate V. Rather Strong
Degree VI	VI. Strong
Degree VII	VII. Very Strong
Degree VIII	VIII. Destructive
Degree IX-XII	IX. Ruinous X. Disastrous XI. Very Disastrous XII. Catastrophic
Insufficient data	

Map data source: UNESCO (1987) through UNEP/GRID-Geneva, 1994, GAUL 2007, Hazard data from UNEP/GRID, the Pacific Disaster Center (PDC), and the Natural Hazard Assessment Network (NATHAN) by the Munich Reinsurance Co.

United Nations Office for the Coordination of Humanitarian affairs (OCHA)
Regional Office for Central and East Africa (ROCEA)
Email: roceainfo@un.org

Appendix 2-List of Sample Codes Used in the Cyclic Testing

Dr =25%	Dr =50%	Dr =75%
Dr-25-SAT-000-STR-0.005	Dr-50-SAT-000-STR-0.005	Dr-75-SAT-000-STR-0.005
Dr-25-SAT-000-STR-0.01	Dr-50-SAT-000-STR-0.01	Dr-75-SAT-000-STR-0.01
Dr-25-SAT-000-STR-0.02	Dr-50-SAT-000-STR-0.02	Dr-75-SAT-000-STR-0.02
Dr-25-SAT-000-STR-0.05	Dr-50-SAT-000-STR-0.05	Dr-75-SAT-000-STR-0.05
Dr-25-SAT-000-STR-0.1	Dr-50-SAT-000-STR-0.1	Dr-75-SAT-000-STR-0.1
Dr-25-SAT-000-STR-0.2	Dr-50-SAT-000-STR-0.2	Dr-75-SAT-000-STR-0.2
Dr-25-SAT-000-STR-0.4	Dr-50-SAT-000-STR-0.4	Dr-75-SAT-000-STR-0.4
Dr-25-SAT-000-STR-0.6	Dr-50-SAT-000-STR-0.6	Dr-75-SAT-000-STR-0.6
Dr-25-SAT-000-STR-0.8	Dr-50-SAT-000-STR-0.8	Dr-75-SAT-000-STR-0.8
Dr-25-SAT-000-STR-1.0	Dr-50-SAT-000-STR-1.0	Dr-75-SAT-000-STR-1.0
Dr-25-SAT-025-STR-0.005	Dr-50-SAT-025-STR-0.005	Dr-75-SAT-025-STR-0.005
Dr-25-SAT-025-STR-0.01	Dr-50-SAT-025-STR-0.01	Dr-75-SAT-025-STR-0.01
Dr-25-SAT-025-STR-0.02	Dr-50-SAT-025-STR-0.02	Dr-75-SAT-025-STR-0.02
Dr-25-SAT-025-STR-0.05	Dr-50-SAT-025-STR-0.05	Dr-75-SAT-025-STR-0.05
Dr-25-SAT-025-STR-0.1	Dr-50-SAT-025-STR-0.1	Dr-75-SAT-025-STR-0.1
Dr-25-SAT-025-STR-0.2	Dr-50-SAT-025-STR-0.2	Dr-75-SAT-025-STR-0.2
Dr-25-SAT-025-STR-0.4	Dr-50-SAT-025-STR-0.4	Dr-75-SAT-025-STR-0.4
Dr-25-SAT-025-STR-0.6	Dr-50-SAT-025-STR-0.6	Dr-75-SAT-025-STR-0.6
Dr-25-SAT-025-STR-0.8	Dr-50-SAT-025-STR-0.8	Dr-75-SAT-025-STR-0.8
Dr-25-SAT-025-STR-1.0	Dr-50-SAT-025-STR-1.0	Dr-75-SAT-025-STR-1.0
Dr-25-SAT-050-STR-0.005	Dr-50-SAT-050-STR-0.005	Dr-75-SAT-050-STR-0.005
Dr-25-SAT-050-STR-0.01	Dr-50-SAT-050-STR-0.01	Dr-75-SAT-050-STR-0.01
Dr-25-SAT-050-STR-0.02	Dr-50-SAT-050-STR-0.02	Dr-75-SAT-050-STR-0.02
Dr-25-SAT-050-STR-0.05	Dr-50-SAT-050-STR-0.05	Dr-75-SAT-050-STR-0.05
Dr-25-SAT-050-STR-0.1	Dr-50-SAT-050-STR-0.1	Dr-75-SAT-050-STR-0.1
Dr-25-SAT-050-STR-0.2	Dr-50-SAT-050-STR-0.2	Dr-75-SAT-050-STR-0.2
Dr-25-SAT-050-STR-0.4	Dr-50-SAT-050-STR-0.4	Dr-75-SAT-050-STR-0.4
Dr-25-SAT-050-STR-0.6	Dr-50-SAT-050-STR-0.6	Dr-75-SAT-050-STR-0.6
Dr-25-SAT-050-STR-0.8	Dr-50-SAT-050-STR-0.8	Dr-75-SAT-050-STR-0.8
Dr-25-SAT-050-STR-1.0	Dr-50-SAT-050-STR-1.0	Dr-75-SAT-050-STR-1.0
Dr-25-SAT-075-STR-0.005	Dr-50-SAT-075-STR-0.005	Dr-75-SAT-075-STR-0.005
Dr-25-SAT-075-STR-0.01	Dr-50-SAT-075-STR-0.01	Dr-75-SAT-075-STR-0.01
Dr-25-SAT-075-STR-0.02	Dr-50-SAT-075-STR-0.02	Dr-75-SAT-075-STR-0.02
Dr-25-SAT-075-STR-0.05	Dr-50-SAT-075-STR-0.05	Dr-75-SAT-075-STR-0.05
Dr-25-SAT-075-STR-0.1	Dr-50-SAT-075-STR-0.1	Dr-75-SAT-075-STR-0.1
Dr-25-SAT-075-STR-0.2	Dr-50-SAT-075-STR-0.2	Dr-75-SAT-075-STR-0.2
Dr-25-SAT-075-STR-0.4	Dr-50-SAT-075-STR-0.4	Dr-75-SAT-075-STR-0.4
Dr-25-SAT-075-STR-0.6	Dr-50-SAT-075-STR-0.6	Dr-75-SAT-075-STR-0.6
Dr-25-SAT-075-STR-0.8	Dr-50-SAT-075-STR-0.8	Dr-75-SAT-075-STR-0.8
Dr-25-SAT-075-STR-1.0	Dr-50-SAT-075-STR-1.0	Dr-75-SAT-075-STR-1.0
Dr-25-SAT-100-STR-0.005	Dr-50-SAT-100-STR-0.005	Dr-75-SAT-100-STR-0.005
Dr-25-SAT-100-STR-0.01	Dr-50-SAT-100-STR-0.01	Dr-75-SAT-100-STR-0.01
Dr-25-SAT-100-STR-0.02	Dr-50-SAT-100-STR-0.02	Dr-75-SAT-100-STR-0.02
Dr-25-SAT-100-STR-0.05	Dr-50-SAT-100-STR-0.05	Dr-75-SAT-100-STR-0.05
Dr-25-SAT-100-STR-0.1	Dr-50-SAT-100-STR-0.1	Dr-75-SAT-100-STR-0.1
Dr-25-SAT-100-STR-0.2	Dr-50-SAT-100-STR-0.2	Dr-75-SAT-100-STR-0.2
Dr-25-SAT-100-STR-0.4	Dr-50-SAT-100-STR-0.4	Dr-75-SAT-100-STR-0.4
Dr-25-SAT-100-STR-0.6	Dr-50-SAT-100-STR-0.6	Dr-75-SAT-100-STR-0.6
Dr-25-SAT-100-STR-0.8	Dr-50-SAT-100-STR-0.8	Dr-75-SAT-100-STR-0.8
Dr-25-SAT-100-STR-1.0	Dr-50-SAT-100-STR-1.0	Dr-75-SAT-100-STR-1.0

Code	Dr-XX-SAT-XXX-STR-XXX

Appendix 3-Sample Test Data from Cyclic Test

Dr-75-SAT-000-STR-0.6

Initialization

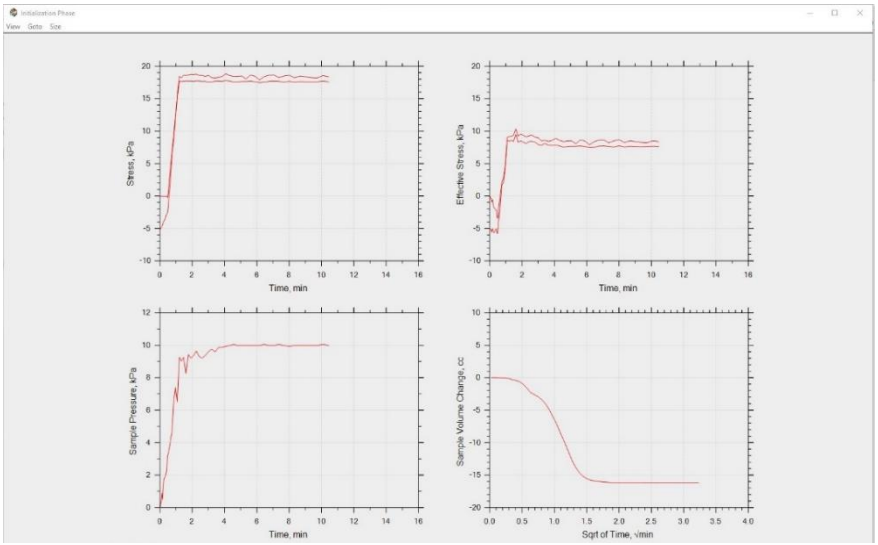

Saturation

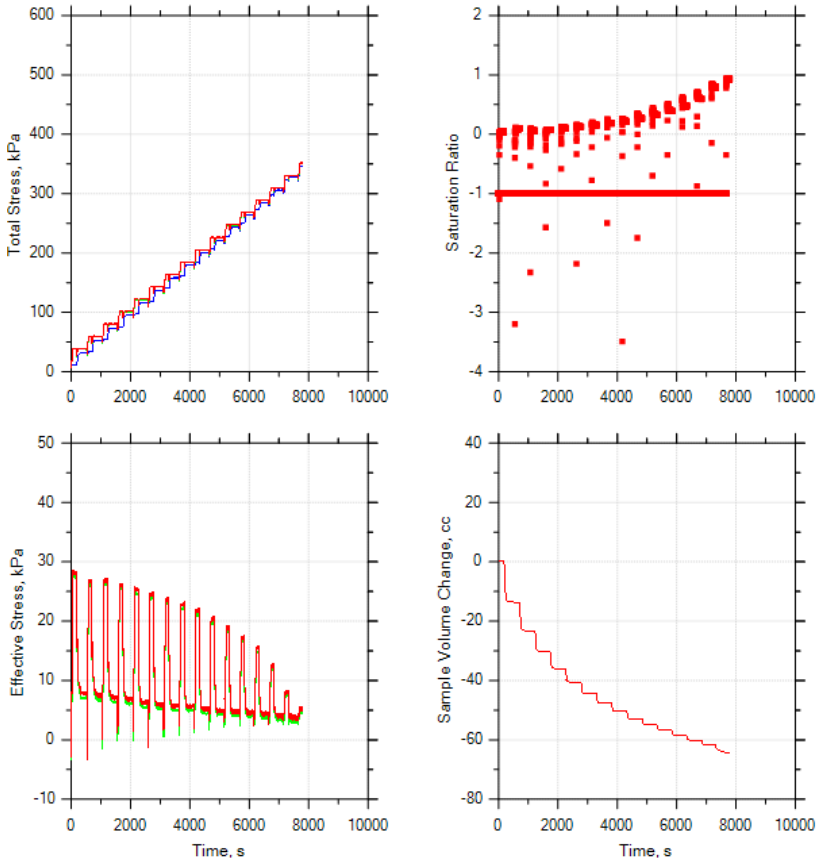

Consolidation

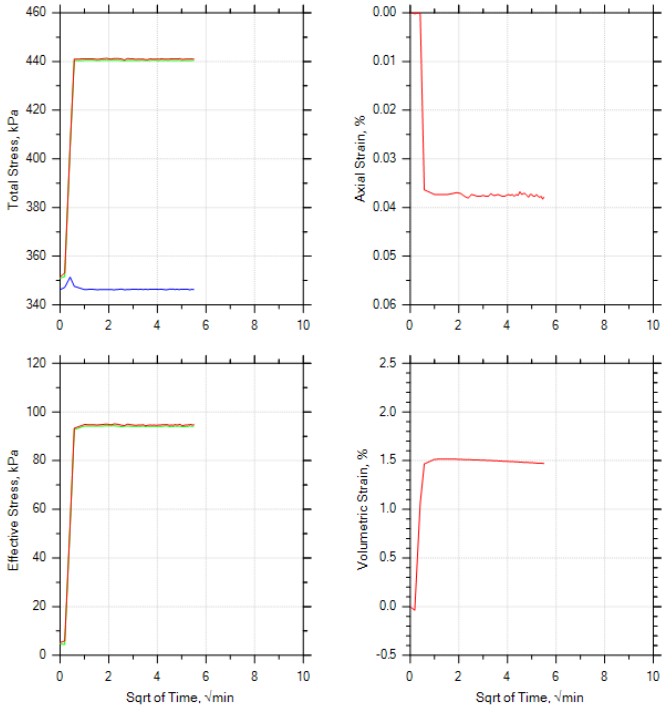

Cyclic

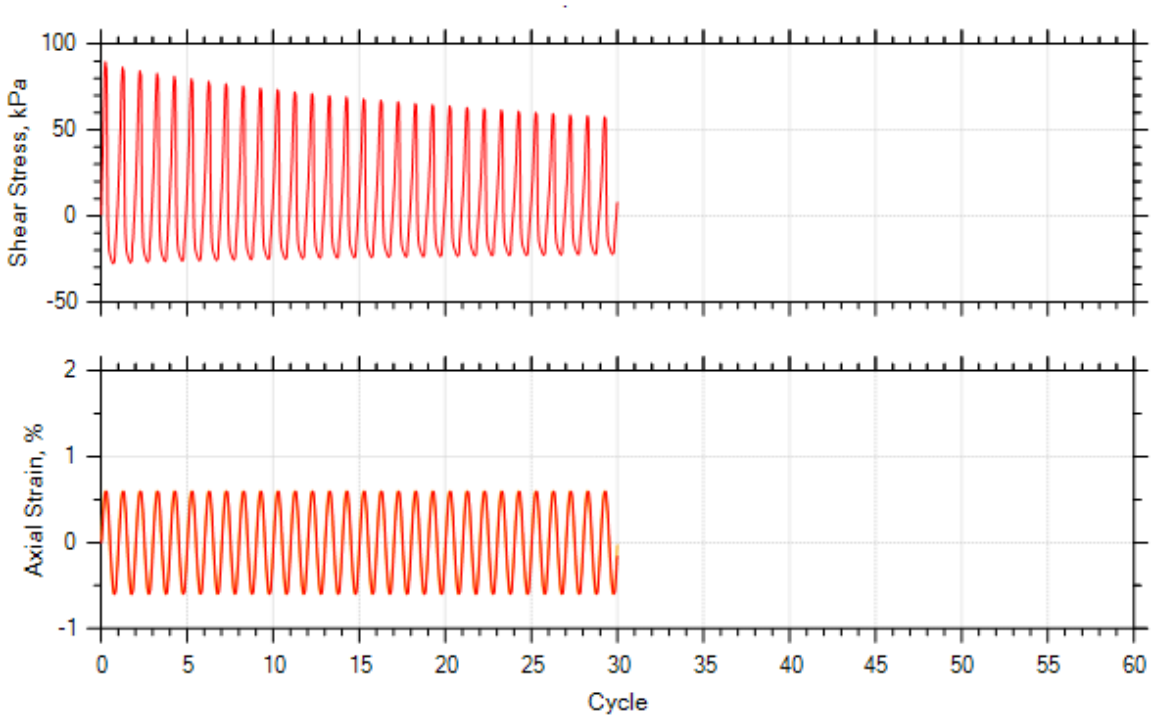

Appendix 4-Summary of the Cyclic Data at 10 Cycles

Relative Density (%)	Saturation Content (%)	Shear Modulus (kPa) at Given Cyclic Axial Strain for 10 Cycles									
		0.005	0.01	0.02	0.05	0.1	0.2	0.4	0.6	0.8	1
Dr-25	SAT-000	66397	61307	52616	35787	19349	15898	10974	8247	6408	5770
	SAT-025	62544	61954	55408	44999	29145	20498	12571	5677	6886	6005
	SAT-050	60592	54900	43647	26927	14713	10761	9434	8018	5832	5745
	SAT-075	57261	50314	40095	23608	12891	8701	7571	5455	4683	4673
	SAT-100	53246	46595	34241	20936	12151	7720	9245	6321	3930	3223
Dr-50	SAT-000	89424	82292	73015	46953	26862	20529	12146	8596	7821	6251
	SAT-025	98525	85786	74991	52178	35350	23830	19651	11520	9600	6889
	SAT-050	90061	80377	54194	38839	21646	15371	12867	10348	8370	5081
	SAT-075	79756	69297	51720	30382	14436	15532	9808	9215	7263	5116
	SAT-100	71988	60572	43736	26775	12111	10907	9063	7718	4498	4925
Dr-75	SAT-000	108080	94957	78010	45994	34296	23861	12004	10151	7497	5114
	SAT-025	110260	100640	86684	60721	38526	29453	16192	12423	10469	8375
	SAT-050	97613	81986	61654	41805	19012	9268	6490	5889	5780	5573
	SAT-075	92110	74967	54511	25286	14380	8355	5426	4277	4221	4083
	SAT-100	76547	73528	48470	25668	13490	8656	6544	4359	3946	3636
		Damping Ratio (%) at Given Cyclic Axial Strain for 10 Cycles									
Dr-25	SAT-000	5.18	8.22	11.51	15.56	17.55	18.61	19.45	19.95	20.37	19.70
	SAT-025	5.93	8.34	13.06	14.68	18.24	19.47	19.48	19.69	20.44	19.95
	SAT-050	6.71	8.58	13.77	17.42	18.97	20.17	20.69	22.15	21.90	21.16
	SAT-075	6.55	9.41	14.53	18.33	20.31	21.61	22.42	23.53	23.74	22.79
	SAT-100	7.12	10.61	15.98	18.60	21.88	23.68	23.41	23.84	24.34	23.47
Dr-50	SAT-000	4.91	7.98	10.09	14.67	15.15	17.03	17.17	18.56	18.35	18.67
	SAT-025	5.10	8.37	11.33	15.90	16.93	18.88	18.84	18.92	19.49	18.89
	SAT-050	5.53	8.73	11.75	15.36	18.09	18.11	19.63	21.55	21.31	20.77
	SAT-075	5.89	8.87	13.05	17.21	17.85	20.81	20.93	21.13	21.79	20.77
	SAT-100	5.99	11.28	17.65	17.63	20.21	23.06	22.74	22.91	23.27	22.81
Dr-75	SAT-000	4.61	7.07	8.89	12.54	15.26	14.85	16.23	16.69	17.04	16.57
	SAT-025	5.24	8.19	9.90	14.66	15.53	16.22	17.73	17.52	18.82	18.48
	SAT-050	4.72	7.98	10.11	13.82	13.91	17.93	18.07	19.01	19.67	18.18
	SAT-075	4.89	8.09	11.35	13.51	17.12	18.86	19.55	20.67	19.72	19.12
	SAT-100	5.62	8.64	11.43	14.29	17.96	18.51	19.83	19.94	20.90	20.57
		Pore Water Pressure Ratio (R_u) at Given Cyclic Axial Strain for 10 Cycles									
Dr-25	SAT-000	0.001	0.000	0.004	0.050	0.102	0.104	0.123	0.134	0.148	0.239
	SAT-025	-0.003	-0.004	0.008	0.081	0.129	0.131	0.212	0.272	0.275	0.566
	SAT-050	0.005	0.011	0.038	0.108	0.164	0.234	0.215	0.298	0.298	0.617
	SAT-075	0.000	0.008	0.038	0.125	0.182	0.155	0.223	0.331	0.415	0.459
	SAT-100	0.004	0.010	0.039	0.163	0.215	0.257	0.243	0.369	0.533	0.665
Dr-50	SAT-000	-0.002	0.001	0.006	0.051	0.114	0.106	0.162	0.152	0.205	0.247
	SAT-025	-0.002	0.000	0.010	0.096	0.166	0.196	0.191	0.246	0.321	0.380
	SAT-050	0.008	0.008	0.026	0.098	0.207	0.228	0.218	0.323	0.315	0.453
	SAT-075	0.007	0.012	0.029	0.150	0.246	0.290	0.432	0.410	0.538	0.640
	SAT-100	-0.003	0.002	0.025	0.134	0.262	0.343	0.341	0.591	0.653	0.864
Dr-75	SAT-000	0.000	0.000	0.006	0.073	0.137	0.170	0.177	0.203	0.240	0.275
	SAT-025	0.003	0.002	0.007	0.115	0.165	0.212	0.238	0.278	0.319	0.361
	SAT-050	0.000	0.004	0.011	0.134	0.236	0.271	0.369	0.342	0.360	0.462
	SAT-075	-0.003	0.000	0.018	0.118	0.283	0.370	0.462	0.540	0.535	0.597
	SAT-100	0.020	0.027	0.043	0.138	0.332	0.377	0.493	0.501	0.759	0.908

Appendix 5-Quality Control

QUALITY CONTROL CHART

Quality Control Parameter: Mass and Back Pressure of Sample Dr-025-SAT-000
Monitoring Solution: Weighing Scale and Sample Flow Trac
Unit: grams and kPa

Corrective Actions:

1 Value Beyond +/- 3s Level
2 Consecutive Values Beyond +/- 2s Level on the Same Side of the Average
11 Consecutive Values on the Same Side of the Average

Triaxial Masses

Average: 323.52
Warning Limit (2s) 0.103
Alarm Limit (3s) 0.154

	1	2	3	4	5	6	7	8	9	10
Actual Measurement	323.590	323.475	323.576	323.595	323.481	323.480	323.506	323.570	323.478	323.492
Cyclic Strain No. (%)	0.005	0.010	0.020	0.050	0.100	0.200	0.400	0.600	0.800	1.000
Remarks	The Mass is Within 2S									

Back Pressure Readings After Saturation Stage

Average: 346.0
Warning Limit (2s) 20.2
Alarm Limit (3s) 30.2

	1	2	3	4	5	6	7	8	9	10
Actual Measurement	341.4	353.3	342.4	343.6	326.3	341.5	351.7	358.1	360.5	341.3
Cyclic Strain No. (%)	0.005	0.010	0.020	0.050	0.100	0.200	0.400	0.600	0.800	1.000
Remarks	The Back Pressure is Within 2S									

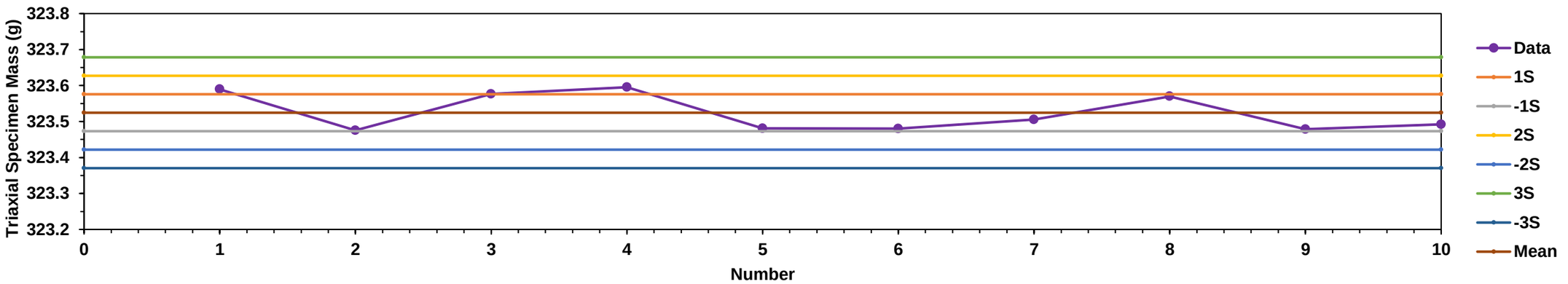

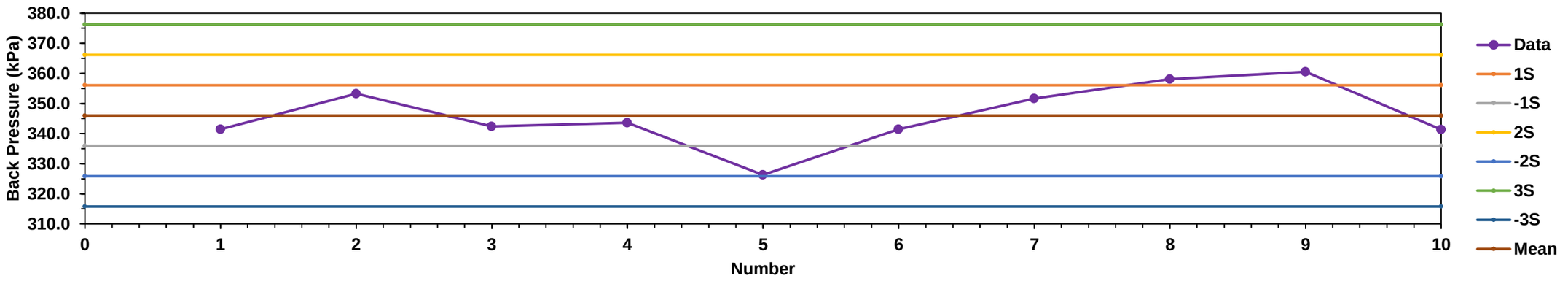

Appendix 6-Characterisation Tests on Cape Flat Sands

PARTICLE SIZE DISTRIBUTION (ASTM D6913/6913M-17)

Oven dry mass	g	1203.6	**Cape Flat Sand Sample 01**
Mass afterwashing	g	1196.6	

	Mass Retained (g)	% Retained	Cumm. % Retained	% Passing
6.7	0	0.00	0.00	100.00
4.75	0	0.00	0.00	100.00
2	0.3	0.02	0.02	99.98
1.18	12.2	1.01	1.04	98.96
0.6	239.8	19.92	20.96	79.04
0.425	318.5	26.46	47.42	52.58
0.3	345.9	28.74	76.16	23.84
0.212	158.9	13.20	89.37	10.63
0.15	93.5	7.77	97.13	2.87
0.063	26.8	2.23	99.36	0.64
Pan	0.7			

Oven dry mass	g	1103.9	**Cape Flat Sand Sample 02**
Mass afterwashing	g	1095.6	

	Mass Retained (g)	% Retained	Cumm. % Retained	% Passing
6.7	0	0.00	0.00	100.00
4.75	0	0.00	0.00	100.00
2	0.1	0.01	0.01	99.99
1.18	10.2	0.92	0.93	99.07
0.6	243.6	22.07	23.00	77.00
0.425	214.9	19.47	42.47	57.53
0.3	343.56	31.12	73.59	26.41
0.212	142.04	12.87	86.46	13.54
0.15	108.6	9.84	96.29	3.71
0.063	32.1	2.91	99.20	0.80
Pan	0.5			

Summary of Geometric Properties

	Sample 01	Sample 02	Average
D_{10}	0.2	0.2	0.200
D_{30}	0.34	0.31	0.325
D_{50}	0.405	0.395	0.400
D_{60}	0.48	0.44	0.460
D_{90}	0.85	0.85	0.850
		C_u	2.300
		C_c	1.148

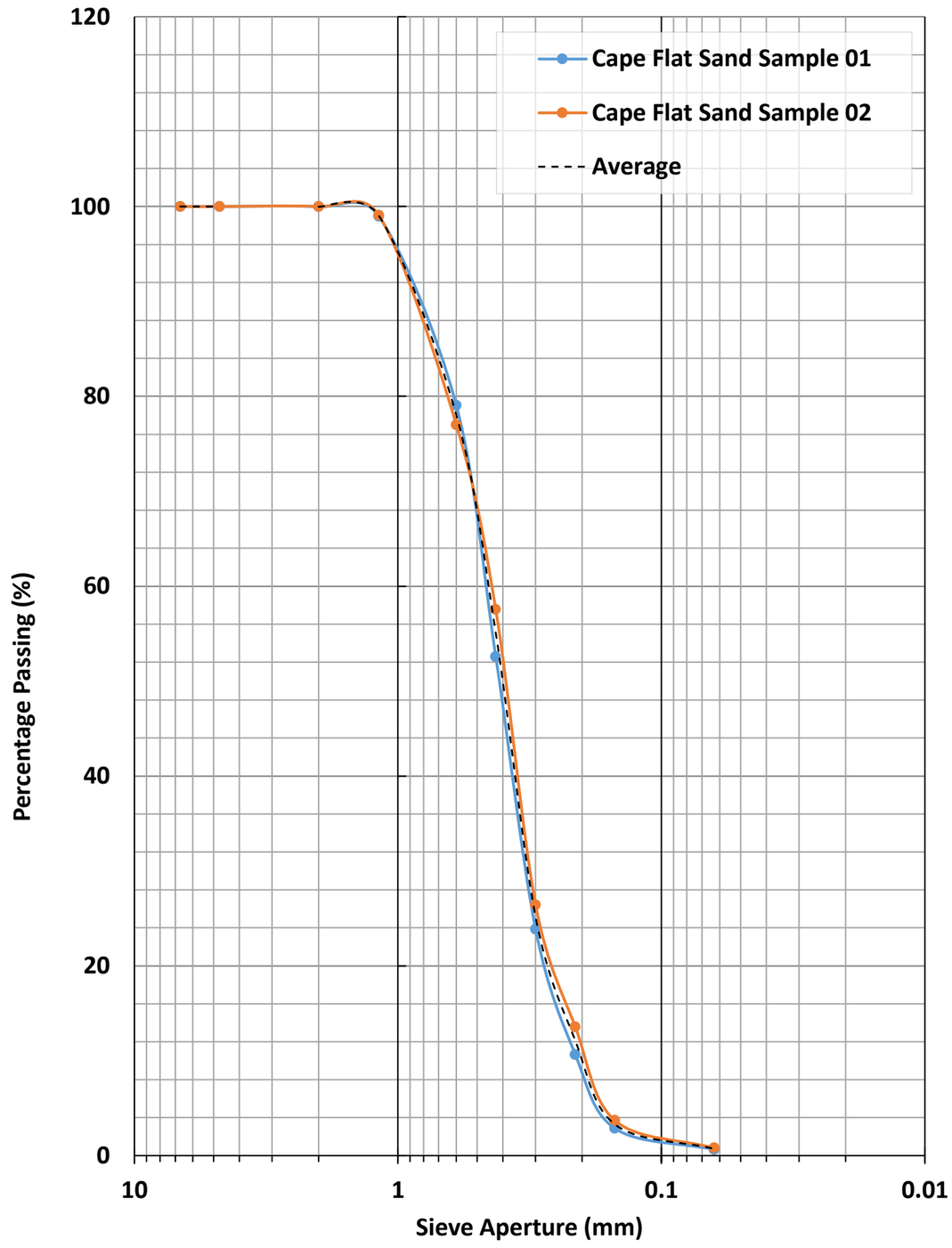

ATTERBERG'S LIMITS (ASTM D4318 - 17e1)

Test Sample: Cape Flat Sands

	LIQUID LIMIT (LL)								PLASTIC LIMIT (PL)	
TEST RUN	**1**		**2**		**3**		**4**		**1**	**2**
Initial Number of Bumps	0		0		0		0			
Final Number of Bumps	12		22		30		35			
Container No.	**A1**	**A2**	**A3**	**A4**	**A5**	**A6**	**A7**	**A8**		
Mass of wet soil + container (g)	18.049	16.142	22.487	22.979	19.955	19.611	22.553	20.721		
Mass of dry soil + container (g)	16.957	15.274	20.244	20.666	18.105	17.825	19.989	18.125		
Mass of container (g)	8.107	8.169	8.122	8.052	9.748	9.707	9.668	8.068		
Mass of moisture (g)	1.09	0.87	2.24	2.31	1.85	1.79	2.56	2.60		
Mass of dry soil (g)	8.85	7.11	12.12	12.61	8.36	8.12	10.32	10.06		
Moisture content (g)	12.34	12.22	18.50	18.34	22.14	22.00	24.84	25.81		
Mean Moisture content (%)	12.3		18.4		22.1		25.3		**Non Plastic (NP)**	

Non Plastic | **Non Plastic**

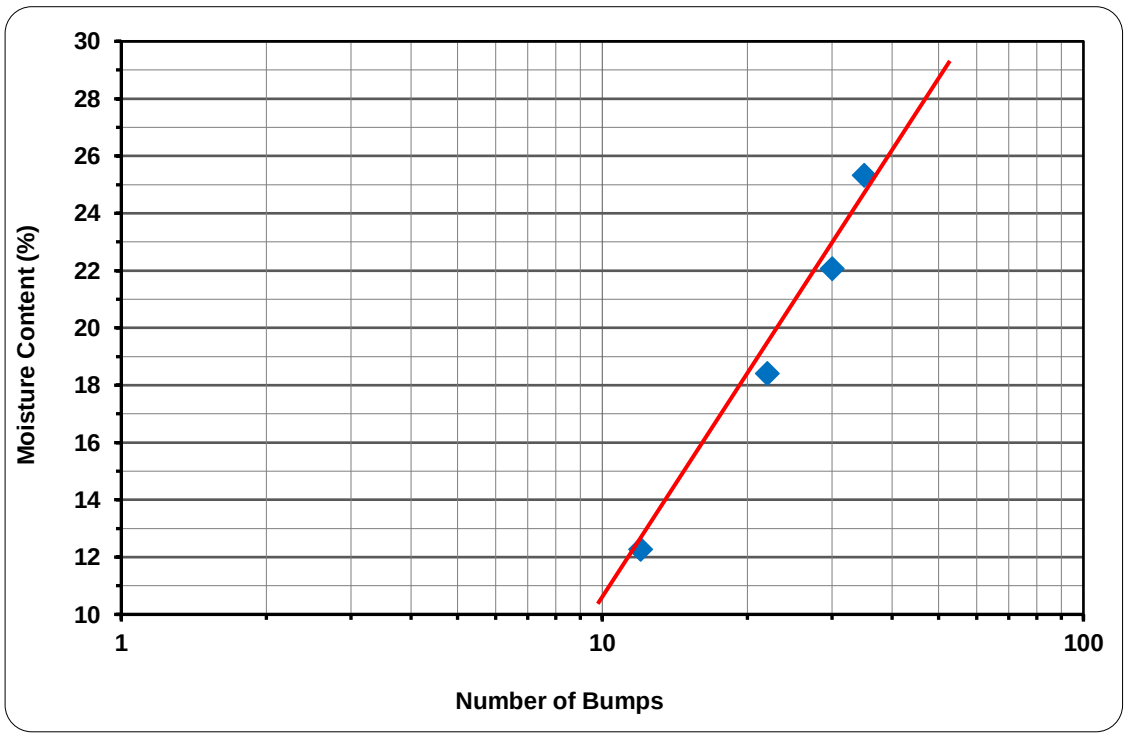

Linear Shrinkage Limit	
Average Initial length (mm)	13.95
Average Oven-dried length (mm)	13.82
Linear shrinkage (%)	0.94

Liquid limit (LL), %	20.3
Plastic Limit (PL), %	NP
Plastic Index (PI), %	NP
Linear shrinkage (%)	0.94

SPECIFIC GRAVITY (ASTM D854-14)

Test Sample: Cape Flat Sands

		1	2	3
Mass of pyconometer (M_p)	g	61.900	39.915	32.830
Mass of pyconometer + sample ($M_{ps,20}$)	g	121.820	99.981	92.817
Mass of pyconometer + sample + water ($M_{pws,20}$)	g	358.846	335.703	330.738
Mass of pyconometer + water ($M_{pw,20}$)	g	321.570	298.310	293.450
Specific Gravity, $G_{s,20}$		2.6462	2.6492	2.6427
Average Specific Gravity, $G_{s,t}$		**2.6460**		
Average Specific Gravity, $G_{s,20}$; with temperature coefficient correction		**2.6460**		

Test Temperature (^{0}C)	20
Temperature coefficient of water, K	1.0000

MINIMUM INDEX DENSITY (ASTM D4254-16)

Loose Density		1	2	3	4
Mass of Mould	kg	5.790	5.790	5.790	5.790
Mass of Mould + Sand	kg	8.839	8.824	8.857	8.838
Mass of Sand	kg	3.049	3.034	3.067	3.048
Loose Density	**kg/m^3**	**1577.3**	**1569.5**	**1586.6**	**1576.7**
Average Loose Density	**kg/m^3**	**1577.54**			

Volume (m^3)	0.001933

e_{min}	0.391

MAXIMUM INDEX DENSITY (ASTM D4253 - 16e1)

		1	2	3	4
Mass of Mould	kg	5.79	5.79	5.79	5.79
Mass of Mould + Sand	kg	10.07	10.055	10.095	10.08
Mass of Sand	kg	3.672	3.679	3.66	3.697
Max. Density	**kg/m^3**	**1899.6**	**1903.2**	**1893.4**	**1912.5**
Average Max Density	**kg/m^3**	**1902.19**			

e_{min}		0.391
e_{max}		0.677
Average Loose Density	**kg/m^3**	1577.54
Average Max Density	**kg/m^3**	1902.19

Appendix 7A-Soil Profile

KANTEY & Ttempler
CONSULTING ENGINEERS
Engineering African Development

CITY OF CAPE TOWN
R300 BRIDGE

HOLE No: BH3
Sheet 1 of 2

JOB NUMBER: 15642GG

Scale 1:50

DRILLING METHOD	CORE REC.	RQD %	FRACT. PER m	TEST OR SAMPLE	VALUE		
	WASH SAMPLE					0.00	Light yellowish brown loose to medium dense very slightly silty fine to medium SAND; REWORKED TRANSPORTED.
	78			SPT	14	1	
	WASH SAMPLE						
	73			SPT	17	2	
	WASH SAMPLE					03/08/2018 ▼	
	87			SPT	6	3	
	WASH SAMPLE					3.00	Grey occasionally speckled black to light greyish brown loose variably silty fine to medium SAND; REWORKED TRANSPORTED.
	89			SPT	22	4	
	WASH SAMPLE					4.00	Brown to light yellowish brown medium dense very slightly silty fine to medium SAND; TRANSPORTED.
	69			SPT	20	5	
	WASH SAMPLE					5.45	Light grey to brownish grey medium dense variably very slightly silty fine to medium SAND; TRANSPORTED.
WASH BORE & CORE	76			SPT	28	6	
	WASH SAMPLE						
	82			SPT	22	7	
	WASH SAMPLE						
	89			SPT	57	8	
	WASH SAMPLE					8.00	Grey to light brownish grey very dense variably very slightly silty fine to medium SAND; TRANSPORTED.
	76	N/A	N/A	SPT	67	9	
	WASH SAMPLE						
	64			SPT	67	10	
	WASH SAMPLE						
	70			SPT	R	11	

KANTEY & TEMPLER
CONSULTING ENGINEERS
Engineering African Development

CITY OF CAPE TOWN
R300 BRIDGE

HOLE No: BH3
Sheet 2 of 2

JOB NUMBER: 15642GG

DRILLING METHOD	CORE REC.	RQD %	FRACT. PER m	TEST OR SAMPLE	VALUE		
	WASH SAMPLE					12	
	70			SPT	R		
	WASH SAMPLE					13	
	76			SPT	55		
	WASH SAMPLE					14	
	27			SPT	46		
	WASH SAMPLE					15	
	73			SPT	32		
NDW4	67					16	
	100			SHELBY			
	67			SPT	48		
	57					17	
	82			SPT	46		
	37					18	
	89			SPT	52		

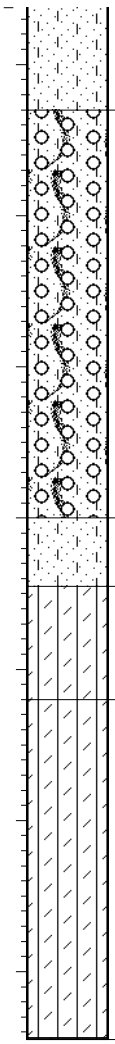

12.30 — Grey to light brownish grey very dense variably very slightly silty medium to coarse SAND containing occasional pockets of subangular fine quartz gravel; TRANSPORTED.

15.00 — Dark grey dense slightly silty fine SAND; TRANSPORTED.

15.45 — Light grey very stiff slightly clayey to clayey SILT; RESIDUAL MALMESBURY.

16.20 — Light grey very stiff slightly clayey to clayey SILT tending to completely to highly weathered very soft rock, occasionally slickensided; RESIDUAL MALMESBURY.

18.45

NOTES

1) Groundwater table measured at 2.45m depth on 03/08/2018.

CONTRACTOR : FAIRBROTHER
MACHINE : LH250
DRILLED BY : NEVILLE
PROFILED BY : DLR

TYPE SET BY : CHANTEL
SETUP FILE : K&T-BO~2.SET

INCLINATION : VERTICAL
DIAM :
DATE :
DATE : 30-07-2018

DATE : 03/09/2018 10:19
TEXT : ..LES\DATA\B156423R300.txt

ELEVATION : N/A
X-COORD : 3757103.285
Y-COORD : 31387.954

HOLE No: BH3
Reinstrumentation

Appendix 7B-SPT Analysis

Level of Water Table (m)		2.45			
Depth (m)	**Actual SPT (N)**	**7C.1-Correlations for BH03 Based on Burt (2007)**			
		Consistency	**N_{cor}**	**D_r**	**Ø**
1	14	medium dense	12	41	31
2	17	medium dense	15	46	33
3	6	loose	6	22	29
4	22	medium dense	21	53	35
5	20	medium dense	18	50	34
6	28	dense	26	62	38
7	22	medium dense	20	53	35
8	57	very dense	51	>85	45
9	67	very dense	58	>85	45
10	67	very dense	56	>85	45
11	60	very dense	49	>85	45
12	60	very dense	48	>85	45
13	55	dense	33	>85	41
14	46	dense	27	81	38
15	32	medium dense	21	67	35
16	48	dense	34	83	41
17	46	dense	32	81	41
18	52	dense	36	>85	41
19					
		loose		Dense & V. Dense	
		M. Dense		Rock (Residual Malmesbury)	

7C.2-Equivalent/Transformed Cross Section for Seismic Geotechnical Analysis and Average Parameters

Depth (m)	**N**	**Consistency**	**Mean N_{cor}**	**Mean D_r**	**Mean Ø**
1	14	medium dense	14	43	31
2	17	medium dense			
3	6	loose	6	22	28
4	22	medium dense	21	55	36
5	20	medium dense			
6	28	dense			
7	22	medium dense			
8	57	very dense	43	>85	41
9	67	very dense			
10	67	very dense			
11	60	very dense			
12	60	very dense			
13	55	dense			
14	46	dense			
15	32	medium dense			
16	48	dense	Rock (Residual Malmesbury)		
17	46	dense			
18	52	dense			
19					

Appendix 7C-Input Parameters for Plaxis 2D Software

7C.1-Soil Material Properties

Parameter	Unit	Medium Dense	Loose Dense	Loose Dense	Medium Dense	Dense-Very Dense		Source of Data
		Dry	Partially Saturated	Saturated	Saturated	Saturated		
		0.00-2.00	2.00-2.45	2.45-3.00	3.00-7.00	7.00-15.00		
		DR050-SAT-000	DR025-SAT-075	DR025-SAT-100	DR050-SAT-100	DR075-SAT-100		
General								-
Material model	-	HS small						-
Type of material behaviour	-	Drained						-
Soil unit weight above phreatic level, ρ_{unsat}	Mg/m^3	1.725	1.931	1.931	1.725	1.725		Research Results
Soil unit weight below phreatic level,ρ_{sat}	Mg/m^3	2.073	2.025	2.025	2.073	2.125		
Soil unit weight above phreatic level, γ_{unsat}	kN/m^3	16.92	18.94	18.94	16.92	16.92		
Soil unit weight below phreatic level, γ_{sat}	kN/m^3	20.34	19.87	19.87	20.34	20.85		
Initial void ratio, $e_{initial}$	-	0.534	0.606	0.606	0.534	0.463		
Parameters								
Secant stiffness in standard drained triaxial test, E_{50}^{ref}	kN/m^2	25,800	13,200	13,200	33,000	51,000		Brinkgreve, Engin, & Engin (2010)
Tangent stiffness for primary oedometer loading, E_{oed}^{ref}	kN/m^2	25,800	13,200	13,200	33,000	51,000		
Unloading / reloading stiffness, E_{ur}^{ref}	kN/m^2	77,400	39,600	39,600	99,000	153,000		
Power for stress-level dependency of stiffness, m	-	0.5	0.5	0.5	0.5	0.5		Plaxis (2020)
Cohesion, c'_{ref}	kN/m^2	0	0	0	0	0		Burt, (2007)
Friction angle, φ'	^{0}	29	28	28	36	41		
Dilatancy angle, ψ	^{0}	0	0	0	0	0		
Shear modulus at very small strains, G_0^{ref}	kN/m^2	106,127	75,173	75,173	106,127	130,447		Research Results
Shear strain at which $G_s = 0.722\ G_0$, $\gamma_{0.7}$	-	1.50E-04	1.75E-04	1.75E-04	1.50E-04	1.25E-04		
Poisson's ratio, ν'_{ur}	-	0.285	0.320	0.400	0.400	0.400		Kumar & Madhusudhan (2012)
Tangent shear modulus, G_{ur}	kN/m^2	30,117	15,000	14,143	35,357	54,643		Brinkgreve, Engin, & Engin (2010)
G_0^{ref}/G_{ur}	-	3.524	5.012	5.315	3.002	2.387		Calculated

7C.2-Material Properties of the Building (Plate properties) and node-to-node anchor

Parameter	Unit	Basement	Superstructure	Source of Data
Plate Properties		-	-	
Material type	-	Elastic; Isotropic	Elastic; Isotropic	Plaxis (2020)
Normal stiffness, (kN/m)	EA	9.00E+06	1.20E+07	
Flexural rigidity, (kNm^2/m)	EI	6.75E+04	1.60E+05	
Weight, (kN/m/m)	w	10	20	
Poisson's ratio,	v	0	0	
Rayleigh damping,	α	0.232	0.232	
	β	8.00E-03	8.00E-03	
Node-node-anchor		Column		
Material type	-	Elastic		
Normal stiffness, (kN)	-	2.50E+06		
Spacing out-of-plane, $L_{spacing}$	-	3		Structure design

7C.3-Equations for Correlations by Brinkgreve, Engin, & Engin (2010)

$E_{50}^{ref} = 60000 D_r/100\ (kN/m^2)$ $E_{oed}^{ref} = 60000 D_r/100\ (kN/m^2)$ $E_{ur}^{ref} = 180000 D_r/100\ (kN/m^2)$	Brinkgreve, Engin, & Engin (2010)

Appendix 7D-Input Parameters for ProShake Software

Layer No.	Material Name	Thickness (m)	Unit Weight (kN/m^3)	G_{max} (MPa)	Soil Model
1	Medium Dense	2.00	16.92	106.1	DR-050-SAT-000
2	Loose Dense	0.45	18.94	75.2	DR-025-SAT-075
3	Loose Dense	0.55	19.87	75.2	DR-025-SAT-100
4	Medium Dense	2.00	20.34	106.1	DR-050-SAT-000
5	Dense	8.00	20.85	130.4	DR-075-SAT-100
6	Rock (Residual Malmesbury)	0.00	23.6	2406.5	Rock (Idriss, 1970)

Appendix 7E-Tabulation of the Output from Plaxis 2D Software

Tabulation of Results from the Free Vibration and Earthquake Analysis of the Building

Point	Frequency [Hz]	Power (u_x)
0	0.00	0.003779
1	0.05	0.003649
2	0.10	0.003504
3	0.15	0.003341
4	0.20	0.003045
5	0.25	0.002705
6	0.30	0.002538
7	0.35	0.002407
8	0.40	0.002581
9	0.45	0.003125
10	0.50	0.004376
11	0.54	0.006510
12	0.59	0.010102
13	0.64	0.017165
14	0.69	0.031340
15	0.74	0.064966
16	0.79	0.163510
17	0.84	0.488715
18	0.89	0.632026
19	0.94	0.292954
20	0.99	0.148435
21	1.04	0.092439
22	1.09	0.066197
23	1.14	0.051880
24	1.19	0.043995
25	1.24	0.038800
26	1.29	0.035766
27	1.34	0.034474
28	1.39	0.033369
29	1.44	0.033334
30	1.49	0.034177
31	1.53	0.035533
32	1.58	0.038017
33	1.63	0.041227
34	1.68	0.045094
35	1.73	0.049592
36	1.78	0.054355
37	1.83	0.058066
38	1.88	0.059210
39	1.93	0.058687
40	1.98	0.055675
41	2.03	0.051419
42	2.08	0.047173
43	2.13	0.042704
44	2.18	0.039019
45	2.23	0.035600
46	2.28	0.032837
47	2.33	0.030492
48	2.38	0.029158
49	2.43	0.028190
50	2.48	0.027679

Point	Dynamic time [s]	u_x [m]
0	0.050	0.0063
1	0.100	0.0054
2	0.150	0.0043
3	0.200	0.0032
4	0.250	0.0021
5	0.300	0.0010
6	0.350	-0.0003
7	0.400	-0.0016
8	0.450	-0.0028
9	0.500	-0.0036
10	0.550	-0.0039
11	0.600	-0.0039
12	0.650	-0.0037
13	0.700	-0.0033
14	0.750	-0.0027
15	0.800	-0.0019
16	0.850	-0.0009
17	0.900	0.0002
18	0.950	0.0013
19	1.000	0.0021
20	1.050	0.0028
21	1.100	0.0032
22	1.150	0.0034
23	1.200	0.0034
24	1.250	0.0032
25	1.300	0.0028
26	1.350	0.0021
27	1.400	0.0013
28	1.450	0.0004
29	1.500	-0.0004
30	1.550	-0.0012
31	1.600	-0.0019
32	1.650	-0.0024
33	1.700	-0.0028
34	1.750	-0.0029
35	1.800	-0.0028
36	1.850	-0.0026
37	1.900	-0.0021
38	1.950	-0.0015
39	2.000	-0.0009
40	2.050	-0.0002
41	2.100	0.0004
42	2.150	0.0010
43	2.200	0.0015
44	2.250	0.0019
45	2.300	0.0021
46	2.350	0.0021
47	2.400	0.0019
48	2.450	0.0016
49	2.500	0.0012
50	2.550	0.0006

Point	Dynamic time [s]	u_x [m]
51	2.600	0.0001
52	2.650	-0.0005
53	2.700	-0.0011
54	2.750	-0.0016
55	2.800	-0.0019
56	2.850	-0.0022
57	2.900	-0.0023
58	2.950	-0.0022
59	3.000	-0.0021
60	3.050	-0.0018
61	3.100	-0.0014
62	3.150	-0.0010
63	3.200	-0.0005
64	3.250	-0.0001
65	3.300	0.0004
66	3.350	0.0007
67	3.400	0.0009
68	3.450	0.0011
69	3.500	0.0011
70	3.550	0.0010
71	3.600	0.0008
72	3.650	0.0005
73	3.700	0.0001
74	3.750	-0.0003
75	3.800	-0.0007
76	3.850	-0.0011
77	3.900	-0.0014
78	3.950	-0.0017
79	4.000	-0.0018
80	4.050	-0.0019
81	4.100	-0.0019
82	4.150	-0.0018
83	4.200	-0.0016
84	4.250	-0.0014
85	4.300	-0.0011
86	4.350	-0.0007
87	4.400	-0.0004
88	4.450	-0.0002
89	4.500	0.0001
90	4.550	0.0003
91	4.600	0.0003
92	4.650	0.0004
93	4.700	0.0003
94	4.750	0.0002
95	4.800	-0.0001
96	4.850	-0.0003
97	4.900	-0.0006
98	4.950	-0.0009
99	5.000	-0.0011

Point	Dynamic time [s]	Arias intensity [m/s]
0	0.000	0.000E+00
1	0.200	1.739E-08
2	0.400	3.844E-08
3	0.600	4.574E-08
4	0.800	4.966E-08
5	1.000	5.028E-08
6	1.200	5.486E-08
7	1.400	5.950E-08
8	1.600	6.100E-08
9	1.800	6.386E-08
10	2.000	6.580E-08
11	2.200	6.689E-08
12	2.400	6.913E-08
13	2.600	7.047E-08
14	2.800	7.123E-08
15	3.000	7.277E-08
16	3.200	7.355E-08
17	3.400	7.419E-08
18	3.600	7.526E-08
19	3.800	7.572E-08
20	4.000	7.621E-08
21	4.200	7.693E-08
22	4.400	7.721E-08
23	4.600	7.759E-08
24	4.800	7.806E-08
25	5.000	7.823E-08
26	5.200	7.853E-08
27	5.400	7.883E-08
28	5.600	7.894E-08
29	5.800	7.917E-08
30	6.000	7.936E-08
31	6.200	7.944E-08
32	6.400	7.960E-08
33	6.600	7.972E-08
34	6.800	7.977E-08
35	7.000	7.989E-08
36	7.200	7.996E-08
37	7.400	8.000E-08
38	7.600	8.009E-08
39	7.800	8.013E-08
40	8.000	8.016E-08
41	8.200	8.022E-08
42	8.400	8.024E-08
43	8.600	8.027E-08
44	8.800	8.030E-08
45	9.000	8.032E-08
46	9.200	8.034E-08
47	9.400	8.036E-08
48	9.600	8.037E-08
49	9.800	8.039E-08
50	10.000	8.040E-08

Point	Dynamic time [s]	Arias intensity [m/s]
51	10.200	8.041E-08
52	10.400	8.042E-08
53	10.600	8.043E-08
54	10.800	8.043E-08
55	11.000	8.044E-08
56	11.200	8.045E-08
57	11.400	8.045E-08
58	11.600	8.045E-08
59	11.800	8.046E-08
60	12.000	8.046E-08
61	12.200	8.046E-08
62	12.400	8.046E-08
63	12.600	8.047E-08
64	12.800	8.047E-08
65	13.000	8.047E-08
66	13.200	8.047E-08
67	13.400	8.047E-08
68	13.600	8.047E-08
69	13.800	8.048E-08
70	14.000	8.048E-08
71	14.200	8.048E-08
72	14.400	8.048E-08
73	14.600	8.048E-08
74	14.800	8.048E-08
75	15.000	8.048E-08
76	15.200	8.048E-08
77	15.400	8.048E-08
78	15.600	8.048E-08
79	15.800	8.048E-08
80	16.000	8.048E-08
81	16.200	8.048E-08
82	16.400	8.048E-08
83	16.600	8.048E-08
84	16.800	8.048E-08
85	17.000	8.048E-08
86	17.200	8.048E-08
87	17.400	8.048E-08
88	17.600	8.048E-08
89	17.800	8.048E-08
90	18.000	8.048E-08
91	18.200	8.048E-08
92	18.400	8.048E-08
93	18.600	8.048E-08
94	18.800	8.048E-08
95	19.000	8.048E-08
96	19.200	8.048E-08
97	19.400	8.048E-08
98	19.600	8.048E-08
99	19.800	8.048E-08
100	20.000	8.048E-08

Tabulation of Results from the Free Vibration and Earthquake Analysis of the Building

Point	Period [s]	PSA ('g')
0	0.150	1.479E-04
1	0.160	1.451E-04
2	0.170	1.424E-04
3	0.180	1.397E-04
4	0.190	1.370E-04
5	0.200	1.344E-04
6	0.210	1.336E-04
7	0.220	1.404E-04
8	0.230	1.464E-04
9	0.240	1.515E-04
10	0.250	1.557E-04
11	0.260	1.591E-04
12	0.270	1.619E-04
13	0.280	1.641E-04
14	0.290	1.658E-04
15	0.300	1.670E-04
16	0.310	1.678E-04
17	0.320	1.683E-04
18	0.330	1.685E-04
19	0.340	1.685E-04
20	0.350	1.683E-04
21	0.360	1.680E-04
22	0.370	1.675E-04
23	0.380	1.668E-04
24	0.390	1.661E-04
25	0.400	1.653E-04
26	0.410	1.645E-04
27	0.420	1.635E-04
28	0.430	1.626E-04
29	0.440	1.616E-04
30	0.450	1.606E-04
31	0.460	1.596E-04
32	0.470	1.585E-04
33	0.480	1.575E-04
34	0.490	1.564E-04
35	0.500	1.553E-04
36	0.510	1.543E-04
37	0.520	1.532E-04
38	0.530	1.521E-04
39	0.540	1.509E-04
40	0.550	1.498E-04
41	0.560	1.486E-04
42	0.570	1.475E-04
43	0.580	1.463E-04
44	0.590	1.451E-04
45	0.600	1.439E-04
46	0.610	1.426E-04
47	0.620	1.414E-04
48	0.630	1.402E-04
49	0.640	1.389E-04
50	0.650	1.377E-04
51	0.660	1.364E-04
52	0.670	1.352E-04
53	0.680	1.339E-04
54	0.690	1.327E-04
55	0.700	1.314E-04
56	0.710	1.302E-04
57	0.720	1.289E-04
58	0.730	1.277E-04
59	0.740	1.269E-04
60	0.750	1.283E-04
61	0.760	1.298E-04
62	0.770	1.312E-04
63	0.780	1.327E-04
64	0.790	1.342E-04
65	0.800	1.356E-04
66	0.810	1.369E-04
67	0.820	1.382E-04
68	0.830	1.394E-04
69	0.840	1.405E-04
70	0.850	1.414E-04
71	0.860	1.423E-04
72	0.870	1.457E-04
73	0.880	1.489E-04
74	0.890	1.518E-04
75	0.900	1.545E-04
76	0.910	1.569E-04
77	0.920	1.591E-04
78	0.930	1.611E-04
79	0.940	1.629E-04
80	0.950	1.644E-04
81	0.960	1.658E-04
82	0.970	1.675E-04
83	0.980	1.706E-04
84	0.990	1.733E-04
85	1.000	1.758E-04
86	1.010	1.779E-04
87	1.020	1.798E-04
88	1.030	1.813E-04
89	1.040	1.837E-04
90	1.050	1.860E-04
91	1.060	1.879E-04
92	1.070	1.894E-04
93	1.080	1.904E-04
94	1.090	1.911E-04
95	1.100	1.914E-04
96	1.110	1.919E-04
97	1.120	1.919E-04
98	1.130	1.915E-04
99	1.140	1.905E-04
100	1.150	1.892E-04
101	1.160	1.874E-04
102	1.170	1.852E-04
103	1.180	1.826E-04
104	1.190	1.796E-04
105	1.200	1.766E-04
106	1.210	1.737E-04
107	1.220	1.706E-04
108	1.230	1.674E-04
109	1.240	1.639E-04
110	1.250	1.604E-04
111	1.260	1.567E-04
112	1.270	1.528E-04
113	1.280	1.490E-04
114	1.290	1.461E-04
115	1.300	1.430E-04
116	1.310	1.400E-04
117	1.320	1.369E-04
118	1.330	1.337E-04
119	1.340	1.305E-04
120	1.350	1.273E-04
121	1.360	1.241E-04
122	1.370	1.209E-04
123	1.380	1.181E-04
124	1.390	1.160E-04
125	1.400	1.138E-04
126	1.410	1.116E-04
127	1.420	1.095E-04
128	1.430	1.073E-04
129	1.440	1.052E-04
130	1.450	1.030E-04
131	1.460	1.009E-04
132	1.470	9.879E-05
133	1.480	9.669E-05
134	1.490	9.461E-05
135	1.500	9.254E-05
136	1.510	9.048E-05
137	1.520	8.845E-05
138	1.530	8.643E-05
139	1.540	8.443E-05
140	1.550	8.246E-05
141	1.560	8.086E-05
142	1.570	7.970E-05
143	1.580	7.855E-05
144	1.590	7.742E-05
145	1.600	7.629E-05
146	1.610	7.518E-05
147	1.620	7.407E-05
148	1.630	7.298E-05
149	1.640	7.190E-05
150	1.650	7.084E-05
151	1.660	6.978E-05
152	1.670	6.874E-05
153	1.680	6.771E-05
154	1.690	6.669E-05
155	1.700	6.568E-05
156	1.710	6.468E-05
157	1.720	6.370E-05
158	1.730	6.273E-05
159	1.740	6.176E-05
160	1.750	6.082E-05
161	1.760	5.988E-05
162	1.770	5.895E-05
163	1.780	5.804E-05
164	1.790	5.714E-05
165	1.800	5.625E-05
166	1.810	5.537E-05
167	1.820	5.450E-05
168	1.830	5.364E-05
169	1.840	5.279E-05
170	1.850	5.196E-05
171	1.860	5.113E-05
172	1.870	5.032E-05
173	1.880	4.952E-05
174	1.890	4.872E-05
175	1.900	4.794E-05
176	1.910	4.717E-05
177	1.920	4.641E-05
178	1.930	4.566E-05
179	1.940	4.492E-05
180	1.950	4.419E-05
181	1.960	4.347E-05
182	1.970	4.276E-05
183	1.980	4.206E-05
184	1.990	4.137E-05
185	2.000	4.068E-05
186	2.010	4.001E-05
187	2.020	3.935E-05
188	2.030	3.870E-05
189	2.040	3.805E-05
190	2.050	3.742E-05
191	2.060	3.679E-05
192	2.070	3.617E-05
193	2.080	3.556E-05
194	2.090	3.496E-05
195	2.100	3.442E-05
196	2.110	3.414E-05
197	2.120	3.386E-05
198	2.130	3.359E-05
199	2.140	3.331E-05
200	2.150	3.304E-05
201	2.160	3.278E-05
202	2.170	3.251E-05
203	2.180	3.225E-05
204	2.190	3.199E-05
205	2.200	3.173E-05
206	2.210	3.148E-05
207	2.220	3.123E-05
208	2.230	3.098E-05
209	2.240	3.074E-05
210	2.250	3.050E-05
211	2.260	3.025E-05
212	2.270	3.002E-05
213	2.280	2.978E-05
214	2.290	2.955E-05
215	2.300	2.932E-05
216	2.310	2.909E-05
217	2.320	2.887E-05
218	2.330	2.864E-05
219	2.340	2.842E-05
220	2.350	2.820E-05
221	2.360	2.799E-05
222	2.370	2.777E-05
223	2.380	2.756E-05
224	2.390	2.735E-05
225	2.400	2.714E-05
226	2.410	2.694E-05
227	2.420	2.674E-05
228	2.430	2.653E-05
229	2.440	2.634E-05
230	2.450	2.614E-05
231	2.460	2.594E-05
232	2.470	2.575E-05
233	2.480	2.556E-05
234	2.490	2.537E-05
235	2.500	2.518E-05
236	2.510	2.500E-05
237	2.520	2.481E-05
238	2.530	2.463E-05
239	2.540	2.445E-05
240	2.550	2.427E-05
241	2.560	2.410E-05
242	2.570	2.392E-05
243	2.580	2.375E-05
244	2.590	2.358E-05
245	2.600	2.341E-05
246	2.610	2.324E-05
247	2.620	2.307E-05
248	2.630	2.291E-05
249	2.640	2.275E-05
250	2.650	2.259E-05
251	2.660	2.243E-05
252	2.670	2.227E-05
253	2.680	2.211E-05
254	2.690	2.196E-05
255	2.700	2.180E-05
256	2.710	2.165E-05
257	2.720	2.150E-05
258	2.730	2.135E-05
259	2.740	2.120E-05
260	2.750	2.106E-05
261	2.760	2.091E-05
262	2.770	2.077E-05
263	2.780	2.063E-05
264	2.790	2.048E-05
265	2.800	2.035E-05
266	2.810	2.021E-05
267	2.820	2.007E-05
268	2.830	1.993E-05
269	2.840	1.980E-05
270	2.850	1.967E-05
271	2.860	1.954E-05
272	2.870	1.941E-05
273	2.880	1.928E-05
274	2.890	1.915E-05
275	2.900	1.902E-05
276	2.910	1.890E-05
277	2.920	1.877E-05
278	2.930	1.865E-05
279	2.940	1.852E-05
280	2.950	1.840E-05
281	2.960	1.828E-05
282	2.970	1.816E-05
283	2.980	1.805E-05
284	2.990	1.793E-05
285	3.000	1.781E-05
286	3.010	1.770E-05
287	3.020	1.759E-05
288	3.030	1.747E-05
289	3.040	1.736E-05
290	3.050	1.725E-05
291	3.060	1.714E-05
292	3.070	1.703E-05
293	3.080	1.693E-05
294	3.090	1.682E-05
295	3.100	1.671E-05
296	3.110	1.661E-05
297	3.120	1.650E-05
298	3.130	1.640E-05
299	3.140	1.630E-05
300	3.150	1.620E-05
301	3.160	1.610E-05
302	3.170	1.600E-05
303	3.180	1.590E-05
304	3.190	1.580E-05
305	3.200	1.571E-05
306	3.210	1.561E-05
307	3.220	1.552E-05
308	3.230	1.542E-05
309	3.240	1.533E-05
310	3.250	1.524E-05
311	3.260	1.514E-05
312	3.270	1.505E-05
313	3.280	1.496E-05
314	3.290	1.487E-05
315	3.300	1.478E-05
316	3.310	1.470E-05
317	3.320	1.461E-05
318	3.330	1.452E-05
319	3.340	1.444E-05
320	3.350	1.435E-05
321	3.360	1.427E-05
322	3.370	1.418E-05
323	3.380	1.410E-05
324	3.390	1.402E-05
325	3.400	1.394E-05
326	3.410	1.386E-05
327	3.420	1.378E-05
328	3.430	1.370E-05
329	3.440	1.362E-05
330	3.450	1.354E-05
331	3.460	1.346E-05
332	3.470	1.339E-05
333	3.480	1.331E-05
334	3.490	1.323E-05
335	3.500	1.316E-05
336	3.510	1.309E-05
337	3.520	1.301E-05
338	3.530	1.294E-05
339	3.540	1.287E-05
340	3.550	1.279E-05
341	3.560	1.272E-05
342	3.570	1.265E-05
343	3.580	1.258E-05
344	3.590	1.251E-05
345	3.600	1.244E-05
346	3.610	1.237E-05
347	3.620	1.231E-05
348	3.630	1.224E-05
349	3.640	1.217E-05
350	3.650	1.211E-05
351	3.660	1.204E-05
352	3.670	1.197E-05
353	3.680	1.191E-05
354	3.690	1.184E-05
355	3.700	1.178E-05
356	3.710	1.172E-05
357	3.720	1.165E-05
358	3.730	1.159E-05
359	3.740	1.153E-05
360	3.750	1.147E-05
361	3.760	1.141E-05
362	3.770	1.135E-05
363	3.780	1.129E-05
364	3.790	1.123E-05
365	3.800	1.117E-05
366	3.810	1.111E-05
367	3.820	1.105E-05
368	3.830	1.099E-05
369	3.840	1.094E-05
370	3.850	1.088E-05
371	3.860	1.082E-05
372	3.870	1.077E-05
373	3.880	1.071E-05
374	3.890	1.066E-05
375	3.900	1.060E-05
376	3.910	1.055E-05
377	3.920	1.049E-05
378	3.930	1.044E-05
379	3.940	1.039E-05
380	3.950	1.034E-05
381	3.960	1.028E-05
382	3.970	1.023E-05
383	3.980	1.018E-05
384	3.990	1.013E-05
385	4.000	1.008E-05
386	4.010	1.003E-05
387	4.020	9.977E-06
388	4.030	9.927E-06
389	4.040	9.878E-06
390	4.050	9.829E-06
391	4.060	9.781E-06
392	4.070	9.732E-06
393	4.080	9.684E-06
394	4.090	9.637E-06
395	4.100	9.590E-06
396	4.110	9.543E-06
397	4.120	9.496E-06
398	4.130	9.450E-06
399	4.140	9.404E-06
400	4.150	9.359E-06
401	4.160	9.313E-06
402	4.170	9.269E-06
403	4.180	9.224E-06
404	4.190	9.180E-06
405	4.200	9.136E-06
406	4.210	9.092E-06
407	4.220	9.049E-06
408	4.230	9.006E-06
409	4.240	8.963E-06
410	4.250	8.921E-06
411	4.260	8.878E-06
412	4.270	8.837E-06
413	4.280	8.795E-06
414	4.290	8.754E-06
415	4.300	8.713E-06
416	4.310	8.672E-06
417	4.320	8.632E-06
418	4.330	8.592E-06
419	4.340	8.552E-06
420	4.350	8.512E-06
421	4.360	8.473E-06
422	4.370	8.434E-06
423	4.380	8.395E-06
424	4.390	8.356E-06
425	4.400	8.318E-06
426	4.410	8.280E-06
427	4.420	8.242E-06
428	4.430	8.205E-06
429	4.440	8.168E-06
430	4.450	8.131E-06
431	4.460	8.094E-06
432	4.470	8.057E-06
433	4.480	8.021E-06
434	4.490	7.985E-06
435	4.500	7.949E-06
436	4.510	7.914E-06
437	4.520	7.878E-06
438	4.530	7.843E-06
439	4.540	7.809E-06
440	4.550	7.774E-06
441	4.560	7.740E-06
442	4.570	7.705E-06
443	4.580	7.671E-06
444	4.590	7.638E-06
445	4.600	7.604E-06
446	4.610	7.571E-06
447	4.620	7.538E-06
448	4.630	7.505E-06
449	4.640	7.472E-06
450	4.650	7.440E-06
451	4.660	7.408E-06
452	4.670	7.376E-06
453	4.680	7.344E-06
454	4.690	7.312E-06
455	4.700	7.281E-06
456	4.710	7.250E-06
457	4.720	7.219E-06
458	4.730	7.188E-06
459	4.740	7.157E-06
460	4.750	7.127E-06
461	4.760	7.097E-06
462	4.770	7.067E-06
463	4.780	7.037E-06
464	4.790	7.007E-06
465	4.800	6.978E-06
466	4.810	6.948E-06
467	4.820	6.919E-06
468	4.830	6.890E-06
469	4.840	6.862E-06
470	4.850	6.833E-06
471	4.860	6.805E-06
472	4.870	6.776E-06
473	4.880	6.748E-06
474	4.890	6.720E-06
475	4.900	6.693E-06
476	4.910	6.665E-06
477	4.920	6.638E-06
478	4.930	6.611E-06
479	4.940	6.584E-06
480	4.950	6.557E-06
481	4.960	6.530E-06
482	4.970	6.503E-06
483	4.980	6.477E-06
484	4.990	6.451E-06
485	5.000	6.425E-06
486	5.010	6.399E-06
487	5.020	6.373E-06
488	5.030	6.347E-06
489	5.040	6.322E-06
490	5.050	6.297E-06
491	5.060	6.272E-06
492	5.070	6.247E-06
493	5.080	6.222E-06
494	5.090	6.197E-06
495	5.100	6.172E-06
496	5.110	6.148E-06
497	5.120	6.124E-06
498	5.130	6.100E-06
499	5.140	6.076E-06
500	5.150	6.052E-06
501	5.160	6.028E-06
502	5.170	6.005E-06
503	5.180	5.981E-06
504	5.190	5.958E-06
505	5.200	5.935E-06
506	5.210	5.912E-06
507	5.220	5.889E-06
508	5.230	5.866E-06
509	5.240	5.843E-06
510	5.250	5.821E-06
511	5.260	5.799E-06
512	5.270	5.776E-06
513	5.280	5.754E-06
514	5.290	5.732E-06
515	5.300	5.710E-06
516	5.310	5.689E-06
517	5.320	5.667E-06
518	5.330	5.645E-06
519	5.340	5.624E-06

Tabulation of Results from the Free Vibration and Earthquake Analysis of the Building

Point	Period [s]	PSA ('g')
520	5.350	5.603E-06
521	5.360	5.582E-06
522	5.370	5.561E-06
523	5.380	5.540E-06
524	5.390	5.519E-06
525	5.400	5.498E-06
526	5.410	5.478E-06
527	5.420	5.457E-06
528	5.430	5.437E-06
529	5.440	5.417E-06
530	5.450	5.397E-06
531	5.460	5.377E-06
532	5.470	5.357E-06
533	5.480	5.337E-06
534	5.490	5.318E-06
535	5.500	5.298E-06
536	5.510	5.279E-06
537	5.520	5.259E-06
538	5.530	5.240E-06
539	5.540	5.221E-06
540	5.550	5.202E-06
541	5.560	5.183E-06
542	5.570	5.164E-06
543	5.580	5.145E-06
544	5.590	5.127E-06
545	5.600	5.108E-06
546	5.610	5.090E-06
547	5.620	5.072E-06
548	5.630	5.053E-06
549	5.640	5.035E-06
550	5.650	5.017E-06
551	5.660	4.999E-06
552	5.670	4.981E-06
553	5.680	4.964E-06
554	5.690	4.946E-06
555	5.700	4.929E-06
556	5.710	4.911E-06
557	5.720	4.894E-06
558	5.730	4.877E-06
559	5.740	4.859E-06
560	5.750	4.842E-06
561	5.760	4.825E-06
562	5.770	4.808E-06
563	5.780	4.792E-06
564	5.790	4.775E-06
565	5.800	4.758E-06
566	5.810	4.742E-06
567	5.820	4.725E-06
568	5.830	4.709E-06
569	5.840	4.692E-06
570	5.850	4.676E-06
571	5.860	4.660E-06
572	5.870	4.644E-06
573	5.880	4.628E-06
574	5.890	4.612E-06
575	5.900	4.596E-06
576	5.910	4.581E-06
577	5.920	4.565E-06
578	5.930	4.550E-06
579	5.940	4.534E-06
580	5.950	4.519E-06
581	5.960	4.503E-06
582	5.970	4.488E-06
583	5.980	4.473E-06
584	5.990	4.458E-06
585	6.000	4.443E-06
586	6.010	4.428E-06
587	6.020	4.413E-06
588	6.030	4.398E-06
589	6.040	4.383E-06
590	6.050	4.369E-06
591	6.060	4.354E-06
592	6.070	4.340E-06
593	6.080	4.325E-06
594	6.090	4.311E-06
595	6.100	4.297E-06
596	6.110	4.282E-06
597	6.120	4.268E-06
598	6.130	4.254E-06
599	6.140	4.240E-06
600	6.150	4.226E-06
601	6.160	4.212E-06
602	6.170	4.199E-06
603	6.180	4.185E-06
604	6.190	4.171E-06
605	6.200	4.158E-06
606	6.210	4.144E-06
607	6.220	4.131E-06
608	6.230	4.117E-06
609	6.240	4.104E-06
610	6.250	4.091E-06
611	6.260	4.077E-06
612	6.270	4.064E-06
613	6.280	4.051E-06
614	6.290	4.038E-06
615	6.300	4.025E-06
616	6.310	4.012E-06
617	6.320	4.000E-06
618	6.330	3.987E-06
619	6.340	3.974E-06
620	6.350	3.961E-06
621	6.360	3.949E-06
622	6.370	3.936E-06
623	6.380	3.924E-06
624	6.390	3.912E-06
625	6.400	3.899E-06
626	6.410	3.887E-06
627	6.420	3.875E-06
628	6.430	3.862E-06
629	6.440	3.850E-06
630	6.450	3.838E-06
631	6.460	3.826E-06
632	6.470	3.814E-06
633	6.480	3.802E-06
634	6.490	3.791E-06
635	6.500	3.779E-06
636	6.510	3.767E-06
637	6.520	3.755E-06
638	6.530	3.744E-06
639	6.540	3.732E-06
640	6.550	3.721E-06
641	6.560	3.709E-06
642	6.570	3.698E-06
643	6.580	3.687E-06
644	6.590	3.678E-06
645	6.600	3.673E-06
646	6.610	3.668E-06
647	6.620	3.662E-06
648	6.630	3.657E-06
649	6.640	3.652E-06
650	6.650	3.646E-06
651	6.660	3.641E-06
652	6.670	3.636E-06
653	6.680	3.630E-06
654	6.690	3.625E-06
655	6.700	3.620E-06
656	6.710	3.614E-06
657	6.720	3.609E-06
658	6.730	3.604E-06
659	6.740	3.598E-06
660	6.750	3.593E-06
661	6.760	3.587E-06
662	6.770	3.582E-06
663	6.780	3.577E-06
664	6.790	3.571E-06
665	6.800	3.566E-06
666	6.810	3.561E-06
667	6.820	3.555E-06
668	6.830	3.550E-06
669	6.840	3.544E-06
670	6.850	3.539E-06
671	6.860	3.534E-06
672	6.870	3.528E-06
673	6.880	3.523E-06
674	6.890	3.518E-06
675	6.900	3.512E-06
676	6.910	3.507E-06
677	6.920	3.501E-06
678	6.930	3.496E-06
679	6.940	3.491E-06
680	6.950	3.485E-06
681	6.960	3.480E-06
682	6.970	3.475E-06
683	6.980	3.469E-06
684	6.990	3.464E-06
685	7.000	3.458E-06
686	7.010	3.453E-06
687	7.020	3.448E-06
688	7.030	3.442E-06
689	7.040	3.437E-06
690	7.050	3.432E-06
691	7.060	3.426E-06
692	7.070	3.421E-06
693	7.080	3.416E-06
694	7.090	3.410E-06
695	7.100	3.405E-06
696	7.110	3.400E-06
697	7.120	3.394E-06
698	7.130	3.389E-06
699	7.140	3.384E-06
700	7.150	3.378E-06
701	7.160	3.373E-06
702	7.170	3.368E-06
703	7.180	3.362E-06
704	7.190	3.357E-06
705	7.200	3.352E-06
706	7.210	3.346E-06
707	7.220	3.341E-06
708	7.230	3.336E-06
709	7.240	3.330E-06
710	7.250	3.325E-06
711	7.260	3.320E-06
712	7.270	3.314E-06
713	7.280	3.309E-06
714	7.290	3.304E-06
715	7.300	3.299E-06
716	7.310	3.293E-06
717	7.320	3.288E-06
718	7.330	3.283E-06
719	7.340	3.278E-06
720	7.350	3.272E-06
721	7.360	3.267E-06
722	7.370	3.262E-06
723	7.380	3.257E-06
724	7.390	3.251E-06
725	7.400	3.246E-06
726	7.410	3.241E-06
727	7.420	3.236E-06
728	7.430	3.230E-06
729	7.440	3.225E-06
730	7.450	3.220E-06
731	7.460	3.215E-06
732	7.470	3.210E-06
733	7.480	3.204E-06
734	7.490	3.199E-06
735	7.500	3.194E-06
736	7.510	3.189E-06
737	7.520	3.184E-06
738	7.530	3.179E-06
739	7.540	3.173E-06
740	7.550	3.168E-06
741	7.560	3.163E-06
742	7.570	3.158E-06
743	7.580	3.153E-06
744	7.590	3.148E-06
745	7.600	3.143E-06
746	7.610	3.138E-06
747	7.620	3.132E-06
748	7.630	3.127E-06
749	7.640	3.122E-06
750	7.650	3.117E-06
751	7.660	3.112E-06
752	7.670	3.107E-06
753	7.680	3.102E-06
754	7.690	3.097E-06
755	7.700	3.092E-06
756	7.710	3.087E-06
757	7.720	3.082E-06
758	7.730	3.077E-06
759	7.740	3.072E-06
760	7.750	3.067E-06
761	7.760	3.062E-06
762	7.770	3.057E-06
763	7.780	3.052E-06
764	7.790	3.047E-06
765	7.800	3.042E-06
766	7.810	3.037E-06
767	7.820	3.032E-06
768	7.830	3.027E-06
769	7.840	3.022E-06
770	7.850	3.017E-06
771	7.860	3.012E-06
772	7.870	3.007E-06
773	7.880	3.002E-06
774	7.890	2.997E-06
775	7.900	2.992E-06
776	7.910	2.987E-06
777	7.920	2.982E-06
778	7.930	2.978E-06
779	7.940	2.973E-06
780	7.950	2.968E-06
781	7.960	2.963E-06
782	7.970	2.958E-06
783	7.980	2.953E-06
784	7.990	2.948E-06
785	8.000	2.944E-06
786	8.010	2.939E-06
787	8.020	2.934E-06
788	8.030	2.929E-06
789	8.040	2.924E-06
790	8.050	2.919E-06
791	8.060	2.915E-06
792	8.070	2.910E-06
793	8.080	2.905E-06
794	8.090	2.900E-06
795	8.100	2.896E-06
796	8.110	2.891E-06
797	8.120	2.886E-06
798	8.130	2.881E-06
799	8.140	2.877E-06
800	8.150	2.872E-06
801	8.160	2.867E-06
802	8.170	2.862E-06
803	8.180	2.858E-06
804	8.190	2.853E-06
805	8.200	2.848E-06
806	8.210	2.844E-06
807	8.220	2.839E-06
808	8.230	2.834E-06
809	8.240	2.830E-06
810	8.250	2.825E-06
811	8.260	2.820E-06
812	8.270	2.816E-06
813	8.280	2.811E-06
814	8.290	2.806E-06
815	8.300	2.802E-06
816	8.310	2.797E-06
817	8.320	2.793E-06
818	8.330	2.788E-06
819	8.340	2.783E-06
820	8.350	2.779E-06
821	8.360	2.774E-06
822	8.370	2.770E-06
823	8.380	2.765E-06
824	8.390	2.761E-06
825	8.400	2.756E-06
826	8.410	2.752E-06
827	8.420	2.747E-06
828	8.430	2.743E-06
829	8.440	2.738E-06
830	8.450	2.734E-06
831	8.460	2.729E-06
832	8.470	2.725E-06
833	8.480	2.720E-06
834	8.490	2.716E-06
835	8.500	2.711E-06
836	8.510	2.707E-06
837	8.520	2.702E-06
838	8.530	2.698E-06
839	8.540	2.694E-06
840	8.550	2.689E-06
841	8.560	2.685E-06
842	8.570	2.680E-06
843	8.580	2.676E-06
844	8.590	2.672E-06
845	8.600	2.667E-06
846	8.610	2.663E-06
847	8.620	2.658E-06
848	8.630	2.654E-06
849	8.640	2.650E-06
850	8.650	2.645E-06
851	8.660	2.641E-06
852	8.670	2.637E-06
853	8.680	2.632E-06
854	8.690	2.628E-06
855	8.700	2.624E-06
856	8.710	2.620E-06
857	8.720	2.615E-06
858	8.730	2.611E-06
859	8.740	2.607E-06
860	8.750	2.603E-06
861	8.760	2.598E-06
862	8.770	2.594E-06
863	8.780	2.590E-06
864	8.790	2.586E-06
865	8.800	2.581E-06
866	8.810	2.577E-06
867	8.820	2.573E-06
868	8.830	2.569E-06
869	8.840	2.565E-06
870	8.850	2.560E-06
871	8.860	2.556E-06
872	8.870	2.552E-06
873	8.880	2.548E-06
874	8.890	2.544E-06
875	8.900	2.540E-06
876	8.910	2.535E-06
877	8.920	2.531E-06
878	8.930	2.527E-06
879	8.940	2.523E-06
880	8.950	2.519E-06
881	8.960	2.515E-06
882	8.970	2.511E-06
883	8.980	2.507E-06
884	8.990	2.503E-06
885	9.000	2.499E-06
886	9.010	2.495E-06
887	9.020	2.491E-06
888	9.030	2.49E-06
889	9.040	2.48E-06
890	9.050	2.48E-06
891	9.060	2.47E-06
892	9.070	2.47E-06
893	9.080	2.47E-06
894	9.090	2.46E-06
895	9.100	2.46E-06
896	9.110	2.45E-06
897	9.120	2.45E-06
898	9.130	2.45E-06
899	9.140	2.44E-06
900	9.150	2.44E-06
901	9.160	2.43E-06
902	9.170	2.43E-06
903	9.180	2.43E-06
904	9.190	2.42E-06
905	9.200	2.42E-06
906	9.210	2.42E-06
907	9.220	2.41E-06
908	9.230	2.41E-06
909	9.240	2.40E-06
910	9.250	2.40E-06
911	9.260	2.40E-06
912	9.270	2.39E-06
913	9.280	2.39E-06
914	9.290	2.38E-06
915	9.300	2.38E-06
916	9.310	2.38E-06
917	9.320	2.37E-06
918	9.330	2.37E-06
919	9.340	2.37E-06
920	9.350	2.36E-06
921	9.360	2.36E-06
922	9.370	2.35E-06
923	9.380	2.35E-06
924	9.390	2.35E-06
925	9.400	2.34E-06
926	9.410	2.34E-06
927	9.420	2.34E-06
928	9.430	2.33E-06
929	9.440	2.33E-06
930	9.450	2.32E-06
931	9.460	2.32E-06
932	9.470	2.32E-06
933	9.480	2.31E-06
934	9.490	2.31E-06
935	9.500	2.31E-06
936	9.510	2.30E-06
937	9.520	2.30E-06
938	9.530	2.29E-06
939	9.540	2.29E-06
940	9.550	2.29E-06
941	9.560	2.28E-06
942	9.570	2.28E-06
943	9.580	2.28E-06
944	9.590	2.27E-06
945	9.600	2.27E-06
946	9.610	2.27E-06
947	9.620	2.26E-06
948	9.630	2.26E-06
949	9.640	2.25E-06
950	9.650	2.25E-06
951	9.660	2.25E-06
952	9.670	2.24E-06
953	9.680	2.24E-06
954	9.690	2.24E-06
955	9.700	2.23E-06
956	9.710	2.23E-06
957	9.720	2.23E-06
958	9.730	2.22E-06
959	9.740	2.22E-06
960	9.750	2.22E-06
961	9.760	2.21E-06
962	9.770	2.21E-06
963	9.780	2.21E-06
964	9.790	2.20E-06
965	9.800	2.20E-06
966	9.810	2.19E-06
967	9.820	2.19E-06
968	9.830	2.19E-06
969	9.840	2.18E-06
970	9.850	2.18E-06
971	9.860	2.18E-06
972	9.870	2.17E-06
973	9.880	2.17E-06
974	9.890	2.17E-06
975	9.900	2.16E-06
976	9.910	2.16E-06
977	9.920	2.16E-06
978	9.930	2.15E-06
979	9.940	2.15E-06
980	9.950	2.15E-06
981	9.960	2.14E-06
982	9.97E+00	2.14E-06
983	9.98E+00	2.14E-06
984	9.99E+00	2.13E-06
985	1.00E+01	2.13E-06

Appendix 8-Tabulation of Output from ProShake

Tabulation of the Summary of Soil Profile Results From ProShake Software

Acceleration Profile		Displacement Profile		Velocity Profile	
Depth (m)	**Acceleration (g)**	**Depth (m)**	**Peak Total Displacement (m)**	**Depth (m)**	**Velocity (m/sec)**
0.00	0.159100	0.00	0.004600	0.00	0.041800
2.00	0.127900	2.00	0.004600	2.00	0.040100
2.45	0.103800	2.45	0.004500	2.45	0.038500
3.00	0.103000	3.00	0.004400	3.00	0.035700
7.00	0.129200	7.00	0.004300	7.00	0.033000
15.00	0.154800	15.00	0.003500	15.00	0.028500

Peak Shear Strain Profile		Effective Shear Strain Profile	
Depth (m)	**Peak Shear Strain (%)**	**Depth (m)**	**Effective Shear Strain (%)**
1.00	0.002940	1.00	0.001911
2.22	0.010330	2.22	0.006715
2.72	0.012690	2.72	0.008248
5.00	0.014040	5.00	0.009126
11.00	0.016180	11.00	0.010517
15.00	0.000600	15.00	0.000390

Appendix 9-Nahanni Earthquake Records

PEER NGA STRONG MOTION DATABASE RECORD
Nahanni Canada, 12/23/1985, Site 3360
ACCELERATION TIME SERIES IN UNITS OF G
NPTS= 3819, DT= 0.0025 SEC,

-8.23E-04	-8.21E-04	-8.18E-04	-8.15E-04	-8.12E-04	-9.88E-03	-3.11E-03	7.24E-04	1.10E-03	-1.54E-03	9.40E-04	1.12E-02	1.90E-02	2.17E-02	1.90E-02	-2.50E-03	-4.10E-03	-4.58E-03	-3.65E-03	-1.09E-03	2.31E-02	1.18E-02	-8.48E-03	-3.66E-02	-6.23E-02	5.62E-02	4.63E-02	2.88E-02	6.03E-03	-1.60E-02
-8.10E-04	-8.07E-04	-8.03E-04	-8.00E-04	-7.97E-04	-5.62E-03	-8.60E-03	-8.31E-03	-3.83E-03	4.29E-03	1.23E-02	4.44E-03	-1.48E-03	-3.95E-03	-3.18E-03	3.43E-03	9.46E-03	1.54E-02	1.91E-02	1.87E-02	-7.73E-02	-8.57E-02	-9.25E-02	-9.24E-02	-8.17E-02	-3.51E-02	-5.06E-02	-5.84E-02	-5.68E-02	-5.07E-02
-7.94E-04	-7.90E-04	-7.87E-04	-7.83E-04	-7.79E-04	1.40E-02	2.15E-02	2.28E-02	1.76E-02	7.97E-03	-7.79E-04	8.52E-04	8.81E-04	-8.59E-06	-6.88E-04	1.34E-02	5.81E-03	-9.53E-04	-5.42E-03	-8.04E-03	-6.45E-02	-4.17E-02	-1.43E-02	9.45E-03	2.01E-02	-4.28E-02	-2.81E-02	-5.06E-03	2.44E-02	6.18E-02
-7.75E-04	-7.71E-04	-7.66E-04	-7.61E-04	-7.56E-04	-4.21E-03	-1.64E-02	-2.48E-02	-2.58E-02	-2.06E-02	-4.25E-04	2.50E-04	1.33E-04	-1.19E-03	-3.36E-03	-1.01E-02	-1.14E-02	-1.14E-02	-9.84E-03	-6.09E-03	1.62E-02	5.43E-03	-2.62E-03	-7.74E-03	-1.51E-02	1.02E-01	1.27E-01	1.19E-01	7.65E-02	1.95E-02
-7.51E-04	-7.46E-04	-7.42E-04	-7.38E-04	-7.35E-04	-1.47E-02	-1.06E-02	-7.55E-03	-5.50E-03	-4.32E-03	-5.28E-03	-5.94E-03	-5.24E-03	-4.02E-03	-3.43E-03	-5.32E-04	4.48E-03	5.65E-03	2.13E-03	-3.66E-03	-2.32E-02	-2.75E-02	-2.89E-02	-2.96E-02	-2.82E-02	-3.22E-02	-8.33E-02	-1.40E-01	-1.74E-01	-1.56E-01
-7.33E-04	-7.32E-04	-7.30E-04	-7.27E-04	-7.22E-04	-1.97E-03	3.41E-03	1.11E-02	1.75E-02	1.90E-02	-4.31E-03	-6.49E-03	-9.36E-03	-1.18E-02	-1.28E-02	-9.10E-03	-1.32E-02	-1.51E-02	-1.43E-02	-1.13E-02	-2.04E-02	-6.03E-03	9.06E-03	1.86E-02	2.05E-02	-1.14E-01	-9.30E-02	-9.01E-02	-7.88E-02	-5.88E-02
-7.15E-04	-7.07E-04	-6.95E-04	-6.80E-04	-6.63E-04	1.63E-02	1.23E-02	8.35E-03	4.61E-03	1.77E-03	-1.10E-02	-6.34E-03	-1.70E-04	5.04E-03	7.41E-03	-7.63E-03	-4.51E-03	-1.91E-03	9.23E-04	4.85E-03	1.47E-02	6.01E-03	1.94E-03	4.38E-03	9.56E-03	-4.46E-02	-3.49E-02	-2.80E-02	-2.58E-02	-2.33E-02
-6.52E-04	-6.46E-04	-6.45E-04	-6.47E-04	-6.54E-04	1.28E-03	3.20E-03	5.59E-03	5.58E-03	8.71E-04	6.21E-03	2.31E-03	-2.27E-03	-6.01E-03	-8.42E-03	9.76E-03	1.41E-02	1.64E-02	1.58E-02	1.13E-02	1.32E-02	1.39E-02	1.31E-02	1.44E-02	1.84E-02	-1.70E-02	-7.11E-03	5.05E-03	1.72E-02	2.60E-02
-6.64E-04	-6.77E-04	-6.86E-04	-6.87E-04	-6.77E-04	-7.55E-03	-1.59E-02	-2.01E-02	-1.90E-02	-1.52E-02	-9.05E-03	-7.65E-03	-4.87E-03	-1.31E-03	2.95E-03	3.02E-03	-7.66E-03	-1.81E-02	-2.41E-02	-2.50E-02	2.16E-02	1.86E-02	7.90E-03	-6.88E-03	-1.95E-02	2.83E-02	2.32E-02	1.36E-02	8.87E-03	1.87E-02
-6.59E-04	-6.33E-04	-6.05E-04	-5.82E-04	-5.70E-04	-1.06E-02	-4.65E-03	4.19E-03	1.59E-02	2.75E-02	8.02E-03	1.35E-02	1.84E-02	2.20E-02	2.35E-02	-2.26E-02	-1.79E-02	-1.40E-02	-1.30E-02	-1.32E-02	-2.64E-02	-2.72E-02	-2.36E-02	-1.84E-02	-1.19E-02	3.61E-02	4.12E-02	2.65E-02	2.38E-03	-1.86E-02
-5.62E-04	-5.54E-04	-5.51E-04	-5.60E-04	-5.78E-04	3.43E-02	3.39E-02	2.59E-02	1.17E-02	-1.62E-03	2.23E-02	1.85E-02	1.30E-02	5.72E-03	-1.91E-03	-1.21E-02	-1.09E-02	-1.16E-02	-1.42E-02	-1.69E-02	-4.18E-03	3.23E-03	7.70E-03	7.46E-03	4.76E-03	-3.59E-02	-5.05E-02	-5.14E-02	-2.84E-02	4.60E-03
-5.98E-04	-6.08E-04	-6.11E-04	-6.20E-04	-6.45E-04	-6.05E-03	-2.38E-03	4.14E-03	9.16E-03	1.22E-02	-6.94E-03	-7.11E-03	-3.81E-03	-1.12E-03	-1.57E-03	-1.79E-02	-1.64E-02	-1.20E-02	-5.40E-03	5.74E-04	4.06E-03	7.76E-03	1.57E-02	2.69E-02	3.79E-02	2.35E-02	2.46E-02	2.06E-02	2.02E-02	2.19E-02
-6.75E-04	-6.77E-04	-6.18E-04	-5.09E-04	-3.86E-04	1.48E-02	1.64E-02	1.49E-02	1.08E-02	7.31E-03	-4.42E-03	-7.83E-03	-1.05E-02	-1.18E-02	-1.05E-02	2.79E-03	5.11E-04	-4.37E-03	-9.44E-03	-1.24E-02	4.41E-02	4.30E-02	3.64E-02	2.67E-02	1.70E-02	2.19E-02	1.88E-02	1.26E-02	5.19E-03	-1.80E-04
-2.97E-04	-2.66E-04	-2.60E-04	-2.29E-04	-1.70E-04	6.89E-03	9.14E-03	1.15E-02	1.13E-02	7.29E-03	-6.50E-03	-1.11E-03	3.56E-03	6.67E-03	8.54E-03	-1.10E-02	-4.97E-03	4.28E-03	1.42E-02	2.22E-02	1.09E-02	1.15E-02	1.67E-02	1.94E-02	1.51E-02	-1.72E-03	1.80E-03	1.27E-02	3.15E-02	5.28E-02
-1.21E-04	-1.39E-04	-2.47E-04	-4.20E-04	-5.86E-04	-3.08E-04	-9.39E-03	-1.69E-02	-1.95E-02	-1.66E-02	9.76E-03	1.10E-02	1.18E-02	1.06E-02	7.69E-03	2.60E-02	2.46E-02	1.88E-02	1.03E-02	1.54E-03	3.92E-03	-1.10E-02	-2.63E-02	-3.89E-02	-4.89E-02	6.85E-02	7.51E-02	7.16E-02	5.79E-02	3.91E-02
-6.85E-04	-6.94E-04	-6.46E-04	-5.80E-04	-5.12E-04	-1.21E-02	-8.33E-03	-4.61E-03	-6.83E-04	1.98E-03	4.79E-03	3.41E-03	4.06E-03	6.71E-03	1.03E-02	-5.39E-03	-1.01E-02	-1.36E-02	-1.68E-02	-1.98E-02	-5.95E-02	-6.74E-02	-6.72E-02	-6.09E-02	-5.35E-02	2.58E-02	2.47E-02	3.34E-02	4.62E-02	5.74E-02
-4.40E-04	-3.77E-04	-3.58E-04	-4.23E-04	-5.61E-04	1.08E-03	-4.51E-03	-1.27E-02	-1.87E-02	-1.82E-02	1.33E-02	1.43E-02	1.28E-02	9.58E-03	5.85E-03	-2.15E-02	-2.13E-02	-2.00E-02	-1.81E-02	-1.63E-02	-4.63E-02	-4.03E-02	-3.64E-02	-3.20E-02	-2.10E-02	5.80E-02	4.08E-02	1.18E-02	-1.49E-02	-3.35E-02
-7.50E-04	-9.65E-04	-1.16E-03	-1.29E-03	-1.35E-03	-1.13E-02	-2.96E-03	2.65E-03	3.56E-03	-2.81E-04	2.49E-03	-9.95E-04	-6.38E-03	-1.48E-02	-2.51E-02	-1.56E-02	-1.60E-02	-1.62E-02	-1.45E-02	-1.08E-02	6.67E-05	2.57E-02	4.27E-02	4.49E-02	3.69E-02	-4.45E-02	-5.05E-02	-5.82E-02	-6.95E-02	-7.78E-02
-1.32E-03	-1.14E-03	-7.94E-04	-2.94E-04	2.50E-04	-6.28E-03	-1.05E-02	-1.03E-02	-5.36E-03	3.28E-03	-3.24E-02	-3.41E-02	-3.25E-02	-2.80E-02	-1.94E-02	-6.17E-03	-2.44E-03	-7.88E-04	-8.80E-04	-1.16E-03	2.24E-02	-1.78E-03	-3.87E-02	-7.89E-02	-9.14E-02	-7.39E-02	-5.17E-02	-1.51E-02	2.13E-02	4.77E-02
6.04E-04	5.66E-04	2.54E-04	-1.81E-05	-1.78E-04	1.30E-02	1.98E-02	2.06E-02	1.68E-02	1.29E-02	-6.22E-03	8.57E-03	2.10E-02	2.92E-02	3.19E-02	-1.02E-03	-2.42E-03	-7.17E-03	-1.35E-02	-1.63E-02	-7.00E-02	-4.82E-02	-4.03E-02	-3.45E-02	-2.15E-02	6.51E-02	7.53E-02	8.21E-02	9.22E-02	1.05E-01
-3.03E-04	-4.58E-04	-6.73E-04	-9.96E-04	-1.41E-03	1.09E-02	8.90E-03	4.66E-03	-2.01E-03	-9.76E-03	2.69E-02	1.59E-02	4.67E-03	-4.22E-03	-1.05E-02	-1.33E-02	-7.93E-03	-4.43E-03	-3.57E-03	-3.51E-03	-1.64E-03	2.42E-02	4.87E-02	6.68E-02	8.24E-02	1.06E-01	8.17E-02	3.40E-02	-1.99E-02	-5.90E-02
-1.86E-03	-2.15E-03	-2.02E-03	-1.43E-03	-5.83E-04	-1.62E-02	-1.94E-02	-1.75E-02	-1.16E-02	-6.05E-03	-1.39E-02	-1.46E-02	-1.27E-02	-9.44E-03	-7.42E-03	-2.64E-03	-1.25E-03	-6.12E-04	-1.22E-03	-2.24E-03	9.87E-02	1.16E-01	1.25E-01	1.18E-01	9.87E-02	-5.94E-02	-2.72E-02	-2.63E-04	8.52E-03	1.05E-02
3.81E-04	1.30E-03	2.00E-03	2.28E-03	2.09E-03	-3.63E-03	-4.41E-03	-7.50E-03	-1.19E-02	-1.63E-02	-6.48E-03	-4.48E-03	-1.46E-04	6.15E-03	1.29E-02	-2.67E-03	-1.90E-03	-2.59E-06	2.27E-03	3.66E-03	7.24E-02	4.65E-02	2.60E-02	1.63E-02	1.26E-02	1.19E-02	8.08E-03	-3.13E-03	-1.77E-02	-2.63E-02
1.59E-03	1.00E-03	5.26E-04	4.06E-04	7.30E-04	-1.83E-02	-1.59E-02	-8.61E-03	2.24E-03	1.36E-02	1.81E-02	2.08E-02	2.08E-02	1.82E-02	1.39E-02	3.63E-03	3.33E-03	5.22E-03	9.97E-03	1.53E-02	-1.03E-03	-2.61E-02	-4.93E-02	-6.46E-02	-7.45E-02	-2.18E-02	-6.45E-03	7.85E-03	9.30E-03	-3.38E-03
1.36E-03	2.02E-03	2.38E-03	2.35E-03	2.11E-03	2.16E-02	2.26E-02	1.87E-02	1.57E-02	1.62E-02	9.90E-03	7.27E-03	5.98E-03	4.75E-03	2.07E-03	1.82E-02	1.83E-02	1.68E-02	1.48E-02	1.19E-02	-7.55E-02	-6.63E-02	-5.23E-02	-3.53E-02	-1.49E-02	-2.05E-02	-3.30E-02	-4.57E-02	-6.94E-02	-1.03E-01
1.89E-03	1.79E-03	1.74E-03	1.67E-03	1.53E-03	1.81E-02	1.89E-02	1.73E-02	1.32E-02	7.34E-03	-2.63E-03	-8.93E-03	-1.51E-02	-1.87E-02	-1.97E-02	7.87E-03	3.37E-03	2.20E-04	4.39E-04	3.73E-03	5.42E-03	2.20E-02	2.98E-02	2.72E-02	2.26E-02	-1.26E-01	-1.17E-01	-7.35E-02	-2.45E-02	5.50E-03
1.33E-03	9.78E-04	4.42E-04	-2.36E-04	-8.37E-04	1.39E-03	-3.14E-03	-5.36E-03	-5.63E-03	-4.60E-03	-1.89E-02	-1.53E-02	-7.61E-03	3.06E-03	1.40E-02	7.54E-03	1.04E-02	1.17E-02	1.12E-02	9.06E-03	2.24E-02	2.27E-02	1.60E-02	1.45E-03	-1.56E-02	2.14E-02	3.42E-02	5.03E-02	7.25E-02	8.85E-02
-1.09E-03	-9.70E-04	-9.20E-04	-1.45E-03	-2.74E-03	-2.60E-03	-9.49E-04	-7.19E-04	-1.56E-03	-2.42E-03	2.09E-02	2.23E-02	2.07E-02	1.74E-02	1.33E-02	4.95E-03	-2.05E-03	-1.22E-02	-2.32E-02	-3.07E-02	-3.27E-02	-4.76E-02	-4.98E-02	-3.74E-02	-2.20E-02	9.35E-02	9.70E-02	9.37E-02	6.68E-02	1.36E-02
-4.49E-03	-6.08E-03	-6.87E-03	-6.62E-03	-5.27E-03	-3.11E-03	-4.05E-03	-5.41E-03	-7.30E-03	-9.83E-03	1.11E-02	1.21E-02	1.53E-02	1.95E-02	2.37E-02	-3.23E-02	-3.09E-02	-3.03E-02	-3.13E-02	-3.20E-02	-8.25E-03	6.11E-03	2.37E-02	4.50E-02	6.25E-02	-4.54E-02	-7.37E-02	-5.84E-02	-2.49E-02	2.20E-03
-3.23E-03	-1.44E-03	-7.43E-04	-1.17E-03	-1.98E-03	-1.24E-02	-1.35E-02	-1.16E-02	-6.08E-03	2.25E-03	2.70E-02	2.80E-02	2.53E-02	1.73E-02	3.27E-03	-2.99E-02	-2.44E-02	-1.63E-02	-7.93E-03	-2.01E-03	6.46E-02	5.29E-02	3.62E-02	1.73E-02	-2.32E-03	1.61E-02	1.93E-02	1.40E-02	8.99E-03	1.58E-02
-2.26E-03	-1.47E-03	3.13E-04	2.41E-03	3.90E-03	1.11E-02	1.78E-02	2.06E-02	2.01E-02	1.81E-02	-1.46E-02	-3.18E-02	-4.42E-02	-5.01E-02	-4.90E-02	1.64E-03	5.28E-03	9.99E-03	1.53E-02	1.93E-02	-1.93E-02	-3.05E-02	-2.95E-02	-1.85E-02	-7.57E-03	3.43E-02	5.08E-02	5.80E-02	5.28E-02	2.80E-02
4.41E-03	4.26E-03	3.83E-03	3.42E-03	3.14E-03	1.55E-02	1.21E-02	8.02E-03	3.89E-03	7.70E-04	-4.24E-02	-3.58E-02	-2.98E-02	-2.09E-02	-7.70E-03	1.99E-02	1.84E-02	1.87E-02	2.40E-02	3.47E-02	2.59E-03	1.60E-02	2.83E-02	3.20E-02	2.76E-02	-1.96E-02	-7.09E-02	-1.01E-01	-1.06E-01	-9.61E-02
2.73E-03	1.94E-03	7.64E-04	-8.07E-04	-2.84E-03	-1.41E-03	-3.41E-03	-4.90E-03	-5.66E-03	-6.55E-03	7.06E-03	1.84E-02	2.34E-02	2.43E-02	2.28E-02	4.94E-02	6.53E-02	7.78E-02	8.43E-02	8.59E-02	1.83E-02	8.41E-05	-3.22E-02	-7.00E-02	-9.12E-02	-8.20E-02	-6.54E-02	-3.99E-02	-7.55E-03	2.17E-02
-5.14E-03	-7.34E-03	-8.77E-03	-8.47E-03	-6.39E-03	-8.70E-03	-1.26E-02	-1.80E-02	-2.39E-02	-2.81E-02	1.90E-02	1.46E-02	1.26E-02	1.33E-02	1.50E-02	8.60E-02	8.72E-02	8.78E-02	8.30E-02	6.93E-02	-8.79E-02	-7.47E-02	-6.51E-02	-5.71E-02	-4.21E-02	4.08E-02	3.82E-02	1.28E-02	-1.91E-02	-4.64E-02
-2.94E-03	1.33E-03	5.54E-03	8.22E-03	8.48E-03	-2.75E-02	-2.11E-02	-1.05E-02	2.10E-03	1.34E-02	1.55E-02	1.27E-02	6.45E-03	-3.57E-04	-3.30E-03	4.63E-02	1.94E-02	-3.26E-03	-1.69E-02	-2.07E-02	-1.94E-02	5.36E-03	3.17E-02	5.15E-02	5.44E-02	-6.11E-02	-6.03E-02	-5.34E-02	-5.10E-02	-4.98E-02
7.18E-03	6.09E-03	5.87E-03	6.09E-03	6.39E-03	2.12E-02	2.52E-02	2.68E-02	2.45E-02	1.65E-02	-1.76E-04	6.25E-03	1.08E-02	1.03E-02	3.97E-03	-2.15E-02	-3.68E-02	-7.57E-02	-1.22E-01	-1.41E-01	4.75E-02	4.48E-02	5.00E-02	5.64E-02	5.44E-02	-3.96E-02	-1.58E-02	1.32E-02	3.84E-02	5.91E-02
6.69E-03	6.71E-03	6.37E-03	5.81E-03	5.07E-03	4.07E-03	-9.35E-03	-1.88E-02	-2.08E-02	-1.76E-02	-6.82E-03	-1.80E-02	-2.38E-02	-2.28E-02	-1.97E-02	-1.17E-01	-7.68E-02	-4.58E-02	-2.92E-02	-2.41E-02	3.64E-02	3.21E-03	-3.35E-02	-6.07E-02	-6.92E-02	7.39E-02	7.37E-02	5.09E-02	1.33E-02	-1.39E-02
4.03E-03	2.69E-03	9.86E-04	-1.41E-03	-4.67E-03	-1.41E-02	-1.25E-02	-1.19E-02	-1.03E-02	-6.20E-03	-1.71E-02	-1.55E-02	-1.50E-02	-1.47E-02	-1.28E-02	-2.33E-02	-1.89E-02	-1.15E-02	-7.42E-03	-7.52E-03	-6.37E-02	-6.11E-02	-6.32E-02	-5.53E-02	-2.66E-02	-1.37E-02	1.10E-03	1.15E-02	1.57E-02	2.13E-02
-8.96E-03	-1.40E-02	-1.80E-02	-1.97E-02	-1.87E-02	6.14E-04	9.27E-03	1.74E-02	2.18E-02	2.06E-02	-7.26E-03	2.25E-03	1.39E-02	2.53E-02	3.33E-02	-4.62E-03	4.85E-03	1.70E-02	2.70E-02	3.21E-02	1.39E-02	4.36E-02	5.11E-02	4.91E-02	5.20E-02	2.96E-02	3.68E-02	4.17E-02	4.83E-02	6.25E-02
-1.46E-02	-9.03E-03	-4.95E-03	-3.22E-03	-1.87E-03	1.35E-02	2.14E-03	-9.82E-03	-1.92E-02	-2.35E-02	3.32E-02	2.46E-02	1.32E-02	4.04E-03	-6.78E-04	2.97E-02	2.00E-02	5.31E-03	-1.27E-02	-3.07E-02	5.69E-02	5.73E-02	5.12E-02	3.69E-02	1.65E-02	8.18E-02	9.50E-02	9.52E-02	8.57E-02	7.23E-02
1.34E-03	6.37E-03	1.11E-02	1.42E-02	1.57E-02	-2.40E-02	-2.44E-02	-2.33E-02	-1.83E-02	-1.02E-02	1.97E-04	5.03E-03	1.08E-02	1.56E-02	1.92E-02	-4.29E-02	-4.33E-02	-3.43E-02	-2.47E-02	-1.69E-02	7.83E-04	-7.59E-03	-1.53E-02	-2.28E-02	-2.14E-02	6.11E-02	5.53E-02	5.21E-02	4.77E-02	4.31E-02
1.44E-02	1.02E-02	4.19E-03	-1.87E-03	-5.69E-03	7.83E-05	1.03E-02	1.72E-02	1.94E-02	1.78E-02	2.20E-02	2.36E-02	2.29E-02	1.93E-02	1.29E-02	-8.04E-03	2.10E-03	9.43E-03	9.14E-03	2.90E-03	-6.25E-04	4.25E-02	9.30E-02	1.29E-01	1.38E-01	4.31E-02	5.23E-02	6.93E-02	8.40E-02	8.50E-02
-5.96E-03	-4.35E-03	-3.46E-03	-4.27E-03	-5.73E-03	1.57E-02	1.66E-02	2.15E-02	2.79E-02	3.21E-02	5.09E-03	-2.57E-03	-8.84E-03	-1.31E-02	-1.53E-02	-1.31E-03	2.99E-04	6.00E-03	1.37E-02	2.26E-02	1.24E-01	1.01E-01	7.23E-02	4.02E-02	2.26E-02	6.91E-02	4.01E-02	7.84E-03	-1.62E-02	-2.86E-02
-6.06E-03	-4.49E-03	-2.13E-03	-4.93E-04	-6.04E-05	3.12E-02	2.39E-02	1.13E-02	-2.77E-03	-1.20E-02	-1.46E-02	-1.07E-02	-6.50E-03	-3.64E-03	-1.45E-03	3.20E-02	4.10E-02	4.96E-02	5.65E-02	6.12E-02	2.22E-02	1.60E-02	-8.30E-03	-4.31E-02	-7.84E-02	-2.86E-02	-2.06E-02	-1.86E-02	-3.12E-02	-5.67E-02
-2.93E-04	-4.97E-04	-4.50E-04	-2.08E-04	1.43E-04	-1.34E-02	-1.10E-02	-8.87E-03	-8.08E-03	-8.53E-03	5.78E-04	2.19E-03	2.97E-03	2.86E-03	2.63E-03	6.66E-02	7.30E-02	7.63E-02	7.32E-02	6.32E-02	-1.08E-01	-1.17E-01	-1.07E-01	-9.96E-02	-1.06E-01	-8.95E-02	-1.12E-01	-1.12E-01	-1.04E-01	-9.37E-02
7.88E-04	2.26E-03	4.50E-03	6.58E-03	7.64E-03	-9.85E-03	-1.07E-02	-1.00E-02	-7.78E-03	-4.47E-03	3.04E-03	4.72E-03	7.69E-03	1.11E-02	1.30E-02	4.63E-02	2.54E-02	8.31E-03	2.40E-03	4.90E-03	-1.16E-01	-1.14E-01	-9.77E-02	-7.68E-02	-6.01E-02	-7.70E-02	-5.22E-02	-2.63E-02	-4.73E-03	6.89E-03
7.69E-03	7.06E-03	5.78E-03	3.88E-03	1.75E-03	-4.37E-04	3.88E-03	7.40E-03	8.52E-03	6.84E-03	1.22E-02	8.50E-03	2.66E-03	-4.44E-03	-1.15E-02	6.43E-03	4.44E-03	3.16E-03	1.97E-03	-5.48E-03	-4.65E-02	-3.18E-02	-1.78E-02	-9.39E-03	-5.67E-03	8.53E-03	8.82E-03	1.05E-02	7.80E-03	-9.14E-04
-4.93E-05	-9.20E-04	-1.34E-04	2.13E-03	4.46E-03	3.35E-03	-8.98E-04	-4.98E-03	-8.13E-03	-1.08E-02	-1.69E-02	-1.91E-02	-1.78E-02	-1.54E-02	-1.40E-02	-2.16E-02	-4.20E-02	-5.97E-02	-6.96E-02	-7.38E-02	-4.76E-03	-6.93E-03	-1.17E-02	-2.05E-02	-3.25E-02	-1.24E-02	-2.26E-02	-2.56E-02	-2.20E-02	-2.10E-02
5.93E-03	6.40E-03	6.14E-03	5.71E-03	5.63E-03	-1.45E-02	-2.00E-02	-2.52E-02	-2.70E-02	-2.47E-02	-1.21E-02	-8.03E-03	-2.30E-03	2.49E-03	4.36E-03	-8.07E-02	-9.42E-02	-1.08E-01	-1.17E-01	-1.19E-01	-4.48E-02	-5.70E-02	-6.83E-02	-7.14E-02	-5.55E-02	-2.46E-02	-2.62E-02	-1.89E-02	-1.37E-03	2.23E-02
5.35E-03	3.63E-03	-6.47E-04	-7.43E-03	-1.48E-02	-2.04E-02	-1.56E-02	-1.13E-02	-9.23E-03	-1.03E-02	3.80E-03	2.27E-03	1.05E-03	6.94E-04	7.53E-04	-1.16E-01	-1.06E-01	-8.67E-02	-5.81E-02	-2.62E-02	-1.63E-02	3.39E-02	7.75E-02	1.07E-01	1.22E-01	4.56E-02	5.81E-02	5.49E-02	4.34E-02	2.97E-02
-1.94E-02	-1.96E-02	-1.64E-02	-1.13E-02	-7.21E-03	-1.28E-02	-1.37E-02	-1.03E-02	-2.29E-03	8.61E-03	1.07E-03	2.09E-03	3.48E-03	4.01E-03	3.19E-03	2.55E-04	1.86E-02	2.87E-02	3.23E-02	3.49E-02	1.17E-01	1.04E-01	1.04E-01	1.16E-01	1.25E-01	1.89E-02	1.54E-02	1.81E-02	2.14E-02	2.16E-02
-5.62E-03	-6.42E-03	-8.50E-03	-9.65E-03	-7.92E-03	1.97E-02	2.73E-02	2.91E-02	2.59E-02	1.97E-02	1.85E-03	9.83E-04	9.16E-04	1.65E-03	3.23E-03	3.77E-02	3.63E-02	2.74E-02	1.47E-02	6.48E-03	1.17E-01	9.16E-02	5.84E-02	3.43E-02	2.79E-02	1.74E-02	8.33E-03	-6.35E-03	-2.52E-02	-4.37E-02
-2.84E-03	4.33E-03	1.11E-02	1.42E-02	1.30E-02	1.18E-02	4.63E-03	1.44E-03	3.51E-03	7.36E-03	5.70E-03	8.31E-03	9.54E-03	8.04E-03	3.62E-03	3.84E-03	1.22E-03	-2.16E-03	-1.92E-03	4.62E-03	3.59E-02	4.80E-02	5.94E-02	6.89E-02	7.49E-02	-5.60E-02	-6.21E-02	-6.62E-02	-7.00E-02	-7.23E-02
9.74E-03	6.46E-03	3.47E-03	5.00E-04	-2.40E-03	7.74E-03	3.35E-03	-3.45E-03	-9.68E-03	-1.34E-02	-2.85E-03	-9.73E-03	-1.45E-02	-1.54E-02	-1.30E-02	1.66E-02	3.05E-02	4.26E-02	5.18E-02	5.79E-02	7.22E-02	5.71E-02	2.92E-02	-5.23E-03	-3.43E-02	-6.95E-02	-6.03E-02	-5.07E-02	-4.58E-02	-3.97E-02
-5.07E-03	-7.58E-03	-8.88E-03	-7.51E-03	-4.16E-03	-1.26E-02	-5.81E-03	4.71E-03	1.58E-02	2.62E-02	-8.18E-03	-1.51E-03	5.66E-03	1.01E-02	9.89E-03	5.84E-02	4.77E-02	2.24E-02	-1.12E-02	-3.54E-02	-4.54E-02	-4.19E-02	-3.75E-02	-3.83E-02	-4.44E-02	-2.29E-02	5.39E-03	3.52E-02	5.31E-02	5.95E-02
2.25E-05	4.97E-03	9.60E-03	1.19E-02	1.07E-02	3.51E-02	3.92E-02	3.57E-02	2.83E-02	2.10E-02	6.52E-03	1.73E-03	-3.28E-03	-6.77E-03	-7.28E-03	-3.78E-02	-2.56E-02	-1.50E-02	-1.44E-02	-1.87E-02	-5.36E-02	-6.16E-02	-6.15E-02	-4.77E-02	-2.17E-02	6.39E-02	7.11E-02	8.18E-02	9.30E-02	9.51E-02
6.78E-03	2.61E-03	2.54E-04	8.44E-05	1.08E-03	1.32E-02	3.93E-03	-4.72E-03	-1.09E-02	-1.56E-02	-4.61E-03	7.63E-04	8.57E-03	1.80E-02	2.70E-02	-2.07E-02	-1.98E-02	-1.91E-02	-1.83E-02	-1.46E-02	6.62E-03	1.97E-02	9.67E-03	-1.32E-02	-4.20E-02	7.69E-02	3.73E-02	-6.72E-03	-3.24E-02	-3.35E-02
2.22E-03	3.10E-03	3.45E-03	3.11E-03	2.03E-03	-2.01E-02	-2.16E-02	-1.90E-02	-1.68E-02	-1.70E-02	3.29E-02	3.32E-02	2.63E-02	1.38E-02	-6.80E-04	-6.85E-03	3.39E-03	1.43E-02	2.27E-02	2.65E-02	-7.48E-02	-1.01E-01	-1.07E-01	-9.90E-02	-9.27E-02	-1.70E-02	2.83E-03	1.

-4.16E-02	-3.49E-02	-2.13E-02	-7.21E-03	-4.01E-04	-2.62E-02	1.70E-03	3.87E-02	6.63E-02	6.98E-02	-2.11E-02	-2.59E-02	-1.95E-02	-2.41E-03	2.13E-02	2.49E-02	2.29E-02	1.75E-02	9.51E-03	4.86E-04	-3.35E-02	-2.91E-02	-3.46E-02	-4.26E-02	-4.37E-02	8.29E-02	7.73E-02	6.34E-02	4.61E-02	3.26E-02
-1.86E-03	-7.87E-03	-1.44E-02	-1.87E-02	-2.04E-02	5.05E-02	2.40E-02	3.57E-03	-8.20E-03	-2.03E-02	4.68E-02	6.71E-02	7.66E-02	7.61E-02	7.06E-02	-8.23E-03	-1.59E-02	-2.33E-02	-3.36E-02	-4.90E-02	-3.25E-02	-1.02E-02	1.38E-02	2.84E-02	2.84E-02	2.03E-02	-7.92E-04	-3.33E-02	-6.15E-02	-7.23E-02
-2.19E-02	-2.45E-02	-2.82E-02	-3.29E-02	-3.81E-02	-4.02E-02	-6.30E-02	-7.25E-02	-6.37E-02	-5.13E-02	6.09E-02	4.35E-02	2.17E-02	2.10E-03	-1.77E-02	-6.88E-02	-8.92E-02	-1.03E-01	-1.02E-01	-8.15E-02	2.13E-02	2.17E-02	3.15E-02	4.21E-02	4.56E-02	-7.66E-02	-8.86E-02	-1.06E-01	-1.18E-01	-1.14E-01
-4.13E-02	-3.87E-02	-2.62E-02	-3.74E-03	2.44E-02	-4.58E-02	-4.46E-02	-4.27E-02	-3.92E-02	-3.51E-02	-4.23E-02	-6.83E-02	-8.69E-02	-9.03E-02	-7.32E-02	-4.98E-02	-2.25E-02	-6.67E-03	3.21E-03	1.03E-02	4.03E-02	2.84E-02	1.66E-02	1.27E-02	1.86E-02	-9.35E-02	-6.50E-02	-4.11E-02	-2.23E-02	-2.61E-03
5.46E-02	8.33E-02	9.37E-02	7.48E-02	3.93E-02	-2.92E-02	-1.44E-02	1.32E-02	4.51E-02	6.80E-02	-3.76E-02	-3.36E-03	8.67E-03	2.45E-03	-5.46E-03	1.13E-02	6.39E-03	-1.70E-03	-1.38E-02	-2.72E-02	2.95E-02	3.68E-02	3.15E-02	1.06E-02	-1.29E-02	1.81E-02	3.40E-02	3.92E-02	2.98E-02	7.96E-03
4.39E-03	-2.04E-02	-3.45E-02	-3.65E-02	-2.63E-02	7.66E-02	7.71E-02	7.44E-02	6.82E-02	5.75E-02	-8.76E-03	-1.33E-02	-2.33E-02	-3.38E-02	-3.83E-02	-3.58E-02	-3.97E-02	-4.35E-02	-4.89E-02	-5.27E-02	-2.34E-02	-2.14E-02	-1.30E-02	1.54E-04	1.55E-02	-1.25E-02	-1.86E-02	-1.23E-02	-7.45E-04	1.34E-02
-9.01E-03	1.32E-02	4.16E-02	6.80E-02	7.90E-02	4.42E-02	3.07E-02	1.57E-02	-2.72E-03	-1.73E-02	-3.72E-02	-3.19E-02	-2.09E-02	-3.31E-03	1.45E-02	-5.00E-02	-3.87E-02	-2.31E-02	-1.10E-02	-4.23E-03	2.66E-02	2.98E-02	2.75E-02	2.16E-02	1.08E-02	2.86E-02	3.93E-02	4.26E-02	4.29E-02	4.57E-02
6.72E-02	3.82E-02	6.69E-03	-1.78E-02	-2.53E-02	-2.10E-02	-1.93E-02	-1.69E-02	-1.23E-02	-4.66E-03	2.42E-02	2.59E-02	2.44E-02	2.27E-02	1.93E-02	-8.94E-04	-1.47E-03	-9.56E-03	-2.30E-02	-2.92E-02	-4.31E-03	-1.91E-02	-2.70E-02	-2.65E-02	-2.39E-02	5.29E-02	6.23E-02	6.93E-02	6.84E-02	5.61E-02
-1.77E-02	-1.09E-02	-1.27E-02	-2.15E-02	-3.48E-02	1.87E-03	5.82E-03	1.23E-02	2.63E-02	4.51E-02	1.20E-02	3.15E-03	-1.78E-03	-1.23E-03	3.81E-03	-1.86E-02	5.71E-03	3.04E-02	4.58E-02	5.32E-02	-2.60E-02	-3.28E-02	-4.12E-02	-4.83E-02	-5.12E-02	3.40E-02	9.33E-03	-1.25E-02	-2.91E-02	-3.81E-02
-4.91E-02	-5.97E-02	-6.56E-02	-6.83E-02	-6.63E-02	6.13E-02	6.97E-02	6.89E-02	5.83E-02	3.92E-02	1.29E-02	2.46E-02	3.44E-02	3.93E-02	3.94E-02	5.66E-02	5.48E-02	4.66E-02	3.51E-02	2.54E-02	-4.57E-02	-2.84E-02	-1.69E-03	2.71E-02	5.34E-02	-4.16E-02	-4.22E-02	-3.71E-02	-2.29E-02	-5.87E-03
-5.70E-02	-4.22E-02	-2.98E-02	-2.31E-02	-1.60E-02	2.13E-02	1.47E-02	1.49E-02	1.04E-02	-4.90E-03	3.52E-02	2.59E-02	1.27E-02	1.33E-03	-4.31E-03	2.16E-02	2.41E-02	2.82E-02	2.91E-02	2.57E-02	7.39E-02	8.28E-02	7.28E-02	4.42E-02	1.55E-02	4.99E-03	1.03E-02	1.29E-02	1.08E-02	4.07E-03
-5.15E-03	5.57E-03	1.38E-02	2.20E-02	3.09E-02	-1.80E-02	-1.78E-02	-1.53E-02	-1.94E-02	-2.77E-02	-7.66E-03	-1.38E-02	-2.43E-02	-3.67E-02	-4.67E-02	2.00E-02	1.45E-02	1.05E-02	6.68E-03	-1.10E-03	2.90E-03	1.91E-03	3.18E-03	7.92E-03	2.32E-02	-2.71E-03	-8.53E-03	-1.32E-02	-1.52E-02	-1.52E-02
3.78E-02	4.06E-02	3.92E-02	3.31E-02	2.33E-02	-3.41E-02	-3.65E-02	-3.62E-02	-3.60E-02	-3.83E-02	-4.75E-02	-3.18E-02	2.60E-03	4.48E-02	8.07E-02	-1.51E-02	-3.32E-02	-5.04E-02	-6.28E-02	-6.69E-02	4.73E-02	6.67E-02	7.23E-02	6.77E-02	5.91E-02	-1.54E-02	-1.69E-02	-1.85E-02	-1.71E-02	-1.05E-02
1.50E-02	1.27E-02	1.47E-02	1.67E-02	1.68E-02	-4.27E-02	-4.70E-02	-4.92E-02	-4.78E-02	-4.14E-02	1.05E-01	1.13E-01	1.02E-01	8.57E-02	8.01E-02	-5.87E-02	-3.65E-02	-7.87E-03	1.16E-02	1.39E-02	4.58E-02	2.20E-02	-1.02E-02	-4.01E-02	-5.95E-02	7.63E-04	1.16E-02	1.90E-02	2.64E-02	3.76E-02
1.66E-02	1.99E-02	2.84E-02	3.90E-02	4.58E-02	-2.95E-02	-1.30E-02	4.88E-03	2.27E-02	4.24E-02	7.79E-02	6.63E-02	4.81E-02	3.21E-02	1.56E-02	6.31E-03	-5.61E-04	-1.38E-03	3.88E-03	1.23E-02	-6.98E-02	-7.57E-02	-8.07E-02	-8.35E-02	-7.90E-02	5.00E-02	5.58E-02	4.99E-02	3.48E-02	1.90E-02
4.71E-02	4.60E-02	4.25E-02	3.18E-02	1.02E-02	5.99E-02	6.89E-02	6.81E-02	5.38E-02	2.21E-02	-8.13E-03	-3.58E-02	-5.61E-02	-5.83E-02	-3.73E-02	2.11E-02	3.04E-02	4.16E-02	5.44E-02	6.49E-02	-6.68E-02	-5.58E-02	-5.17E-02	-4.87E-02	-3.81E-02	9.89E-03	7.36E-03	5.99E-03	2.41E-03	-3.37E-03
-1.65E-02	-3.89E-02	-5.22E-02	-5.32E-02	-4.45E-02	-1.87E-02	-5.40E-02	-7.41E-02	-8.09E-02	-8.15E-02	2.27E-03	3.81E-02	4.99E-02	4.25E-02	3.38E-02	6.59E-02	5.35E-02	2.87E-02	-5.97E-03	-4.38E-02	-1.91E-02	1.28E-03	1.67E-02	2.79E-02	3.33E-02	-1.07E-02	-1.81E-02	-2.23E-02	-2.15E-02	-1.81E-02
-3.63E-02	-3.16E-02	-2.45E-02	-1.33E-02	-3.43E-03	-7.50E-02	-6.39E-02	-5.70E-02	-5.35E-02	-4.14E-02	3.30E-02	3.34E-02	2.18E-02	-1.52E-03	-2.51E-02	-7.39E-02	-8.54E-02	-8.28E-02	-7.98E-02	-7.88E-02	2.87E-02	1.50E-02	1.05E-03	-3.11E-03	5.33E-03	-1.46E-02	-1.12E-02	-8.56E-03	-7.76E-03	-8.22E-03
4.95E-03	1.73E-02	3.12E-02	3.84E-02	3.37E-02	-1.61E-02	1.21E-02	3.00E-02	3.51E-02	3.21E-02	-4.35E-02	-5.25E-02	-5.00E-02	-4.43E-02	-3.94E-02	-7.21E-02	-5.33E-02	-2.57E-02	-2.55E-04	1.99E-02	2.17E-02	3.82E-02	4.39E-02	3.29E-02	1.43E-02	-8.38E-03	-7.03E-03	-3.41E-03	2.98E-03	1.15E-02
1.79E-02	-9.11E-04	-1.26E-02	-1.57E-02	-1.48E-02	2.34E-02	5.42E-03	-1.62E-02	-2.79E-02	-2.99E-02	-2.72E-02	-2.87E-03	2.76E-02	5.59E-02	6.81E-02	4.07E-02	6.35E-02	7.78E-02	7.32E-02	5.30E-02	7.28E-04	-5.20E-03	-6.83E-03	-6.57E-03	-3.76E-03	1.90E-02	1.95E-02	8.97E-03	-8.66E-03	-2.40E-02
-1.26E-02	-8.62E-03	-5.07E-03	-6.36E-03	-1.35E-02	-3.25E-02	-4.14E-02	-5.21E-02	-5.47E-02	-3.94E-02	6.61E-02	6.94E-02	7.66E-02	7.31E-02	5.53E-02	2.75E-02	7.76E-03	6.32E-04	3.46E-03	1.25E-02	4.00E-03	1.80E-02	3.39E-02	4.62E-02	5.55E-02	-3.13E-02	-3.19E-02	-2.78E-02	-2.06E-02	-1.13E-02
-2.36E-02	-3.13E-02	-3.15E-02	-2.30E-02	-9.40E-03	-3.59E-03	4.06E-02	6.70E-02	6.68E-02	5.87E-02	3.47E-02	2.27E-02	2.38E-02	3.14E-02	3.28E-02	2.77E-02	4.77E-02	6.46E-02	6.94E-02	5.72E-02	6.52E-02	7.44E-02	7.81E-02	7.25E-02	5.64E-02	-2.36E-03	4.76E-03	1.27E-02	2.39E-02	3.47E-02
3.94E-03	1.20E-02	1.27E-02	8.71E-03	3.74E-03	5.83E-02	6.38E-02	6.42E-02	5.31E-02	3.57E-02	2.56E-02	1.85E-02	1.61E-02	1.39E-02	9.70E-03	3.04E-02	-1.23E-03	-2.47E-02	-3.65E-02	-4.30E-02	3.59E-02	1.97E-02	9.90E-03	4.03E-03	1.42E-03	3.94E-02	3.80E-02	3.20E-02	2.08E-02	5.71E-03
-9.94E-04	-5.76E-03	-7.52E-03	-1.73E-03	1.24E-02	2.40E-02	2.24E-02	2.39E-02	2.10E-02	1.28E-02	5.40E-03	1.70E-03	-3.72E-03	-1.28E-02	-2.39E-02	-4.77E-02	-4.66E-02	-3.39E-02	-9.74E-03	1.50E-02	2.00E-03	2.08E-03	-1.02E-03	-5.43E-03	-9.30E-03	-6.39E-03	-1.09E-02	-1.04E-02	-9.29E-03	-9.31E-03
3.10E-02	4.43E-02	4.29E-02	2.62E-02	2.42E-03	3.45E-03	-2.61E-03	-2.03E-03	6.19E-03	1.79E-02	-3.71E-02	-5.42E-02	-7.33E-02	-9.01E-02	-9.56E-02	2.99E-02	3.59E-02	3.48E-02	2.63E-02	1.15E-02	-1.31E-02	-1.70E-02	-2.07E-02	-2.43E-02	-2.85E-02	-9.46E-03	-7.50E-03	-3.33E-03	-6.87E-05	-4.51E-04
-1.81E-02	-3.05E-02	-3.20E-02	-2.52E-02	-1.81E-02	2.62E-02	2.72E-02	1.99E-02	3.39E-03	-2.09E-02	-8.68E-02	-7.34E-02	-6.14E-02	-5.25E-02	-4.64E-02	-8.16E-03	-2.59E-02	-3.32E-02	-3.12E-02	-2.57E-02	-3.36E-02	-3.94E-02	-4.50E-02	-4.74E-02	-4.21E-02	-4.12E-03	-9.21E-03	-1.32E-02	-1.40E-02	-1.15E-02
-1.17E-02	2.89E-04	1.96E-02	3.80E-02	4.75E-02	-4.34E-02	-5.10E-02	-4.50E-02	-3.75E-02	-3.08E-02	-3.93E-02	-2.60E-02	-4.35E-03	2.35E-02	5.01E-02	-1.71E-02	-3.56E-03	1.02E-02	1.62E-02	1.03E-02	-2.52E-02	2.57E-03	3.24E-02	5.61E-02	7.46E-02	-6.79E-03	-1.77E-03	1.66E-03	3.02E-03	3.44E-03
4.98E-02	4.91E-02	4.68E-02	4.44E-02	4.51E-02	-1.72E-02	5.06E-03	2.73E-02	3.41E-02	2.58E-02	6.98E-02	8.30E-02	9.02E-02	9.05E-02	8.86E-02	-5.77E-03	-2.42E-02	-3.66E-02	-4.14E-02	-4.30E-02	9.23E-02	1.08E-01	1.15E-01	1.04E-01	7.21E-02	3.95E-03	4.60E-03	4.77E-03	3.89E-03	1.91E-03
4.91E-02	5.34E-02	5.49E-02	5.34E-02	4.99E-02	2.25E-02	3.21E-02	4.62E-02	5.62E-02	6.15E-02	8.83E-02	8.30E-02	6.39E-02	3.45E-02	7.90E-03	-4.32E-02	-3.96E-02	-2.86E-02	-1.15E-02	5.55E-03	2.65E-02	-2.17E-02	-6.28E-02	-9.24E-02	-1.12E-01	-4.92E-04	-2.15E-03	-2.53E-03	-2.23E-03	-2.13E-03
4.39E-02	3.40E-02	1.87E-02	-9.50E-05	-1.53E-02	6.29E-02	5.74E-02	4.14E-02	1.85E-02	-2.81E-03	-8.48E-03	-1.73E-02	-2.51E-02	-3.89E-02	-5.81E-02	2.12E-02	4.27E-02	7.18E-02	9.92E-02	1.07E-01	-1.17E-01	-9.80E-02	-5.42E-02	-8.20E-03	1.40E-02	-2.70E-03	-3.90E-03	-5.32E-03	-6.28E-03	-5.74E-03
-2.19E-02	-2.54E-02	-3.50E-02	-5.22E-02	-6.91E-02	-2.23E-02	-4.45E-02	-6.16E-02	-6.80E-02	-6.62E-02	-7.43E-02	-8.34E-02	-8.55E-02	-7.66E-02	-5.19E-02	8.74E-02	5.76E-02	3.24E-02	1.66E-02	5.64E-03	1.76E-02	2.34E-02	4.09E-02	6.36E-02	7.79E-02	-2.61E-03	3.42E-03	1.06E-02	1.51E-02	1.41E-02
-7.91E-02	-8.29E-02	-8.25E-02	-7.83E-02	-7.05E-02	-5.40E-02	-3.33E-02	-1.72E-02	-1.39E-02	-1.82E-02	-1.78E-02	9.77E-03	2.16E-02	1.65E-02	-3.20E-03	-1.20E-02	-3.62E-02	-5.71E-02	-7.59E-02	-8.92E-02	7.01E-02	3.36E-02	-2.06E-02	-6.40E-02	-7.87E-02	1.08E-02	9.84E-03	1.19E-02	1.45E-02	1.55E-02
-6.15E-02	-5.62E-02	-5.60E-02	-5.79E-02	-5.86E-02	-2.11E-02	-1.82E-02	-8.89E-03	4.47E-03	1.99E-02	-2.72E-02	-4.19E-02	-4.49E-02	-4.36E-02	-4.25E-02	-8.40E-02	-6.07E-02	-3.77E-02	-3.06E-02	-3.34E-02	-7.32E-02	-6.41E-02	-6.22E-02	-6.49E-02	-5.69E-02	1.38E-02	1.01E-02	6.81E-03	5.15E-03	4.30E-03
-5.63E-02	-5.07E-02	-4.31E-02	-3.63E-02	-3.38E-02	3.65E-02	5.14E-02	5.96E-02	5.49E-02	3.36E-02	-3.72E-02	-2.25E-02	-2.22E-03	1.31E-02	1.84E-02	-3.16E-02	-2.14E-02	-1.33E-02	-9.82E-03	-2.56E-03	-2.61E-02	1.96E-02	5.13E-02	4.97E-02	3.19E-02	3.36E-03	2.22E-03	1.03E-03	-2.03E-04	-1.55E-03
-3.92E-02	-5.07E-02	-5.98E-02	-5.88E-02	-4.74E-02	2.99E-03	-2.44E-02	-4.43E-02	-5.67E-02	-6.01E-02	1.79E-02	1.67E-02	1.78E-02	2.25E-02	3.03E-02	6.25E-03	8.22E-03	3.31E-03	-2.94E-03	-8.90E-03	2.39E-02	3.10E-02	4.22E-02	4.46E-02	3.16E-02	-3.03E-03	-4.68E-03	-6.50E-03	-8.24E-03	-9.32E-03
-3.04E-02	-1.38E-02	-1.73E-03	4.00E-03	6.47E-03	-5.77E-02	-5.82E-02	-6.48E-02	-7.12E-02	-6.89E-02	3.90E-02	4.70E-02	5.45E-02	6.12E-02	6.43E-02	-1.36E-02	-1.37E-02	-8.99E-03	-4.69E-03	-4.31E-03	7.45E-03	-1.29E-02	-2.00E-02	-2.14E-02	-2.67E-02	-9.12E-03	-7.10E-03	-3.21E-03	1.28E-03	4.49E-03
1.30E-02	2.58E-02	4.19E-02	5.80E-02	7.21E-02	-5.59E-02	-4.08E-02	-3.30E-02	-2.99E-02	-2.25E-02	5.91E-02	4.22E-02	1.62E-02	-6.37E-03	-1.68E-02	-6.85E-03	-9.98E-03	-1.25E-02	-1.35E-02	-1.18E-02	-3.49E-02	-3.81E-02	-3.00E-02	-1.09E-02	1.59E-02	5.80E-03	5.86E-03	5.40E-03	4.94E-03	4.80E-03
7.99E-02	7.94E-02	7.41E-02	6.57E-02	5.10E-02	-6.55E-03	1.45E-02	3.84E-02	6.82E-02	1.03E-01	-2.01E-02	-2.15E-02	-1.82E-02	-5.97E-03	1.07E-02	-5.93E-03	4.47E-03	1.67E-02	3.01E-02	4.79E-02	4.70E-02	7.01E-02	7.42E-02	6.80E-02	6.49E-02	4.64E-03	3.90E-03	2.71E-03	1.79E-03	1.47E-03
2.81E-02	3.02E-03	-1.17E-02	-1.33E-02	-9.86E-03	1.30E-01	1.37E-01	1.24E-01	9.63E-02	6.33E-02	2.15E-02	2.23E-02	1.64E-02	7.07E-03	-2.50E-03	6.47E-02	7.11E-02	6.63E-02	5.28E-02	3.08E-02	6.88E-02	7.63E-02	8.25E-02	8.41E-02	8.12E-02	1.50E-03	1.60E-03	1.89E-03	2.55E-03	3.42E-03
-3.21E-03	8.59E-03	2.52E-02	4.02E-02	4.96E-02	3.79E-02	1.87E-02	-8.53E-03	-4.56E-02	-7.61E-02	-8.51E-03	-8.88E-03	-2.80E-03	1.23E-02	3.84E-02	7.25E-03	-5.99E-03	-7.07E-03	-3.30E-03	2.30E-03	7.64E-02	7.23E-02	6.69E-02	5.53E-02	3.60E-02	4.11E-03	4.48E-03	4.62E-03	4.48E-03	4.00E-03
5.71E-02	6.53E-02	7.01E-02	6.39E-02	4.41E-02	-8.99E-02	-9.11E-02	-8.09E-02	-5.76E-02	-2.56E-02	6.99E-02	8.77E-02	7.81E-02	4.74E-02	4.23E-03	1.24E-02	2.60E-02	3.61E-02	4.02E-02	4.32E-02	1.28E-02	-6.30E-03	-1.67E-02	-2.13E-02	-2.73E-02	3.51E-03	3.33E-03	3.36E-03	3.29E-03	2.97E-03
1.90E-02	3.99E-03	5.34E-03	1.32E-02	1.57E-02	-1.35E-03	2.37E-03	-6.93E-03	-1.39E-02	-1.33E-02	-3.86E-02	-6.54E-02	-6.52E-02	-4.67E-02	-3.30E-02	4.99E-02	6.00E-02	6.99E-02	7.48E-02	7.01E-02	-3.91E-02	-5.57E-02	-7.37E-02	-8.92E-02	-9.81E-02	2.46E-03	1.96E-03	1.62E-03	1.41E-03	1.23E-03
1.04E-02	1.44E-03	-8.24E-03	-1.79E-02	-2.71E-02	-1.24E-02	-1.97E-02	-3.43E-02	-4.75E-02	-5.35E-02	-2.88E-02	-2.15E-02	-5.00E-03	1.07E-02	1.57E-02	5.29E-02	2.72E-02	-5.02E-04	-2.86E-02	-5.21E-02	-9.63E-02	-8.27E-02	-6.34E-02	-4.77E-02	-3.60E-02	1.05E-03	9.21E-04	9.06E-04	1.01E-03	1.16E-03
-3.38E-02	-3.48E-02	-2.72E-02	-1.09E-02	6.99E-03	-5.31E-02	-4.82E-02	-3.83E-02	-2.48E-02	-1.31E-02	1.27E-02	9.89E-03	1.05E-02	1.33E-02	1.54E-02	-6.98E-02	-8.35E-02	-8.23E-02	-6.45E-02	-4.37E-02	-2.19E-02	-3.96E-03	1.14E-02	1.89E-02	1.62E-02	1.22E-03	1.18E-03	1.10E-03	9.84E-04	7.97E-04
1.68E-02	1.50E-02	3.47E-03	-1.41E-02	-2.95E-02	-7.70E-03	-7.67E-03	-1.19E-02	-2.27E-02	-4.19E-02	1.46E-02	1.08E-02	5.35E-03	-4.38E-04	-5.54E-03	-2.88E-02	-2.07E-02	-1.47E-02	-4.33E-03	1.02E-02	2.47E-03	-1.76E-02	-3.23E-02	-3.45E-02	-2.55E-02	5.08E-04	1.56E-04	-2.21E-04	-6.30E-04	-9.93E-04
-3.31E-02	-2.27E-02	-3.79E-03	1.40E-02	2.31E-02	-6.43E-02	-7.82E-02	-7.88E-02	-7.26E-02	-6.54E-02	-9.50E-03	-1.35E-02	-1.87E-02	-2.48E-02	-3.13E-02	1.72E-02	8.82E-03	-7.99E-03	-2.46E-02	-3.68E-02	-8.36E-03	1.44E-02	3.69E-02	5.35E-02	6.53E-02	-1.15E-03	-1.05E-03	-8.16E-04	-5.76E-04	-3.41E-04
2.42E-02	2.23E-02	2.05E-02	2.07E-02	2.35E-02	-5.63E-02	-4.56E-02	-3.68E-02	-2.85E-02	-1.39E-02	-3.80E-02	-4.44E-02	-4.94E-02	-5.13E-02	-4.90E-02	-4.47E-02	-5.24E-02	-6.31E-02	-7.60E-02	-8.90E-02	6.64E-02	4.96E-02	1.83E-02	-1.59E-02	-4.84E-02	-1.12E-04	4.39E-05	9.67E-05	8.97E-05	5.59E-05
2.80E-02	3.27E-02	3.76E-02	4.36E-02	5.11E-02	7.49E-03	3.03E-02	4.75E-02	5.27E-02	4.40E-02	-4.32E-02	-3.49E-02	-2.54E-02	-2.07E-02	-2.80E-02	-1.06E-01	-1.30E-01	-1.50E-01	-1.47E-01	-1.10E-01	-7.89E-02	-9.35E-02	-7.88E-02	-4.92E-02	-2.49E-02	-1.09E-05	-1.15E-04	-2.17E-04	-2.76E-04	-3.06E-04
5.86E-02	6.24E-02	5.82E-02	4.33E-02	1.98E-02	2.54E-02	8.88E-03	4.51E-03	8.50E-03	1.20E-02	-4.65E-02	-6.50E-02	-7.36E-02	-7.24E-02	-6.49E-02	-5.53E-02	-1.16E-02	1.12E-02	2.70E-02	4.88E-02	-4.91E-03	1.41E-02	2.94E-02	4.55E-02	6.67E-02	-3.41E-04	-3.86E-04	-4.13E-04	-4.04E-04	-3.77E-04
-4.63E-03	-2.32E-02	-3.40E-02	-3.60E-02	-3.01E-02	1.09E-02	5.69E-03	-2.72E-03	-1.40E-02	-2.67E-02	-5.32E-02	-4.07E-02	-3.28E-02	-2.97E-02	-2.42E-02	7.41E-02	8.98E-02	8.66E-02	7.08E-02	5.18E-02	8.49E-02	9.16E-02	9.18E-02	9.14E-02	8.89E-02	-3.60E-04	-3.57E-04	-3.55E-04	-3.47E-04	-3.39E-04
-2.18E-02	-1.48E-02	-8.25E-03	-5.10E-03	-1.33E-02	-3.83E-02	-4.57E-02	-4.59E-02	-3.68E-02	-2.11E-02	-8.43E-03	1.89E-02	4.99E-02	7.24E-02	8.11E-02	3.25E-02	1.57E-02	3.70E-03	-3.46E-03	-2.02E-03	7.58E-02	4.43E-02	2.36E-04	-4.19E-02	-7.37E-02	-3.38E-04	-3.44E-04	-3.52E-04	-3.64E-04	-3.81E-04
-3.10E-02	-4.18E-02	-3.37E-02	-1.19E-02	6.87E-03	-6.99E-03	2.11E-03	1.33E-02	3.51E-02	7.05E-02	8.08E-02	7.67E-02	6.92E-02	5.66E-02	3.89E-02	1.44E-02	4.55E-02	7.73E-02	9.67E-02	1.05E-01	-9.46E-02	-1.07E-01	-1.13E-01	-1.14E-01	-1.16E-01	-4.03E-04	-4.24E-04	-4.40E-04	-4.51E-04	-4.61E-04
8.10E-03	-9.96E-03	-3.93E-02	-6.39E-02	-7.16E-02	1.12E-01	1.44E-01	1.48E-01	1.31E-01	1.11E-01	2.34E-02	1.63E-02	1.43E-02	1.10E-02	3.93E-03	1.05E-01	8.95E-02	5.35E-02	5.05E-03	-3.63E-02	-1.19E-01	-1.17E-01	-1.03E-01	-8.50E-02	-6.39E-02	-4.72E-04	-4.83E-04	-4.95E-04	-5.08E-04	-5.21E-04
-6.69E-02	-5.87E-02	-4.75E-02	-3.15E-02	-1.70E-02	9.47E-02	7.35E-02	4.16E-02	5.65E-03	-1.59E-02	-5.06E-03	-1.30E-02	-1.83E-02	-2.11E-02	-2.01E-02	-6.22E-02	-8.10E-02	-9.97E-02	-1.12E-01	-1.06E-01	-3.52E-02	-1.30E-03	1.74E-02	6.46E-03	-1.22E-02	-5.34E-04	-5.47E-04	-5.59E-04	-5.72E-04	-5.84E-04
-1.27E-02	-1.67E-02	-1.95E-02	-1.34E-02	2.19E-03	-2.04E-02	-2.68E-02	-4.80E-02	-8.12E-02	-1.07E-01	-1.28E-02	4.90E-04	1.52E-02	2.68E-02	3.50E-02	-7.25E-02	-2.46E-02	1.25E-02	2.85E-02	3.55E-02	-1.08E-02	8.69E-03	2.97E-02	4.34E-02	4.97E-02	-5.97E-04	-6.09E-04	-6.22E-04	-6.33E-04	-6.45E-04
2.27E-02	3.93E-02	4.33E-02	3.27E-02	1.13E-02	-1.17E-01	-1.23E-01	-1.31E-01	-1.34E-01	-1.22E-01	4.05E-02	4.12E-02	3.29E-02	1.43E-02	-6.27E-03	4.45E-02	5.40E-02	5.61E-02	4.76E-02	3.12E-02	5.47E-02	6.58E-02	8.15E-02	8.76E-02	6.84E-02	-6.57E-04	-6.68E-04	-6.79E-04	-6.90E-04	
-1.22E-02	-2.52E-02	-2.28E-02	-1.54E-02	-1.31E-02	-1.00E-01	-8.00E-02	-6.72E-02	-5.44E-02	-3.24E-02	-1.58E-02	-7.30E-03	1.63E-02	4.23E-02	5.73E-02	1.22E-02	-3.59E-03	-1.27E-02	-1.59E-02	-1.60E-02	2.01E-02	-4.07E-02	-7.90E-02	-7.18E-02	-4.33E-02					
-1.31E-02	-7.77E-03	4.74E-03	1.68E-02	1.94E-02	-2.53E-03	2.95E-02	6.04E-02	8.28E-02	8.87E-02	6.00E-02	5.61E-02	4.96E-02	3.98E-02	2.56E-02	-1.16E-02	1.79E-03	2.33E-02	4.08E-02	4.30E-02	-3.11E-02	-4.07E-02	-5.76E-02	-7.21E-02	-8.05E-02					
1.09E-02	-4.64E-03	-1.94E-02	-2.30E-02	-9.71E-03	7.93E-02	5.91E-02	3.38E-02	1.67E-02	1.29E-02	1.15E-02	3.66E-03	1.05E-03	-1.50E-03	-4.72E-03	3.07E-02	1.18E-02	-5.55E-03